TECHNISCHE
UNIVERSITÄT
WIEN
Vienna | Austria

New Approaches In Vibrational Spectroscopy For Particle Sensing At The Micro- And Nanoscale

A thesis submitted for the degree of
Doctor of Technical Sciences

at
Technische Universität Wien
Faculty of Technical Chemistry
Institute of Chemical Technologies and Analytics
Division Environmental Analytics, Process Analytics and Sensors

under the supervision of
Prof. Dr. Bernhard Lendl

defended by
Karin Wieland
0826345

_____   _____
Place, Date   Karin Wieland

When you cannot measure it, when you cannot express it in numbers, your knowledge is of a meager and unsatisfactory kind.

Sir William Thomson, Lord Kelvin (1824-1901)
"Electrical Units of Measurement" lecture 1883

II

Kurzfassung

Diese Arbeit beinhaltet die Anwendung der Schwingungsspektroskopie zur off-line und in-line Analyse von Partikelsystemen (*P. chrysogenum* Sporen, Stärke Partikel, PMMA Partikel, liposomale Nanocarrier) im Mikro- und Nanomaßstab.

Off-line Raman Mikrospektroskopie wurde in Kombination mit einer PLS-DA verwendet, um eine Klassifizierung zwischen lebenden und toten *P. chrysogenum* Sporen (≈ 1-3 µm im Durchmesser) zu erzielen. Informationen bezüglich der Lebensfähigkeit von Organismen, die in der pharmazeutischen Industrie zur Produktion von Wirkstoffen eingesetzt werden, ist wichtig im Bezug auf optimale Prozessführung, um bessere Fermenter-Auslastungen und höhere Produkterträge zu erreichen. Während die Klassifizierung anhand von off-line Raman Spektroskopie erfolgreich gezeigt werden konnte, leidet die in-line Spektroskopie von Partikeln in einer Suspension oft an einer verhältnismäßig geringeren Signalstärke. Durch die Kombination von in-line Raman Sonden und dem Prinzip der Ultraschall Partikelmanipulation kann die Empfindlichkeit von in-line Messungen deutlich verbessert und zusätzlich ein gewisses Maß an Selektivität erreicht werden. Dazu wurden 2 Prototypen mit unterschiedlichen Geometrien als Aufsatz für in-line Raman Sonden entwickelt und anhand von zwei Partikelsystemen (Stärke und PMMA Partikel) mit einem Durchmesser im unteren Mikrometerbereich charakterisiert. Unter Beachtung der Vorgaben der FDA (Food and Drug Administration), um den Einsatz in der (Bio-)Prozessüberwachung zu ermöglichen, wurden die Prototypen aus 1.4404 Edelstahl gefertigt und an die Geometrie an jene eines D25 Ingold-Stutzens adaptiert. Der Aufsatz ermöglicht die Ausbildung eines stehenden Ultraschall-Feldes, in dessen Knotenebenen Partikel aufkonzentriert werden können. Durch die Aufkonzentrierung der Partikel im Fokus des Raman Lasers konnte in der parallelen Anordnung von Raman Laser und Schallwellenausbreitungsrichtung eine ≈ 30-fache Erhöhung der Empfindlichkeit gezeigt werden. Sind Raman Laser und Schallwellenausbreitungsrichtung im rechten Winkel zueinander angeordnet, so gewinnt man zusätzlich Selektivität für die in-line Messungen. Je nach Frequenz des Ultraschalls kann selektiv die flüssige oder feste Phase (Partikel) in den Fokus des Raman Lasers gebracht werden, was die separate Untersuchung von beiden Phasen in gerührten Suspensionen ermöglicht.

Darüber hinaus wurden im Rahmen dieser Arbeit Partikel im sub-Mikrometerbereich (Liposome mit einem Durchmesser von ≈ 100 nm) anhand der Schwingungsspektroskopie untersucht. Liposome werden zum Transport von hoch toxischen oder reaktiven Wirkstoffen verwendet. Diese werden von der Lipid-Doppelschicht eingeschlossen, wobei das Liposom eine schützende Hülle um den Wirkstoff bildet und somit für einen sicheren Transport z. B zum Tumor, wo der Wirkstoff freigesetzt werden soll, sorgt. Die Variabilität bei der Herstellung dieser Transportvesikel führt allerdings zu unterschiedlichen Verkapselungseffizienzen (= Menge an Wirkstoff, die tatsächlich im einzelnen Liposom verkapselt ist). Daher ist die Untersuchung der Verkapselungseffizienz in einzelnen

Nanocarriern besonders wichtig im Bezug auf Arzneimittelzulassung, um die Menge des tatsächlich verabreichten Wirkstoffes zu bestimmen. Unterschiedliche experimentelle Ansätze basierend auf IR und Raman Spektroskopie, zwei optische Methoden, deren laterale Auflösung durch das Beugungslimit begrenzt ist, werden in dieser Arbeit gezeigt. Während konfokale Raman und SNOM-SERS Spektroskopie wenig erfolgversprechende Ergebnisse lieferten, erlaubt die Kombination von IR Spektroskopie und Rasterkraftmikroskopie (AFM-IR) die Detektion von chemischer Information mit einer lateralen Auflösung von ≤ 20 nm. Bei Verwendung der Resonanz-verstärkten AFM-IR Spektroskopie im Kontakt-Mode sind aufgrund der mechanischen Eigenschaften der Probe (weich, mechanisch nachgebend) einige Probleme zu berücksichtigen wie beispielsweise die geringe Kraftübertragung von der Probe auf die Spitze des AFM Cantilevers oder hohe Scherkräfte, die auf die Probe wirken. Bessere Ergebnisse konnten anhand der AFM-IR Spektroskopie im Tapping-Mode erzielt werden. Dabei wird das Messsignal durch eine heterodyne Detektion ausgelesen, was den qualitativen Nachweis des chemotherapeutischen Wirkstoffs in einzelnen Liposomen basierend auf der spezifischen Absorption im mittleren Infrarot-Bereich ermöglichte. Dabei konnten eine laterale Auflösung von ≈ 10 nm und eine Empfindlichkeit, die die Wirkstoff-Detektion im Zeptomol-Bereich erlaubt, gezeigt werden.

ABSTRACT

In this thesis, vibrational spectroscopy is employed for in-line and off-line analysis of particle systems (*P. chrysogenum* spores, starch particles, PMMA particles, liposomal nanocarriers) at the micro- and nanoscale.

Off-line Raman micor-spectroscopy in combination with PLS-DA was used to develop a classifier that differentiates *P. chrysogenum* spores (≈ 1-3 μm in diameter) based on their viability. Knowledge on the viability of organisms used in the pharmaceutical industry is directly linked to optimized process control, better work-loads and higher yields. However, while the classification of living and dead spores based on off-line Raman spectroscopy was demonstrated, the Raman signal of particles in a suspension detected by in-line probes usually suffers from low signal sensitivity. Leveraging ultrasonic particle manipulation in combination with in-line probes, two prototypes with different geometries were designed as add-on for Raman in-line probes and characterized with particles in the lower μm-range (starch and PMMA) to allow in-line measurements with increased sensitivity and selectivity. Two custom-made prototypes fabricated out of 1.4404 stainless-steel were designed to fit a D25 Ingold port and ensuring FDA-compatibility to enable applications in (bio-)process monitoring. These add-ons allow to build-up an acoustic resonator in front of the Raman probe resulting in the formation of an ultrasonic quasi-standing wave field that enables accumulation of particles in the nodal planes. An increase in sensitivity of ≈ 30 was demonstrated by accumulating particles in the focus of the Raman laser (parallel arrangement of Raman laser and acoustic wave propagation). Furthermore, the perpendicular arrangement of ultrasonic wave and laser propagation allows to add selectivity to Raman in-line sensing; depending on the ultrasonic frequency, either the liquid or solid phase can be moved in the laser focus allowing selective investigation of both components of stirred suspensions.

Furthermore, this thesis reports on the research efforts made for the characterization of even smaller particles: liposomes with a diameter of ≈ 100 nm. Liposomes are used as drug delivery systems, especially for highly toxic or reactive substances where the lipid bilayer forms a protective shell around the encapsulated cargo. However, variabilities in liposome preparation necessitate the investigation of encapsulation efficiency in individual nanocarriers to ensure drug approval and efficacy. Experimental results based on IR and Raman spectroscopy which are both optical-based methods and, hence, diffraction-limited in the achievable spatial resolution, are illustrated. Confocal Raman and SNOM-SERS spectroscopy are shown having minor success for the investigation of such small samples. Therefore, AFM-IR, the combination of atomic force microscopy (AFM) and IR spectroscopy which allows to detect chemical-specific information but with a lateral resolution ≤ 20 nm, was employed for final investigation. For contact mode resonant AFM-IR spectroscopy, several challenges were faced, such as low sample-tip force, high mechanical shear force which is exerted onto the sample, and careful selection of the contact resonance frequency tracking range. Leveraging the novel tapping mode

AFM-IR method based on heterodyne detection, detection of the chemotherapeutic drug in individual liposomes based on its characteristic mid-IR fingerprint was demonstrated with impressive sensitivity (zeptomol range) and lateral resolution (≈ 10 nm).

ACKNOWLEDGEMENTS

x

TABLE OF CONTENT

ABBREVIATIONS

AFM	atomic force microscopy
AFM-IR	atomic force microscopy infrared spectroscopy
Ag	silver
AgNO$_3$	silver nitrate
ATR	attenuated total reflection
Au	gold
BALF	bronchoalveolar lavage fluid
Br	bromine
Br-IPM	bromo-isophosphoramide
CaF$_2$	calcium fluoride
DFU	colony-forming unit
E. coli	*Escherichia coli*
EDX	energy dispersive X-ray spectroscopy
ENAS	electrostatic nanometer aerosol sampler
FDA	Food and Drug Administration
FIR	far-infrared
FN	false negative
FP	false positive
FTIR	Fourier transform infrared
GFP	green fluorescent protein
HCA	hierarchical cluster analysis
IB	inclusion body
IR	infrared
LOD	limit of detection
LSPR	localized surface plasmon resonance
MALDI	matrix assisted desorption ionization

MCT	mercury cadmium telluride
MIR	mid-infrared
N.A.	numerical aperture
nES-GEMMA	nano electrospray gas-phase electrophoretic mobility molecular analysis
$NH_2OH \cdot HCl$	hydroxylamine hydrochloride
NIR	near-infrared
NP	nanoparticle
OPO	optical parametric oscillator
P. chrysogenum	*Penicillium chrysogenum*
PCA	principal component analysis
PI	phosphatidylinositol
PLC	phospholipid composition
PLL	phase locked loop
PLS-DA	partial least squares- discriminant analysis
PLS-R	partial least squares regression
PMMA	poly(methyl methacrylate)
PMT	photomultiplier tube
PSF	point spread function
PTIR	photothermal induced resonance
PZT	lead zirconate titanate
QCL	quantum cascade laser
R6G	Rhodamine 6G
RMSECV	root mean square error of cross-validation
ROC	receiver operating characteristic
SEM	scanning electron microscopy
SERS	surface enhanced Raman scattering
SNOM	scanning optical near-field microscopy

SNR	signal to noise ratio
TN	true negative
TOF-SIMS	time-of-flight – secondary ion mass spectrometry
TP	true positive
UPM	ultrasonic particle manipulation
ZnS	zinc sulfide
ZnSe	zinc selenide

1   Theoretical introduction

1.1   Vibrational spectroscopy

Vibrational spectroscopy is a well-established method in Analytical Chemistry that allows direct, label-free, and non-destructive investigation of gaseous, liquid, and solid samples based on light-matter-interaction. Below, Raman and mid-infrared spectroscopy are discussed as the two most frequently used techniques to study the chemical composition of molecules based on vibrational and rotational energy transitions.

1.1.1   Infrared spectroscopy

In the following paragraphs, a brief description of the basic principle of infrared spectroscopy is given based on the comprehensive works by Peter R. Griffiths and James A. de Haseth[1], and John M. Chalmers[2], respectively, which the reader is referred to for a thorough introduction.

The infrared range in the electromagnetic spectrum covers the region from 0.78 μm to 1000 μm and is sub-divided into near (0.78 μm - 2.50 μm; NIR), mid (2.50 μm - 25 μm; MIR) and far (25 μm - 1000 μm; FIR) infrared regions. Due to the interaction of infrared light and matter, energy is absorbed by the molecules inducing molecular vibrations.

For a molecule to be IR active, a temporary change of the dipole moment μ is required during oscillation. The number of vibrations to be expected for a linear molecule with N atoms is given by 3N-5, while a non-linear molecule has 3N-6 degrees of freedom. Considering a diatomic molecule with the atomic masses m_1 and m_2 being connected by a bond with the force constant k (Figure 1 right), the frequency v of the only vibrational mode possible for this molecule (3N-5 = 1 for N = 2) is given by

$$v = \frac{1}{2\pi}\sqrt{\frac{k}{\mu}}$$

(1)

with the reduced mass $\mu = {m_1 m_2}/{(m_1 + m_2)}$. Based on this approach, the frequencies of localized vibrations (stretching, bending, twisting, etc.) such as -OH, C=O, $-CH_2$, etc. can be estimated also for large molecules. For example, the displacement of triple-bonded carbon atoms ($C \equiv C$) appears at higher frequencies in the infrared spectrum compared to double-bonded carbon atoms ($C = C$) due to the higher force constant for triple-bonded carbon atoms. Apart from localized vibrations, additional absorption bands due to the contribution of several atoms are observed. Hence, molecules with similar functional groups, but different spatial arrangement can be differentiated. Typically,

these bands are localized in the so-called *fingerprint region* of the IR spectrum ($\approx$ 500 cm^{-1} - 1900 cm^{-1}). The energy of photons for FIR and MIR light allows excitation of rotational and vibrational energy states, whereas with NIR excitation, broad absorption features of vibrational combination bands and overtones are observed.

The energy needed for displacement from the equilibrium position is based on the model of the harmonic oscillator (Figure 1 left) which describes the potential energy *E* as a function of the inter-nuclear distance *r*. The energy *E* is defined as

$$E = h\nu \left(n + \frac{1}{2}\right) \tag{2}$$

with Planck's constant h, the vibrational quantum number $n = 0,1,2,\dots$, and the fundamental frequency ν. The harmonic oscillator only allows transitions of $\Delta n = \pm 1$. For higher n, the description of vibrational energy states is more accurate using the anharmonic Morse potential (Figure 1 left). Therefore, equation 2 is extended by an additional term (second order approximation of Morse potential) including the anharmonicity constant χ as follows

$$E = h\nu \left(n + \frac{1}{2}\right) + h\nu\chi \left(n + \frac{1}{2}\right)^2 \tag{3}$$

Note that the model of the anharmonic (Morse-type) oscillator also allows transitions of $|\Delta n| > 1$, hence, overtone vibrations are possible.
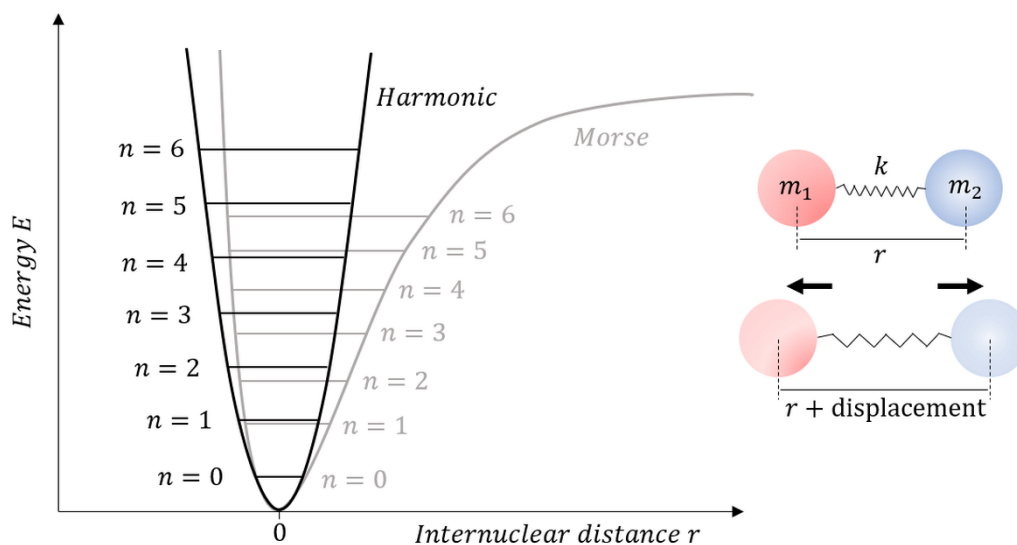
Figure 1. Model of harmonic and anharmonic (Morse-type) oscillator with vibrational energy levels n = 1-6 (left). Considering a diatomic molecule (right) with the masses m_1 and m_2 being connected by a bond (k = force constant), the oscillation of the molecule can be described by the harmonic oscillator.

1.1.1.1 Spatially resolved IR spectroscopy

Depending on the chemical composition of the sample – homogenous, or heterogenous - IR spectroscopy can either be used for collecting single spectra, or images allowing to color the scanned sample area based on the spectral features of the sample reflecting its chemical composition. For IR imaging, either single point spectra (Figure 2 a) are acquired at each pixel of the image (raster scan mode) which can be time-consuming, or a focal plane array (FPA) detector with a defined number of pixels (up to 128x128 pixels for a 340x340 μm^2 area of commercially available FPAs) is used (Figure 2 b). This allows simultaneous acquisition of the spectra and, hence, comes with a significant reduction in measurement time.

_____
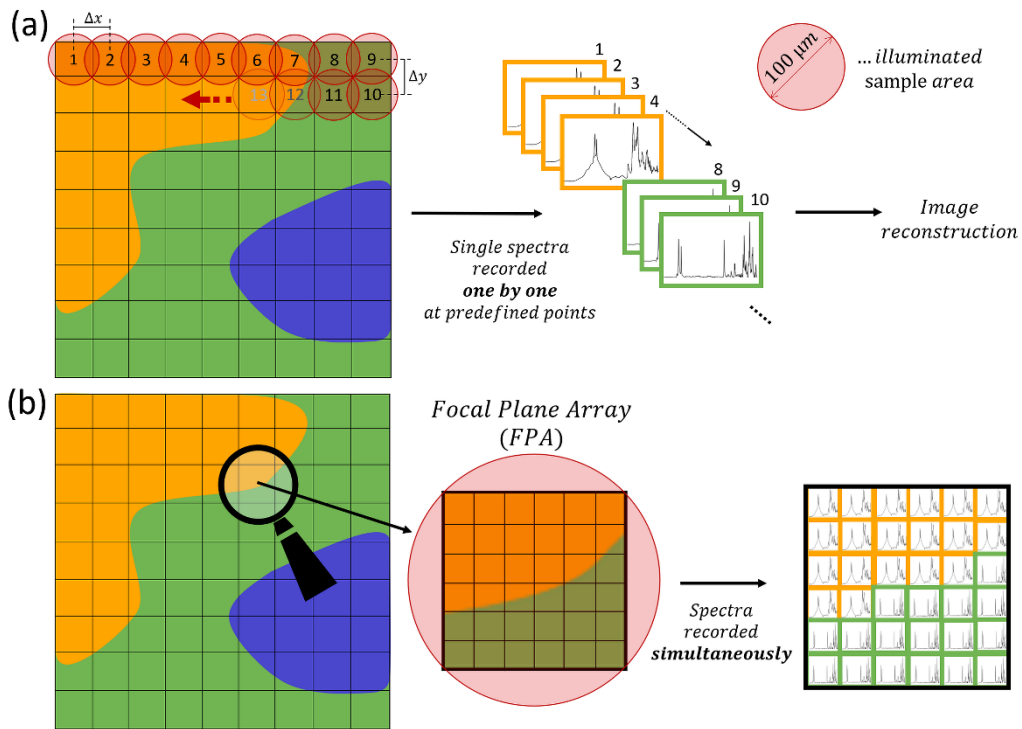
Figure 2. (a) For single point imaging (raster scan), the single spectra are recorded at predefined measurement spots. (b) In FPA imaging, the transmitted or reflected light is focused onto an arrangement of detector elements instead of a single point detector. Hence, depending on the illuminated sample area and the number of pixels on the detector array, a lateral resolution in the low µm-range is achieved.

For single point spectra, the sample area illuminated by the IR source (globar) typically is ≈ 100 µm allowing IR images with a step size of 100 µm in x- and y-direction. This is a ≈ 17x higher value compared to the lateral resolution of ≈ 6 µm (calculated for λ = 1800 cm^{-1} and *N.A.* 0.6) which would theoretically be achievable according to the Rayleigh criterion (see equation 16). This criterion defines two closely spaced objects to be spatially resolved if the maximum of the intensity profile (point spread function, PSF) of object 1 is placed at the first minimum of the PSF of object 2 (Figure 3).
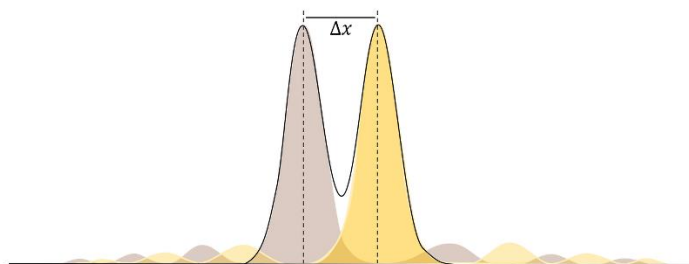
Figure 3. Sketch demonstrating the Rayleigh criterion for two objects to be spatially resolved on the image plane.

Due to the large area illuminated by the IR source (≈ 5 mm - 10 mm) a smaller sampling area requires a smaller aperture at the expense of a loss in signal intensity. In contrast, FPA imaging, allows as significant improvement in terms of lateral resolution. Here, the illuminated sample area is similar to single point spectra, however, the transmitted or reflected light which usually is focused on a single-element detector is now focused onto an arrangement of detector elements (e.g. 64x64, or 128x128 pixels). Hence, the intensity per pixel element is lower compare to the single-element detector. However, based on the size of the FPA and the number of pixels, a nominal lateral resolution of ≈ 2 µm (for a 100x100 µm^2 illuminated sample area with a 64x64 pixel array detector) can be achieved.

1.1.2 Raman spectroscopy

The following introduction on Raman spectroscopy is mainly based on literature by D. Long[3], T. Dieing, O. Hollricher and J. Toporski[4], and various chapters from the *Handbook of Vibrational Spectroscopy*[2], a comprehensive work on vibrational spectroscopy. The cited literature is recommended for further reading.

Raman spectroscopy is the detection of inelastically scattered light corresponding to vibrational transitions in the molecule, hence, providing characteristic, molecule- specific information. The photon energy is significantly higher compared to IR spectroscopy, therefore, excitation to higher energy levels is possible (Figure 4).
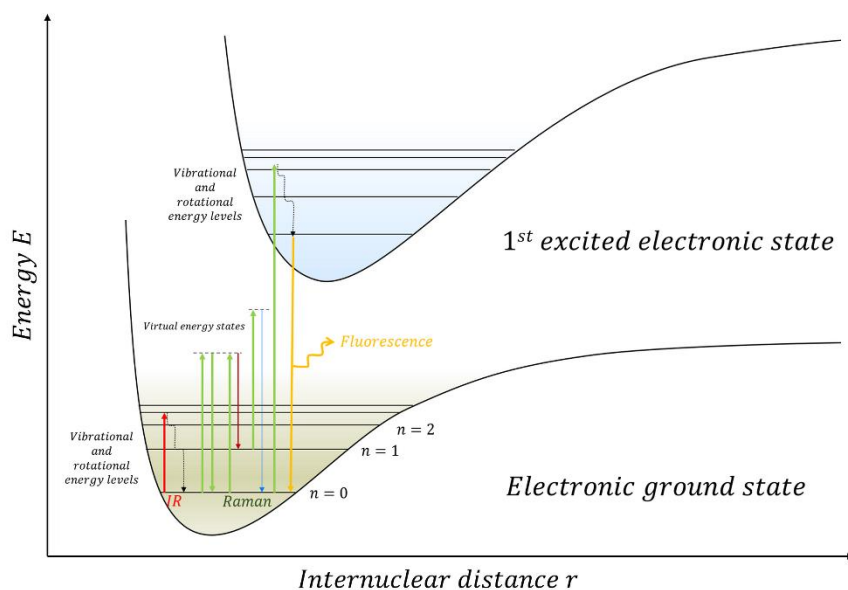
Figure 4. Energy diagram showing the excitation of vibrational and rotational energy levels in IR spectroscopy while a significantly higher energy input in Raman spectroscopy allows excitation to the energetically higher virtual states. Excitation of the first electronic states with subsequent relaxation results in fluorescence. Adapted by permission from Springer International Publishing AG: Springer Nature Introduction to the Fundamentals of Raman Spectroscopy, Dietzek B.; Cialla D.; Schmitt M.; Popp J. in Confocal Raman Microscopy, ©Springer International Publishing AG (2018)

A monochromatic light source, typically in the visible to near-IR range, is used to interact with the molecules. Based on this energy input, electrons are excited to higher, virtual energy states. Upon relaxation, the electrons fall back onto lower energy levels and the surplus in energy is released in the form of light. The backscattered photons can either be of the same (Rayleigh; elastically scattered photons), lower (Stokes) or higher (anti-Stokes) energy compared to the incident photons as indicated in the energy diagram in Figure 4. The Raman spectrum depicts this difference in the energy of inelastically scattered photons relative to the incident laser radiation as wavelength shift. Note that only 1 in $10^6 - 10^8$ of the incident photons are inelastically scattered, therefore Raman is known to be a weak scattering effect.[5] For anti-Stokes scattering, the molecule is already at a higher vibrational energy state before interaction with the incident laser light, but falls back to a lower energy state upon relaxation. Based on the Boltzmann distribution, the number of molecules in an excited state at room temperature is low, hence, anti-Stokes scattering has a significantly lower occurrence probability than Stokes scattering. An increase in temperature, however, slightly changes this relationship. As an example, the population at the energy level corresponding to the S-S stretch vibration[6] at 470 cm^{-1} (Raman shift) based on the Boltzmann distribution (equation 4) is calculated. The Boltzmann distribution describes the population N_i at a certain energy level i compared to the number of molecules in the ground state N_0 for a given temperature T as

$$\frac{N_i}{N_0} = e^{\frac{-\Delta E}{k_B T}} \tag{4}$$

Where k_B is Boltzmann's constant ($1.38*10^{-23}$ J/K) and ΔE is the energy difference between the ground and the excited state depicted in the Raman spectrum at 470 cm^{-1} (Raman shift). The unit of the term $k_B\,T$ is [J] and, hence, must be converted to [cm^{-1}] based on the relation of energy E and the wavelength λ according to

$$E = h\omega = hc\frac{1}{\lambda} \tag{5}$$

Considering T_1 = 293.15 K (20 °C) and T_2 = 373.15 K (100 °C), the calculated values for the corresponding terms are $k_B\,T_1$ = 204 cm^{-1} and $k_B\,T_2$ = 259 cm^{-1}. The resulting population for each temperature is

$$\frac{N_i}{N_0} = e^{\frac{-470}{204}} \sim 10\% \; at \; T_1 = 20°C \tag{6}$$
$$\frac{N_i}{N_0} = e^{\frac{-470}{259}} \sim 16\% \; at \; T_2 = 100°C$$

And illustrates ≈6 % higher population at 100 °C and, hence, a 6 % higher probability for anti-Stokes scattering compared to measurements at room temperature (20 °C).

In the classical theory, the Raman effect is described as modulation of the incident electric field E with the angular frequency ω_0 (equation 7) due to its interaction with vibrating molecules.

$$E = E_0 \cos(\omega_0 t) \tag{7}$$

Interaction of incident light and the molecule induces a dipole μ described as

$$\mu = \alpha E \tag{8}$$

with the polarizability tensor α as proportionality constant between the induced dipole μ and the electric field E. The polarizability is key property for a molecule to be considered Raman active and describes the distortion of a molecule's electron cloud upon interaction with the incident light. The changing internuclear distance q of an oscillating molecule is described as

$$q = q_0 \cos(\omega_R t) \tag{9}$$

with ω_R being one of the eigenfrequencies of the molecule. In the expansion of the polarizability tensor into a Taylor series as function of the intermolecular distance the value of higher terms is so small such that they can be neglected.

$$\alpha(q) = \alpha_0 + \left(\frac{\partial \alpha}{\partial q}\right)_0 q + \cdots \tag{10}$$

If we substitute the electric field, the polarizability tensor, and the internuclear distance of an oscillating molecule by their respective descriptions (equations 7, 9 and 10) in equation 8 describing the induced dipole, the following description is obtained after applying the trigonometric formula for the multiplication of two cosine functions:

$$
\begin{aligned}
\mu = \alpha E &= \left(\alpha_0 + \left(\frac{\partial \alpha}{\partial q}\right)_0 q\right) E_0 \cos(\omega_0 t) \\
&= \alpha_0 E_0 \cos(\omega_0 t) + \left(\frac{\partial \alpha}{\partial q}\right)_0 E_0 \cos(\omega_0 t) q_0 \cos(\omega_R t) \\
&= \alpha_0 E_0 \cos(\boldsymbol{\omega_0} t) \\
&\qquad + \frac{1}{2}\left(\frac{\partial \alpha}{\partial q}\right)_0 E_0 \cos\big((\boldsymbol{\omega_0 - \omega_R})t\big) \\
&\qquad + \frac{1}{2}\left(\frac{\partial \alpha}{\partial q}\right)_0 E_0 \cos\big((\boldsymbol{\omega_0 + \omega_R})t\big)
\end{aligned}
\tag{11}
$$

The three sum terms in equation 11 describe the three possible scenarios that an incident photon can undergo upon interaction with a molecule: i) The photon is scattered elastically (**Rayleigh scattering**) which means that the backscattered photon has the same energy as the incident one or ii) the photon is scattered inelastically and the backscattered photon is of lower energy (**Stokes Raman scattering**) or iii) higher energy (**anti-Stokes Raman scattering**) compared to the incident photon. The resulting Raman spectrum of, e. g., sulfur powder is depicted in Figure 5. Note that the anti-Stokes part (highlighted in blue) in the spectrum mirrors the Stokes shifted fingerprint (highlighted in red) in the spectrum but with significantly lower intensity.
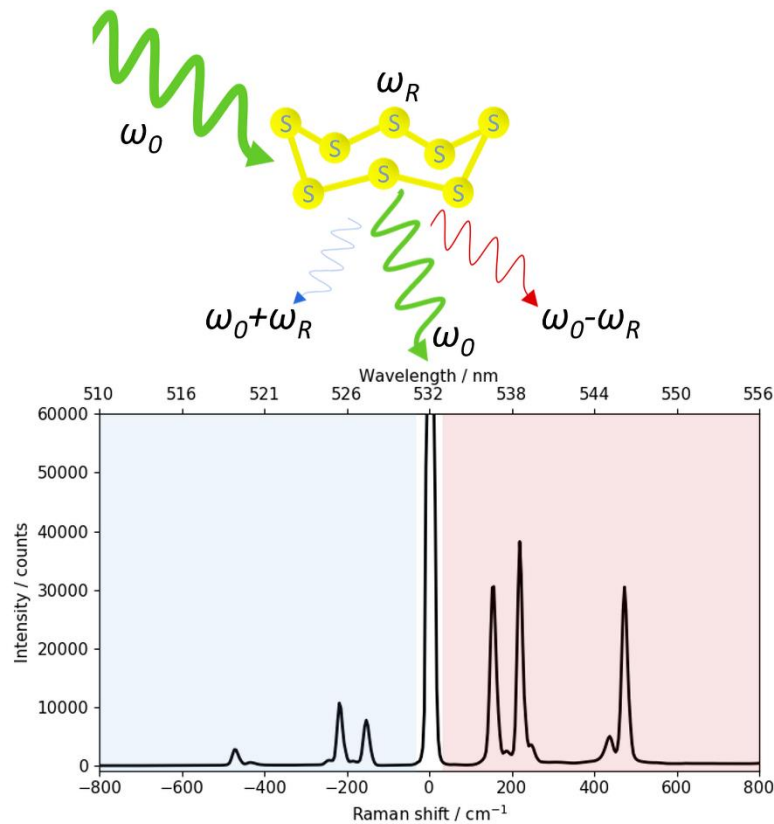
Figure 5. Elastically (ω_0) and inelastically (ω_0 - ω_R, ω_0 + ω_R) scattered light of a sulfur molecule with the resulting Stokes (highlighted in red) and anti-Stokes region (highlighted in blue) in the respective Raman spectrum.

1.1.2.1 Surface Enhanced Ramana Scattering (SERS)

Surface enhanced Raman scattering (SERS) allows enhancement of the weak Raman signal by several orders of magnitude (up to 10^8) such that monolayer and single molecule detection become possible. A SERS substrate is needed which usually consists of metal nanoparticles (NPs) of defined size and shape. The incident laser light interacts with the NPs and resonantly excites the local surface plasmon resonance of the nanoparticles which results in an enhanced emitted radiation of the same frequency. Upon interaction, only vibrations oscillating in the same direction as the electromagnetic field vector is pointed to, are enhanced. Typically, silver and gold NPs are used since their resonances fall within the visible region of the electromagnetic spectrum. While gold NPs are more stable, silver NPs show higher signal enhancement effects. Note that SERS is a 2-step-process (Figure 6): First, the incident radiation is enhanced due to interaction with the NPs. The enhanced radiation interacts with the molecule of interest before another signal enhancement occurs as consequence of the second interaction with the NPs.
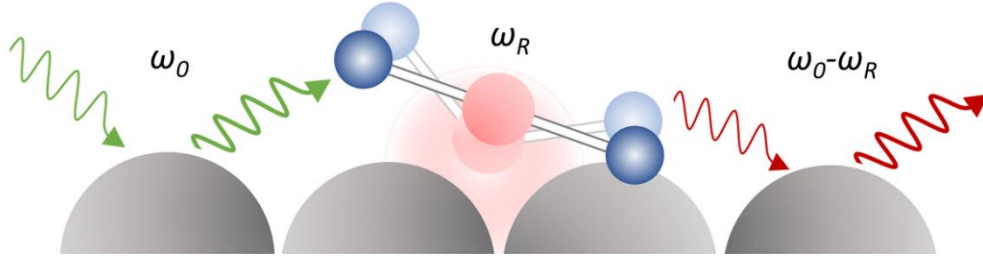
Figure 6. The incident light and the scattered Stokes light, respectively, are electromagnetically enhanced.

Hence, the SERS intensity considering the Stokes shifted Raman photons is given by the following equation 12.[7]

$$I_{SERS} = I_0(\omega_0) * I(\omega_0 - \omega_R) = |E_0(\omega_0)|^2 * |E(\omega_0 - \omega_R)|^2 \tag{12}$$

Note that SERS is a very surface-selective effect which only applies for samples in very close proximity to the SERS substrate (roughly within 5-10 nm)[7,8]. Simplifying $E_0(\omega_0 - \omega_R) \approx E_0(\omega_0)$ for $\omega_R << \omega_0$, I_{SERS} can be approximated by the following expression

$$I_{SERS} \approx |E_0(\omega_0)|^4 \tag{13}$$

With the electric field strength being proportional to the distance *R* from the surface of the NP to the molecule

$$E \sim \frac{1}{R^3} \tag{14}$$

the SERS intensity can be described as

$$I_{SERS} \sim \frac{1}{R^{12}} \tag{15}$$

highlighting the SERS effect's surface sensitivity.

The Leopold-Lendl method is very prominent for the preparation of readily usable Ag NPs.[9] Briefly, $AgNO_3$ is reduced to elemental Ag using $NH_2OH \cdot HCl$ while all by-products are in the gas phase and do not affect the final SERS substrate. However, here, only little control concerning uniformity of NP-shape is possible. The shape of the SERS substrate is very important. If the NPs are not uniformly shaped, sharp edges might have an antenna effect resulting in a different SERS spectrum of the same substance since only the vibrations aligned in the same direction as the electromagnetic field vector is pointing to are enhanced. Additional enhancement is observed in hotspots between two NPs that are

in a very narrow distance to each other (Figure 7). Hence, controlled agglomeration of NPs in colloidal suspensions is intended.[10]
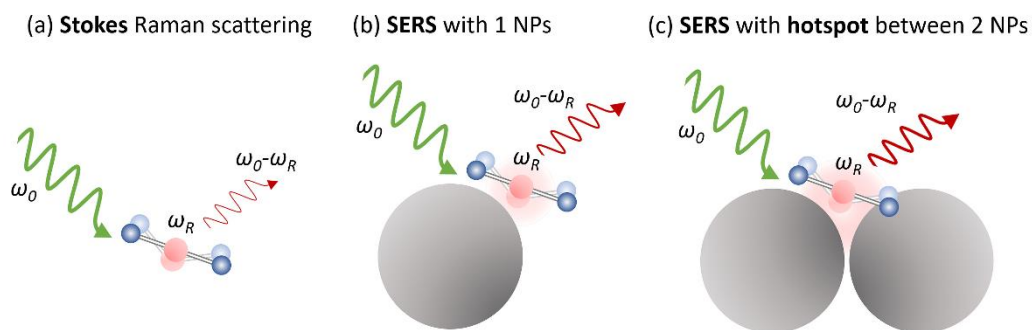
Figure 7. SERS promises an up to 10^8 signal enhancement compared to conventional Raman scattering intensity. An even higher signal enhancement is achieved in hotspots between adjacent nanoparticles (NPs).

1.1.3   Comparing IR and Raman spectroscopy

As mentioned previously, the key property for molecules to be Raman active is the change in polarizability α upon interaction with the incident laser light $\left(\left(\frac{\partial \alpha}{\partial q}\right)_0 \neq 0\right)$ whereas for IR spectroscopy, a change in the dipole moment μ needs to occur $\left(\left(\frac{\partial \mu}{\partial q}\right)_0 \neq 0\right)$. These considerations provide the basic selections rules for Raman and IR spectroscopy. Considering a linear triatomic molecule (see Figure 8), the symmetric stretch vibration is Raman active, but IR inactive since the polarizability in this mode changes while the dipole moment does not change sign when passing through the equilibrium configuration. For the asymmetric stretch, and the bending vibration, however, the polarizability shows symmetrical behavior around the y-axis approximating 0 for small displacements while the sign of the dipole moment changes when passing the equilibrium state. Therefore, these two vibrations are IR active, but Raman inactive as indicated by the slope of both curves around the equilibrium position (q = 0) with $\left(\frac{\partial \alpha}{\partial q}\right)_0 = 0$ and $\left(\frac{\partial \mu}{\partial q}\right)_0 \neq 0$.

Figure 8. Basic guidelines for a molecule to be Raman and/or IR active, respectively Triatomic molecule and the according derivatives of polarizability α and dipole moment μ as a function of the normal coordinate q. Adapted by permission from Springer International Publishing AG: Springer Nature Introduction to the Fundamentals of Raman Spectroscopy, Dietzek B.; Cialla D.; Schmitt M.; Popp J. in Confocal Raman Microscopy, ©Springer International Publishing AG (2018)

Despite of these selection rules, samples are typically both, Raman and IR active. To decide, which method is best suitable for which application, a few key points need to be considered:

(i)   Conventional IR and Raman spectroscopy are diffraction limited resulting in a lateral resolution Δx of $\approx$ 6 μm[11,12] (calculated for λ = 1800 cm^{-1} and *N.A.* 0.6) for IR while Raman allows sub-μm resolution; depending on the numerical aperture (N.A.) of the objective and the laser excitation wavelength (equation 16), Raman allows a Δx of $\approx$ 330 nm (calculated for λ = 488 nm and *N.A.* 0.9) and promises an improvement by roughly 1/3 for confocal Raman microscopy.

$$\Delta x \approx 0.61 \frac{\lambda_{laser}}{N.A.} \tag{16}$$

Low excitation wavelengths and objectives with a high numerical aperture are preferred for imaging purposes that require high lateral resolution. The lateral resolution also defines the distance/step size between single pixels of a Raman or IR map, respectively. In order to avoid information loss in the mapping (step size > lateral resolution), the number of pixels per line and the

number of lines per image are limited by the lateral resolution, mainly set by the objective and the excitation wavelength. Balancing signal to noise ratio (SNR), lateral resolution and imaging time, typical Raman map sizes are in the range of tens to a few hundred micrometers. Here, IR imaging, e.g., in combination with a focal plane array detector (FPA) allowing a nominal resolution of ≈ 2 µm, is better suited for imaging areas that exceed an edge length of 1 mm.

(ii)   In Raman spectroscopy, the sample is exposed to more thermal stress compared to IR spectroscopy. Raman scattering intensity I_{Raman} is directly proportional to the intensity of the incoming laser intensity which is proportional to the inverse of the excitation wavelength to the power of 4:

$$I_{Raman} \sim I_{laser} \sim \left(\frac{1}{\lambda}\right)^4 \tag{17}$$

Therefore, excitation wavelengths in the visible (488 nm, 532 nm or 633 nm) are preferred. Usually, careful adaptation of the laser power is needed, especially for biological samples, and thin layered samples in material science, to avoid carbonization of the sample. Higher laser power is directly linked to a higher or detectable Raman signal, and a better SNR, while the high thermal stress may jeopardize the sample's integrity. Here, IR spectroscopy might be the better choice.

(iii)   Fluorescence – the excitation to the first electronic state (Figure 4) – is a competing effect to the Raman scattering because fluorescence is roughly 6 orders of magnitude more intense. The weak Raman signal is hidden underneath the broad fluorescence bands which results in quick saturation of the detector hindering any detection of Raman scattered photons. To circumvent this, higher wavelengths in the NIR (e. g. 785 nm) are used for Raman excitation which for the most part avoids fluorescence, but in return results in a weaker Raman signal intensity (see equation 17) and a poorer lateral resolution. Alternatively, IR spectroscopy can be employed.

(iv)   Water is a strong IR absorber hindering the detection of molecules in aqueous environment or samples with high water content (e.g., cells) due to the dominating broad absorption features of water in the IR spectrum. In contrast to that, water is a weak Raman scatterer, favorizing Raman spectroscopy for the investigation of biological samples in aqueous environment.

1.2   Scanning-probe techniques

The optical methods described so far have one common drawback in terms of spatial resolution: they are diffraction limited which hampers imaging of samples or sample features that are in the lower or sub-μm size range such as single cells[11], metal organic frameworks[13], or 2D materials[14,15]. A slight increase in the spatial resolution is achieved by confocal microscopy. Here, the point spread function (PSF) is narrower due to the confocal pinhole whose size can be adjusted to cut off photons from surrounding sample regions to be collected at the detector. The spatial resolution can be improved by ≈ 1/3. The smaller the pinhole, the better the resolution, but the lower the number of photons reaching the detector. Hence, the gain in resolution comes with the cost in signal intensity. As mentioned earlier, IR imaging with a FPA (focal plane array) detector allows a lateral resolution of ≈ 2 μm (for a 100x100 μm^2 illuminated sample area with a 64x64 pixel array detector). Apart from these approaches in the far-field, scanning probe near-field techniques such as scanning near-field optical microscopy (SNOM), atomic force microscopy (AFM) and the combination thereof with IR spectroscopy (AFM-IR) may be employed. These methods promise a lateral resolution from $\leq 150\ nm$ (SNOM) to $\leq 50\ nm$ (AFM-IR) to $\leq 1\ nm$ (AFM). Additionally, tip-enhanced Raman spectroscopy (TERS) - the combination of AFM and Raman – allows a lateral resolution $\leq 20\ nm.$[16] TERS is an aperture-less near field spectroscopy technique, where a metal-coated AFM cantilever tip is positioned in close vicinity to the sample surface. Similar to SERS, the incident and scattered laser light resonantly excite the localized surface plasmon resonance of the metal NP which in contrast to SERS is now located on the AFM tip. Hence, TERS is a surface-sensitive method which only allows signal enhancement near the sample surface where the TERS tip is positioned. This localized signal enhancement in turn allows a spatial resolution beyond the diffraction limit.[17–20]

A comparison of the lateral resolution achieved with various spectroscopy-based methods used in this thesis (IR, Raman, confocal Raman, SNOM-Raman, AFM-IR) is given in Figure 9 in relation to a round-shaped, 80 nm-diameter sample.

_____
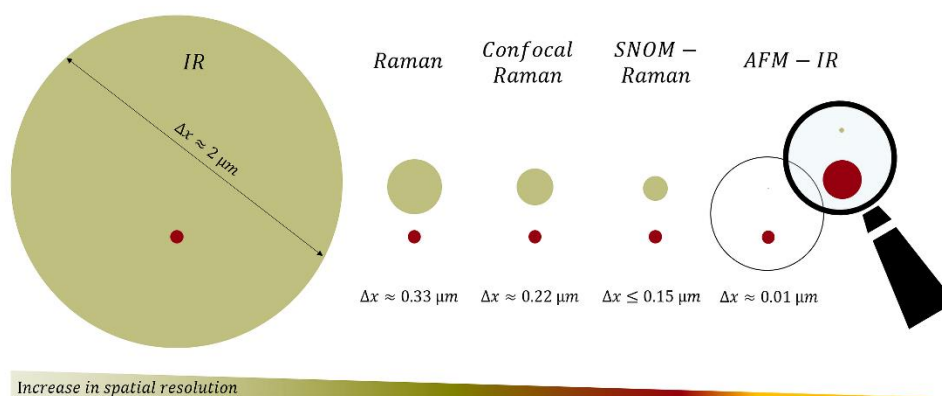
Figure 9. Comparing the spatial resolution of techniques used in this thesis: IR, Raman, confocal Raman, SNOM-Raman and AFM-IR spectroscopy. Diameter of the green-colored disc displays the achievable spatial resolution for each method. The red-colored disc represents an 80 nm-diameter sample. AFM-IR data is magnified by a factor of 3 indicated by the magnification glass for better visibility.

1.2.1   Atomic force microscopy (AFM)

AFM is a raster scanning technique where a probe is moved across the sample in close vicinity to its surface. Due to sample-tip-interaction, information on the sample's topography is obtained with sub-nanometer resolution. Besides of topographical information, AFM is also employed to extract information on the mechanical, electrical, or magnetic properties of the sample such as adhesion, stiffness or conductivity. An overview of AFM imaging modes is given in the review article by Dufrêne et al[21]. The following paragraphs aim to give a basic introduction to AFM and are based on the book by P. Eaton and P. West[22] which is also recommended for further reading.

Considering the basic operation principle of an AFM, the AFM tip located at the free end of the cantilever is placed in close vicinity to the sample's surface. With the tip-sample distance getting smaller, attractive - mainly van der Waals – forces cause the cantilever to "snap" into contact with the sample surface resulting in a bending of the cantilever. Further decrease in the tip-sample distance leads to repulsive forces which cause bending of the cantilever in the opposite direction. The deformation of the cantilever is detected by a weak laser that is reflected off the back of the cantilever onto a 4-quadrant photodiode. Due to the cantilever deformation, the position of the laser on the detector changes, hence topographical information is extracted (Figure 10 a). Depending on the AFM mode (e.g., constant force), a feedback control adapts the tip-sample distance depending on the tip-sample interaction (e.g., an increase in tip-sample force results in a moving the tip away from the sample surface; a decrease in tip-sample force causes a move towards the sample surface) such that it stays in the attractive regime until the distance is too high and the cantilever snaps off the sample surface. The tip-sample

interaction during approach and retraction is illustrated by the force-distance curve in Figure 10 b.
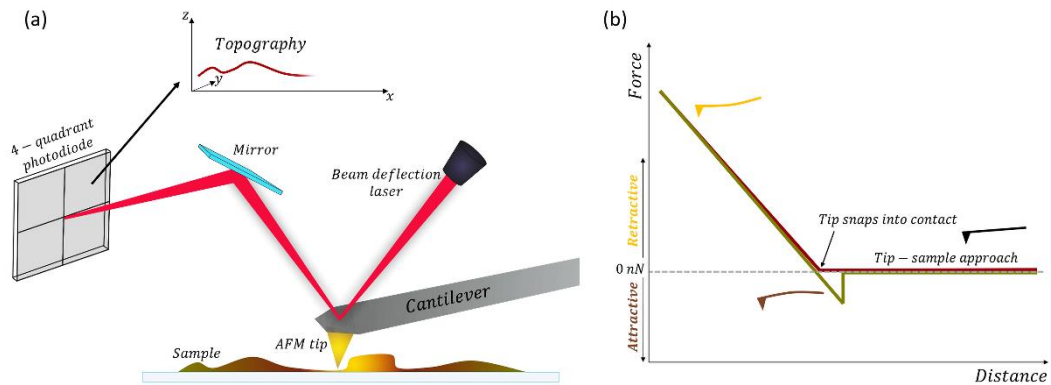
Figure 10. (a) AFM sketch: The AFM tip is positioned in close vicinity to the sample. Depending on tip-sample interaction, bending of the cantilever occurs which is detected by the beam deflection laser reflected off the back of the cantilever onto a 4-quadrant photodiode. (b) Force-distance curve of AFM tip approach (red line) and retraction (green line).

There are mainly two operation modes to be distinguished for recording AFM images: contact (constant force) and tapping mode (constant amplitude). In *contact mode*, the sample surface is scanned by the tip while keeping the tip-sample force constant. Changes in the topography lead to a change in the tip-sample force which is balanced by the piezoelectrics readjusting the tip-sample distance. During contact-mode measurements, for the most part, the tip is in contact with the sample surface. Hence, for mechanically compliant samples, this mode is prone to sample deformation and destruction due to the high shear forces the sample is exposed to. On the other hand, *tapping mode* AFM permits less tip-sample contact since the cantilever oscillates with a constant amplitude close to the sample surface. Changes in the topography lead to changes in the oscillation amplitude of the cantilever which is balanced by readjusting the tip-sample distance accordingly. For tapping-mode measurements, the sample-tip interaction is significantly reduced, favoring it for the investigation of soft/biological samples.

17

Figure 11. AFM cantilever operation modes. (a) In contact mode, the tip-sample distance is regulated in a feedback loop such that the tip-sample force remains constant. (b) In tapping mode, the tip-sample distance is regulated such that the oscillation amplitude of the cantilever remains constant.

In this thesis, tapping mode AFM images were acquired of eGFP (enhanced green fluorescent protein) inclusion body samples intracellularly produced by E. coli which was used as host organism in the biotechnological process (Publication VII, p. 165 ff). Inclusion bodies (IBs) are incorrectly folded, and thus, inactive protein aggregates which require a refolding process in downstream bioprocessing to recover protein activity. However, despite of the refolding step, IBs have high primary yields, high product purity and are easily separated from cell debris. *E. coli* is a commonly used host organism for recombinant protein production that is mostly used in combination with a specific pET (plasmid for expression by bacteriophage T7 RNA polymerase) expression system for IB production. Here, the expression of eGFP was induced by lactose, instead of the commonly used IPTG (isopropyl-β-D-galactopyranoside) since lactose increases cell fitness for longer protein production, and enhances correct protein folding, hence, the refolding yield is increased as well. Based on SEM and AFM microscopy, a correlation between IB size and lactose uptake during IB production was determined. With higher lactose uptake, bigger IBs are produced which is of advantage since the surface area is minimized (compared to small IBs) and thus potential adhesion of impurities is lessened.

1.2.2   Aperture Scanning Near - field Optical Microscopy (A-SNOM)

Scanning near-field optical microscopy (SNOM) is an optical method that allows to circumvent the diffraction limit and to achieve a lateral resolution of $\Delta x \leq 150$ nm. In design and operation principle, the SNOM tip is similar to an AFM tip, except that it has an aperture of defined size at the end of the pyramidal tip. The laser light is focused through the aperture *A* placed in close proximity to the sample onto the sample surface

(Figure 12). Due to the narrow distance between aperture and sample surface, only the sample fraction corresponding to the tip aperture is illuminated. Hence, the lateral resolution is determined by the tip aperture which is typically between 60 nm and 150 nm. The transmitted light is detected by a photomultiplier tube (PMT) while the sample's topography is recorded based on the cantilever's beam deflection signal.
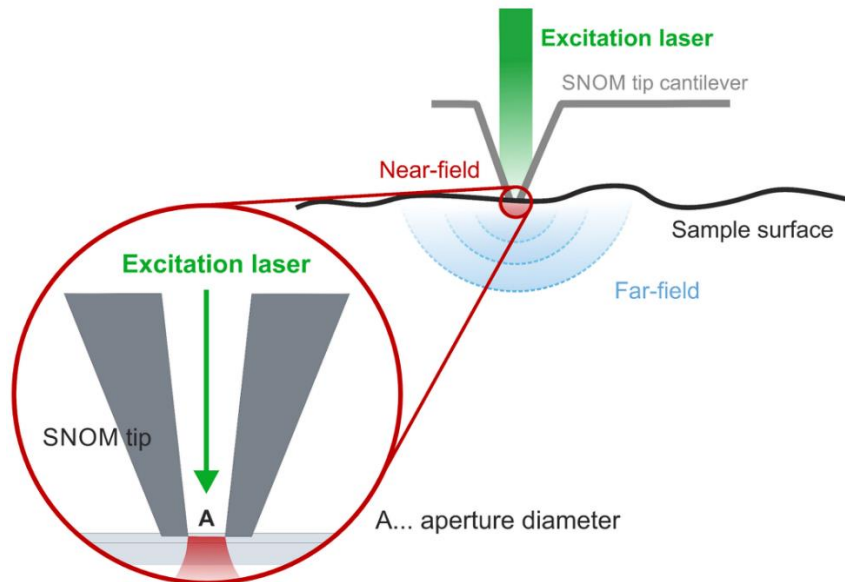
Figure 12. Basic concept of A-SNOM. The laser is focused into the pyramidal tip and illuminates the sample surface through the aperture A of defined diameter. The transmitted light is detected on a PMT.

Replacing the PMT by a spectrograph, high resolution Raman spectroscopy is theoretically possible. Experiments, however, suffer from poor signal intensity due to the small fraction of the incident laser light that actually interacts with the sample. As an example, transmission Raman and SNOM-Raman spectra of sulfur – a good Raman scatterer - were recorded (Figure 13). Band ratios of three vibrational sulfur modes located at 154 cm^{-1}, 221 cm^{-1} and 476 cm^{-1}, respectively, were calculated and averaged, concluding a loss in signal intensity by a factor of ≈360 due to the small SNOM tip aperture (here, < 150 nm).

_____

Figure 13. (a) Transmission Raman spectrum of sulfur power. (b) SNOM-Raman spectrum of sulfur powder acquired in transmission mode.

1.2.3   Atomic Force Microscopy Infrared (AFM-IR)

AFM-IR – also called photothermal induced resonance (PTIR) – combines infrared spectroscopy and atomic force microscopy to detect chemical-specific information, but with the lateral resolution of an AFM. When pulsed, infrared light interacts with an absorbing sample, the sample heats up and thus expands for a very short time. The photothermal expansion of the sample is detected by the AFM cantilever sitting right on top of it. Since the amplitude of the deflected cantilever signal is proportional to the local IR absorption, the near-field IR spectra look very similar to far-field IR spectra allowing straight-forward data interpretation based on well-established far-field IR databases.[11,23,24]

1.2.3.1   Contact mode AFM-IR

Contact mode AFM-IR is the legacy implementation of the AFM-IR technique. For a basic description of contact mode AFM, the reader is referred to section 1.2.1 (p. 16 ff.).

AFM-IR instruments are built in either one of two configurations: top or bottom illumination (Figure 14). For the latter one, the sample needs to be placed on an IR transparent prism (e.g., ZnSe or ZnS) such that the IR radiation can interact with the sample based on the attenuated total reflection (ATR) principle. When light propagating through a medium of higher refractive index n_1 (here, the prism) hits the interface to a medium of lower refractive index n_2 (here, the sample) at a defined angle θ with $\theta > \theta_{crit}$, it is totally reflected. The critical angle θ_{crit} is defined as[1]

$$\theta_{crit} = \arcsin\left(\frac{n_2}{n_1}\right) \qquad (18)$$

A small part of the incident light can penetrate into the medium of lower refractive index. The resulting evanescent field has the same frequency as the incident light, but the amplitude exponentially decays with increasing distance to the interface (= penetration depth). The penetration depth d_p defined as the distance where the amplitude of the electric field has decreased to $\frac{1}{e}^{th}$ of its initial value is given by

$$d_p = \frac{\lambda}{2\pi n_1 \sqrt{sin^2\theta - \left(\frac{n_2}{n_1}\right)^2}} \qquad (19)$$

Typically, d_p is in the order of magnitude of the wavelength λ of the incident light. Hence, the incident light can interact with the sample placed on top of the prism, however, the sample's thickness is limited to ≈ 1 μm (sample thickness $\ll d_p$) to have the sample placed in the area of highest evanescent field amplitude. However, in order to stay in the linear range of the AFM-IR signal, the sample thickness should be < 0.5 μm according to Ramer et al.[25] who give a thorough treatment on what parameters affect the AFM-IR signal and how to overcome or avoid these effects altogether. Additionally, bottom illumination allows near-field IR spectroscopy of samples in aqueous environment[26] which for far-field IR measurements is only possible on a very limited extent due to high IR absorption of water. In the configuration here, the sample that is placed e.g., in a water droplet on the prism is irradiated by the IR source. At this point, the IR light is absorbed by both, the sample and the water. However, the AFM tip is placed on top of the sample, thus, only the photothermal expansion of the sample is detected. This allows the study of protein secondary structure in their native, aqueous environment with nanoscale lateral resolution as was shown by Ramer et al[27].

In top illumination (Figure 14 b), the selection of sample carrier (substrate) is less critical. Essentially, every substrate applicable for AFM measurements (e.g. silicon wafers, Au or Ag coated substrates, mica, etc.) can be used. To avoid absorption of the silicon AFM cantilever, Au-coated probes are employed In addition, near-field plasmonic enhancement effects can be exploited to increase the AFM-IR signal intensity[28].

_____
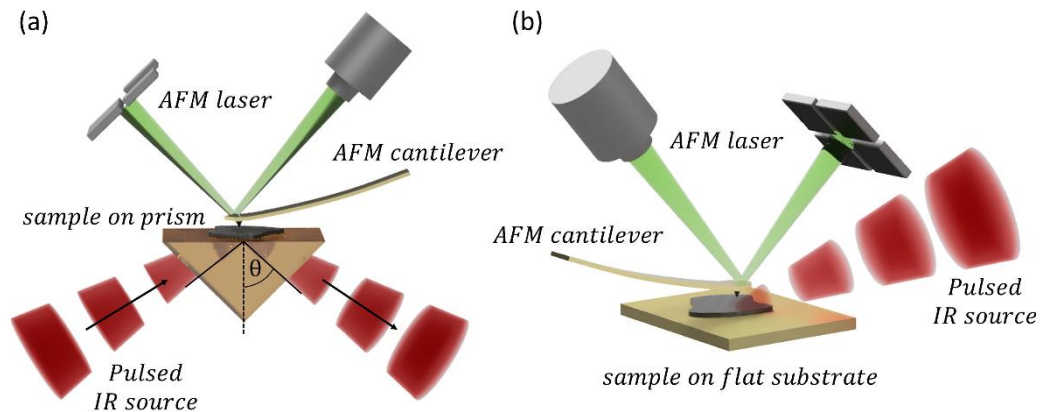
Figure 14. (a) Bottom illumination based on the ATR principle with the angle of the incident laser beam $\theta > \theta_{crit}$. The sample is placed on an IR transparent prism. (b) Top illumination where the sample can be placed on a flat substrate. Adapted by permission from Springer Nature: Tsinghua University Press, Nano Research Nanoscale chemical imaging of individual chemotherapeutic cytarabine-loaded liposomal nanocarriers, Wieland, K.; Ramer, G.; Weiss, V. U.; Allmaier, G.; Lendl, B.; Centrone, A. © Tsinghua University Press and Springer-Verlag GmbH, part of Springer Nature (2019)

Another way of signal enhancement is contingent upon the choice of IR source used for AFM-IR measurements. As mentioned previously, the photothermal expansion of the irradiated, absorbing sample is detected by the AFM cantilever. Due to the force transfer from the sample to the tip, an oscillatory response of the cantilever is induced. Note that pulsed IR laser sources are employed for AFM-IR measurements. Typically, AFM-IR measurements are performed with an optical parametric oscillator (OPO) or a quantum cascade laser (QCL). For what is important here, the lasers used for commercial AFM-IR set-ups mainly differ in the achievable repetition rate and the spectral range they cover. OPOs are lasers with a repetition rate of ≤ 1 kHz while QCLs allow repetition rates up to the low MHz-range but are more limited in the spectral range they cover compared to OPOs. For low laser repetition rates, the cantilever performs a transiently decaying oscillation due to the force impulse on the tip caused by the expanding sample. However, if the laser repetition rate is set to one of the contact resonance frequencies of the cantilever, constant resonant excitation of the cantilever is achieved instead of the transiently decaying oscillation. The AFM-IR signal enhancement scales with the Q-factor of the cantilever which typically is ≈ 100, hence, a significant improvement in detection sensitivity is achieved.[28,29] The method is then called *resonance-enhanced* or *resonant AFM-IR spectroscopy*.

A lot of contributions interplay in the AFM-IR signal generation. A brief theoretical treatment on the AFM-IR signal generation by Dazzi et al[30] using the notation of Ramer et al[25] is summarized here. The AFM-IR signal can be written as a multiplicative term of several contributions.

- The cantilever contribution H_{AFM} which is a function of the cantilever's properties such as stiffness, frequency, shape, etc.

- The mechanical contribution H_m, a function of the tip-sample contact stiffness, the thermal expansion coefficient of the sample and the sample thickness.
- The thermal contribution H_{th} which describes the thermal properties of the sample
- The optical contribution H_{opt}, a function of the light absorbed by the sample.
- The laser power of the incident laser I_{inc} which is typically measured in the background spectrum

All the contributions add up to the AFM-IR signal described as

$$S_{AFM-IR} \propto H_{AFM} H_m H_{th} H_{opt}(\lambda) I_{inc}(\lambda) \qquad (20)$$

Note that three out of five terms in equation 20 are wavelength-independent. Hence, contributions from $H_{AFM} H_m H_{th}$ in the AFM-IR spectrum can be eliminated by calculating band ratios.

In *resonant* AFM-IR spectroscopy, another important factor needs to be considered: the contact resonance frequency and the tracking thereof. In far-field IR spectroscopy, the IR signal is proportional to the analyte concentration which also accounts for near-field IR spectroscopy. A decrease in signal intensity for resonant AFM-IR spectroscopy, however, can either indicate a decrease of the analyte concentration in the sample or an unnoticed shift in the contact resonance frequency (Figure 15). Hence, for reliable resonant AFM-IR spectroscopy, and especially for imaging purposes, a continuous tracking and readjustment of the resonance frequency e.g., through a phase looked loop (PLL), is indispensable.
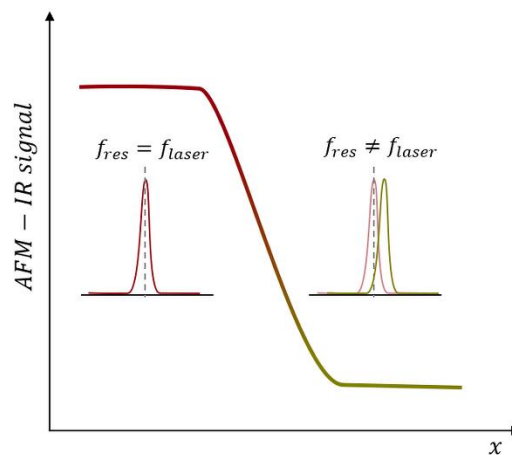
Figure 15. Decrease in resonant AFM-IR signal intensity due to a change in the cantilever's contact resonance frequency (f$_{res}$) without frequency tracking and, hence, without readjustment of the repetition rate of the laser (f$_{laser}$).

The influence of the sample's material properties on the contact resonance frequency of the cantilever is elucidated by approximation of the tip-sample interaction by the spring model. Based on

$$\frac{f_{res}}{f_0} = \sqrt{\frac{k_c + k_{t-s}}{k_c}} \tag{21}$$

With the resonance frequency of the free cantilever f_0, and k_c being the cantilever's spring constant, the cantilever's contact resonance frequency f_{res} is proportional to the spring constant k_{t-s} of the spring representing the tip-sample contact stiffness. k_{t-s} is obtained by the linear approximation of the force distance curve around the equilibrium position z_{eq} of the tip

$$k_{t-s} = \frac{\partial F(z)}{\partial z}\Bigg|_{z=z_{eq}} \tag{22}$$

with the tip-sample force F as a function of the tip-sample distance z. Hence, soft samples with low tip-sample force transfer will have low k_{t-s} resulting in a shift of f_{res} to lower frequencies. A thorough treatment on the importance of resonance tracking, especially for imaging purposes, is given by Ramer et al[31].

1.2.3.2 Tapping mode AFM-IR

As mentioned earlier in section 1.2.1 (p. 16 ff.), tapping mode AFM reduces the tip-sample contact, hence, the likelihood for sample damage of soft samples is decreased compared to contact mode AFM. Also, resonance tracking is not required in this mode due to the reduced tip-sample contact, hence, the effect of the sample's material properties on the resonance frequency is negligible. The signal read-out for resonant tapping mode AFM-IR measurements avails itself of the heterodyne detection scheme[32–34] to demodulate the cantilever amplitude signal which, here, is a mixture of the cantilever's oscillation amplitude and the photothermal expansion of the sample. In practice, the cantilever is driven to oscillate at the first resonance frequency f_1 and the heterodyne detection is e.g., at the second resonance frequency f_2. The laser repetition rate f_{laser} is set to match the difference between f_1 and f_2 (Figure 16). Typical values for f_1 and f_{laser} are 50 kHz and 300 kHz, respectively. In order to isolate the change in the cantilever's oscillation amplitude attributed by the sample's photothermal expansion, the two frequencies (f_1 and f_{laser}) are mixed in a non-linear way according to

$$A_{c1}\cos(f_1 t) * A_{ex}\cos(f_{laser}t) \tag{23}$$
$$= \frac{1}{2}A_{c1}A_{ex}\big[\cos\big(t(f_1 + f_{laser})\big) + \cos\big(t(f_1 - f_{laser})\big)\big]$$

With the cantilever's oscillation amplitude A_{c1} and the increased amplitude due to the sample's photothermal expansion A_{ex}. A lock-in amplifier is used to detect the amplitude at f_1+f_{laser} from which A_{ex} can be derived.
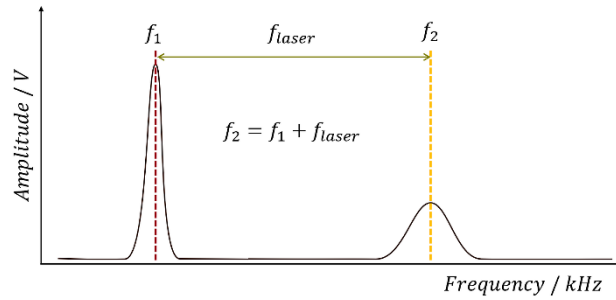
Figure 16. For heterodyne detection, the laser repetition rate f_{laser} is set to match the difference between first (f_1) and second (f_2) resonance frequency of the cantilever.

_____

1.3   Ultrasonic particle manipulation

Acoustic particle manipulation in suspensions is based upon acoustic radiation forces that act on particles in a standing wave field, typically dragging them into the nodal planes of the acoustic standing wave field. A detailed description of the principle of ultrasonic particle manipulation, the design and operation of devices, and application examples are given by Gröschl et al.[35–37]

An acoustic resonator consisting of a transducer and reflector, is needed for generating the standing wave field. The acoustic wave propagates from the transducer to the opposite side (reflector), where it is reflected and superimposes with the incoming acoustic wave, forming a quasi-standing wave field (Figure 17) consisting of nodal and anti-nodal planes emerging perpendicular to the propagation direction of the sound wave. Reflection of the acoustic wave is the result of acoustic impedance mismatch at the boundary of the resonator. The acoustic impedance Z of a material is given by its density ρ and the speed of sound in the medium c_m according to

$$Z = \rho * c_m \tag{24}$$

As a rule of thumb, the greater the difference in acoustic impedance Z, the better the wave is reflected.

The term "quasi-standing" wave field accounts for the amplitude decrease of the wave propagating in the resonator resulting from losses mainly due to the viscosity of the medium, the presence of particles in the medium, and absorption in the boundary surface of the resonator. Hence, superposition of incident and reflected wave does not result in the formation of a pure standing wave field.
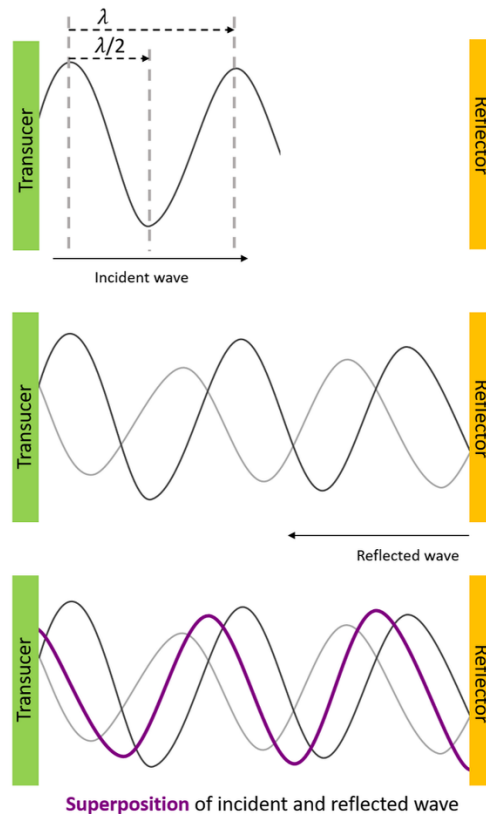
Figure 17. Superposition of incident and reflected wave in an acoustic resonator results in the formation of a quasi-standing wave field.

The transducer's main purpose is to achieve high acoustic intensities in the resonator, hence, PZT (lead zirconate titanate) ceramics are typically employed. For applications in liquid environment, the PZT needs to be separated from the liquid by an electrically insulating carrier, here, Macor ceramics (Corning Inc., USA). Macor is a glass-ceramic with similar mechanical properties as borosilicate glass which according to Gröschl et al[36] is a well suited carrier material, but has the benefit of better machinability. One of the eigenfrequencies of the transducer composed of a PZT, a thin glue layer and Macor as carrier, is at ≈ 2 MHz. Employing this frequency, particles with a diameter of 1 µm up to a few 100 µm can be manipulated. Note that transducer and reflector surfaces need to be arranged in an exact, plane-parallel way to one another. Based on calculations by Gröschl et al[36], changing the angle by 0.05 ° for a distance of 32 mm between transducer and reflector, the resonance quality factor Q decreases by ≈ 10 %. Q describes the sound attenuation ability of a resonator; the higher the quality factor, the more acoustic energy is stored in the resonator.

In a resonant system where the distance between transducer and reflector is set to be a multiple of the half-wavelength of the acoustic wave, the amplitudes of the sinusoidal propagating waves reach a maximum. Considering a 2 MHz-wave in aqueous environment with 1482.66 m/s being the speed of sound in water at T = 20°C[38], the half-wavelength of the acoustic wave is ≈ 371 µm. Since the potential size of the liquid layer between transducer and reflector is mainly limited by attenuation of the sound wave in the liquid medium, typical resonator sizes employed in this work for aqueous suspensions were between 2.5 mm (≈ 7*λ/2) and 10 mm (≈ 27*λ/2). Resonant systems are considered more effective since constructive or destructive interference of incoming and reflected wave is largely avoided, however, these systems also require constant and precise monitoring of the resonant condition.

Particle manipulation in an acoustic standing wave field mainly depends on the primary acoustic radiation force F_z^{rad} acting on the particles with radius R. Considering a sound wave of wavelength λ propagating in z-direction in a suspension with particles of $R \ll \lambda$, F_z^{rad} is defined as

$$F_z^{rad} = 4\pi \cdot \Phi(\tilde{\kappa}, \tilde{\rho}) \cdot (kR)^3 \cdot E_{ac} \cdot \sin(2kz) \tag{25}$$

Where k is the wavenumber of the acoustic wave in the resonator. As can be seen in equation 25, F_z^{rad} strongly depends on the particle radius ($F_z^{rad} \sim R^3$). Furthermore, the primary acoustic radiation force is influenced by density ρ, and compressibility κ of both, particles (subscript p) and medium (subscript 0), and by the ratios (marked with tilde) thereof (see equation 27) as expressed by the acoustic contrast factor $\Phi(\tilde{\kappa}, \tilde{\rho})$ defined as

$$\Phi(\tilde{\kappa}, \tilde{\rho}) = \frac{1}{3}\left(\frac{5\tilde{\rho} - 2}{2\tilde{\rho} + 1} - \tilde{\kappa}\right) \tag{26}$$

$$\tilde{\rho} = \rho_p/\rho_0 , \tilde{\kappa} = \kappa_p/\kappa_0 \tag{27}$$

With the compressibility $\kappa = 1/\rho \cdot c^2$ being inversely proportional to density ρ and speed of sound c in the respective system. Note that the sign of the acoustic contrast factor indicates whether particles are drawn into areas of nodal or anti-nodal planes of the acoustic standing wave field (Figure 18); for $\rho_p > \rho_0$, $\Phi(\tilde{\kappa}, \tilde{\rho})$ has a positive sign indicating that particles are forced into the nodal planes while for $\rho_p < \rho_0$, $\Phi(\tilde{\kappa}, \tilde{\rho})$ has a negative sign and the particles are drawn into anti-nodal planes.

_____

Acoustic standing wave
field with *nodal* *and*
anti − nodal *planes*

$\rho_p > \rho_0, \Phi(\tilde{\kappa}, \tilde{\rho}) > 0$
$\mathrm{e.\,g.}$, PMMA in water

$\rho_p < \rho_0, \Phi(\tilde{\kappa}, \tilde{\rho}) < 0$
$\mathrm{e.\,g.}$, oil in water
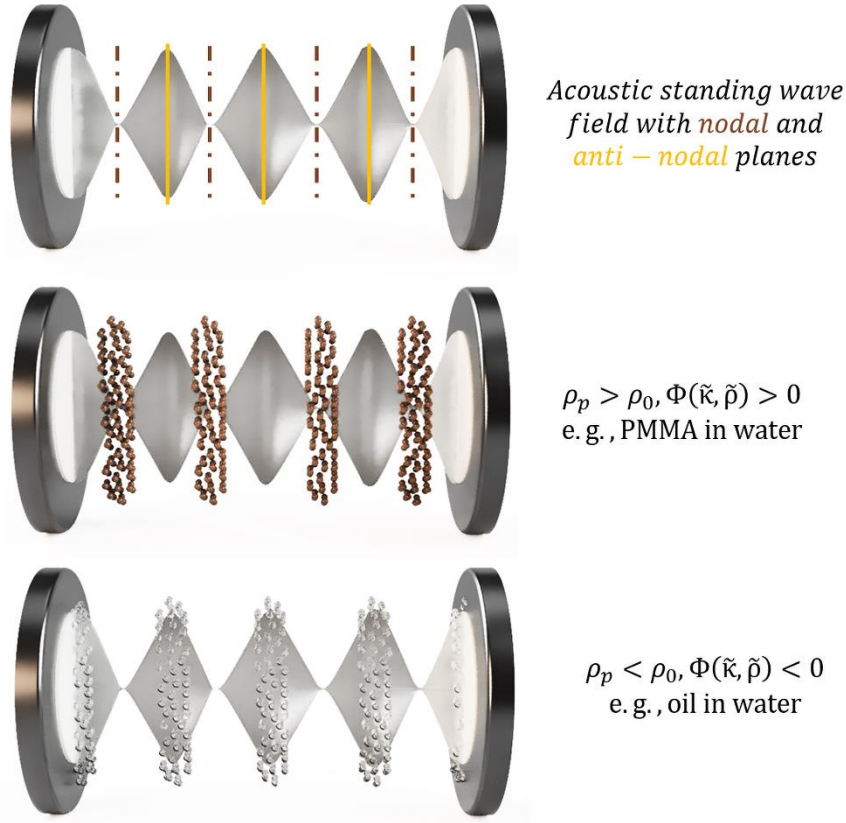
Figure 18. Acoustic resonator with quasi-standing wave field consisting of nodal and anti-nodal planes. Particles with higher density compared to the medium are forced into nodal planes, whereas particles with lower density compared to the surrounding medium will accumulate in anti-nodal planes.

The acoustic energy density E_{ac} describes the energy transmitted into the medium by

$$E_{ac} = \frac{p_a^2}{4\rho_0 c_0^2} \tag{28}$$

With the acoustic pressure amplitude p_a and the speed of sound in the medium c_0.

Additional, less intense forces influence the particle arrangement within a nodal plane, e.g., the transverse primary radiation force F_{xy}^{rad}, or the secondary radiation force F_{xyz}^i. F_{rad}^z is the result of uneven acoustic amplitude distribution along the transducer surface and acts perpendicular to the acoustic pressure wave propagation direction.[39] F_{xyz}^i describes particle-particle interactions and, hence, affects the local arrangement of closely-spaced particles in nodal planes.[40]

1.3.1 Prototype design for in-line probes

In the course of this work, two ultrasonic resonators as add-ons for Raman in-line probes were designed (prototype design by Stefan Tauber, TU Wien, Austria) and tested for their performance in stirred suspensions. The dimensions of both prototypes were adapted to match a D25 Ingold port. Choosing this standard, complex geometries in the design of the add-ons needed to be realized requiring 3D printing by selective laser melting (Citim GmbH, Germany) for the fabrication of 1.4404 stainless-steel prototypes with a classical machining step for surface finishing as the last part of the prototype fabrication. All the materials were chosen based on FDA-compatibility enabling applications in (bio-)process monitoring. Therefore, O-ring sealings (designed according to ISO 3601 standard) fabricated out of FKM - a fluoroelastomer offering high chemical and heat (in the range of 253 K- 598 K) resistance – were employed. As mentioned earlier, Macor was selected as material for the liquid facing carrier plate of the transducer.

Two different arrangements concerning the Raman excitation laser propagation and the ultrasonic wave propagation direction (parallel and perpendicular) were investigated to achieve higher sensitivity and selectivity for Raman in-line measurements due to the combination with ultrasonic particle manipulation. For each arrangement, a prototype was designed as described in the following sections 1.3.1.1 (p. 31 ff.) and 1.3.1.2 (p. 33 ff.).

1.3.1.1 The parallel arrangement

In the parallel arrangement, the laser and acoustic wave propagation direction are arranged in a parallel way to one another. The transducer is placed on the opposite side of the probe head which acts as reflector. Hence, nodal and anti-nodal planes emerge parallel to the lens of the probe head as depicted in Figure 19. Considering homogenously distributed particles in an aqueous suspension, the primary acoustic radiation force F_z^{rad} forces the particles into the nodal planes of the standing wave field, hence, arranges them in planes perpendicular to the laser propagation direction while the transverse primary radiation force F_{xy}^{rad} affects the particle arrangement in the nodal planes. Especially for low particle concentrations, conventional Raman spectroscopy suffers from poor signal intensities due to the low number of particles in the collection cone of the probe. In the arrangement presented here, however, particles are forced into nodal planes and, hence, into the laser focus as soon as the acoustic resonator is active allowing a significant enhancement in signal sensitivity.
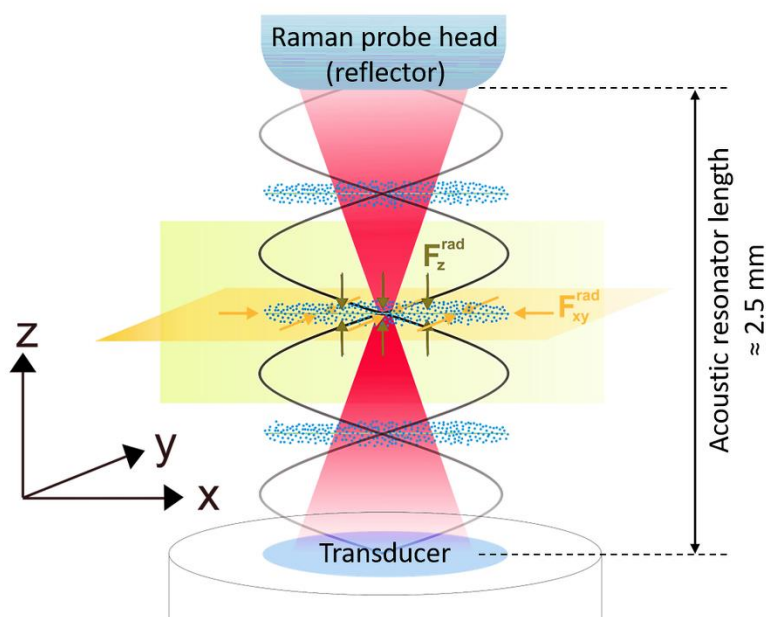
Figure 19. Sketch depicting the parallel arrangement of laser and ultrasonic wave propagation direction. The probe head acts as reflector to build-up the acoustic resonator directly in front of the probe. The primary acoustic radiation force arranges the particles in planes parallel to the probe head.

Considering the Raman spectrum of Macor in water (Figure 20) recorded with an in-line Raman probe (785 nm excitation laser), it is obvious that except for the band depicted at 1640 cm^{-1} (water) there are a lot of bands in the fingerprint region evoked by Macor-specific vibrations, hence, this background needs to be avoided when collecting Raman spectra of the particles in the nodal planes to circumvent possible spectral interferences. The limiting factor for the length of the acoustic resonator was the focal length of 2.4 mm of the available in-line probe. Due to this long focal length, 2.5 mm was determined to be a sufficient distance to avoid Macor-specific bands (Figure 20) in the Raman spectrum while maintaining an acoustic field strong enough for particle trapping in stirred suspensions. With an acoustic frequency of ≈ 2 MHz, 6-7 layers of particles accumulating in the nodal planes are to be expected with this resonator length.
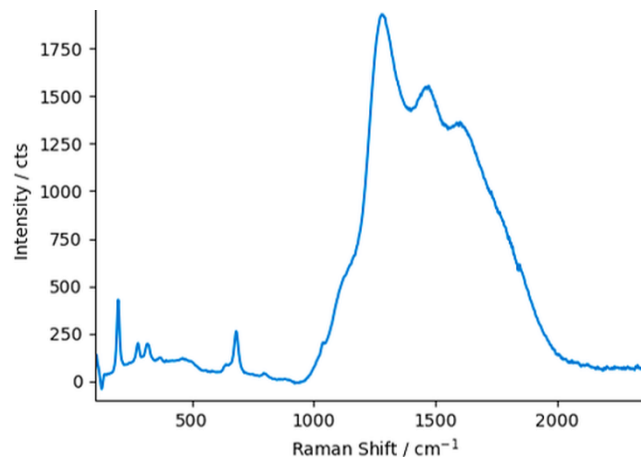
Figure 20. Raman spectrum of Macor ceramics measured in water.

1.3.1.2 The perpendicular arrangement

In the parallel arrangement, the Raman probe sees either homogenously distributed particles (low particle signal) or particles concentrated in nodal planes (high particle signal). In contrast, with the perpendicular arrangement, where laser and acoustic wave propagation are arranged perpendicular to one another, an additional feature – namely, selectivity – is gained for in-line Raman sensing. This can be explained as follows.

By changing the frequency of the acoustic wave from one eigenfrequency of the system to another one, the position of nodal planes changes, allowing the laser focus to be set not only on (Figure 21 a), but also between nodal planes (Figure 21 b). In contrast to the parallel arrangement, the prototype now utilizes Macor ceramics on both sides of the acoustic resonator.

_____
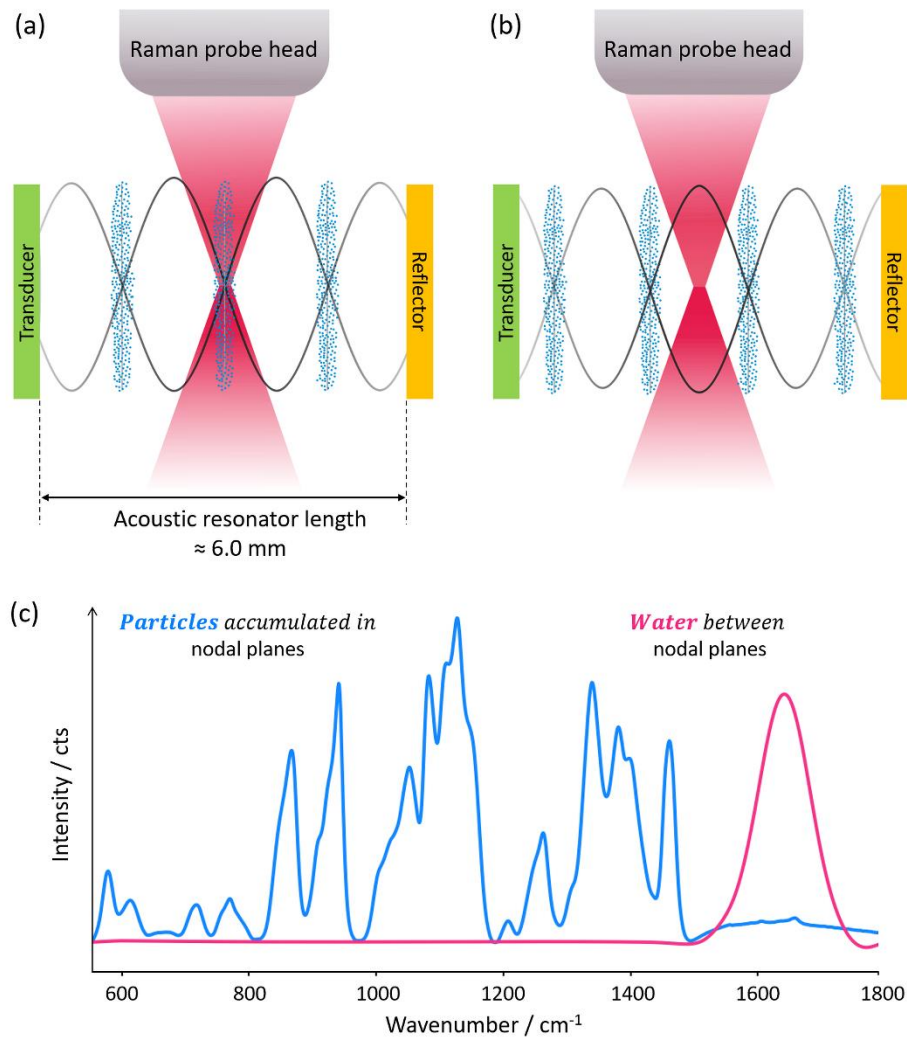
Figure 21. Sketch depicting the perpendicular arrangement of laser and ultrasonic wave propagation direction in the acoustic resonator with 6 mm distance between transducer (insulating Macor layer) and reflector (Macor). a) The particles accumulated in the nodal planes are in the laser focus. b) A change to another eigenfrequency of the acoustic resonator moves the particle-layer out of the probe's focus allowing to investigate the liquid phase (here: water) of the suspension. c) Raman spectra exemplarily shown for starch particles (corresponding to the arrangement in panel -a) and water (corresponding to the arrangement in panel -b) highlight the gain in selectivity due to the perpendicular arrangement.

For measurements on nodal planes where particles are accumulated, a significant gain in signal sensitivity is achieved – similar, or even better than with the parallel arrangement. The main drawback of the first arrangement was the decrease in the overall achievable signal enhancement due to nodal planes with accumulated particles located between the laser focus and the probe head blocking the backscattered Raman photons from being detected. In this case, a Raman probe with short focal length (typically in the size range of one half-wavelength of the employed acoustic wave) would be advantageous. For

measurements on the nodal planes of the perpendicular arrangement, less blocking of backscattered photons was observed resulting in higher enhancement factors. Additionally, investigation of the liquid carrier medium is possible by adapting the frequency of the ultrasonic wave to match one of the other eigenfrequencies of the acoustic resonator. This change in frequency is enough to move the particles in the nodal planes out of the laser focus which consequently is set on the area depleted of particles. Hence, the liquid phase of a given suspension can selectively be investigated (Figure 21 c).

The design and fabrication of the prototype that allows perpendicular arrangement was challenging in order to fulfill the necessary requirements regarding geometry and precision. Therefore, limitations in strength and stability of the acoustic wave field must be considered for the first iteration of this prototype used in this work is. Also, the requirements on the focal length of the Raman probe is different. While a short focal length would be desirable for the parallel arrangement, the perpendicular one currently requires a focal length of ≈ 10 mm. Since no such probe was to our availability, a custom-made probe was fabricated using a stainless-steel tube and an anti-reflection coated lens (Plano Convex Lens, Newport Corp.). Raman measurements in cyclohexane with both probes (custom-made and commercial probe) revealed good agreement in terms of band position and overall signal intensity (Figure 22).
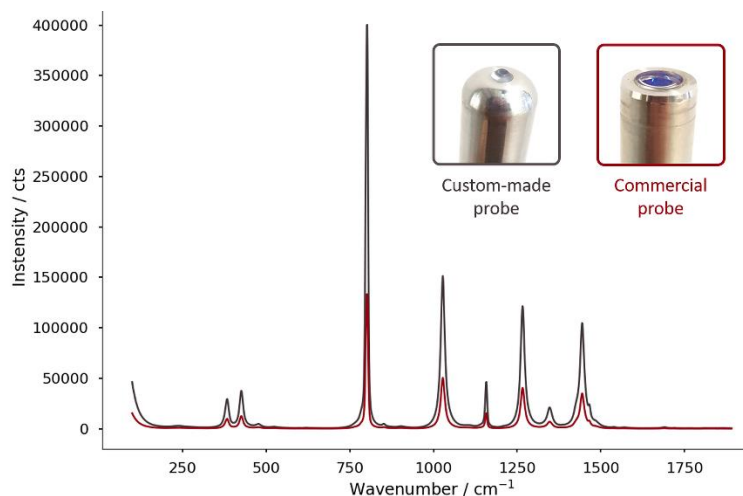
Figure 22. Raman spectra of cyclohexane recorded with the commercial (grey,) and the custom-made probe (red), respectively.

1.4   A selection of useful chemometric tools for data analysis

Extensive investigation of a sample, and vibrational maps of defined sample areas lead to large datasets that are acquired resulting in tedious data processing that challenges the processing power of the operator's PC. Especially, when Raman or IR maps are recorded, not all details of the imaged area are important; sometimes, samples do not have sharp edges, hence, part of the substrate is also part of the vibrational image. Also, the sample might have unwanted open cracks or pores that may cause temporal loss of laser focus or the sample contains other features that can/should be excluded from the dataset before data processing. Chemometric data analysis helps to reduce the dimensionality of the dataset, to focus on the main differences in the recorded maps, and at the same time reduce processing time and required calculation power.

1.4.1   Supervised and unsupervised algorithms

In the following paragraphs, two unsupervised algorithms, namely HCA and PCA, and one supervised algorithm (PLS-DA) which were used within this work, are introduced based on the e-book of H. Lohninger[41] and the book *Chemometrics* by M. Otto[42]. In addition, two application examples are given at the end of this section which report on data recorded within this thesis.

1.4.1.1   Hierarchical Cluster Analysis (HCA)

The basic assumption of HCA is that data points of a n-dimensional dataset that are in close proximity to each other in the n-dimensional space, are similar, e. g., carry similar spectroscopic information. Hence, groups of data points (=clusters) are formed based on similarities between them. First, each spectrum of the data matrix is described as vector before the pair of points with the smallest distance is determined and merged to a single point (panel 1 to 2 in Figure 23). Iterative determination of the pair with the smallest distance measure leads to the formation of clusters (panel 1-5 in Figure 23). The result is visualized in the form of a dendrogram where distances between single clusters indicate the degree of similarity between them (short distance indicates high similarity and vice versa).
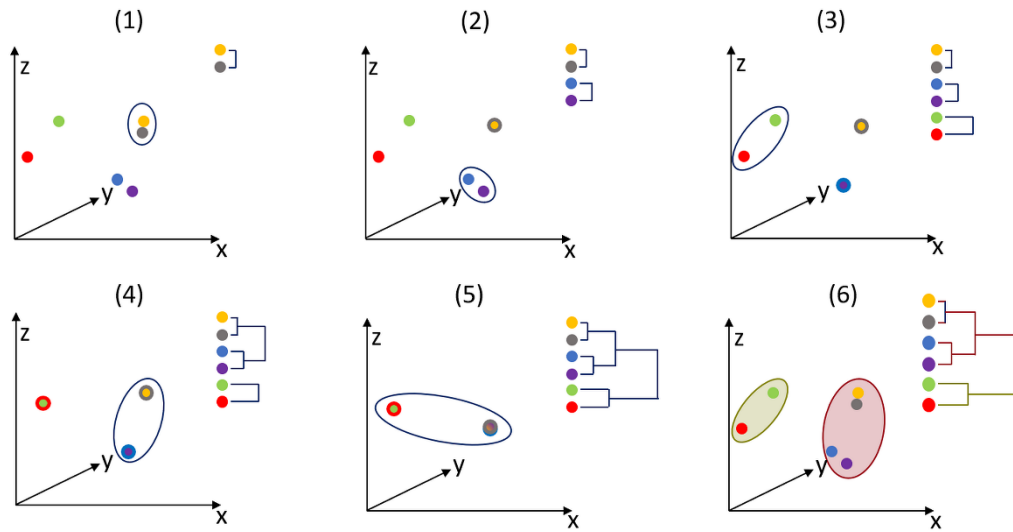
Figure 23. Basic concept of HCA. Datapoints in the n-dimensional (here: n=3) space are clustered according to their distance/similarity to each other.

Several different distance measures (e.g., Manhattan, Euclidean, or Mahalanobis distance) and algorithms (e.g., single-linkage, average-linkage or Ward's minimum variance) may be employed to determine the distance of every point in space to every other point and build-up the according dendrogram. One of the most commonly used metrices is the Euclidean distance measure, typically in combination with Ward's method[43] (fusion of clusters based on the criterion of keeping the increase of variance due to cluster fusion to a minimum). According to the Euclidean distance measure, the distance d_{ij} between datapoint i and j in the n-dimensional space is described as the root square of the sum of squared distances

$$d_{ij} = \sqrt{\sum_{i=1}^{n} \left(x_{ik} - x_{jk}\right)^2} \tag{29}$$

With k being the index of coordinates. Hence, in a 3-dimensional space (k = 1, 2, 3), the distance d_{ij} between point $i(a_{i1}, b_{i2}, c_{i3})$ and $j(a_{j1}, b_{j2}, c_{j3})$, is given by

$$d_{ij} = \sqrt{\left(a_{i1} - a_{j1}\right)^2 + \left(b_{i2} - b_{j2}\right)^2 + \left(c_{i3} - c_{j3}\right)^2} \tag{30}$$

Depending on the degree of detail that is claimed by the individual dataset, the number of clusters can be selected in an unsupervised way (panel 6 in Figure 23). Hence, HCA is a

powerful tool to reduce the heterogeneity of a dataset to clusters of similar data points, e. g., spectra or pixels that carry similar spectral information.

1.4.1.2 Principal Component Analysis (PCA)

PCA is another unsupervised algorithm which is based on the rotation of the coordinate system. The high-dimensional data matrix is projected onto a lower dimensional space to facilitate data analysis. The data matrix X is decomposed to two matrices S and L such that

$$X = S * L^T + E \tag{31}$$

Where L^T is the transposed loading matrix, S is the score matrix, and E the error matrix (portion of the dataset that is not fully explained by the first few components; ideally, noise of the data) as illustrated in Figure 24.
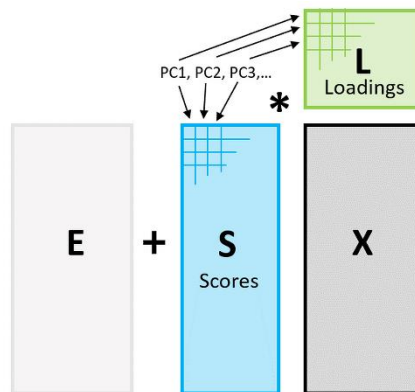
Figure 24. In PCA, the original data matrix is decomposed to a loadings matrix (L) and a scores matrix (S). Multiplication of the transposed L and S results in the original data matrix X reduced by the error matrix E.

In an iterative approach, the first principal component (PC1, first axis in the new coordinate system) is determined by finding the direction in space that exhibits the greatest variance (Figure 25 left). The second principal component (PC2) points to the direction of greatest variance perpendicular to PC1. This step is repeated for all n dimensions which results in a new orthogonal coordinate system (Figure 25 right) arranged such that the first few principal components explain most of the variance in the data.

_____
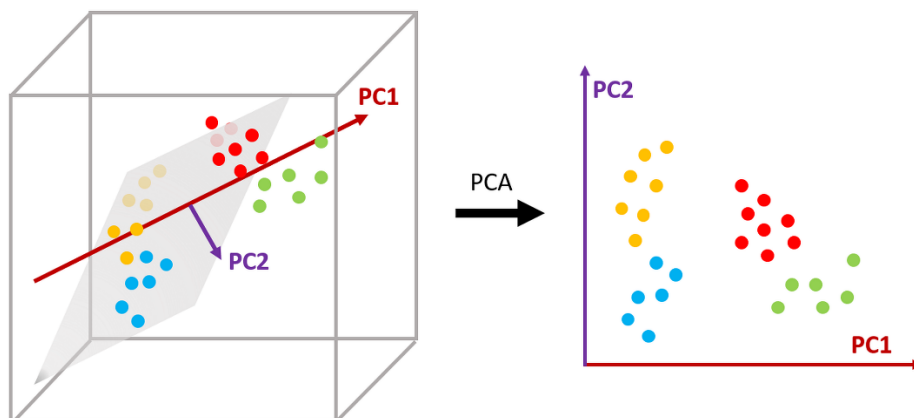
Figure 25. Basic concept of PCA. Rotation of the original coordinate system (left) according to the direction of greatest variance in the n-dimensional (here: n=3) space results in a new coordinate system (right).

The scores are the coordinates in the new, rotated coordinate system. They are calculated by multiplying the coordinates of the original coordinate system with the loadings. Therefore, the loadings reflect the contribution/weighting of each datapoint (e.g., spectral feature) to the variance of the dataset described by the corresponding principal component.

PCA is a powerful tool to reduce the dimensionality of the dataset focusing on the spectra/ spectral features/ pixels that carry the information explaining most of the variance in the dataset. It can also be used to reduce noise in the spectral data. Multiplication of loadings and score matrix (without the noise ideally described by the error matrix) results in the original, noise-reduced dataset.

1.4.1.3   Partial Least Squares – Discriminant Analysis (PLS-DA)

PLS-DA is a supervised classification algorithm that is best explained by starting with an introduction to PLS Regression (PLS-R). PLS-R, or simply PLS, is a linear calibration method that has proven itself useful when analyzing noisy and/or collinear datasets. It connects independent variables X (e. g. spectra/ selected spectral features) with dependent variables Y (target variable, e. g. concentration of more than one compound in a chemical mixture) such that Y can be predicted by X based on the PLS model. Therefore, PCA of X, and Y, respectively is performed before a regression model that correlates the scores of PCA 1 and 2 is defined.

The basic principle of PLS is illustrated in Figure 26. First, X and Y are decomposed into a score (T and U for X and Y, respectively), loading (P and Q for X and Y, respectively) and error matrix (E and F for X and Y, respectively). Then, the scores of both PCAs are set into correlation by a regression model (inner relation U=B*T) such that the covariance

between the transformed matrices T and U is maximized while the error matrix E is minimized.
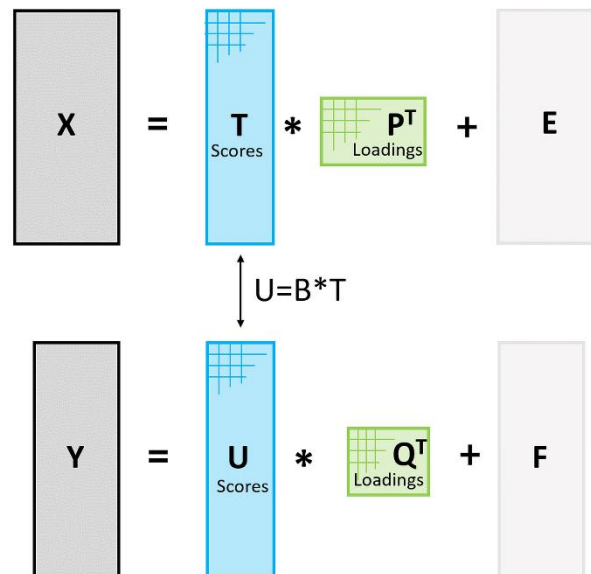
*Figure 26. Basic concept of PLS-R. PCA of X and Y is performed before the scores of each matrix decomposition are set in relation to each other via a regression model (U=B*T).*

The optimal number of components (= latent variables) is determined in a cross-validation process where the dataset is divided into a calibration set that is used to build the model, and a validation set where the model is subsequently applied to. Typically, several iterations of this step are performed to ensure reliability of the model. Depending on the dataset, roughly 10 -30 % of the data is used for validation purposes where the RMSECV (root mean square error of cross-validation) value as measure of model performance is calculated.

PLS-DA is a supervised classification method based on the concept of PLS except that here, Y is a dichotomized target variable (e. g., yes/no answer depending on a certain threshold value). For class assignment, a matrix consisting of indicator variables for each class is created where the number of columns corresponds to the number of classes (e.g. 3 in Figure 27). Considering the example in Figure 27, several IR or Raman spectra which should be assigned to 3 different classes were recorded with the according intensity values in the data matrix X and the class assignment in the matrix Y.
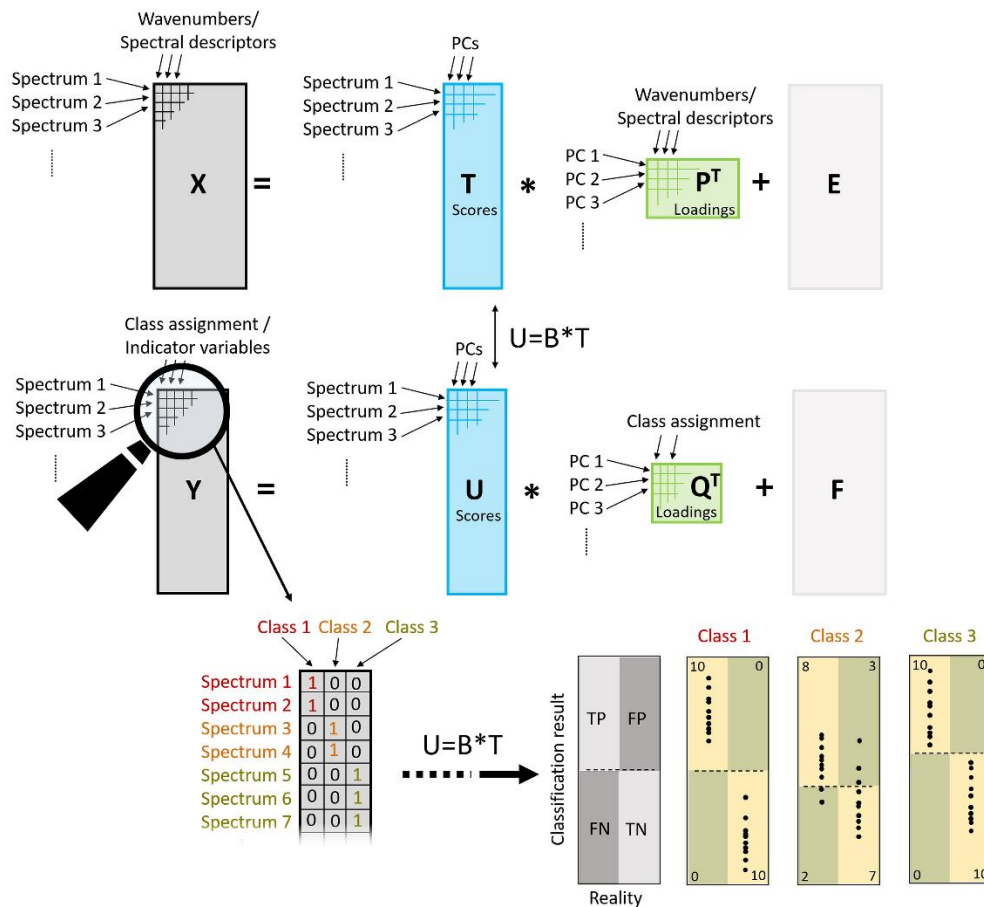
Figure 27. Example of PLS-DA for spectral data that should be assigned to three different classes (class 1, 2, 3). The classification result is shown in the lower half for all three classes. TP = true positive, FP = false positive, FN = false negative, TN = true negative.

After calculating the PLS-DA-model, the result is depicted for each class as a comparison of real class assignment and classifier result. Hence, four results are possible:

1) True positive (TP): The spectrum belongs to class 1 which is confirmed by the classifier.
2) False positive (FP): The spectrum does not belong to class 1, but the classification result indicates otherwise.
3) True negative (TN): The spectrum does not belong to class 1 which is confirmed by the classifier.
4) False negative (FN): The spectrum does not belong to class 1, but the classification result indicates otherwise.

Hence, in Figure 27, class 1 and 3 indicate good classification (all spectra were assigned correctly) while the PLS-DA classifier did not work well for class 2 (5 misclassifications). The dashed line in the classification result box indicates the threshold value for each class.

This value can either be determined through cross-validation or ROC (receiver operating characteristic) curve. The ROC curve results from plotting the FP-rate against the TP-rate as a function of the threshold value (Figure 28). The ideal threshold value allows 100% TP and no FP classification. A compromise is found in the threshold value at the point which is closest to this ideal description.
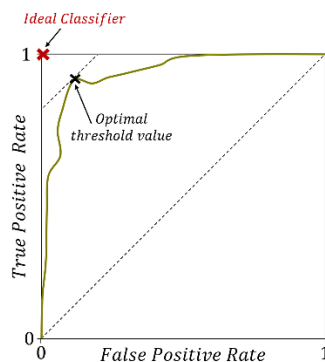
Figure 28. ROC curve for determination of the optimal threshold value which is the one that is closest to the upper left corner of the plot (= ideal classifier).

1.4.2   Application examples for multivariate data analysis

Data preprocessing and multivariate analysis are two essential tools every spectroscopists requires for detailed analysis, especially of large datasets. Basic processing steps such as baseline correction and data scaling, first and second derivative calculation, standardization etc. are summarized by Baker et al for IR spectroscopy[44] and by Butler et al for Raman spectroscopy[45]. Note that both articles focus on the analysis of biological materials. In the following paragraph, FTIR imaging data of lung tissue and multi-sensor based chemical imaging are discussed highlighting the power of multivariate data analysis.

1.4.2.1   FTIR and MALDI-MS imaging of lung tissue (Publication V)

The motivation for this study was to investigate the effect of amorphous silica NPs on the phospholipid composition (PLC) of lung tissue by means of MALDI-MS and FTIR imaging. In the case of lung inflammation due to crystalline silica, a change in the PLC is detected upon examination of the bronchoalveolar lavage fluid[46] (BALF; a fluid that is sprayed into a part of the lung via a bronchoscope and collected by the same tool). While crystalline silica may cause progressive fibrosis or even cancer[47], amorphous silica NPs are known to be responsible for transient lung inflammation[48,49]. However, up to now, their effect on the PLC of lung tissue has not been studied.

8 µm thick cryosections of rat lung after intratracheal instillation of amorphous silica NPs with an average size of 25 nm were fixed on a CaF$_2$ slide. Single point FTIR spectra were recorded in transmission mode employing a 15x Cassegrain objective with a step size of 100 µm. Automated raster scanning with the Bruker Hyperion 3000 FTIR microscope equipped with a liquid nitrogen cooled single point MCT detector was performed covering a sample area of 7.1 x 6.5 mm^2. For more detailed information on sample preparation and parameter settings, the reader is referred to Publication V (p. 133 ff.).

In a monovariate data analysis approach, the CH stretch vibration region around 2900 cm^{-1}, typically assigned to lipids[44,50], was integrated using a 2-point-baseline subtraction to extract first information on areas of higher or lower lipid content of the imaged sample area. The raw spectra recorded at roughly 60 different measurement positions are shown exemplarily in Figure 29. Not that in the raster scan image, a single spectrum was recorded at each pixel resulting in total of 4615 spectra that were acquired in the selected sample area. Superposition of the local distribution of the integrated CH stretch vibrations (highlighted in grey in Figure 29) with the white light image of the imaging area (Figure 29 right-hand side) indicates some areas of the sample with higher CH stretch intensity/ lipid content. Based on the white light image, however, this structure is assigned to a bronchiole. Other than indicating the contours of the bronchiole, the monovariate data analysis approach does not allow more detailed data analysis. So far, the essential information seems to be hidden in the n-dimensional, hyperspectral data cube.
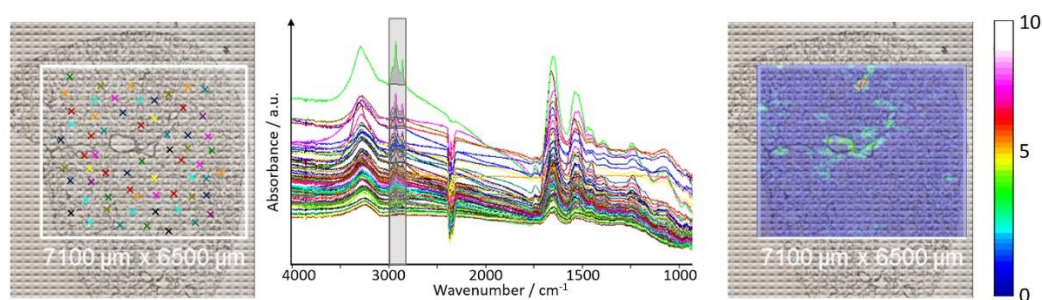
Figure 29. White light image of a 8 µm thick cryosection of a rat lung on CaF$_2$. FITR imaging area is marked in white. Measurement position of single FTIR spectra are marked in the image on the left. The overlay of the local distribution of the integrated CH stretch vibration (highlighted in grey in the spectra in the middle) with the white light image on the right side indicates minor success on the detection of the spatial lipid distribution.

For subsequent multivariate data analysis, the spectral data was pre-processed in several, successive steps:

1) To reduce the dimensionality of the data matrix, the spectral region covered by a single spectrum was reduced from 400 cm^{-1} – 4000 cm^{-1} to 1000 cm^{-1} - 3600 cm^{-1}.

This region contains all the spectral information on lipids and proteins required for data analysis.

2) Spectra were baseline corrected using the Lieber algorithm (3rd order polynomial, 30 iterations) and scaled between 0 and 1 for better comparison.

3) 13 spectral descriptors (see table in Figure 30) were defined allowing to further reduce the dimensionality of the data cube. Spectral descriptors have the advantage that the subsequently applied analysis algorithms only focus on the predefined spectral areas of interest, however, entailing the risk of accidentally excluding crucial information. Hence, detailed sample knowledge is required for defining a complete list of spectral descriptors.

4) PCA was applied to exclude pixels with poor SNR or pixels that were part of the FTIR imaging area but not of particular interest for the analysis, e. g., areas without lung tissue (areas outside of the sample, or lung areas containing bronchioles or blood vessels).

Spectral descriptor	Wavenumber / cm^{-1}	Band assignment
1	2958	$\nu_{as}(CH_3)$ of acyl chains (lipids)
2	2924	$\nu_{as}(CH_2)$ of acyl chains (lipids)
3	2852	$\nu_s(CH_2)$ of acyl chains (lipids)
4	1740	$\nu(C=O)$ of lipids; ester $\nu(C=O)$ of phospholipids
5	1726	$\nu(C=O)$ of fatty acid ester
6	1653	Amide I
7	1535	Amide II
8	1450	$\delta(CH_2)$, lipids, fatty acids
9	1385	$\delta(CH_3)$
10	1225	$\nu_{as}(PO_2^-)$; symmetric stretching of phosphate groups in phospholipids
11	1163	$\nu(C-OH)$ of oligosaccharides
12	1080	$\nu_s(PO_2^-)$

ν_s ... symmetric stretch, ν_{as} ... asymmetric stretch, δ ... bending
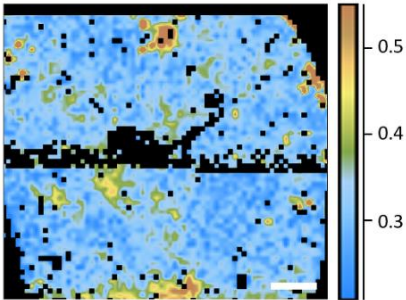
Figure 30. List of spectral descriptors with the corresponding band assignments[50] (left) and pixels excluded from data analysis marked in black (right)

Pixels excluded from subsequent data analysis based on PCA are depicted in black in Figure 30 (right). The remaining spectral data was investigated applying HCA (Euclidean distance measure, Ward's method) to the standardized (mean = 0.0, standard deviation = 1.0) data. The dendrogram (panel -a in Figure 31) indicates differentiation of two distinct clusters colored in red, and blue, respectively. The according distribution of cluster 1 (red) and cluster 2 (blue) indicate distinct areas of the lung tissue that differ from each other in the spectral fingerprint (panel -b in Figure 31). Superposition of the MALDI-MS ion image depicting the areas of PI 34:1 overexpression in the lung tissue of a co-located cryosection with the distribution of the blue cluster 2, indicates good correlation. Based on fluorescence staining, it could be shown that areas of PI overexpression correlate well with areas affected by silica NPs (related data shown in Publication V, p. 133 ff.). Calculating the difference spectrum of the mean spectra of blue and red cluster allows to highlight major spectral differences between the two clusters. The difference spectrum in Figure 31 (black spectrum in panel -d) shows more intense vibrations resulting

45

from lipids such as the asymmetric CH$_2$ stretch vibration v_{as}(CH$_2$) at 2918 cm^{-1}, or the symmetric CH$_2$ stretch vibration v_s(CH$_2$) at 2850 cm^{-1}. Additionally, the blue cluster illustrates higher intensity of the band at 1734 cm^{-1} evoked by carbonyl stretch vibrations of esters of fatty acids. The dashed, grey lines mark these vibrations in the difference spectrum in Figure 31 d. In contrast to that, a decrease of band intensities in the spectral ranges of 1695-1620 cm^{-1}, 1580-1480 cm^{-1} and 3095-3450 cm^{-1} (assigned to proteins: Amide I, Amide II, Amide A, respectively)[50] is observed corresponding to the areas highlighted in grey in Figure 31 d. Hence, the cluster analysis of FTIR spectral data clearly outlines areas of higher lipid and phospholipid content (blue cluster) whereas the red cluster highlights areas of comparatively higher protein content.
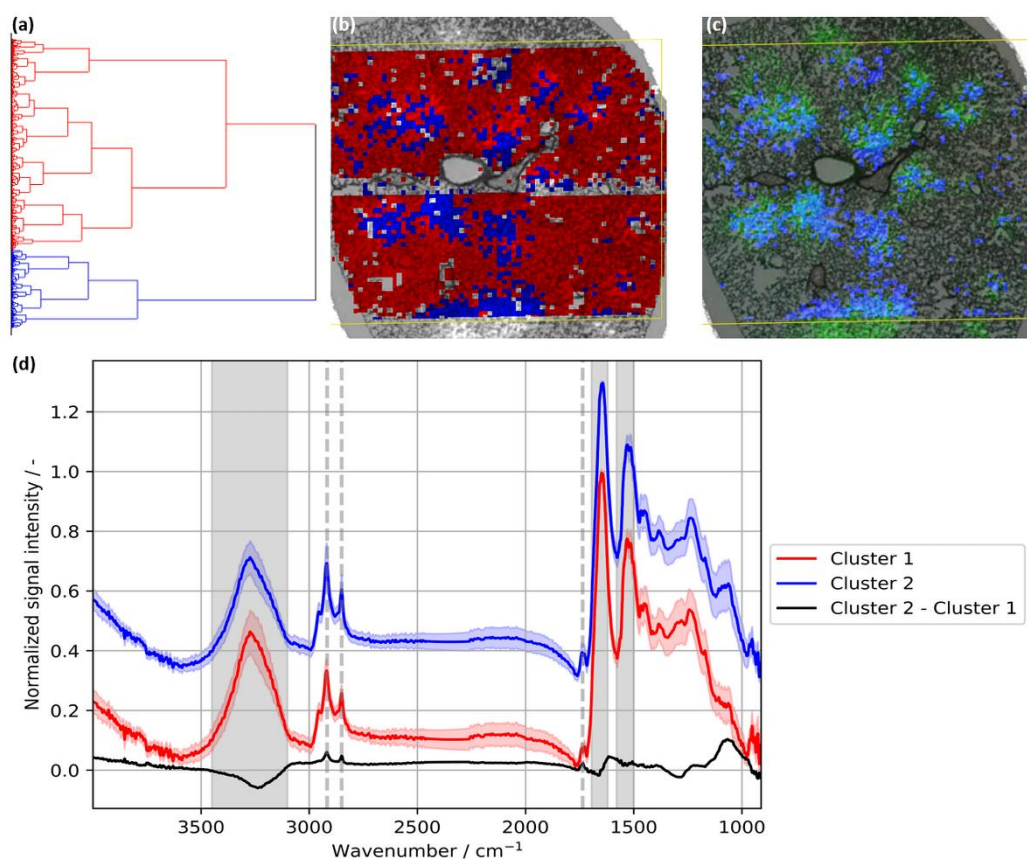
Figure 31. a) Dendrogram depicting that the data set consists of two main clusters (red and blue). b) Lateral distribution of red and green cluster. c) Superposition of blue cluster based on FTIR spectroscopy with the MALDI-MS ion image depicting overexpression of PI shows good correlation. d) Mean and single standard deviation of the spectra representing the red, and blue cluster (plotted in the respective colors), respectively. The difference spectrum (black) of blue minus red cluster average spectrum indicates higher lipid content in the blue cluster (lipid-specific bands are marked by grey dashed lines) while the red cluster shows higher protein content (protein-specific areas highlighted in grey). Adapted with permission by CC-BY License (https://creativecommons.org/licenses/by/4.0/) from Phosphonate Coating of SiO$_2$ Nanoparticles Abrogates

It was demonstrated that images obtained by different analytical methods – PI 34:1 ion image revealed by means of MALDI-MS and tissue sections containing higher lipid and less protein content revealed by means of FTIR imaging – correlate well exhibiting an inhomogeneous round-shaped distribution around NP-affected areas throughout the investigated tissue section. Thus, FTIR hyperspectral imaging as a non-destructive tool has proven to be very useful for identifying local accumulation of lipids which are co-located with areas of PI overexpression as detected by MALDI-MS imaging. Hence, infrared spectroscopy can be used to study cytotoxic effects induced by silica NPs in lung tissue.

1.4.2.2 Multi-sensor-based chemical analysis (Publication VI)

Another example of chemometric-based data interpretation is given in Publication VI (p. 151 ff.) where multi-sensor imaging approaches in combination with multivariate data analysis are employed for chemical structure determination. Samples from three different scientific areas (aerosol chemistry, biology, material science) were investigated based on their vibrational (Raman imaging), elemental (EDX) and mass spectrometric (TOF-SIMS) fingerprint. A combined multi-sensor, hyperspectral data cube consisting of a selection of spectral descriptors for each method was generated for subsequent multivariate analysis. This allows to create a representative color-coded image based on both, chemical and elemental information, simultaneously. Key challenges of this approach include

(i)   the selection of a substrate that can be used for all analytical methods,

(ii)   finding an appropriate way to mark the measurement position which must be identical for every analysis method and

(iii)   combining methods that allow comparable lateral resolution (the resolution of the combined data cube is limited by the method with the worst lateral resolution).

Here, the employed analytical methods allow resolutions from ≈ 200 nm (Raman) to ≈ 100 nm (TOF-SIMS), to ≈ 50 nm (EDX). Also, the order in which the different methods are applied to the sample needs to be considered depending on whether the analytical method is destructive (TOF-SIMS) or non-destructive (Raman, EDX), or requires sputtering to enhance imaging contrast or allows insulating materials to be measured (TOF-SIMS, EDX). Furthermore, the sample needs to have a lifespan of at least one day (each analysis methods requires several hours) and must be stable under vacuum conditions (SOF-SIMS). The combined, multisensory approach provides a more complete picture of the sample. Additionally, over-interpretation of data is prevented due to simultaneous cross-checks with complementary analytical methods which is especially helpful for complex samples as shown for tumor cells, a ceramic composite and an environmental aerosol sample.

As an example, the study of the tumor cells is elucidated here in more detail. The investigated tumor cells were pretreated with a Br-containing prodrug whose inactive form (evofosfamide, also known as TH-302) is activated in the oxygen-reduced environment (hypoxia) of tumor cells by decomposition to bromo-isophosphoramide (Br-IPM; active form). Br-IPM acts as DNA cross-linker which hampers DNA replication and thus inhibits tumor cell proliferation.[51] For combined data analysis, the acquired data sets (Raman, EDX, TOF-SIMS) were fused to one multi-sensor, hyperspectral data cube using ImageLab software (Epina GmbH, Austria). To assure good alignment between layers from different analytical methods, linear affine transformation was performed based on user-defined anchor points.[52] 9 spectral descriptors were selected representing characteristic chemical and elemental sample features in the Raman, EDX and TOF-SIMS data. First, PCA of the standardized spectral descriptors was performed. To illustrate the correlation of the selected spectral descriptors across the employed analytical methods, HCA of the loadings of the first few PCs can be performed. Here, loadings of PC1 and PC2 were selected based on the criterion of maximizing the distance between clusters[53] resulting in a well-structured dendrogram. Figure 32 a depicts the distinct separation of two main groups of clusters of the HCA dendrogram. The distribution of these two groups superimposed with the white light image of the tumor cells is shown in Figure 32 b. The orange-colored cluster represents the nuclei of the cells which is confirmed by Raman (Amide I band, CH stretching), EDX (N K_α line) and TOF-SIMS data (CNO$^-$ at m/z 42.00 and CN- at m/z 26.00), while the blue cluster colors the Br-containing (EDX: Br L_α; TOF-SIMS: both Br isotopes ^{81}Br and ^{79}Br), lipid-rich (Raman: CH_2 stretching of lipids) areas of the tumor cells. The image in Figure 32 b captures cell mitosis in the cell on the right sight indicated by the presence of two nuclei in the separating cell. In contrast, the cell on the left only contains one nucleus which might indicate the tumor-killing impact of the drug or a cell which might undergo cell mitosis but not at the moment captured by this image. A detailed study varying incubation time of the drug and comparison to untreated tumor cells would help clarify this uncertainty. Based on Raman spectroscopic data, the drug distribution would not have been accessible, however, due to elemental analysis, the presence of the Br-containing drug in the cells can be visualized highlighting the advantage of combining complementary, analytical methods.
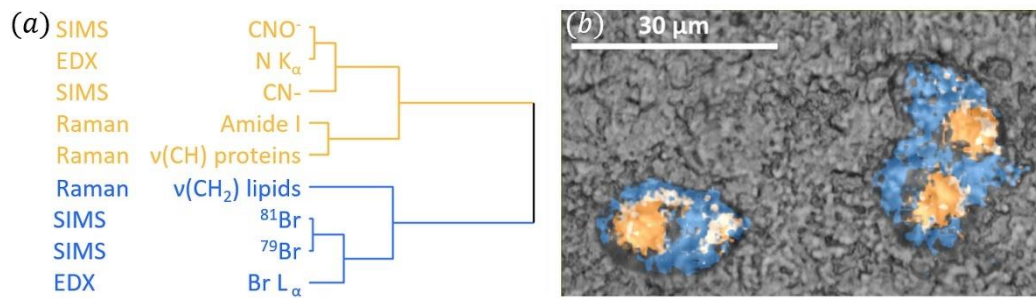
Figure 32. (a) HCA dendrogram of the loadings of the first 2 PCs indicates two distinct clusters colored in orange and blue. (b) The distribution of both clusters is shown in the respective colors superimposed with the white light image of the tumor cells. Adapted with permission by CC-BY License (https://creativecommons.org/licenses/by/4.0/) from Image-Based Chemical Structure Determination; Ofner J., Brenner F., Wieland K. et al; Scientific Reports, 2017, 7, 6832, 10.1038/s41598-017-07041-x

2   Results and introduction to the publications

In process analytical technology (PAT), analytical methods are employed to gain a more detailed insight into the (bio-)process. Process monitoring can be performed in different ways depending on the measurement location (in or outside of the bioreactor/vessel) and the timespan between sampling and obtaining the analysis result (Figure 33):

- *Off-line* analysis requires manual sampling before the analysis is performed either somewhere in the same facility or is sent to an external lab. This procedure usually requires hours or days to get the analysis result, therefore, it is not applicable for process control purposes. However, valuable insights into process understanding might be gained.
- *At-line* analysis also requires manual sampling, however, the analysis instrument is located close to the vessel, hence, the time delay from sampling to obtaining the analysis result is shorter compared to off-line analysis.
- *On-line* analysis allows automated sampling, e.g., through a by-pass system, with subsequent, direct analysis methods, e.g. through a transparent window, whereas for
- *In-line* analysis, the sensor is placed in the vessel to allow in-situ measurements.
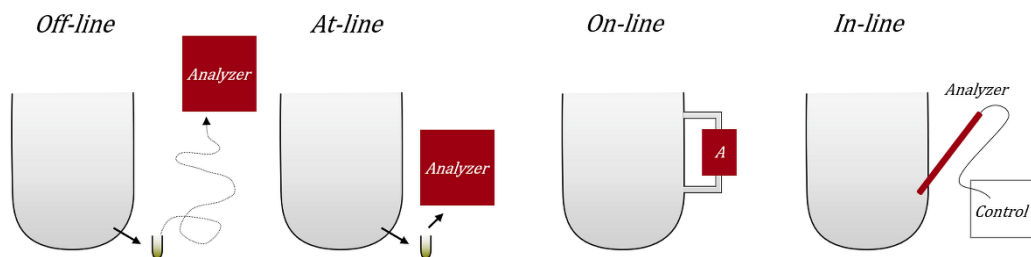
Figure 33. Instruments in process analytical technology differ depending on the sampling and the measurement location.

The timescale for on-line and in-line measurements is reduced to minutes, or even seconds compared to off-line and at-line analysis (hours, up to days). In contrast, higher requirements in terms of instrument robustness are required for in-line analysis since in-line sensors are in direct contact with the sample and, thus, need to be autoclavable.

Each (bio-) reactor is equipped with numerous sensors to measure and adjust the physical and chemical variables of the process such as temperature, pH, flow rate, O_2 and CO_2 concentration (in liquid and gas phase), substrate feeding rate, etc.[54] Theses sensors allow real-time monitoring of the parameters that are needed to control and model the (bio-) process. In addition, they can be used for an indirect process control approach since changes in the process can be derived from them. For example, in fermentations with

microorganism, the respiratory quotient (RQ) defined as the ratio of CER (CO_2 evolution rate) and OUR (oxygen uptake rate) can be used as an indicator of the cells' metabolic state (different pathways require different energy, hence RQ changes)[55,56]. However, considering process optimization approaches at laboratory scale, information on the biomass growth and production efficiency typically requires frequent sampling for subsequent off-line or at-line analysis to determine e.g., the optical density (OD) with a UV/Vis spectrometer and/or the dry-weight of centrifuged biomass pellets for biomass growth monitoring.[54] Additionally, chromatography is used to determine metabolite concentrations. In contrast, in-line, spectroscopy-based sensors enable access to biomass growth, product or (unwanted) by-product in real-time which might be crucial for process control purposes.[57,58]

2.1 Off-line and in-line spectroscopy - based analysis at the microscale

Both, IR and Raman spectroscopy, are readily employed for reaction monitoring in process analytical technology since they allow non-destructive identification of the components in the (bio-) reactor in a reasonable amount of time (a few minutes).[59–61] However, compared to off-line instrumentations, in-line probes usually suffer from poor sensitivity. Hence, for low analyte concentrations, off-line spectroscopy-based analysis is preferable but at the cost of losing real-time access to the analyte information. Another way to gain sensitivity is the combination of ultrasonic particle manipulation with in-line probes, which was shown by Koch et al[62] for in-line IR spectroscopy. As a continued development, the combination with Raman in-line probes is implemented in this thesis.

The following paragraphs highlight the sensitivity of off-line Raman spectroscopy for the analysis of *P. chrysogenum* spores' viability. As a first step towards more sensitive in-line Raman spectroscopy, the combination with ultrasonic particle manipulation is demonstrated for particles in the lower µm-range. Two different prototype geometries are characterized to improve not only the sensitivity, but also the selectivity of in-line Raman probes.

2.1.1 Classification of *P. chrysogenum* spores based on confocal Raman spectroscopy (Publication I)

In this publication, off-line confocal Raman spectroscopy was used in combination with PLS-DA to develop a classifier for the determination of spore inoculum quality. Specifically, *P. chrysogenum* spores were investigated prior to cultivation/gemination meaning that spores are in a dormant state without metabolic activity. *P. chrysogenum* is a filamentous fungus that is readily employed in pharmaceutical industry to produce the β-lactam antibiotic penicillin. A typical penicillin production process consists of several steps:

1) Cultivation of spore inoculum and transfer to a batch process to achieve high biomass concentration. At this point, process parameters are adjusted such that the concentration of the producing fungi is maximized.
2) In the subsequent fed-batch process, the substrate feed rate, among other parameters, is regulated such that high production yields are achieved.
3) At the end of the fed-batch process, when a considerable part of the producing agents is dead and the product yield starts to decrease, the bioprocess is stopped.
4) Biomass is separated from the product which is purified and enriched in the so-called downstream process.

To maximize product yield, minimize production time and exploit bioreactors at optimal work-load, real-time adjustment of process parameters is required. The earlier a problem,

e.g., a small growth rate, is encountered, the earlier counteraction measures can be taken to avoid loss in time, product and money.

Storage significantly affects the spore inoculum's quality. For example, based on in-house knowledge of the industrial cooperation partner, 90 % of the spores are considered non-viable after 1 year of storage time. Hence, a quality control step is needed before cultivation. While there are analytical protocols available to determine spore viability (fluorescence staining, counting colony forming units (CFUs), etc.), they all require metabolic activity. Moreover, some of them are time-consuming, require staining or are not sufficiently reliable.[63–66] In contrast, Raman spectroscopy offers a destruction-free, fast, label-free approach with minimal sample preparation that has been proven very useful for chemical composition investigation of single bacterial cells[67], and fungal spores[68], respectively. In addition to identification approaches of bacteria[69,70] and different fungal spores[71–73] based on their Raman spectroscopic fingerprint, successful in-vivo imaging of human cells or yeast cells, typically in combination with multivariate statistics, was demonstrated by Klein et al[74], or Ando et al[75], and is summarized in reviews by Schie et al[76], or Smith et al[77]. Here, Raman spectroscopy is used to classify fungal spores based on their viability through investigation of isolated, single spores. The main challenges in this study were:

- As most biological systems, *P. chyrsogenum* spores show autofluorescence. To avoid excitation of fluorescence and, thus, saturation of the detector, a Raman excitation laser wavelength of 785 nm (diode laser with 300 mW nominal output power) was chosen.
- Spores are small (1-3 μm in diameter), thin (≈ 2 μm) samples (Figure 34) requiring a 100x objective, and thermolabile, hence, the laser power needed to be reduced to 4.5 mW to avoid heating effects and carbonization of the sample. Since the intensity of the Raman photons correlates with the intensity of the incident photons (see equation 17), longer integration times were needed to balance low laser power and signal to noise ratio.
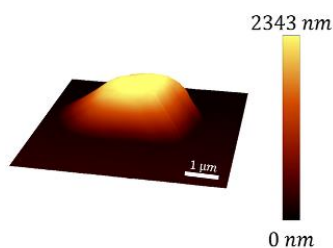
Figure 34. Topography image of a single P. chrysogenum spore.

- To avoid spectral interference with components of the medium where the spores are stored in, a 1:500 dilution step was implemented as sole sample preparation step. Finally, 1 µl droplets were placed on a CaF$_2$ substrate, and let dry at room temperature before Raman analysis. Hence, the dilution step also had a second function: isolation of the spores on the substrate.
- A reference for dead spores was selected carefully since typical procedures (e.g., exposure to thermal stress, ethanol, etc.)[78] are also reflected in the Raman spectrum. Based on fluorescence staining of a sample aliquot, more than 95 % of spores stored for longer than 1 year were determined to be dead. Hence, as reference for dead spores, samples older than 1 year were used.

Finally, Raman spectra of 129 living, and dead spores, respectively, were collected based on a raster scan method where each measurement position is selected manually before the automated measurement is started. To build a PLS-DA model, 178 out of 258 spectra were used as calibration set, while the remaining 80 spectra were used as validation set. Based on 3 latent variables, the PLS-DA model with a sensitivity and specificity of > 95 % was obtained highlighting a successful implementation of Raman spectroscopy for the classification of *P. chrysogenum* spores based on their viability.

2.1.2 Ultrasound-enhanced Raman spectroscopy (Publication II)

In the previous paragraph, the sensitivity of Raman spectroscopy in off-line analysis was demonstrated. However, to reduce the timespan between sampling and obtaining the analysis result, real-time analysis is desirable which allows direct process control and additionally circumvents the risk of sample alteration between sampling and the time of measurement. Since in-line Raman spectroscopy suffers from low signal intensity due to the small cross-section, the combination with ultrasonic particle manipulation (UPM) promises to push the limits of conventional Raman spectroscopy in terms of sensitivity and selectivity. Leveraging UPM, particles that are subject to the acoustic forces can either be concentrated in the focus of the Raman laser (increase in sensitivity) or moved out of the laser focus (addition of selectivity). For a theoretical introduction to acoustic particle manipulation and the two arrangements discussed below, the reader is referred to section 1.3 and subsections (p. 27 ff).

2.1.2.1 Experimental data of parallel arrangement

In the parallel arrangement, Raman laser and acoustic wave propagation are arranged parallel to each other. Figure 35 a depicts the 3D-printed, 1.4404 stainless-steel prototype designed as add-on for in-line Raman probes. Two particle systems (starch and PMMA) in aqueous environment were chosen for testing and characterization of the prototype. The particles mainly differ in size with starch particles (diameter ≈ 10 µm) being 3-times the

size of the PMMA particles (diameter ≈ 3 µm). Considering that the primary acoustic radiation force scales with the particle radius to the power of three ($F_z^{rad} \sim R^3$), F_z^{rad} is ≈ 37x stronger for starch particles. Six different concentrations for each particle system were investigated. The concentration range was chosen such that the Raman signal of the highest concentration of homogenously distributed particles in a stirred suspension was close to zero without ultrasonic particle manipulation. As soon as the UPM was active, particles were drawn in the nodal planes of the acoustic standing wave field resulting in a strong increase in Raman signal intensity (Figure 35). In addition, repeated phases with and without UPM show good reproducibility. Typical results for this kind of measurements are shown for two concentrations of starch and PMMA particles, respectively, in Figure 35. Note that the increase in signal intensity is slower for PMMA particles during UPM-active phases compared to starch particles. This is due to the strong particle size dependency of the primary acoustic radiation force as discussed previously. Concentrations as low as 0.016 g/L for starch, and 0.063 g/L for PMMA were accessible due to UPM while no Raman signal at all was collectable without UPM using identical parameter settings. The limit of detection (LOD) without UPM for the same parameter settings were determined to be 0.5 g/L for starch, and 2.0 g/L for PMMA, respectively. Therefore, a 30x improvement of the LOD was demonstrated due to the combination of Raman in-line probes with UPM. However, the linear dependency of concentration and Raman signal is lost to a great extent. Depending on the material properties of the particles, stirrer speed, particle collection time in the nodal planes, photon collection time on the detector, timespan between activation of UPM and the start of the Raman measurement, etc. a certain concentration-dependency would be possible, however with a significantly reduced dynamic range.
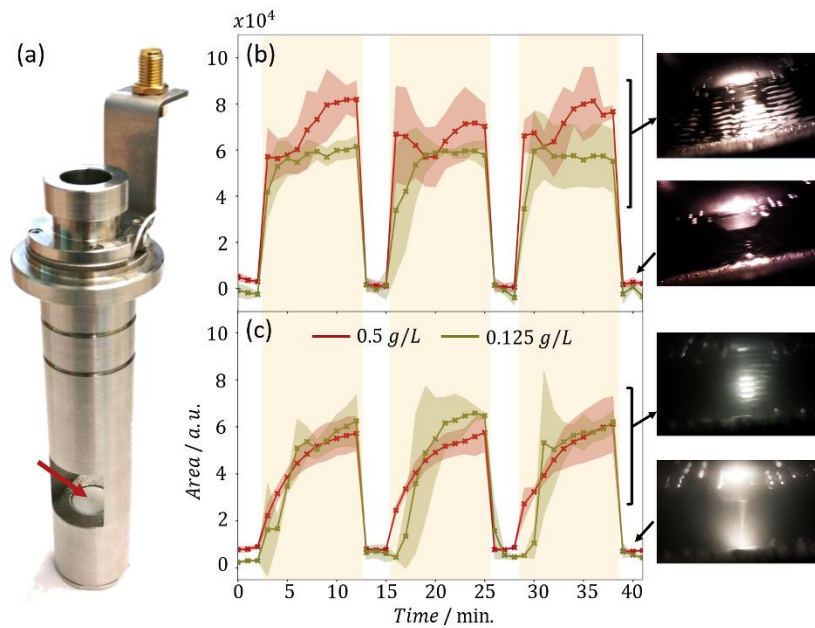
Figure 35. (a) Prototype add-on for in-line probes allowing the parallel arrangement. Macor surface is marked by a red arrow. Starch (b) and PMMA (c) integrated band intensities for 3 consecutive phases with (highlighted in orange) and without ultrasonic particle manipulation indicate a strong increase in signal sensitivity. Video images with and without acoustic particle manipulation highlight the effect of F_z^{rad} on both particle systems.

To avoid blocking of the backscattered photons by layers of agglomerated particles in the nodal planes between laser focus and probe head, the ideal distance between transducer and reflector (probe head) would be of similar size as the acoustic wavelength (here ≈ 740 µm). Limitations in the focal distance of the available Raman probes, however, required the acoustic resonator to be 2.5 mm long. Hence, even higher signal enhancement might be achievable if probes with a shorter focal length were employed.

2.1.2.2   Experimental data of perpendicular arrangement

The aim of the perpendicular arrangement of Raman laser and the acoustic standing wave field was to add both, increased sensitivity and selectivity, to in-line Raman measurements. Details on the perpendicular arrangement and the design of the prototype are given in section 1.3.1.1 (p. 31 ff.). Due to challenges in the geometrical arrangement for fulfilling the requirements to fit a D25 Ingold port, a preliminary study was conducted with a UV/Vis cuvette placed on a manually operated xyz-stage. Two piezoelectric elements were glued on opposite sides of the cuvette generating an acoustic resonator with a pathlength of 10 mm. The moving of nodal planes in and out of the laser focus due to the change in the frequency of the acoustic waves was imitated by moving the cuvette with a step size of 50 µm in the direction of the acoustic standing wave field (perpendicular to the nodal planes) using a mechanical translation stage while keeping

the ultrasonic frequency constant. Based on these experiments, an increase in signal intensity by a factor of 42 was demonstrated using 6 g/L starch in deionized water. Additionally, when the laser focus was located between nodal planes, the Raman signal was lower compared to the signal of the stirred suspension without UPM. Since most of the particles are forced into nodal planes during active UPM, the areas between nodal planes are depleted from particles allowing investigation of the liquid phase (see Figure 36).

Finally, for in-line measurements of starch particles in deionized water with the prototype (Figure 36 c) allowing the perpendicular arrangement, similar, or higher enhancement in Raman signal intensity could be demonstrated. Also, a change in the ultrasonic frequency by ≈ 30 kHz allowed to move the starch particles accumulated in the nodal planes out of the laser focus as confirmed by the Raman spectra (Figure 36 b, d). Due to the transverse primary radiation force F_{xy}^{rad} which impacts the rearrangement of particles induced by the change in the resonance frequency of the acoustic resonator, with the current prototype, particles temporarily fall out of the laser focus instead of being moved vertically out of the focus (Figure 36 a). Nevertheless, it is important to note that this is a reversible effect and allows selective investigation of the liquid phase.
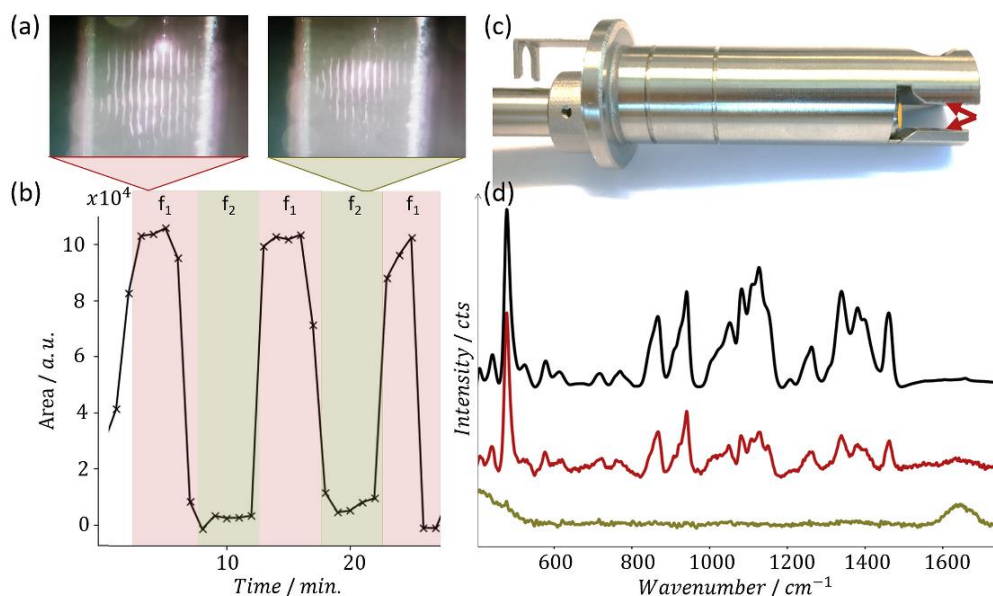
Figure 36. Perpendicular arrangement. (a) Video images of starch particles arranged in the nodal planes of the acoustic standing wave field for two different ultrasonic frequencies. (b) Change of starch signal intensity depending on the ultrasonic frequency (f_1 highlighted in red, or f_2 highlighted in green). (c) Prototype add-on for Raman in-line probe. Red arrows mark the position of transducer and reflector. The position of the probe head is marked in orange. (d) Raman spectra recorded at f_1 (red; particles in laser focus) and f_2 (green; particles out of laser focus) in comparison with a reference spectrum of starch powder (black). Spectra are offset-shifted.

To conclude, in Publication II, two arrangements for the combination of Raman in-line probes with UPM are introduced. The parallel arrangement allows a ≈ 30-fold increase of the LOD showing a strong improvement in sensitivity. In addition, the perpendicular arrangement promises similar, or even better signal improvement factors with the benefit of adding selectivity to in-line measurements as nodal planes can selectively be moved into or out of the laser focus. Hence, the backscattered photons carry chemical-specific information either from the solid (nodal plane with accumulated particles is in the focus of the Raman laser) or liquid phase (laser focus is in the area between nodal planes depleted from particles).

The combination of in-line Raman probes with ultrasonic particle manipulation is a promising approach to allow more sensitive, real-time, in-situ Raman measurements in the reaction vessel as shown in the previous paragraphs. However, since the primary acoustic radiation force F_z^{rad} strongly depends on the particle size ($F_z^{rad} \sim R^3$), this method allows particle manipulation typically down to a particle diameter of ≈ 1 µm. With fine-tuning of the system in terms of compressibility and density ratios of particles and medium, viscosity of the medium or decreasing the acoustic resonator's length, lower particle diameters might still be subject to the influence of F_z^{rad}, but Brownian motion will likely prevail over the acoustic forces for particles diameters ≤ 0.5 µm.[79,80]

2.2 Off-line spectroscopy - based analysis at the nanoscale (Publication III and IV)

The aim of Publications III (p. 111 ff.) and IV (p. 123 ff.) was to develop a spectroscopy-based method for the investigation of nanocarriers. Specifically, single nanocarrier analysis was desired to qualitatively access the presence or absence of encapsulated cargo material. Preliminary studies were based on off-line Raman spectroscopy drawing on experiences gained in the investigation of *P. chrysogenum* spores (Publication I, p. 87 ff.) while the ultimate method of choice in terms of sensitivity and lateral resolution was the combination of AFM microscopy and IR spectroscopy, short AFM-IR.

2.2.1 Liposomal drug delivery and liposomal cytarabine

Liposomes are micro- and nanometer-scaled structures employed to transport a very small aqueous volume enclosed within the lipid bilayer. Their surface can be functionalized with a great variety of ligands such as polyethylene glycol (PEG), antibodies, carbohydrates, and many more.[81,82] Due to their exceptional structural and functional versatility in addition to biocompatibility and biodegradability, liposomes are used as delivery systems for highly toxic[83–85] or reactive drugs[86]. The liposome forms a protective layer around the encapsulated substance enabling improved drug stability and reduced toxic side-effects.[83,87–91] If and how much of the drug is effectively encapsulated in a single liposome is an important parameter for clinical approval and efficacy. However, in liposome production, a great batch to batch variability in the encapsulation efficiency (EE) is encountered in addition to an up to 50 % EE-variability within a single batch.[92] There are numerous methods (e.g., CE[93], NMR[94], HPLC[95], etc.) available that allow the determination of EE in a bulk measurement. Nonetheless, to produce more uniform nanomedicines for drug delivery, sensitive, high throughput methods are required to monitor EE in single nanocarriers. If the encapsulated drug does not fluoresce, typically labelling with fluorescent dyes is required to allow single-nanocarrier measurements.[92,96]

In this thesis, liposomal cytarabine as a non-fluorescent chemotherapeutic drug was investigated. Cytarabine – also called cytosine arabinoside (araC) – is clinically approved for treatment of lymphomatous meningitis.[97] Due to its close chemical similarity to one of the DNA nucleosides (cytosine deoxyribose), it intercalates into the DNA, stops DNA replication and, hence, proliferation of the cancer cells.[98] Liposomes composed of hydrogenated L-α-phosphatidylcholine (HSPC), cholesterol (Chol) and 1,2-dioctadecanoyl-sn-glycero-3-phosphoethanolamine (PE (18:0 / 18:0), DSPE) with a molar ratio of 5.7 : 3.8 : 0.5 (HSPC : Chol : DSPE) were prepared according to the thin-film hydration method which promises high encapsulation efficiencies.[99,100] After an additional extrusion step, unilamellar vesicles containing cytarabine dissolved in buffer (= drug-loaded liposomes), or buffer solution (= empty liposomes) were obtained with a diameter of ≈ 100 nm.

2.2.2   Collection method

For imaging purposes, the liposomes needed to be placed on flat substrates. However, the deposition method used for *P. chrysogenum* spores in Publication I (p. 87 ff.) was not applicable here, since liposomes tend to burst upon placing droplets of liposomes in suspension on the substrate to let dry at room temperature (Figure 37 b). Hence, nES-GEMMA (nano electrospray gas-phase electrophoretic mobility molecular analysis) was employed for gentle, destruction free deposition on the substrate (Figure 37 a). nES-GEMMA allows separation of single-charged analytes in the gas-phase at ambient pressure according to their size. Two modes of operation are possible:

1) By tuning the electric field across a certain particle size range and detecting the number of particles per particle diameter via a particle counter, the *size distribution* can be determined.

2) By adjusting the electric field to a constant voltage value, *particles of a certain diameter* can be selected and *collected* on a substrate placed in an electrostatic nanometer aerosol sampler (ENAS).

nES-GEMMA has already proven its applicability for the investigation of nanoparticles[101–104], exosomes[105], or liposomes[106–108]. In addition to a size-selection step prior to liposome collection, nES-GEMMA allows to adjust the particle distribution density on the substrate depending on the collection time. Briefly, particles are brought into gas-phase through an electrospray process resulting in single and multiple charged particles. After charge equilibration, single charged particles are separated according to their size via a laminar sheath flow in a tunable electric field. The particles are collected on the substrate positioned on top of an electrode in the ENAS. After deposition, liposomes have a width of ≈ 200 nm, and a thickness of ≈ 40 nm (Figure 37 a).
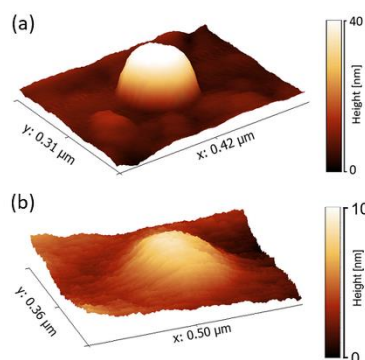
Figure 37. (a) Tapping mode AFM image of a liposome deposited via nES-GEMMA. (b) Tapping mode AFM image of a liposome deposited by placing a droplet of liposome suspension on a substrate and let dry at room temperature.

2.2.3 Raman spectroscopy - based investigation of liposomes

Based upon the investigation of single spores in Publication I (p. 87 ff.), confocal Raman spectroscopy was envisaged for preliminary studies of liposomes. Besides the fact that only 1 Raman spectrum per liposome would be possible due to the diffraction limited lateral resolution of ≈ 200 nm, several approaches were attempted:

i) *Confocal Raman images* of empty liposomes collected on CaF_2 were successfully acquired. However, the signal intensity was low and the spatial resolution insufficient as shown in Figure 38. The structures in the Raman map depicting the integrated CH stretch vibration (highlighted in grey in panel -b in Figure 38) are blurry and measure 300 to 350 nm in width compared to ≈ 200 nm according to the AFM height map (panel -a in Figure 38).
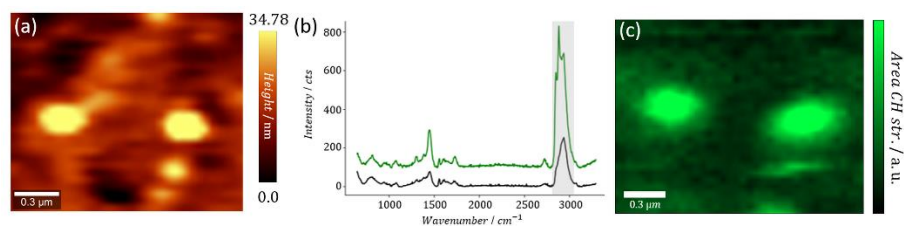
Figure 38. (a) Height map of liposomes collected on CaF_2. (b) Exemplary Raman spectra of areas on (green) and between (black) liposomes depicting similar spectral fingerprint. (c) Spatial distribution of CH stretch vibration highlighted in grey in panel -b. Adapted with permission by CC-BY License (https://pubs.acs.org/page/policy/authorchoice_ccby_termsofuse.html) from Native Nano-electrospray Differential Mobility Analyzer (nES GEMMA) Enables Size Selection of Liposomal Nanocarriers Combined with Subsequent Direct Spectroscopic Analysis; Weiss V. U., Wieland K., Schwaighofer A., Lendl B., Allmaier G.; Analytical Chemistry, 2019, 91, 3860-3868, 10.1021/acs.analchem.8b04252

ii) *A-SNOM* (see section 1.2.2 on p. 18 ff. for an introduction to A-SNOM) images of liposomes collected on thin glass substrates were acquired in transmission mode which provided a spatial resolution < 150 nm but at the expense of losing the spectroscopic information. The combination of Raman spectroscopy and A-SNOM theoretically enables high resolution Raman imaging, but ≈ 360x-loss in signal intensity needs to be considered as demonstrated in section 1.2.2 (p. 18 ff.) for sulfur.

iii) To achieve both - high lateral resolution and access to the sample's chemical composition - we opted for the combination of *A-SNOM and SERS* (see section 1.1.2.1 on p. 9 ff. for an introduction to SERS). Considering that SERS is a highly surface-sensitive method ($I_{SERS} \sim \frac{1}{R^{12}}$), only the Raman signal of samples placed in close vicinity to the SERS substrate (10-15 nm)[7,8] is enhanced. With an estimated lipid bilayer thickness of ≈ 5 nm, a theoretical possibility of detecting the substance encapsulated in the liposomes based on SERS was given. A-SNOM-SERS test measurements of 20 mM Rhodamine 6G (R6G; one of the most prominent substances used for testing the performance of SERS substrates) placed on a thin glass slide in combination with Ag-NPs prepared according to the Leopold-Lendl method[9] showed promising signal intensity (Figure 39 d). Hence, R6G-loaded liposomes were prepared and collected (Figure 39 a). In two separate approaches, Ag-NP solution was added prior, and after nES-GEMMA collection, respectively. Both preparation methods, however, resulted in liposome destruction. Placing a droplet of Ag-NP solution to let dry at room temperature after nES-GEMMA collection resulted in bursting of the liposomes (similar to liposome droplets deposition in Figure 37 b). However, nES-GEMMA collection on top of the Ag-NPs also failed due to the rough surface of the SERS substrate as supported by topography maps (Figure 39 b). Moreover, R6G signal was detected throughout the entire Ag-NPs-covered surface (Figure 39 c, e) supporting the presumption that the detected R6G is no longer encapsulate in the liposomes.

Having exploited all possible Raman-based measurement techniques available in our lab without notable success necessitated a re-evaluation of the selected analytical method.
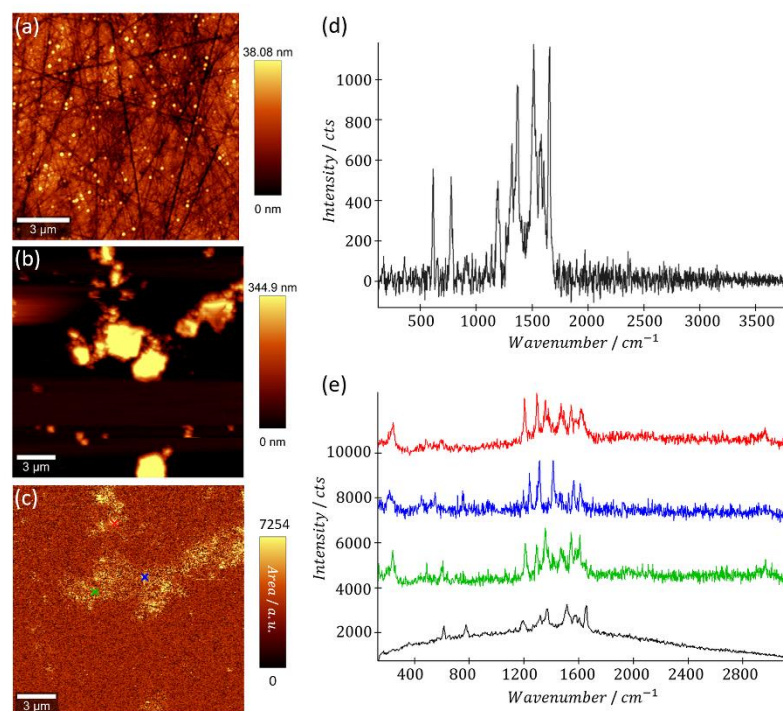
Figure 39. (a) Tapping mode AFM map of liposomes collected via nES-GEMMA on CaF$_2$ substrate. (b) Tapping mode AFM map of liposomes collected via nES-GEMMA on a thin glass substrate with Ag-NPs. (c) The intensity distribution map of R6G spectral fingerprint. (d) A-SNOM SERS reference spectrum (baseline corrected) of 20 mM R6G. (e) Representative A-SNOM SERS spectra (red, blue, green) collected on the substrate with R6G-loaded liposomes and Ag-NPs compared to a R6G reference spectrum (black). The color coded measurement positions are marked in panel -c.

2.2.4   Infrared spectroscopy - based investigation of liposomes

In comparison to SERS and A-SNOM SERS, the combination of AFM and IR spectroscopy - AFM-IR (see section 1.2.3 and subsections on p. 20 ff. for an introduction to AFM-IR) - offers better lateral resolution and is a less surface-sensitive method since it provides chemical information integrated on the whole sample thickness, even in excess of 1 µm.[109–111] Thus, AFM-IR might be best suited to investigate encapsulated cargo.

In order to record AFM-IR single spectra, the AFM cantilever tip is positioned on top of the sample structure whose photothermal expansion should be recorded. Then the laser is tuned across the spectral range of interest (e.g. fingerprint region from 900-1800 cm^{-1}). The sample absorbs light at specific wavenumbers resulting in a higher cantilever amplitude and, hence, in an elevated AFM-IR signal compared to wavenumbers where no absorption occurs. Additionally, AFM-IR maps can be recorded by selecting the wavenumber of interest (e.g. marker band of one compound in a mixture) and scanning the cantilever across a certain area (typically 5x5 µm^2 or 10x10 µm^2). Only in areas where

the sample absorbs, the cantilever amplitude is higher resulting in a higher AFM-IR signal compared to non-absorbing components in the scanned area.

First measurements were performed in contact mode, the legacy implementation of AFM-IR. FTIR reference measurements in a transmission flow cell of empty (buffer-loaded) liposomes, cytarabine-loaded liposomes and cytarabine dissolved in buffer were recorded. Based on these measurements, chemically selective marker bands for the identification of the liposomal bilayer and the encapsulated drug were determined. The main characteristics of a marker band are unequivocal identifiability (no spectral overlap with other components) and high signal intensity. Specifically, the C=O stretch vibration at 1734 cm^{-1} was chosen as liposome marker band[112] while the band at 1528 cm^{-1} allocated to C=N and C=C stretch vibrations of pyrimidines[98,113] was selected as cytarabine marker band (Figure 43 e). Since liposomes are small (sample thickness ≈ 40 nm), soft samples, several challenges needed to be overcome.

(i)   Mechanically compliant samples, such as liposomes, allow only a weak force transfer from the photothermally expanding sample to the tip of the AFM cantilever, hence, the tip-sample contact stiffness $k_{t\text{-}s}$ is low (see equation 22 on p. 24) resulting in a weak cantilever deflection and a low AFM-IR signal. Consequently, the AFM-IR signal distribution map of the lipid marker band (1734 cm^{-1}) initially indicates lower lipid signal on the liposomes (Figure 40 b) compared to the substrate (e.g., Au coated glass, ZnS or ZnSe). To account for this effect resulting from significantly different stiffness values of sample and substrate, the signal was referenced to the spatially unspecific silicon band of the AFM cantilever at 1260 cm^{-1} (Figure 40 c). The corrected AFM-IR map of the lipid marker band is depicted in Figure 40 d.
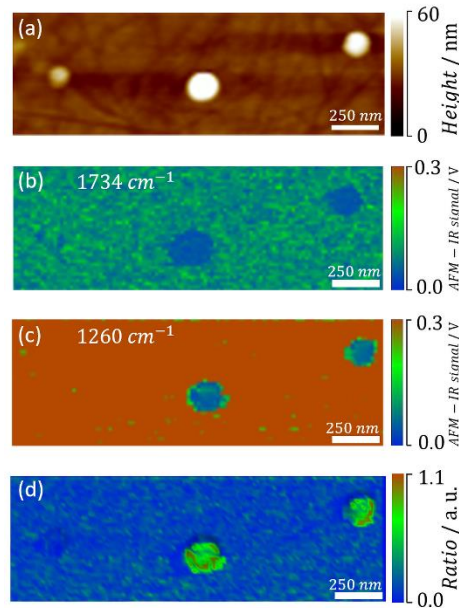
Figure 40. (a) Height map of two buffer-loaded liposomes. The ratio of the AFM-IR intensity maps for the lipid marker band at 1734 cm^{-1} (b) and the silicon band at 1260 cm^{-1} (c) is shown in panel -d. Adapted by permission from Springer Nature: Tsinghua University Press, Nano Research Nanoscale chemical imaging of individual chemotherapeutic cytarabine-loaded liposomal nanocarriers, Wieland, K.; Ramer, G.; Weiss, V. U.; Allmaier, G.; Lendl, B.; Centrone, A. © Tsinghua University Press and Springer-Verlag GmbH, part of Springer Nature (2019)

(ii)   For imaging purposes, the pulsed IR source is tuned to a specific wavelength (here, one of the marker bands) and the selected area is scanned while the contact resonance frequency f_{res} is continuously tracked employing PLL mode. The tracking of f_{res} is crucially important for reliable AFM-IR imaging (see Figure 15 and the discussion thereof in section 1.2.3.1 on p. 20 ff.). Abrupt changes in the mechanical properties (e.g., stiff substrate, soft sample) lead to an equally abrupt change of the cantilever's contact resonance frequency f_{res} (low tip-sample force -> low tip-sample contact stiffness k_{t-s} -> f_{res} shifts to lower frequencies; see equations 21 and 22 on p. 24). To avoid PLL tracking failure, the tracking range was restricted to the third cantilever mode (Figure 41) where the contact resonance frequencies of sample and substrate are sufficiently separated compared to lower cantilever modes due to the stronger dependency of f_{res} on k_{t-s} for higher modes.[114] This way, reliable tracking on the liposome was assured while f_{res} reaches the upper limit on the considerably stiffer substrate.
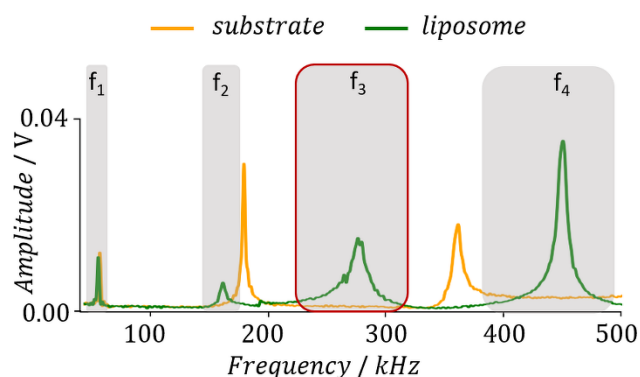
Figure 41. Contact resonance frequencies of the AFM cantilever in contact with the substrate (orange), or the liposome (green), respectively. The first 4 modes of the cantilever being in contact with the sample are highlighted in grey. The contact resonance frequency selected for the restricted PLL range is marked in red. Adapted by permission from Springer Nature: Tsinghua University Press, Nano Research Nanoscale chemical imaging of individual chemotherapeutic cytarabine-loaded liposomal nanocarriers, Wieland, K.; Ramer, G.; Weiss, V. U.; Allmaier, G.; Lendl, B.; Centrone, A. © Tsinghua University Press and Springer-Verlag GmbH, part of Springer Nature (2019)

(iii)   Contact mode AFM-IR exhibits high shear forces onto the sample risking sample deformation and/ or destruction indicated by the change in topography from the first to the last of 4 consecutive scans (Figure 42) performed in contact, and tapping mode, respectively. Hence, tapping mode AFM-IR is preferred for soft samples.
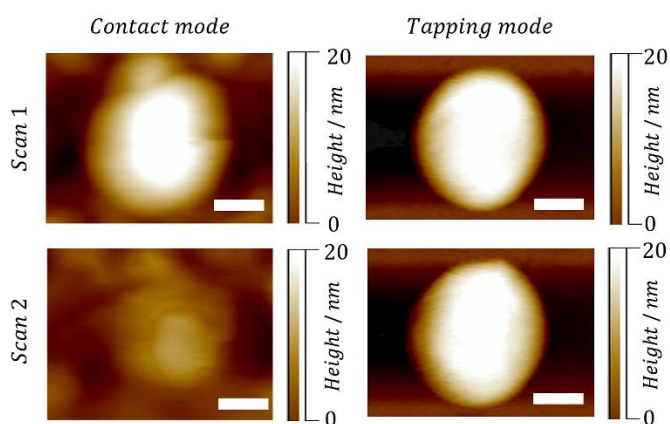
Figure 42. First and last of 4 consecutive AFM scans in contact (left), and tapping mode (right), respectively. Adapted by permission from Springer Nature: Tsinghua University Press, Nano Research Nanoscale chemical imaging of individual chemotherapeutic cytarabine-loaded liposomal nanocarriers, Wieland, K.; Ramer, G.; Weiss, V. U.; Allmaier, G.; Lendl, B.; Centrone, A. © Tsinghua University Press and Springer-Verlag GmbH, part of Springer Nature (2019)

Figure 43 summarizes the contact mode AFM-IR results of cytarabine-loaded liposomes. The ratio map of drug (Figure 43 b) and lipid (Figure 43 c) intensity distribution of a single

liposome depicts higher cytarabine signal in the middle of the liposome (red in Figure 43 d) compared to the edge region. This result was verified by collecting AFM-IR spectra in the middle and at the edge of the liposome depicting a distinct spectral difference at 1528 cm^{-1} corresponding to the cytarabine marker (Figure 43 e). Note that a slight deformation of the liposome is visible in the two consecutive AFM-IR scans depicting the cytarabine, and lipid distribution, respectively (Figure 43 b and c).
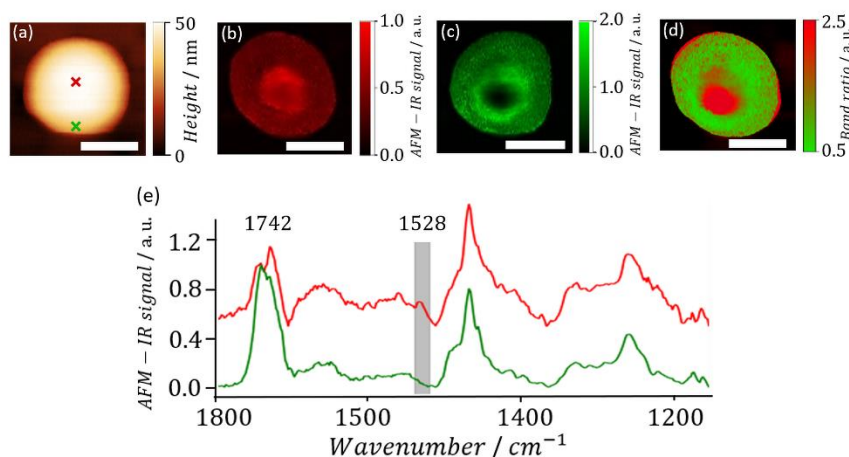
Figure 43. Topography map of a single, cytarabine-loaded liposome. Cytarabine (b) and lipid (c) intensity distribution in the liposome depicted in panel -a. (d) Drug/Lipid ratio indicating higher cytarabine signal in the middle of the liposome. (e) AFM-IR spectra recorded in the middle (red) and the edge (green) of the liposome. Color-coded measurement positions are marked in panel -a. The cytarabine marker band is highlighted in grey. The scale bars are 100 nm. Adapted by permission from Springer Nature: Tsinghua University Press, Nano Research Nanoscale chemical imaging of individual chemotherapeutic cytarabine-loaded liposomal nanocarriers, Wieland, K.; Ramer, G.; Weiss, V. U.; Allmaier, G.; Lendl, B.; Centrone, A. © Tsinghua University Press and Springer-Verlag GmbH, part of Springer Nature (2019)

Tapping mode AFM-IR promises less sample-tip contact and thus lessens the risk of sample deformation and/or destruction. Since in tapping mode AFM-IR the cantilever amplitude signal is the sum of the cantilever's oscillation amplitude and the photothermal expansion of the sample, the amplitude signal needs to be demodulated by non-linear mixing of the cantilever's oscillation frequency f_1 and the repetition rate of the laser f_{laser}. In practice, the laser repetition rate is set to match the difference frequency of f_1 and one of the higher cantilever modes, e.g., f_2, where the heterodyne detection is measured (see section 1.2.3.2 on p. 24 ff. for more information).

Tapping AFM-IR maps were recorded of cytarabine-loaded liposomes following the same procedure as for contact mode AFM-IR measurements. The ratio maps of cytarabine and lipid distribution (Figure 44 b, d) verified the result of contact mode AFM-IR measurements but with significantly lower sample destruction rate. Additionally, buffer-loaded liposomes were scanned as negative control at the same wavenumbers as the

cytarabine-loaded ones. The ratio map of cytarabine and lipid map rightly indicates the absence of cytarabine in buffer-loaded liposomes (Figure 44 f). Based on CE measurements and an estimated cargo volume encapsulated in a single liposome, the number of cytarabine molecules per liposome was assessed. A detailed explanation on the calculation of cytarabine concentration in a single liposome is given in the supporting information of Publication IV. An estimated concentration of $\approx 1.7 \cdot 10^{-21}$ mol ($\approx 10^3$ molecules) was determined highlighting the impressive sensitivity of tapping mode AFM-IR spectroscopy. Additionally, the lateral resolution was determined to be ≈ 10 nm based on the change in cytarabine signal intensity from 20 % to 80 % of the maximum value (Figure 44 g). This also exceeds the reported lateral resolution of ≈ 20 nm of contact mode AFM-IR spectroscopy.[115]
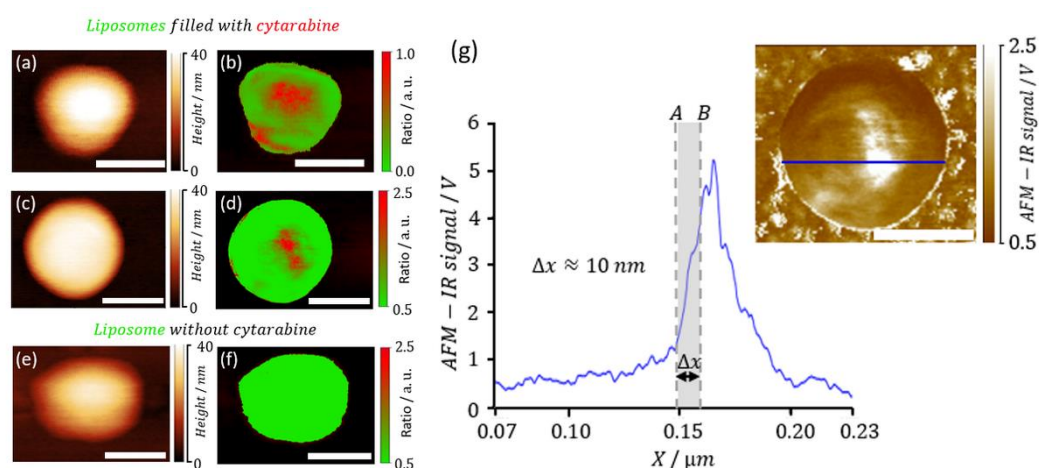
Figure 44. Topography maps (a, c, e) and drug/lipid ratio maps of two cytarabine-loaded liposomes (b, d) and one buffer-loaded (f) liposome. (g) The line profile from the AFM-IR map depicting the cytarabine-specific band distribution in a cytarabine-loaded liposome. Based on the change in cytarabine signal intensity from 20 % to 80 % of the maximum value, the lateral resolution of ≈ 10 nm was determined. Adapted by permission from Springer Nature: Tsinghua University Press, Nano Research Nanoscale chemical imaging of individual chemotherapeutic cytarabine-loaded liposomal nanocarriers, Wieland, K.; Ramer, G.; Weiss, V. U.; Allmaier, G.; Lendl, B.; Centrone, A. © Tsinghua University Press and Springer-Verlag GmbH, part of Springer Nature (2019)

3   Conclusion and outlook

In this thesis, Raman and Infrared micor-spectroscopy have been employed for off-line and in-line analysis of different particles systems (*P. chyrsogenum* spores, starch, PMMA, liposomal nanocarrier). Both methods are diffraction-limited regarding the achievable lateral resolution, however, different approaches for imaging beyond the diffraction limit were introduced and applied for off-line analysis. In contrast, ultrasonic particle manipulation was used to increase the sensitivity and selectivity of in-line Raman probes for improved (bio-)process monitoring. Moreover, data analysis based on multivariate statistics was discussed and exemplified on two publications as an essential tool for spectroscopists to break down n-dimensional data sets and identify the variables that carry the essential information to answer specific questions.

A PLS-DA classifier based on Raman off-line analysis was developed for determining the viability of *P. chrysogenum* spores prior to cultivation. This classifier allows to determine the percentage of living and dead spores upon label-free, non-destructive analysis with a sensitivity and specificity of >95 %. Nonetheless, the performance of a supervised classification algorithm such as PLS-DA can only be as good as the calibration data set used to train the algorithm. The true performance of the model will need further evaluation and comparison with established techniques such as labeling with fluorescent dyes or CFU (colony forming units) counting. In addition, the spectra acquisition can be automated for future measurements utilizing a suitable pattern recognition algorithm that would allow to automatically detect and measure single spores on a sample carrier. Also, the dilution step and sample deposition on the substrate can be automated by a flow injection analysis scheme with two channels to dilute the sample prior to placing one droplet of defined volume (e.g. 1 µl) on the substrate. Another improvement step might be the determination of spore viability in-line. Since the difference in the spectral fingerprint between living and dead spores has been very subtle in off-line Raman spectra and in-line analysis typically suffers from reduced sensitivity, this approach requires a significant improvement in sensitivity for in-line probes. At the same time, an improved sensitivity would also be advantageous for in-line monitoring of other substances such as metabolites, by-products, impurities, and many more that, up to now, are typically below the LOD of commercial Raman spectrometers for in-line analysis.

The combination of ultrasonic particle manipulation with in-line Raman probes was introduced in this thesis as one way to allow improved sensitivity and selectivity through the arrangement of Raman laser and ultrasonic standing wave field. For the parallel arrangement, improvements in the LOD by a factor of ≈ 30 were demonstrated. However, even higher signal intensity is possible using a Raman probe with a different focal length. The in-line probe used in this work has a working distance of 2.4 mm necessitating an acoustic reflector length of 2.5 mm. Apart from higher ultrasonic wave attenuation due to the longer travel distance in the liquid/ viscous medium which results in a weakened ultrasonic standing wave field, the detection of backscattered Raman photons is hindered

by additional layers of particle agglomerations in the nodal planes between laser focus and probe head. Hence, the recorded Raman signal is weaker compared to what might be possible. Reducing the focal length of the probe head to ½ λ of the acoustic wave allows to get rid of these additional layers and, thus, promises even higher signal intensities and a stronger acoustic wave field.

With the perpendicular arrangement, a similar increase in signal sensitivity as for the parallel arrangement was observed. In addition, changing the resonance frequency of the acoustic resonator to the next stable one leads to a shift in the nodal planes allowing to selectively investigate the liquid phase depleted from particles. However, the size limitations due to the requirement of fitting a D25 Ingold port necessitated a complex geometry for this prototype at the cost of ultrasonic field stability. On the one hand, this is due to a reduced transducer size. On the other hand, soldering of the signal transmission cable to the PZT element is required, hence, a removable and resealable lid at the back-side of the transducer is required. In the first iteration, the specific part of the prototype needs to be heated up in order to remove or seal the lid due to thermal expansion of the material. This process, however, probably has an impact on the plane-parallelism of transducer and reflector which is crucial for the quality factor of the resonator. Therefore, a different approach of opening and sealing this lid and an increase in the transducer's surface is desired for the second iteration of this prototype to allow a stronger acoustic wave field.

Furthermore, until now, in both arrangements for ultrasonic particle manipulation in combination with Raman in-line probes, the frequency of the ultrasonic wave in the resonator was set and controlled manually. For vessels without temperature control or for reaction monitoring with changing temperature settings, it needs to be considered that the speed of sound in water is temperature‑dependent, hence, the ultrasonic frequency in a resonant system requires continuous monitoring and readjustment. Future developments will focus on the automation of this procedure to ensure optimal resonance frequency tracking.

For the investigation of particles below 1 µm, the cargo material encapsulated in single liposomes with ≈ 100 nm in diameter was studied. Liposomes are used for drug delivery of highly toxic or reactive substances used in e.g., cancer therapy. Due to great variability in liposome production, the encapsulation efficiency in single nanocarriers needs to be studied to allow accurate drug administration. Initially, different implementations of off-line Raman spectroscopy such as confocal Raman or SNOM-SERS, where employed. The lateral resolution of ≈220 nm (calculated for λ = 488 nm and N.A. = 0.9) of confocal Raman imaging would allow one spectrum per liposome with a diameter of ≈ 100 nm. Hence, by controlling the particle collection time to ensure low particle distribution density on the substrate, the investigation of single liposomes based on confocal Raman imaging might be possible. However, since the signal intensity of buffer-loaded liposomes was already low, the chances of recording a Raman signal of the encapsulated cargo of significantly

lower concentration are modest. Therefore, to increase lateral resolution and signal sensitivity, SNOM-SERS spectra of R6G-loaded liposomes were recorded. Despite the surface sensitivity of SERS, the estimated lipid bilayer thickness of ≈ 5 nm might theoretically allow the detection of SERS signal of the encapsulated cargo. However, the Ag-NPs used as SERS substrate caused destruction of the liposomes. A different SERS substrate (e.g. flat triangular-shaped Au-layer or plasmonic nanoholes) might have shown better compatibility for destruction-free collection of liposomes.

Compared to SERS, AFM-IR - the combination of AFM and IR spectroscopy – is not a surface-sensitive method but allows a lateral resolution of $\leq$ 20 nm. Liposomes are soft samples, hence, contact mode AFM-IR exerted a lot of mechanical stress on them leading to sample deformation and/or destruction for consecutive scans. Also, tracking of the contact resonance frequency of the AFM cantilever required careful selection of the tracking range to ensure continuous tracking. Nonetheless, successful imaging of drug distribution inside single carriers was accomplished. In contrast, tapping mode AFM-IR requires a heterodyne detection scheme to demodulate the cantilever amplitude signal (= AFM cantilever oscillation + photothermal expansion of the sample) and read out the photothermal expansion of the sample. Tapping mode AFM-IR measurements confirmed the previously performed contact mode AFM-IR measurements for the detection of non-fluorescent, encapsulated cargo (here, the chemotherapeutic drug cytarabine) inside single liposomal nanocarriers. Future investigations may focus on the quantitative aspect of the encapsulated cargo detection. Since there is a linear dependency of sample thickness and AFM-IR signal up to ≈ 500 nm, quantification should be possible once an according calibration has been established. This approach might be interesting for other encapsulated, highly toxic substances where the encapsulation efficiency is of crucial importance to allow more precise drug administration. Furthermore, a new formulation for the treatment of acute myeloid leukemia has recently been FDA approved implying two chemotherapeutic drugs (cytarabine and daunorubicin) in a single liposome.[116] Formulations with two encapsulated drugs require a thorough investigation based on chemical-specific information with nanoscale lateral resolution to study the local distribution and ratio of both drugs in single nanocarriers. Hence, tapping mode AFM-IR imaging might give valuable insights for the characterization of these drug formulations.

4 Bibliography

(1)   *Fourier Transform Infrared Spectrometry*; Griffiths, P. R.; de Haseth, J. A., Reds; Second Edi.; John Wiley & Sons, Inc.: Hoboken, New Jersey, 2007.

(2)   *Handbook of Vibrational Spectroscopy*; Griffiths, P.; Chalmers, J. M., Reds; John Wiley & Sons, Ltd, 2002.

(3)   Long, D. A. *The Raman Effect - A Unified Treatement of the Theory of Raman Scattering by Molecules*; John Wiley & Sons, LTD, 2002.

(4)   Dieing, T.; Hollricher, O.; Toporski, J. *Confocal Raman Microscopy*; Springer-Verlag Berlin Heidelberg, 2010.

(5)   Huang, W. E.; Li, M.; Jarvis, R. M.; Goodacre, R.; Banwart, S. a. *Shining light on the microbial world: The application of Raman microspectroscopy.*; 1st ed; Elsevier Inc., 2010; Vol 70.

(6)   Anderson, A.; Loh, Y. T. Low temperature Raman spectrum of rhombic sulfur. *Can. J. Chem.* **1969**, *47*, 879–884.

(7)   Schlücker, S. Surface-enhanced Raman spectroscopy: concepts and chemical applications. *Angew. Chem. Int. Ed. Engl.* **2014**, *53*, 4756–4795.

(8)   Lal, S.; Grady, N. K.; Goodrich, G. P.; Halas, N. J. Profiling the Near Field of a Plasmonic Nanoparticle with Raman-Based Molecular Rulers. *Nano Lett.* **2006**, *6*, 2338–2343.

(9)   Leopold, N.; Lendl, B. A New Method for Fast Preparation of Highly Surface-Enhanced Raman Scattering (SERS) Active Silver Colloids at Room Temperature by Reduction of Silver Nitrate with Hydroxylamine Hydrochloride. *J. Phys. Chem. B* **2003**, *107*, 5723–5727.

(10)   *Surface Enhanced Raman Spectroscopy*; Schlücker, S., Red; WILEY-VCH, 2011.

(11)   Dazzi, A.; Prater, C. B.; Hu, Q.; Chase, B. D.; Rabolt, J. F.; Marcott, C. AFM – IR : Combining Atomic Force Microscopy and Infrared Spectroscopy for Nanoscale Chemical Characterization. *Appl. Spectrosc.* **2012**, *66*, 1365–1384.

(12)   Nasse, M. J.; Walsh, M. J.; Mattson, E. C.; Reininger, R.; Kajdacsy-Balla, A.; Macias, V.; Bhargava, R.; Hirschmugl, C. J. High-resolution Fourier-transform infrared chemical imaging with multiple synchrotron beams. *Nat. Methods* **2011**, *8*, 1–12.

(13)   Katzenmeyer, A. M.; Canivet, J.; Holland, G.; Farrusseng, D.; Centrone, A. Assessing Chemical Heterogeneity at the Nanoscale in Mixed-Ligand Metal-Organic Frameworks with the PTIR Technique. *Angew. Chemie (International ed.)* **2014**, *53*, 2852–2856.

(14)   Brown, L. V; Davanco, M.; Sun, Z.; Kretinin, A.; Chen, Y.; Matson, J. R.; Vurgaftman, I.; Sharac, N.; Giles, A. J.; Fogler, M. M.; *et al.* Nanoscale Mapping

and Spectroscopy of Nonradiative Hyperbolic Modes in Hexagonal Boron Nitride Nanostructures. *Nano Lett.* **2018**, *18*, 1628–1636.

(15)   Rosenberger, M. R.; Wang, M. C.; Xie, X.; Rogers, J. A.; Nam, S.; King, W. P. Measuring individual carbon nanotubes and single graphene sheets using atomic force microscope infrared spectroscopy. *Nanotechnology* **2017**, *28*, 355707.

(16)   Kumar, N.; Mignuzzi, S.; Su, W.; Roy, D. Tip-enhanced Raman spectroscopy : principles and applications. *EPJ Tech. Instrum.* **2015**, *2*.

(17)   Deckert-gaudig, T.; Kurouski, D.; Hedegaard, M. A. B.; Singh, P.; Lednev, I. K.; Deckert, V. Spatially resolved spectroscopic differentiation of hydrophilic and hydrophobic domains on individual insulin amyloid fibrils. *Nat. Sci. Reports* **2016**, 1–9.

(18)   Deckert, V.; Deckert-Gaudig, C.; Diegel, M.; Götz, I.; Langelüddecke, L.; Scheidewind, H.; Sharma, G.; Singh, P.; Singh, P.; Trautmann, S.; *et al.* Spatial resolution in Raman spectroscopy. *Faraday Discuss.* **2015**, *177*, 9–20.

(19)   Pozzi, E. A.; Sonntag, M. D.; Jiang, N.; Klingsporn, J. M.; Hersam, M. C.; Van Duyne, R. P. Tip-Enhanced Raman Imaging: An Emergent Tool for Probing Biology at the Nanoscale. *ACS Nano* **2013**, *7*, 885–888.

(20)   Shao, F.; Dai, W.; Zhang, Y.; Zhang, W.; Schlu, D.; Zenobi, R. Chemical Mapping of Nanodefects within 2D Covalent Monolayers by Tip-Enhanced Raman Spectroscopy. *ACS Nano* **2018**, *12*, 5021–5029.

(21)   Dufrêne, Y. F.; Ando, T.; Garcia, R.; Alsteens, D.; Martinez-Martin, D.; Engel, A.; Gerber, C.; Müller, D. J. Imaging modes of atomic force microscopy for application in molecular and cell biology. *Nat. Nanotechnol.* **2017**.

(22)   Eaton, P.; West, P. *Atomic Force Microscopy*; Oxford University Press, 2010.

(23)   Centrone, A. Infrared Imaging and Spectroscopy Beyond the Diffraction Limit. *Annu. Rev. Anal. Chem.* **2015**, *8*, 101–126.

(24)   Dazzi, A.; Prater, C. B. AFM-IR : Technology and Applications in Nanoscale Infrared Spectroscopy and Chemical Imaging. *Chem. Rev.* **2017**, *117*, 5146–5173.

(25)   Ramer, G.; Aksyuk, V. A.; Centrone, A. Quantitative Chemical Analysis at the Nanoscale Using the Photothermal Induced Resonance Technique. *Anal. Chem.* **2017**, *89*, 13524–13531.

(26)   Jin, M.; Lu, F.; Belkin, M. A. High-sensitivity infrared vibrational nanospectroscopy in water. *Light Sci. Appl.* **2017**, *6*, e17096.

(27)   Ramer, G.; Ruggeri, F. S.; Levin, A.; Knowles, T. P. J.; Centrone, A. Determination of Polypeptide Conformation with Nanoscale Resolution in Water. *ACS Nano* **2018**, *12*, 6612–6619.

(28)   Lu, F.; Jin, M.; Belkin, M. A. Tip-enhanced infrared nanospectroscopy via molecular expansion force detection. *Nat. Photonics* **2014**, *8*, 307–312.

(29)   Lu, F.; Belkin, M. A. Infrared absorption nano-spectroscopy using sample photoexpansion induced by tunable quantum cascade lasers. *Opt. Express* **2011**, *19*.

(30)   Dazzi, A.; Glotin, F.; Carminati, R. Theory of infrared nanospectroscopy by photothermal induced resonance. *J. Appl. Phys.* **2010**, *107*, 124519.

(31)   Ramer, G.; Reisenbauer, F.; Steindl, B.; Tomischko, W.; Lendl, B. Implementation of Resonance Tracking for Assuring Reliability in Resonance Enhanced Photothermal Infrared Spectroscopy and Imaging. *Appl. Spectrosc.* **2017**, *71*, 2013–2020.

(32)   Verbiest, G. J.; Rost, M. J. Beating beats mixing in heterodyne detection schemes. *Nat. Commun.* **2015**, *6*, 1–5.

(33)   Prater, C.; Kjoller, K. Multiple Modulation Heterodyne Infrared Spectroscopy, 2012.

(34)   Rajapaksa, I.; Uenal, K.; Wickramasinghe, H. K. Image force microscopy of molecular resonance: A microscope principle. *Appl. Phys. Lett.* **2010**, *97*, 3–5.

(35)   Gröschl, M. Ultrasonic Separation of Suspended Particles - Part I : Fundamentals. *Acta Acust.* **1998**, *84*, 432–447.

(36)   Gröschl, M. Ultrasonic Separation of Suspended Particles - Part II: Design and Operation of Separation Devices. *Acta Acust.* **1998**, *84*, 632–642.

(37)   Gröschl, M.; Burger, W.; Handl, B.; Doblhoff-Dier, O.; Gaida, T.; Schmatz, C. Ultrasonic Separation of Suspended Particles - Part III : Application in Biotechnology. *Acta Acust.* **1998**, *84*, 815–822.

(38)   Greenspan, M.; Tschiegg, C. E. Speed of sound in water by a direct method. *J. Res. Natl. Inst. Stand. Technol.* **1957**, *59*, 249–254.

(39)   Benes, E.; Gröschl, M.; Nowotny, H.; Trampler, F.; Radel, S.; Gherardini, L.; Hawkes, J. J.; König, R.; Delouvroy, C. Ultrasonic separation of suspended particles. *Proc. IEEE Ultrason. Symp.* **2001**, 649–659.

(40)   Radel, S. Ultrasonically Enhanced Settling : The effects of ultrasonic plane wave fields on suspensions of the yeast Saccharomyces cerevisiae, 2002.

(41)   Lohninger, H. *Fundamentals of Statistics*; Epina GmbH: Pressbaum, 2012.

(42)   Otto, M. *Chemometrics*; WILEY-VCH, 2017.

(43)   Ward, J. H. J. Hierarchical Grouping to Optimize an Objective Function. *J. Am. Stat. Assoc.* **2010**, *58*, 236–244.

(44) Baker, M. J.; Trevisan, J.; Bassan, P.; Bhargava, R.; Butler, H. J.; Dorling, K. M.; Fielden, P. R.; Fogarty, S. W.; Fullwood, N. J.; Heys, K. A.; *et al.* Using Fourier transform IR spectroscopy to analyze biological materials. *Nat. Protoc.* **2014**, *9*, 1771–1791.

(45) Butler, H. J.; Ashton, L.; Bird, B.; Cinque, G.; Curtis, K.; Esmonde-white, K.; Fullwood, N. J.; Gardner, B.; Martin-, P. L.; Walsh, M. J.; *et al.* Using Raman spectroscopy to characterise biological materials. *Nat. Protoc.* **2016**, *11*, 1–47.

(46) Adachi, H.; Hayashi, H.; Sato, H.; Dempo, K.; Akino, T. Characterization of phospholipids accumulated in pulmonary-surfactant compartments of rats intratracheally exposed to silica. *Biochem. J.* **1989**, *262*, 781–786.

(47) Napierska, D.; Thomassen, L. C.; Lison, D.; Martens, J. A.; Hoet, P. H. The nanosilica hazard: another variable entity. *Part. Fibre Toxicol.* **2010**, *7*, 39.

(48) Weber, K.; Bosch, A.; Bu, M.; Gopinath, C.; Hardisty, J. F.; Krueger, N.; McConnell, E. E.; Oberdörster, G. Aerosols of synthetic amorphous silica do not induce fibrosis in lungs after inhalation : Pathology working group review of histopathological specimens from a subchronic 13-week inhalation toxicity study in rats. *Toxicol. Res. Appl.* **2018**, *2*, 1–17.

(49) Johnston, C. J.; Driscoll, K. E.; Finkelstein, J. N.; Baggs, R.; O'Reilly, M. A.; Carter, J.; Gelein, R.; Oberdörster, G. Pulmonary chemokine and mutagenic responses in rats after subchronic inhalation of amorphous and crystalline silica. *Toxicol. Sci.* **2000**, *56*, 405–413.

(50) Movasaghi, Z.; Rehman, S.; ur Rehman, D. I. Fourier Transform Infrared (FTIR) Spectroscopy of Biological Tissues. *Appl. Spectrosc. Rev.* **2008**, *43*, 134–179.

(51) Pourmorteza, M.; Rahman, Z. U.; Young, M. Evofosfamide, a new horizon in the treatment of pancreatic cancer. *Anti-Canger Drugs* **2016**, *27*.

(52) Lohninger, H.; Ofner, J. Multisensor hyperspectral imaging as a versatile tool for image-based chemical structure determination. *Spectrosc. Eur.* **2014**, *26*.

(53) Ofner, J.; Kamilli, K. A.; Eitenberger, E.; Friedbacher, G.; Lendl, B.; Held, A.; Lohninger, H. Chemometric Analysis of Multisensor Hyperspectral Images of Precipitated Atmospheric Particulate Matter. *Anal. Chem.* **2015**, *87*, 9413–9420.

(54) Alford, J. S. Bioprocess control : Advances and challenges. *Comput. Chem. Eng.* **2006**, *30*, 1464–1475.

(55) Meyer, C.; Beyeler, W. Control Strategies for Continuous Bioprocesses Based on Biological Activities. *Biotechnol. Bioeng.* **1984**, 916–925.

(56) Zeng, A.-P.; Byun, T.-G.; Posten, C.; Deckwer, W.-D. Use of Respiratory Quotient as a Control Parameter for Optimum Oxygen Supply and Scale-up of 2 , 3 - Butanediol Production under Microaerobic Conditions. *Biotechnol. Bioeng.* **1994**, *44*, 1107–1114.

(57)   Landgrebe, D.; Haake, C.; Höpfner, T.; Beutel, S.; Hitzmann, B.; Scheper, T.; Rhiel, M.; Reardon, K. F. On-line infrared spectroscopy for bioprocess monitoring. *Appl. Microbiol. Biotechnol.* **2010**, *88*, 11–22.

(58)   Rowland-jones, R. C.; Berg, F. Van Den; Racher, A. J.; Martin, E. B.; Jaques, C. Comparison of Spectroscopy Technologies for Improved Monitoring of Cell Culture Processes in Miniature Bioreactors. *Biotechnol. Prog.* **2017**, *33*, 337–346.

(59)   Biechele, P.; Busse, C.; Solle, D.; Scheper, T.; Reardon, K. Sensor systems for bioprocess monitoring. *Eng. Life Sci.* **2015**, *15*, 469–488.

(60)   Beer, T. De; Burggraeve, A.; Fonteyne, M.; Saerens, L.; Remon, J. P.; Vervaet, C. Near infrared and Raman spectroscopy for the in-process monitoring of pharmaceutical production processes. *Int. J. Pharm.* **2011**, *417*, 32–47.

(61)   Esmonde-white, K. A.; Cuellar, M.; Uerpmann, C.; Lenain, B.; Lewis, I. R. Raman spectroscopy as a process analytical technology for pharmaceutical manufacturing and bioprocessing. *Anal. Bioanal. Chem.* **2017**, 637–649.

(62)   Koch, C.; Brandstetter, M.; Wechselberger, P.; Lorantfy, B.; Plata, M. R.; Radel, S.; Herwig, C.; Lendl, B. Ultrasound-Enhanced Attenuated Total Reflection Mid-infrared Spectroscopy In-Line Probe: Acquisition of Cell Spectra in a Bioreactor. *Anal. Chem.* **2015**, *87*, 2314–2320.

(63)   Ehgartner, D.; Herwig, C.; Neutsch, L. At-line determination of spore inoculum quality in Penicillium chrysogenum bioprocesses. *Appl. Microbiol. Biotechnol.* **2016**, *100*, 5363–5373.

(64)   Rakotonirainy, M. S.; Héraud, C.; Lavédrine, B. Detection of viable fungal spores contaminant on documents and rapid control of the effectiveness of an ethylene oxide disinfection using ATP assay. *Luminescence* **2003**, *18*, 113–121.

(65)   Yu, S. Q.; Trione, E. J.; Ching, T. M. Biochemical Determination of the Viability of Fungal Spores and Hyphae. *Mycol. Soc. Am.* **1984**, *76*, 608–613.

(66)   Mesquita, N.; Portugal, A.; Piñar, G.; Loureiro, J.; Coutinho, A. P.; Trovão, J.; Nunes, I.; Botelho, M. L.; Freitas, H. Flow cytometry as a tool to assess the effects of gamma radiation on the viability, growth and metabolic activity of fungal spores. *Int. Biodeterior. Biodegradation* **2013**, *84*, 250–257.

(67)   Schuster, K. C.; Reese, I.; Urlaub, E.; Gapes, J. R.; Lendl, B. Multidimensional Information on the Chemical Composition of Single Bacterial Cells by Confocal Raman Microspectroscopy. *Anal. Chem* **2000**, *72*, 5529–5534.

(68)   Noothalapati, H.; Sasaki, T.; Kaino, T.; Kawamukai, M.; Ando, M.; Hamaguchi, H.; Yamamoto, T. Label-free Chemical Imaging of Fungal Spore Walls by Raman Microscopy and Multivariate Curve Resolution Analysis. *Sci. Rep.* **2016**, *6*.

(69)   Huang, W. E.; Griffiths, R. I.; Thompson, I. P.; Bailey, M. J.; Whiteley, A. S. Raman microscopic analysis of single microbial cells. *Anal. Chem.* **2004**, *76*, 4452–4458.

(70) Maquelin, K.; Choo-Smith, L. P.; van Vreeswijk, T.; Endtz, H. P.; Smith, B.; Bennett, R.; Bruining, H. a; Puppels, G. J. Raman spectroscopic method for identification of clinically relevant microorganisms growing on solid culture medium. *Anal. Chem.* **2000**, *72*, 12–19.

(71) De Gussem, K.; Vandenabeele, P.; Verbeken, A.; Moens, L. Chemotaxonomical identification of spores of macrofungi: possibilities of Raman spectroscopy. *Anal. Bioanal. Chem.* **2007**, *387*, 2823–2832.

(72) Ghosal, S.; MacHer, J. M.; Ahmed, K. Raman microspectroscopy-based identification of individual fungal spores as potential indicators of indoor contamination and moisture-related building damage. *Environ. Sci. Technol.* **2012**, *46*, 6088–6095.

(73) De Gussem, K.; Vandenabeele, P.; Verbeken, A.; Moens, L. Raman spectroscopic study of Lactarius spores (Russulales, Fungi). *Spectrochim. Acta. A. Mol. Biomol. Spectrosc.* **2005**, *61*, 2896–2908.

(74) Klein, K.; Gigler, A. M.; Aschenbrenner, T.; Monetti, R.; Bunk, W.; Jamitzky, F.; Morfill, G.; Stark, R. W.; Schlegel, J. Label-free live-cell imaging with confocal Raman microscopy. *Biophys. J.* **2012**, *102*, 360–368.

(75) Ando, M.; Hamaguchi, H. Molecular component distribution imaging of living cells by multivariate curve resolution analysis of space-resolved Raman spectra. *J. Biomed. Opt.* **2014**, *19*.

(76) Schie, I. W.; Huser, T. Methods and Applications of Raman Microspectroscopy to Single-Cell Analysis. *Appl. Spectrosc. OA* **2013**, *67*, 813–828.

(77) Smith, R.; Wright, L.; Ashton, L. Raman spectroscopy : an evolving technique for live cell studies. *Analyst* **2016**, *141*, 3590–3600.

(78) Dao, T.; Bensoussan, M.; Gervais, P.; Dantigny, P. Inactivation of conidia of Penicillium chrysogenum, P. digitatum and P. italicum by ethanol solutions and vapours. *Int. J. Food Microbiol.* **2008**, *122*, 68–73.

(79) Barani, A.; Paktinat, H.; Janmaleki, M.; Mohammadi, A.; Mosaddegh, P.; Fadaei-Tehrani, A.; Sanati-Nezhad, A. Biosensors and Bioelectronics Micro fl uidic integrated acoustic waving for manipulation of cells and molecules. *Biosens. Bioelectron.* **2016**, *85*, 714–725.

(80) Neer, P. L. M. J. Van; Rasidovic, A.; Volker, A. W. F. A study of nanoparticle manipulation using ultrasonic standing waves. *2013 IEEE Int. Ultrason. Symp.* **2013**, 1915–1918.

(81) Peer, D.; Karp, J. M.; Hong, S.; Farokhzad, O. C.; Margalit, R.; Langer, R. Nanocarriers as an emerging platform for cancer therapy. *Nat. Nanotechnol.* **2007**, *2*, 751–760.

(82) Torchilin, V. P. Recent advances with liposomes as pharmaceutical carriers. *Nat.*

Rev. Drug Discov. **2005**, *4*, 145–160.

(83)   Sercombe, L.; Veerati, T.; Moheimani, F.; Wu, S. Y.; Hua, S. Advances and Challenges of Liposome Assisted Drug Delivery. *Front. Pharmacol.* **2015**, *6*, 286.

(84)   Caldeira, S.; Lopes, D. A.; Ferreira, S.; Leite, E. A.; Oliveira, M. C. Liposomes as Carriers of Anticancer Drugs. In *Cancer Treatment - Conventional and Innovative Approaches*; InTech, 2013; bll 85–124.

(85)   Cagdas, M.; Sezer, A. D.; Bucak, S. Liposomes as Potential Drug Carrier Systems for Drug Delivery. In *Application of Nanotechnology in Drug Delivery*; InTech, 2014; bll 1–50.

(86)   Young, S. A.; Smith, T. K. Lipids and Liposomes in the Enhancement of Health and Treatment of Disease. In *Drug Discovery and Development - From Molecules to Medicine*; InTech, 2015; bll 133–162.

(87)   Germain, M.; Meyre, M.; Pou, L.; Paolini, M.; Berjaud, C.; Bergere, M.; Levy, L.; Pottier, A. Priming the body to receive the therapeutic agent to redefine treatment benefit/risk profile. *Sci. Rep.* **2018**, *8*, 4797.

(88)   Zhang, Y.; Chan, H. F.; Leong, K. W. Advanced materials and processing for drug delivery : The past and the future. *Adv. Drug Deliv. Rev.* **2013**, *65*, 104–120.

(89)   Venditto, V. J.; Szoka Jr, F. C. Cancer nanomedicines : So many papers and so few drugs ! *Adv. Drug Deliv. Rev.* **2013**, *65*, 80–88.

(90)   Allen, T. M.; Cullis, P. R. Liposomal drug delivery systems: From concept to clinical applications. *Adv. Drug Deliv. Rev.* **2013**, *65*, 36–48.

(91)   Kim, J. Liposomal drug delivery system. *J. Pharm. Investig.* **2016**, *46*, 387–392.

(92)   Lohse, B.; Bolinger, P.; Stamou, D. Encapsulation Efficiency Measured on Single Small Unilamellar Vesicles. *JACS Commun.* **2008**, *130*, 14372–14373.

(93)   Franzen, U.; Nguyen, T. T. T. N.; Vermehren, C.; Gammelgaard, B.; Østergaard, J. Characterization of a liposome-based formulation of oxaliplatin using capillary electrophoresis : Encapsulation and leakage. *J. Pharm. Biomed. Anal.* **2011**, *55*, 16–22.

(94)   Zhang, X.; Patel, A. B.; Graaf, R. A. De; Behar, K. L. Determination of liposomal encapsulation efficiency using proton NMR spectroscopy. *Chem. Phys. Lipids* **2004**, *127*, 113–120.

(95)   Ohnishi, N.; Yamamoto, E.; Tomida, H.; Hyodo, K.; Ishihara, H.; Kikuchi, H.; Tahara, K.; Takeuchi, H. Rapid determination of the encapsulation efficiency of a liposome formulation using column-switching HPLC. *Int. J. Pharm.* **2013**, *441*, 67–74.

(96)   Chen, C.; Zhu, S.; Wang, S.; Zhang, W.; Cheng, Y.; Yan, X. Multiparameter

Quantification of Liposomal Nanomedicines at the Single-Particle Level by High-Sensitivity Flow Cytometry. *ACS Appl. Mater. Interfaces* **2017**, *9*, 13913–13919.

(97) Pillai, G. Nanomedicines for Cancer Therapy : An Update of FDA Approved and Those under Various Stages of Development. *Pharm. Pharm. Sci.* **2014**, *1*, 1–13.

(98) El-Subbagh, H. I.; Al-Badr, A. A. Cytarabine. In *Profiles of Drug Substances, Excipients, and Related Methodology*; Brittain, H. G., Red; Elsevier Inc., 2009; bll 37–113.

(99) Jesorka, A.; Orwar, O. Liposomes: technologies and analytical applications. *Annu. Rev. Anal. Chem.* **2008**, *1*, 801–832.

(100) Kirby, C.; Gregoriadis, G. Dehydration-rehydration vesicles: A simple method for high yield drug entrapment in liposomes. *Nat. Biotechnol.* **1984**.

(101) Dudkiewicz, A.; Wagner, S.; Lehner, A.; Chaudhry, Q.; Pietravalle, S.; Tiede, K.; Boxall, A. B. A.; Allmaier, G.; Tiede, D.; Grombe, R.; *et al.* A uniform measurement expression for cross method comparison of nanoparticle aggregate size distributions. *Analyst* **2015**, *140*, 5257–5267.

(102) Hinterwirth, H.; Wiedmer, S. K.; Moilanen, M.; Lehner, A.; Waitz, T.; Lindner, W.; Lämmerhofer, M. Comparative method evaluation for size and size-distribution analysis of gold nanoparticles. *J. Sep. Sci.* **2013**, *36*, 2952–2961.

(103) Kallinger, P.; Weiss, V. U.; Lehner, A.; Allmaier, G.; Szymanski, W. W. Analysis and handling of bio-nanoparticles and environmental nanoparticles using electrostatic aerosol mobility. *Particuology* **2013**, 14–19.

(104) Weiss, V. U.; Lehner, A.; Kerul, L.; Grombe, R.; Kratzmeier, M.; Marchetti-Deschmann, M.; Allmaier, G. Characterization of cross-linked gelatin nanoparticles by electrophoretic techniques in the liquid and the gas phase. *Electrophoresis* **2013**, *34*, 3267–3276.

(105) Chernyshev, V. S.; Rachamadugu, R.; Hsun Tseng, Y.; Belnap, D. M.; Jia, Y.; Branch, K. J.; Butterfield, A. E.; Pease III, L. F.; Bernard, P. S.; Skliar, M. Size and shape characterization of hydrated and desiccated exosomes. *Anal. Bioanal. Chem.* **2015**, *407*, 3285–3301.

(106) Epstein, H.; Afergan, E.; Moise, T.; Richter, Y.; Rudich, Y.; Golomb, G. Number-concentration of nanoparticles in liposomal and polymeric multiparticulate preparations: Empirical and calculation methods. *Biomaterials* **2006**, *27*, 651–659.

(107) Urey, C.; Weiss, V. U.; Gondikas, A.; Von Der Kammer, F.; Hofmann, T.; Marchetti-Deschmann, M.; Allmaier, G.; Marko-Varga, G.; Andersson, R. Combining gas-phase electrophoretic mobility molecular analysis (GEMMA), light scattering , field flow fractionation and cryo electron microscopy in a multidimensional approach to characterize liposomal carrier vesicles. *Int. J. Pharm.* **2016**, *513*, 309–

318.

(108) Weiss, V. U.; Urey, C.; Gondikas, A.; Golesne, M.; Friedbacher, G.; Von der Kammer, F.; Hofmann, T.; Andersson, R.; Marko-Varga, G.; Marchetti-Deschmann, M.; *et al.* Nano electrospray gas-phase electrophoretic mobility molecular analysis (nES GEMMA) of liposomes: applicability of the technique for nano vesicle batch control. *Analyst* **2016**, *141*, 6042–6050.

(109) Lahiri, B.; Holland, G.; Centrone, A. Chemical Imaging Beyond the Diffraction Limit: Experimental Validation of the PTIR Technique. *Small* **2013**, *9*, 439–445.

(110) Mayet, C.; Dazzi, A.; Prazeres, R.; Allot, F.; Glotin, F.; Ortega, J. M. Sub-100 nm IR spectromicroscopy of living cells. *Opt. Lett.* **2008**, *33*, 1611–1613.

(111) Dazzi, A.; Prazeres, R.; Glotin, F.; Ortega, J. M.; Al-Sawaftah, M.; de Frutos, M. Chemical mapping of the distribution of viruses into infected bacteria with a photothermal method. *Ultramicroscopy* **2008**, *108*, 635–641.

(112) Lewis, R. N. A. H.; Mcelhaney, R. N.; Pohle, W.; Mantsch, H. H. Components of the Carbonyl Stretching Band in the Infrared Spectra of Hydrated 1 , 2-Diacylglycerolipid Bilayers : A Reevaluation. *Biophys. J.* **1994**, *67*, 2367–2375.

(113) Socrates, G. *Infrared and Raman Characteristic Group Frequencies*; John Wiley & Sons, LTD, 2001.

(114) Rabe, U.; Janser, K.; Arnold, W. Vibrations of free and surface-coupled atomic force microscope cantilevers : Theory and experiment. *Rev. Sci. Instrum.* **1996**, *67*, 3281–3293.

(115) Katzenmeyer, A. M.; Holland, G.; Kjoller, K.; Centrone, A. Absorption Spectroscopy and Imaging from the Visible through Mid- Infrared with 20 nm Resolution. *Anal. Chem.* **2015**, *87*, 3154–3159.

(116) Nikanjam, M.; Capparelli, E. V; Lancet, J. E.; Louie, A.; Schiller, G. Persistent Cytarabine and Daunorubicin Exposure after administration of Novel Liposomal Formulation CPX-351: Population Pharmacokinetic Assessment. *Cancer Chemother Pharmacol* **2018**, *81*, 171–178.

5   Scientific publications

A list of contributions to the individual scientific publications divided into little (x), medium (xx) and high (xxx), is given hereafter in the following Table I.

Table I. Contributions to scientific publications from low (x), to medium (xx), to high (xxx)

	Publication						
	I	II	III	IV	V	VI	VII
Data acquisition	xxx	xxx	xxx	xx	x	x	xx
Data analysis	xxx	xxx	xxx	xxx	xxx	xx	x
Interpretation	xxx	xxx	xxx	xxx	xxx	xx	x
Manuscript contribution	xxx	xxx	xxx	xxx	xx	x	x

5.1   Publication I

Toward a Noninvasive, Label-Free Screening Method for Determining Spore Inoculum Quality of Penicillium chrysogenum Using Raman Spectroscopy

Karin Wieland, Julia Kuligowski, Daniela Ehgartner, Georg Ramer, Cosima Koch, Johannes Ofner, Christoph Herwig, Bernhard Lendl; *Applied Spectroscopy* 2017, 71, 2661-2669

Toward a Noninvasive, Label-Free Screening Method for Determining Spore Inoculum Quality of *Penicillium chrysogenum* Using Raman Spectroscopy

Karin Wieland[1], Julia Kuligowski[1,2], Daniela Ehgartner[3], Georg Ramer[1], Cosima Koch[1], Johannes Ofner[1], Christoph Herwig[3], and Bernhard Lendl[1]

Abstract

We report on a label-free, noninvasive method for determination of spore inoculum quality of *Penicillium chrysogenum* prior to cultivation/germination. Raman microspectroscopy providing direct, molecule-specific information was used to extract information on the viability state of spores sampled directly from the spore inoculum. Based on the recorded Raman spectra, a supervised classification method was established for classification between living and dead spores and thus determining spore inoculum quality for optimized process control. A fast and simple sample preparation method consisting of one single dilution step was employed to eliminate interfering signals from the matrix and to achieve isolation of single spores on the sample carrier (CaF_2). Aiming to avoid any influence of the killing procedure in the Raman spectrum of the spore, spores were considered naturally dead after more than one year of storage time. Fluorescence staining was used as reference method. A partial least squares discriminant analysis classifier was trained with Raman spectra of 258 living and dead spores (178 spectra for calibration, 80 spectra for validation). The classifier showed good performance when being applied to a 1 µL droplet taken from a 1:1 mixture of living and dead spores. Of 135 recorded spectra, 51% were assigned to living spores while 49% were identified as dead spores by the classifier. The results obtained in this work are a fundamental step towards developing an automated, label-free, and noninvasive screening method for assessing spore inoculum quality.

Introduction

Penicillium chrysogenum, also known as *Penicillium notatum*, is a filamentous fungus accounted to the genus of Ascomycetes.[1,2] Originally discovered by the Scottish microbiologist Alexander Fleming in 1928,[3] it is well-known in the pharmaceutical industry and beyond for producing β-lactam antibiotic penicillin.[4] After it had found its first widespread use in World War II, penicillin has been a valuable part of our medical system ever since.[5] Today, penicillin production on an industrial scale is carried out following optimized fermentation protocols. Due to its importance and widespread use in today's medical supply system, the optimization of bioprocess parameters for

[1]Institute of Chemical Technologies and Analytics, TU Wien, Vienna, Austria
[2]Neonatal Research Unit, Health Research Institute Hospital La Fe, Valencia, Spain
[3]Christian Doppler Laboratory on Mechanistic and Physiological Methods for Improved Bioprocesses, Institute of Chemical Engineering, TU Wien, Vienna, Austria

Corresponding author:
Bernhard Lendl, Institute of Chemical Technologies and Analytics, TU Wien, Getreidemarkt 9/164-UPA, 1060 Vienna, Austria.
Email: bernhard.lendl@tuwien.ac.at

efficient production of penicillin is of great interest. This can be achieved by improving biotechnological process control of *P. chrysogenum* fermentation.

Usually, fungal spore inoculum is directly transferred into a batch process where the spores germinate and hyphal growth takes place. The aim of the batch process is achieving maximum biomass concentration under optimum growth conditions. In a subsequent fed-batch, the focus is set upon achieving a high product yield in a short time.

Biotechnological process control is strongly linked to the physiology and morphology of the producing agent.[6] Monitoring the fermentation process by a variety of probes providing data on oxygen content, nitrogen content, pH, temperature, and numerous other important parameters is essential for accessing information on (growth) conditions in the bioreactor. Based on this knowledge, process parameters can be readjusted accordingly throughout the process for optimal growth and production conditions.

Efficient process control crucially depends on detailed knowledge about biochemical processes occurring in the bioreactor. Analytical tools for understanding complex mechanisms and obtaining insight into the physiological state of spores, especially at an early state, are key for cost-efficient process controls resulting in high product yields and operations at optimal workloads since the quality of spore inoculum can be directly linked to germination ability and antibiotic production.[7] Driven by economic need, the development of stable and reliable analytical methods for accessing the viability of spores prior to a batch process is essential.

It is well-known that a spore inoculum's quality decreases with storage time. For example, after one year of storage, more than 90% of *P. chrysogenum* spores are considered dead.[a] Thus, a quality control step is required for obtaining information about the viability of the deployed spores such that process parameters (C-source, oxygen content, stirrer velocity, etc.) of the subsequent batch process can be adapted accordingly for optimal growth and penicillin production.

Spore quality can be assessed by a number of analytical protocols such as counting of colony-forming units (CFU) on a nutrient agar, determination of adenylate energy charge, or application of fluorescence microscopy, all of which are either time-consuming and/or based on the use of staining procedures. No direct measurement technique for live/dead classification has been reported so far for fungal spores. Moreover, these analytical protocols usually require spores with metabolic activity that they do not have in the dormant state. Thus, cultivation is a necessary step for the subsequently mentioned approaches.

The current state-of-the-art method for determination of spore quality is based on counting CFUs where the nutrient agar is inoculated with spores of a certain dilution. This method is easy and straightforward, but time-consuming as growth usually requires several days and thus it is not applicable for real-time monitoring. Also, it lacks in reproducibility and suffers from overlapped or not clearly visible colonies leading to underestimation of spore viability.[8,9] Paul et al. proposed an automatic imaging analysis based on a simple black and white microscope image of spores prepared on a sample carrier followed by a series of image post-processing steps. These are used to eliminate cell debris and medium components in the image to access spore viability based on the size and form of spores during germination.[9] However, this method is likely to eliminate spores of similar size as cell debris and vice versa. Thus, it offers the risk of miscounting the actual number of viable spores. Another approach to access spore viability is to measure Adenosine triphosphate (ATP) content and determine adenylate energy charge (EC) thereof, respectively;[10] the level of both is higher for living spores than dead ones. Although these methods are less time-consuming than counting CFUs, ATP has to be extracted beforehand which adds an additional sample preparation step. ATP content is often determined using the luciferin–luciferase assay.[11] The obtained results have to be taken with precaution as they strongly depend on the extraction efficiency. Thus, this method is not applicable as quality control step in industrial environments.

Another promising approach for accessing spore viability is flow cytometry in combination with fluorescent stains.[8,12] Whereas flow cytometry is a very fast and elegant method, it implies the disadvantage of requiring sample staining. Several staining kits are commercially available for live/dead differentiation; however, these have been developed and optimized for bacteria (usually *E. coli*). Therefore, careful and time-consuming adaptation of such staining protocols for fungal spore viability studies is needed in order to determine incubation time and avoid cell leakage of the fluorescent stain. Moreover, the majority of biological samples shows autofluorescence that can bias classification. Fluorescent dyes are not only cost-intensive, they are usually carcinogenic and thus implicate problematic handling and provision of designated work spaces. Fluorescein diacetate (FDA) is a widely used fluorescent stain, which is converted to fluorescein by living organisms resulting in emission of green fluorescence. This implies that spores need to be cultivated beforehand to achieve successful staining as they do not have metabolic activity while being in the dormant state. In addition, spores tend to form clusters that are particularly disadvantageous for analysis performed with a flow cytometer.

Here, we introduce Raman spectroscopy for assessing spore viability. Raman spectroscopy is a powerful tool for obtaining molecule-specific information in a label-free, non-destructive approach.[13,14] It has proven itself to be a very useful technique for identifying different fungal spores,[15,16] bacteria,[17–19] imaging of human cells,[20,21] in vivo imaging of yeast cells,[22] or investigating the chemical composition of single bacterial and fungal cells.[23,24] Further, chemometric

methods such as hierarchical cluster analysis (HCA), principal component analysis (PCA), partial least squares discriminant analysis (PLS-DA), or multivariate curve resolution with alternating least squares (MCR-ALS) are used for detailed data analysis and interpretation.

We report on a label-free, noninvasive imaging method for investigation of spore inoculum quality by employing Raman microspectroscopy. A PLS-DA model for the classification of living and dead spores was established based on the direct molecule specific information of Raman spectra giving access to spore viability prior to cultivation.

Materials and Methods

Samples

Spore samples were taken from spore inocula of an industrial *P. chrysogenum* strain for penicillin production kindly provided by Sandoz (Kundl, Austria). Samples were stored in the fridge at 269 K.

Living Spores

Living spores were directly sampled from spore inoculum and immediately prepared for Raman and fluorescent measurements. Staining with FDA (fluorescein diacetate) showed that most of the spores (>95%) were alive at the time of sample collection. Sample preparation and measurement was performed on the same day.

Dead Spores

Typical protocols for preparation of dead spores are exposure to thermal stress by microwave radiation or destruction of cell membrane by ethanol.[25] These procedures by themselves are also reflected in the Raman spectrum of the spores since they affect the chemical composition. Such spectra are thus not representative for naturally dead spores and cannot be used for establishing a spectroscopy-based classification method. The definition of dead spores or more specifically finding an appropriate reference for dead spores is challenging. Based on FDA/PI reference staining and subsequent fluorescence microscopy, more than 95% of spores in spore suspensions older than one year could be considered dead. Thus, spores older than one year were used for training the classifier for naturally dead spores.

Sample Preparation

To ensure that media components and salts from phosphate-buffered saline (PBS) do not interfere with the Raman signal of the spore, they have to be removed prior to recording the spectrum. This can be done by washing the samples with deionized water (centrifugation, removal of supernatant, addition of water, vortexing thoroughly, and repetition of the whole procedure), which in general is quite time-consuming. We were able to completely replace the washing steps by one single dilution step that makes the whole process more time-efficient and thus applicable for the process analytical environment. Diluting the spore inoculum by a ratio of 1:500 with deionized water proved to be sufficient for removing media components and buffer salts. Moreover, isolation of single spores on the sample carrier could be achieved by this dilution step for improved Raman imaging; 1 μL of diluted sample was transferred onto a 2 mm-thick CaF$_2$ slide (Raman grade, Crystran Ltd.) and allowed to dry at room temperature for a few minutes. CaF$_2$ was chosen as substrate as it exhibits a flat Raman baseline in the fingerprint range.[23]

Experimental Methods

Raman spectra were collected using a WITec alpha300 RSA+ confocal Raman microscope equipped with a 785 nm excitation laser, corresponding spectrometer (UHTS 300 spectrometer optimized for 785 nm excitation wavelength, *f*/4 300 mm focal length) with a 600 groove/mm grating, and a highly sensitive, thermoelectrically cooled charge-coupled device (CCD) camera (Deep Depletion CCD), a motorized sample stage (<1 μm reproducibility), and an additional piezo-stage on top of it enabling a lateral positioning accuracy of less than 2 nm.

The near-infrared 785 nm diode laser (300 mW, laser class 3B) with a laser power adjusted to 4.5 mW was used for Raman excitation to prevent autofluorescence and thermal damage of spores of *P. chrysogenum*. For efficient imaging of spores with a diameter in the low micrometer range, spectra were recorded with 100× magnification (Zeiss objective, N.A. 0.9). Balancing spatial resolution and overall Raman signal, a fiber diameter (confocal pinhole) of 100 μm was used, yielding a laser spot diameter of approximately 1 μm. A spectral resolution of approximately 3 cm^{-1} was achieved employing a 600 groove/mm grating (BLZ = 750 nm).

A single spectrum for each spore of a 1 μL droplet was collected using the raster scan option of the ControlFOUR control software (WITec). With this option, the focus is set once before all the spores are manually selected, the coordinates saved in a list and single positions measured subsequently. Ten scans with an integration time of 10 s each were accumulated for each single Raman spectrum.

Data Analysis

Data Preprocessing

Single Raman spectra of living and dead spores of three different measurement days were arranged in a matrix containing 130 single spectra of living spores and 135 spectra of naturally dead (untreated, more than one year old) spores.

A total of seven spectra dominated by spectral noise and only containing background contributions were eliminated from subsequent data analysis such that the final PLS-DA model was based upon 258 Raman spectra with each spectrum representing one single spore. The first step of data preprocessing consisted of reducing the data matrix by selecting the spectral range of 1000–1900 cm^{-1}, where significant Raman intensities of the spores were located (Fig. 1). A Savitzky–Golay filter with a window size of 21 (second order polynomial) was used for smoothing single spectra to achieve a better signal-to-noise (S/N) ratio and facilitate data analysis without losing important spectral features. Biological samples tend to show autofluorescence, which leads to an increased baseline in their Raman spectra. Thus, baseline correction was performed in a subsequent step by fitting a second order polynomial through defined areas (1050–1130 cm^{-1} and 1660–1735 cm^{-1}, see Fig. 1d) of the spectrum. The z-focus of the Raman microscope was only set at the beginning of each measurement series. Hence, variations in overall Raman intensity may occur which do not result from the sample itself. Thus, the area under each spectrum was set to 1 assuming that the number of Raman photons reaching the CCD detector is independent from spore viability and eliminating the influence of varying sample thickness. For model development, the data were mean centered (subtraction of mean spectrum) and scaled to unit standard deviation (Mean = 0, StdDev = 1) to set the focus on spectral differences potentially indicative of spore viability. Data processing and modeling were performed using Solo+MIA 8.1 (Eigenvector Research).

Partial Least Squares Discriminant Analysis

The PLS-DA method[26] is a supervised classification algorithm and widely used method to develop classification models differentiating between two sets of data based on specific characteristics. Essentially, this method establishes a regression model that mathematically relates the spectral fingerprint with the target variable containing the according class membership information (spore viability: dead/alive). Therefore, rotation of both the matrix containing the spectra and the target variable is performed to achieve maximum correlation between spectra and target variable. The scores of the first few principal components are then set into correlation through a regression model. Classification is based upon exceeding or falling short of a certain threshold value producing dichotomous variables. The optimal number of components can be empirically determined
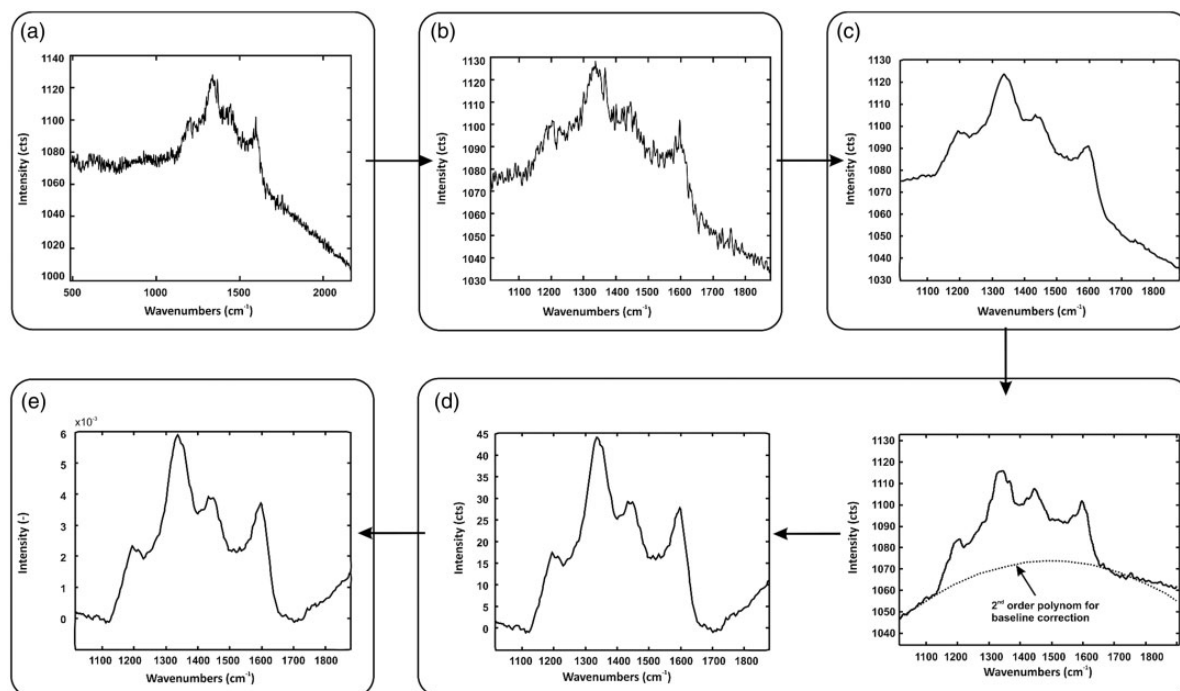
Figure 1. Data preprocessing of spectra prior to autoscaling (mean centering and scaling each variable to unit standard deviation). (a) Raw Raman spectrum of a spore. (b) Reduction of data matrix to focus on the part of the spectrum that contains significant Raman intensities of the spores and to reduce dimensionality of the data set for more efficient data analysis. (c) Savitzky–Golay smoothing with a window size of 21 and a second order polynomial to improve the S/N ratio. (d) Second order polynomial plotted through a number of specific points of the spectrum (1050–1130 cm^{-1} and 1660–1735 cm^{-1}) for baseline correction to remove fluorescent background. (e) Normalization to area 1 based on the assumption that the number of Raman photons reaching the detector is constant and independent from spore viability.
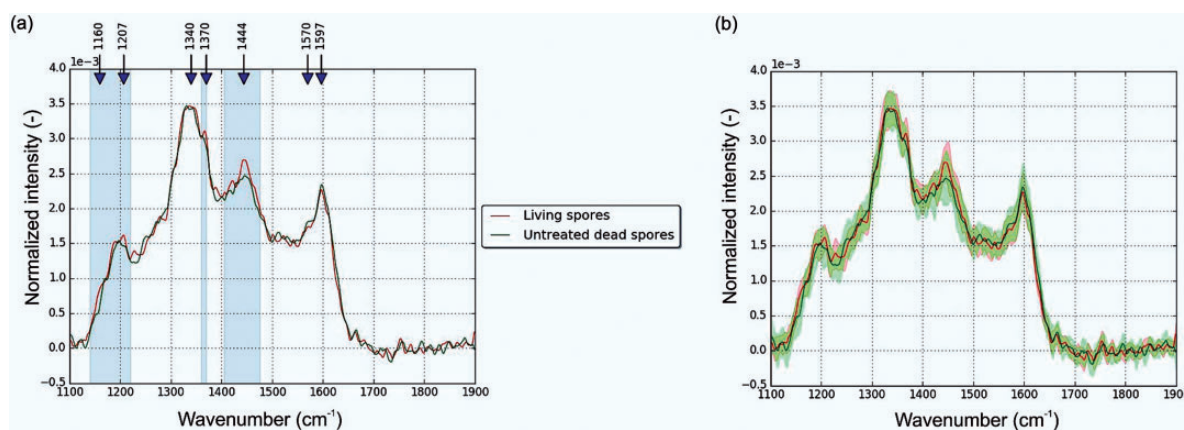
Figure 2. (a) Mean Raman spectrum of living (red) and dead spores (green); blue areas mark the region of spectral differences between the classes. (b) Mean and standard deviation of spectral fingerprint of living and dead spores, respectively.

through cross validation. For testing the performance of the established model, the data set is randomly divided into a calibration set which is used for building the model and a validation set to which the model is applied.

Results and Discussion

Raman Spectra of Living and Dead Spores

Raman spectra of living and dead spores were recorded using identical parameter settings. The mean spectra as well as the standard deviation of living and dead spores, respectively, that were used for establishing the PLS-DA model are depicted in Fig. 2b. There are several minor differences in the spectral fingerprint of both classes (highlighted in blue in Fig. 2a), the most intense of them is indicated by the band at 1444 cm^{-1} which is very characteristic for vibrations of lipids (Table I). However, including the standard deviation of each class, those differences vanish within the variance of the mean value. Thus, based on visual examination of the spore spectra, no clear distinction between the two classes is possible. Therefore, chemometric methods are needed for identification of appropriate spectral features/descriptors to access viability information.

The data set used to establish the classification model was chosen in a way to take account for variations that may occur within a series of measurements such as varying environmental conditions (temperature, humidity), varying content of components within different spore inocula, sample handling, etc. Thus, spectra from three different measurement days and two different spore inocula were selected. To assess the overall similarity of the spore spectra, unsupervised clustering was performed. By doing so, the influence of day-to-day variation as well as differences in spore variability on the Raman spectra could be studied. Ward's method was applied for HCA using Mahalanobis Distance. As depicted in the dendrograms (Fig. 3), spectra

Table I. Tentative band assignments for Raman bands of *P. chrysogenum* spores.

Band position (cm^{-1})	Band assignment[13,27–30]
1160	ν(C–C)
1207	Tyrosine, phenylalanine, protein, amide III
1340	δ(CH), adenine, guanine, tyrosine, tryptophan
1370	δ_s(CH$_2$), adenine, thymine, guanine
1444	δ(CH$_2$) lipids
1570	ν(C=C), δ(N–H), ν(C–N), adenine, guanine
1597	Protein, ν(C=C) aromatic compounds

of single measurement days almost have as much in common as spectra of different spore viability (Fig. 3). Although, single clusters of measurement days 1 and 2 tend to have more overlapping areas, measurement day 3 has a very dominant branch of the dendrogram and seems to differ more from the rest of the spectra. This HCA result confirms that even though measurements are performed in air-conditioned laboratories, the day-to-day variations are observable in the spectra. The inherent variance in spectra that is not related to differences between the two classes cannot be experimentally eliminated and thus has to be taken into account when building a classification model. As a consequence, the calibration set needs to be large enough to include all possible inevitable variations in the spore spectra to ensure the establishment of a stable classification model with high specificity and sensitivity.

Principal component analysis confirms the results of HCA. The score plots of PC 1 versus PC 2 of the same data set (Fig. 4) with identical data preprocessing shows some differentiation between living and dead spores as
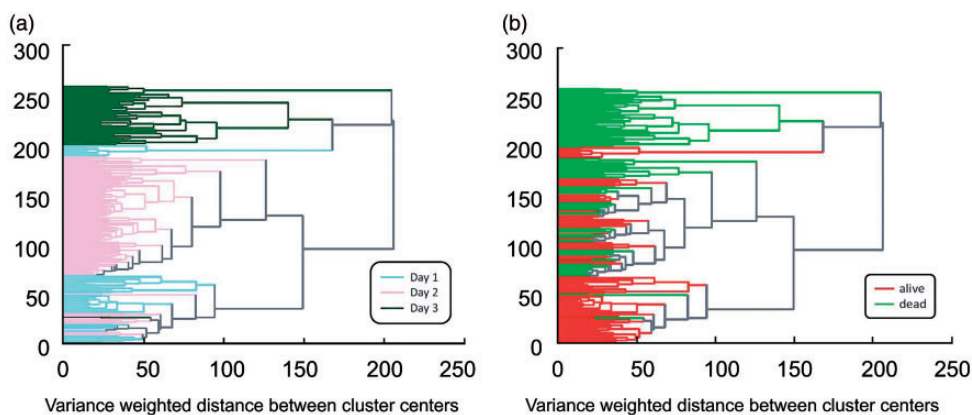
Figure 3. Dendrogram of HCA acquired from spore data (living and dead) at three different measurement days: (a) measurement days marked in blue, pink, and dark green; (b) viability marked in red (alive) and green (dead).
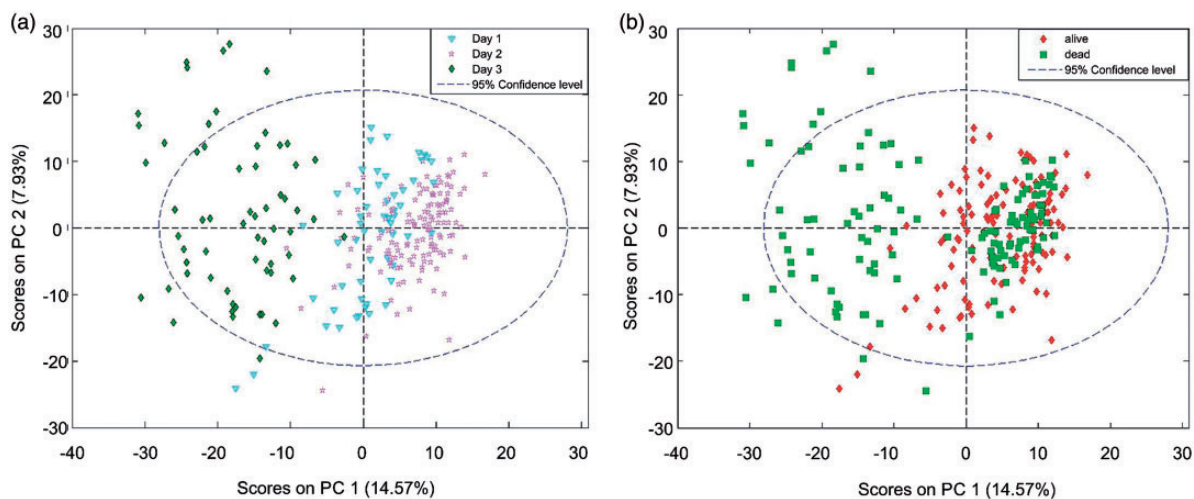
Figure 4. Score plot of PC 1 versus PC 2 acquired from spore data (living and dead) at three different measurement days: (a) measurement days marked in blue, pink, and dark green; (b) viability marked in red (alive) and green (dead).
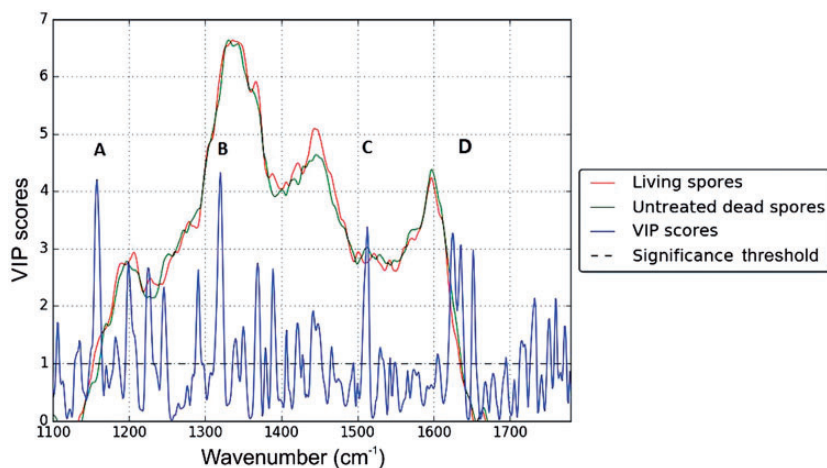
Figure 5. Variable importance in projection scores for the PLS-DA model based on the calibration set containing 178 spore spectra and mean spectra of each class.

well as large contributions due to day-to-day variations Fig. 4. Hierarchical cluster analysis and PCA as unsupervised classification methods can differentiate between living and dead spores to some extend but they are not specific enough
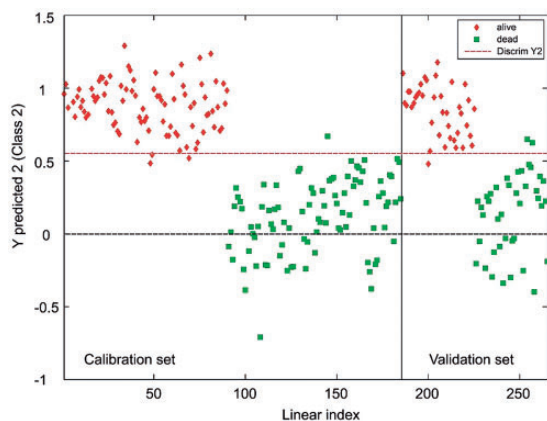
Figure 6. Score plot of calibration (178 spectra) and validation (80 spectra) set.

Table 2. Parameters of PLS-DA model for calibration, cross-validation (CV), and prediction.

	Sensitivity	Specificity	Class. err.
Calibration	0.989	0.966	0.023
CV	0.945	0.908	0.073
Prediction	0.950	0.975	0.038

(Fig. 3b and Fig. 4b). However, the information seems to be masked by other, more dominant features in the spectral data cube. Hence, PLS-DA as supervised classification technique was applied subsequently as method of choice as it allows targeted, knowledge-based classification. Thus, the focus can be directed on subtler differences between two classes instead of picking out the major variations or close similarities in the data set as PCA and HCA, respectively, do.

The Partial Least Squares Discriminant Analysis Model for Live/Dead Differentiation of P. chrysogenum Spores

Upon exclusion of Raman spectra dominated by spectral noise (see Data Preprocessing), the PLS-DA model was built on the spectral fingerprint (1000–1900 cm^{-1}) of the remaining 258 spores (50% living and dead spores, respectively).

The data set was split into a calibration set consisting of 178 spectra used to build the model and a validation set (80 spectra) to which the model was applied. Three latent variables were chosen based on venetian blinds cross-validation which was performed by dividing the data set into ten sub-validation sets. Variable importance in projection (VIP) scores point out those variables most important for the differentiation between two classes. It appears that the assignment of living and dead spores to the corresponding class relies, among others, on four main Raman bands located at: (A) 1160 cm^{-1}; (B) 1320 cm^{-1}; (C) 1512 cm^{-1}; and (D) 1620 cm^{-1} (Fig. 5) Raman shift. Whereas these bands can be assigned to ν(C–C), δ(C–H) as well as isolated and aromatic ν(C=C) vibrations,[13,27–30] it is difficult to
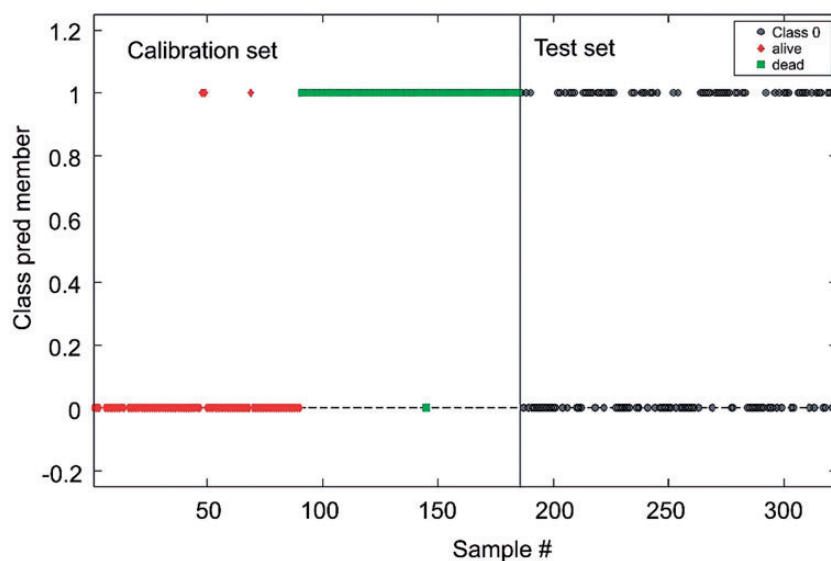
Figure 7. Classification result (calibration set on the left and test set on the right side of the graph) of the PLS-DA model applied to the Raman spectra of a 1 μL droplet consisting of living and dead spores in a 1:1 ratio.

draw a clear picture on the relevance of specific molecules for the class assignment living or dead especially since the analysis was performed on spores directly taken from spore inoculum prior to any cultivation. This means that the spores are still in a dormant state and do not have any metabolic activity, making the classification an even more challenging task.

The score plot containing the calibration and validation data set depicted in Fig. 6 shows a promising result for life/dead differentiation of spores based on label-free Raman spectroscopy. With a sensitivity as well as specificity of >95% and a classification error of 4% regarding the test data prediction, the established PLS-DA model seems to be suitable for viability study of *P. chrysogenum* spores (Table 2).

Another test data set was used upon demonstrating the model's suitability for spore viability studies based on the molecule specific Raman scattering and independent from any influence that different measurement days might have. Spore suspensions of living and dead spores were mixed in a 1:1 ratio. After dilution, 1 μL of the mixture was dried on CaF_2 and measured immediately. Every single spore of this droplet was manually selected and the according coordinates added to the list of measurement positions where Raman spectra where collected consecutively. Knowing that the droplet on the sample carrier ideally contains 50% living and 50% dead spores, the model was applied to the data set. Out of the 135 spore spectra, the model assigned 66 to the class of dead spores (49% dead spores) and 69 to the one of living spores (51% viable spores), revealing an excellent classification result (Fig. 7).

Conclusion

We present a label-free, noninvasive classification method for viability study of *P. chrysogenum* spore inoculum based on Raman spectroscopy. The PLS-DA model shows good performance for live/dead differentiation in the current validation data sets. It has to be noted that a model can only be as stable as the references it is based on. This particular task was a big challenge in the presented study as biological systems tend to change over time and thus might already be dead when considered alive and vice versa. However, this effect could be mitigated as one of the main focus points of this work was to develop a fast and easy sample preparation procedure to keep the time between sample collection/preparation and measurement as short as possible (<1 h).

Interference by the Raman signals of medium components (different salts from buffer, C– source, N– source, etc.) was successfully eliminated. The single dilution step combined suppression of the interference perfectly with the goal of fast and simple sample preparation.

So far, measurement positions were chosen manually which represents a critical source of errors as single spores might accidentally be missed or selected more than once for collecting a Raman spectrum. This can be circumvented by employing the available LabVIEW interface with a suitable pattern recognition algorithm of NI Vision. Finally, the dilution step could be automated using a flow injection analysis scheme, paving the way for developing an automated screening method for the determination of spore inoculum's quality.

Conflict of Interest

The authors report there are no conflicts of interest.

## Funding

Note

a. Information based on in-house knowledge of the industrial cooperation partner

References

1. Z. Zhao, H. Liu, Y. Luo, S. Zhou, et al. "Molecular Evolution and Functional Divergence of Tubulin Superfamily in the Fungal Tree of Life". Sci. Rep. 2014. 4: 6746.
2. M. a van den Berg, R. Albang, K. Albermann, J.H. Badger, et al. "Genome Sequencing and Analysis of the Filamentous Fungus *Penicillium chrysogenum*". Nat. Biotechnol. 2008. 26(10): 1161–1168.
3. A. Fleming. "On the Antibacterial Action of Cultures of a *Penicillium*, with Special Reference to their Use in the Isolation of *B. influenza*". Br. J. Exp. Pathol. 1929. 10(3): 226–236.
4. T.R. van der Lende, P. Breeuwer, T. Abee, W.N. Konings, et al. "Assessment of the Microbody Luminal pH in the Filamentous Fungus *Penicillium chrysogenum*". Biochim. Biophys. Acta. 2002. 1589(2): 104–111.
5. A.L. Demain, S. Sanchez. "Microbial Drug Discovery: 80 Years of Progress". J. Antibiot. (Tokyo). 2009. 62(1): 5–16.
6. T. Wucherpfennig, K.A. Kiep, H. Driouch, C. Wittmann, et al. Morphology and Rheology in Filamentous Cultivations. Adv. Appl. Microbiol. 72: 89–136.
7. G.M. Smith, C.T. Calam. "Variations in Inocula and their Influence on the Productivity of Antibiotic Fermentations". Biotechnol. Lett. 1980. 2(6): 261–266.
8. D. Ehgartner, C. Herwig, L. Neutsch. "At-Line Determination of Spore Inoculum Quality in Penicillium chrysogenum Bioprocesses". Appl. Microbiol. Biotechnol. 2016. 100(12): 5363–5373.
9. G.C. Paul, C.A. Kent, C.R. Thomas. "Viability Testing and Characterization of Germination of Fungal Spores by Automatic Image Analysis". Biotechnol. Bioeng. 1993. 42(1): 11–23.
10. M.S. Rakotonirainy, C. Héraud, B. Lavédrine. "Detection of Viable Fungal Spores Contaminant on Documents and Rapid Control of the Effectiveness of an Ethylene Oxide Disinfection Using ATP Assay". Luminescence. 2003. 18(2): 113–121.
11. S.Q. Yu, E.J. Trione, T.M. Ching. "Biochemical Determination of the Viability of Fungal Spores and Hyphae". Mycol. Soc. Am. 1984. 76(4): 608–613.
12. N. Mesquita, A. Portugal, G. Piñar, J. Loureiro, et al. "Flow Cytometry as a Tool to Assess the Effects of Gamma Radiation on the Viability,

Growth and Metabolic Activity of Fungal Spores". Int. Biodeterior. Biodegrad. 2013. 84: 250–257.

13. W.E. Huang, M. Li, R.M. Jarvis, R Goodacre, et al. "Shining Light on the Microbial World: The Application of Raman Microspectroscopy". Adv. Appl. Microbiol. 70: 153–186.

14. R. Petry, M. Schmitt, J. Popp. "Raman Spectroscopy-A Prospective Tool in the Life Sciences". Chem. Phys. Phys. Chem. 2003. 4(1): 14–30.

15. S. Ghosal, J.M. MacHer, K. Ahmed. "Raman Microspectroscopy-Based Identification of Individual Fungal Spores as Potential Indicators of Indoor Contamination and Moisture-Related Building Damage". Environ. Sci. Technol. 2012. 46(11): 6088–6095.

16. K. De Gussem, P. Vandenabeele, A. Verbeken, et al. "Raman Spectroscopic Study of Lactarius Spores (Russulales, Fungi)". Spectrochim. Acta, Part A. 2005. 61(13–14): 2896–908.

17. W.E. Huang, R.I. Griffiths, I.P. Thompson, M.J. Bailey, et al. "Raman Microscopic Analysis of Single Microbial Cells". Anal. Chem. 2004. 76(15): 4452–4458.

18. D. Yang, H. Zhou, C. Haisch, R. Niessner, et al. "Reproducible *E. coli* Detection Based on Label-Free SERS and Mapping". Talanta. 2016. 146: 457–463.

19. K. Maquelin, L.P. Choo-Smith, T. van Vreeswijk, H.P. Endtz, et al. "Raman Spectroscopic Method for Identification of Clinically Relevant Microorganisms Growing on Solid Culture Medium". Anal. Chem. 2000. 72(1): 12–19.

20. M. Miljković, T. Chernenko, M.J. Romeo, B. Bird, et al. "Label-Free Imaging of Human Cells: Algorithms for Image Reconstruction of Raman Hyperspectral Datasets". Analyst. 2010. 135(8): 2002–2013.

21. K. Klein, A.M. Gigler, T. Aschenbrenner, R. Monetti, et al. "Label-Free Live-Cell Imaging with Confocal Raman Microscopy". Biophys. J. 2012. 102(2): 360–368.

22. M. Ando, H. Hamaguchi. "Molecular Component Distribution Imaging of Living Cells by Multivariate Curve Resolution Analysis of Space-Resolved Raman Spectra". J. Biomed. Opt. 2014. 19(1): 011016.

23. K.C. Schuster, I. Reese, E. Urlaub, J.R. Gapes, et al. "Multidimensional Information on the Chemical Composition of Single Bacterial Cells by Confocal Raman Microspectroscopy". Anal. Chem. 2000. 72(22): 5529–5534.

24. H. Noothalapati, T. Sasaki, T. Kaino, M. Kawamukai, et al. "Label-Free Chemical Imaging of Fungal Spore Walls by Raman Microscopy and Multivariate Curve Resolution Analysis". Sci. Rep. 2016. 6: 27789.

25. T. Dao, M. Bensoussan, P. Gervais, P. Dantigny. "Inactivation of Conidia of *Penicillium chrysogenum, P. digitatum* and *P. italicum* by Ethanol Solutions and Vapours". Int. J. Food Microbiol. 2008. 122(1–2): 68–73.

26. R.G. Brereton, G.R. Lloyd. "Partial Least Squares Discriminant Analysis: Taking the Magic Away". J. Chemom. 2014. 28: 213–225.

27. G. Socrates. Infrared and Raman Characteristic Group Frequencies. Chichester, UK: John Wiley and Sons, 2001.

28. Y. Chen, J. Dai, X. Zhou, Y. Liu, et al. "Raman Spectroscopy Analysis of the Biochemical Characteristics of Molecules Associated with the Malignant Transformation of Gastric Mucosa". PLoS One. 2014. 9(4): e0093906.

29. K. Maquelin, C. Kirschner, L.-P. Choo-Smith, N. van den Braak, et al. "Identification of Medically Relevant Microorganisms by Vibrational Spectroscopy". J. Microbiol. Methods. 2002. 51: 255–271.

30. Q. Matthews, A. Jirasek, J. Lum, X. Duan, et al. "Variability in Raman Spectra of Single Human Tumor Cells Cultured in Vitro: Correlation with Cell Cycle and Culture Confluency". Appl. Spectrosc. 2010. 64(8): 871–887.

5.2   Publication II

In-line Ultrasound-enhanced Raman spectroscopy Allows for Highly Sensitive Analysis with Improved Selectivity in Suspensions

Karin Wieland, Stefan Tauber, Christoph Gasser, Lukas A. Rettenbacher, Laurin Lux, Stefan Radel, Bernhard Lendl; *submitted to Analytical Chemistry*

In-line ultrasound-enhanced Raman spectroscopy allows for highly sensitive analysis with improved selectivity in suspensions

Karin Wieland, Stefan Tauber, Christoph Gasser, Lukas A. Rettenbacher, Laurin Lux, Stefan Radel, Bernhard Lendl*

Institute of Chemical Technologies and Analytics. Research Division Environmental, Process Analytics and Sensors, TU Wien, 1060 Vienna, Austria

ABSTRACT: Raman spectroscopy is a non-destructive characterization method offering chemical-specific information. However, the cross-section of inelastically (Raman) scattered light is very low compared to elastically (Rayleigh) scattered light, resulting in weak signal intensities in Raman spectroscopy. Despite providing crucial information in off-line measurements, it usually is not sensitive enough for efficient, in-line process control in conjunction with low particle concentrations. To overcome this limitation, two custom-made 1.4404 stainless-steel prototype add-ons were developed for in-line Raman probes that enable ultrasound particle manipulation and thus concentration of particles in suspensions in the focus of the Raman excitation laser. Depending on size and density differences between particles and the carrier medium, particles are typically caught in the nodal planes of a quasi-standing wave field formed in an acoustic resonator in front of the sensor. Two arrangements were realized with regard to the propagation direction of the ultrasonic wave relative to the propagation direction of the laser. The parallel arrangement improved the limit of detection (LOD) by a factor of ≈30. In addition to increased sensitivity, the perpendicular arrangement offers increased selectivity: modifying the frequency of the ultrasonic wave field allows the liquid or solid phase to be moved into the focus of the Raman laser. The combination of in-line Raman spectroscopy with ultrasound particle manipulation holds promise to push the limits of conventional Raman spectroscopy, hence broadening its field of application to areas where previously Raman spectroscopy has not had sufficient sensitivity for accurate, in-line detection.

Raman spectroscopy is a valuable tool for direct, fast, non-destructive, and label-free investigation of gaseous, liquid, and solid samples.[1–5] Especially for process monitoring purposes, Raman offers the possibility of real-time reaction monitoring in aqueous environments by analyzing chemical fingerprints specific to the analyte of interest.[6–8] While Raman offers unique insights for process control, it suffers from low signal intensity due to its small cross-section. In-line probes for process monitoring are currently insufficiently sensitive to access small changes in the spectral fingerprint that might be crucial for the differentiation of two very chemically similar components (e.g., polymorphs in crystallization processes) or for early detection of the formation of a specific analyte. Earlier detection of wanted or unwanted analytes in (bio-)processes allows better adaption and optimization of these processes. Efficient process control is directly linked to improved production cycles, resulting in more efficient work load systems and hence more cost-efficient production. Koch et al. have performed highly sensitive in-line ultrasound-enhanced attenuated total reflection (ATR) mid-infrared spectroscopy in bioreactors by using ultrasonic standing wave fields to manipulate particles, pushing the analyte against the surface of the ATR element and thus into the evanescent field.[9] Combination of ultrasound particle manipulation (UPM) with Raman spectroscopy as a less water-sensitive method has also been shown to facilitate spectroscopy in aqueous suspensions while simultaneously allowing significantly higher signal intensities. In these experiments, a flow cell was used to investigate theophylline crystals or yeast cells or to perform surface-enhanced Raman spectroscopy (SERS).[10,11]

Herein, we introduce a prototype add-on made of stainless steel for fiber-optic in-line Raman probes that allows UPM, hence enabling measurements with significantly lower limits of detection (LODs). Briefly, an acoustic resonator is built in front of the probe. Homogenously distributed particles in a stirred suspension are either drawn into pressure or anti-pressure areas of the acoustic standing wave field depending on the material properties, such as particle size, density, and compressibility, of the particles and the surrounding medium and the ratios thereof. The design of an ultrasound add-on for in-line Raman probes furthers two main goals: (i) improve the sensitivity of in-line Raman probes for particle measurements, and (ii) enhance selectivity of in-line Raman measurements of suspensions to selectively investigate either the solid or liquid phase of a two-component system. To this end, two different designs were realized: (a) Arranging the ultrasonic wave parallel to the direction of laser propagation allows investigation of two model aqueous systems (starch and PMMA) that differ mainly in particle size. Improvements in the LOD by a factor of ≈30 were achieved, highlighting the potential of this technique to further extend the lower end of the accessible concentration range of conventional Raman spectroscopy. (b) Arranging the ultrasonic wave perpendicular to the direction of laser propagation not only offers improved sensitivity but also allows particles to be selectively moved into or out of the Raman laser focus by changing the frequency of the ultrasonic waves. Hence, detailed investigation of either the liquid phase or the solid phase is possible.

Ultrasonic particle manipulation

The combination of Raman spectroscopy with UPM was achieved by developing a prototype add-on to a Raman in-line probe that allows the formation of an ultrasound standing wave field and thus concentration of particles right in front of the Raman sensor. An acoustic resonator consisting of a transducer and a reflector was employed to generate the ultrasound standing wave field. Superposition of the incoming and reflected waves results in the formation of a quasi-standing wave field within the resonator. By placing this resonator in a suspension, particles are forced into the nodal or anti-nodal planes of the standing wave field mainly due to the primary axial radiation force F_z^{rad} acting on them. Considering a suspension with particles of radius r and a wavelength λ of the pressure wave propagating in the z-direction, the primary axial radiation force F_z^{rad} for particles with $r \ll \lambda$ can be described as

$$F_z^{rad} = 4\pi \cdot \Phi(\tilde{\kappa}, \tilde{\rho}) \cdot (kr)^3 \cdot E_{ac} \cdot \sin(2kz) \qquad (1)$$

where the acoustic contrast factor $\Phi(\tilde{\kappa}, \tilde{\rho})$ is defined as

$$\Phi(\tilde{\kappa}, \tilde{\rho}) = \frac{1}{3}\left(\frac{5\tilde{\rho} - 2}{2\tilde{\rho} + 1} - \tilde{\kappa}\right) \qquad (2)$$

with density ratio $\tilde{\rho} = \rho_p / \rho_0$ of the particles ρ_p and the surrounding medium ρ_0 and compressibility ratio $\tilde{\kappa} = \kappa_p / \kappa_0 = \frac{1}{\rho_p \cdot c^2} / \frac{1}{\rho_0 \cdot c^2}$. Furthermore, F_z^{rad} is proportional to the acoustic energy factor E_{ac}, which describes the energy brought into the system as

$$E_{ac} = \frac{p_a^2}{4\rho_0 c_0^2} \qquad (3)$$

where p_a is the acoustic pressure amplitude, ρ_0 is the density of the medium, and c_0 is the speed of sound in the medium. The primary axial radiation force is predominantly affected by the radius of the particles and by the density and compressibility ratios of the particles and the medium. Other, less intense, forces also affect the local particle arrangement within the nodal planes (see Figure 1a): The action of the transverse primary radiation force F_{xy}^{rad} perpendicular to the sound propagation direction results from uneven amplitude contributions and is hence an effect of deviations from an ideal resonator. The secondary radiation force F_{xyz}^i describes the interaction between closely spaced particles in the nodal planes. Detailed descriptions of these forces are given elsewhere.[12–15]

Experimental Section

Ultrasonic resonator

Prototype ultrasound add-ons to in-line Raman probes were fabricated out of 1.4404 stainless steel by selective laser melting. The dimensions of both prototypes were adapted to fit a D25 Ingold port. The 1-mm-thick piezoelectric ceramics (PZT, PI Ceramic GmbH, Germany) with printed silver electrodes were isolated from the aqueous suspension via an additional layer of Macor ceramics (Corning Inc., NY), forming the ultrasound transducer. Macor is a machinable glass-ceramic with chemical and mechanical properties similar to those of glass. All designs and materials used fall within FDA rules. The electrical signal for the ultrasonic transducer was generated using a frequency power synthesizer (FPS 2540, PSI Systems, Austria). The ultrasonic field intensity and frequency were manually controlled, and the electrical power was set in the range 1–3 W. A

frequency of $\approx$2 MHz, corresponding to a sound wavelength in aqueous environment of $\approx$740 µm, was applied, resulting in a distance of $\approx$370 µm between nodal planes. Two fundamentally different designs (see Figure 1a and b) were tested: In the first setup, the ultrasound standing wave field was set parallel to the propagation direction of the Raman laser. This allowed use of the lens of the Raman probe as a reflector for the acoustic resonator. In the second setup, the ultrasound wave field was oriented perpendicular to the propagation direction of the Raman laser. Thus, another Macor reflector was used to reflect the ultrasound waves. The second setup allows additional selectivity of the Raman measurements. The laser focus can be set either on or between the nodal planes depending on the frequency of the ultrasonic wave, allowing either the nodal or anti-nodal plane to be moved into the focus point of the excitation laser. Hence, the scattered photons will carry chemical-specific information of either the solid or liquid phase, enabling single-phase investigation in, e.g., stirred suspensions. The prototype design and manufacturing for the perpendicular arrangement required sophisticated engineering approaches to ensure compliance with the geometry restrictions necessary for fitting to a D25 Ingold port. These spatial arrangement limitations necessitated a Raman probe with a focal length of 10 mm, which exceeds the focal length of commercial Raman probes for in-line measurements available in our lab by roughly a factor of 4. Consequently, a probe with a suitable focal length was fabricated using a stainless-steel tube and an anti-reflection-coated 8-mm-diameter lens (Plano Convex Lens, Newport Corp.). Raman measurements in cyclohexane with the custom-made and the commercially available probe revealed identical Raman spectra in terms of band positions and higher signal intensity for the custom-made probe (see Figure S3 in the Supporting Information). Therefore, the latter probe was used for in-line Raman measurements when employing the prototype that allows perpendicular arrangement of the Raman laser and ultrasonic wave propagation directions. A simplified setup was used for the initial test measurements, consisting of a commercial UV/Vis cuvette with filling capacity of 3.5 mL (6030-OG, spectral range 360–2500 nm, Hellma GmbH, Germany) placed in a 3D-printed holder and fixed onto a manually operated xyz-stage (graduation: 10 µm; Thorlabs Inc., NJ). This setup allows the change in frequency of the ultrasonic waves to be mimicked by changing the position of the cuvette perpendicular to the Raman laser propagation direction. Line scans covering a distance of 1 mm along the propagation direction of the ultrasonic waves (y-direction) were performed with a step size of 50 µm.

Raman measurements

Raman measurements employed an RXN1 Raman system (Kaiser Optical Systems Inc., an Endress+Hauser company, MI) equipped with a 785 nm laser and a low-frequency grating that allows access to the spectral region between 100 cm^{-1} and 1890 cm^{-1} (Raman shift). Single spectra were recorded at maximum laser power (550 mW) using a charge-coupled device (CCD) detector. Balancing signal-to-noise ratio (SNR) and measurement time, three spectra were accumulated with an integration time of 15 s each at 1-min measurement intervals. The settings used to acquire Raman spectra as well as parameters such as stirrer speed, vessel volume, and size of the resonator were kept constant for comparative purposes. Parameter settings for Raman measurements needed to be carefully adapted. Identical parameter settings were also used for measurements in a defined particle concentration range. Particle concentration and parameter settings were determined based on a balance

between overall measurement time and SNR of single spectra. A strong increase in signal intensity was observed with active UPM. Hence, to stay within the dynamic range of the CCD, experimental parameters were chosen such that the Raman signal was just detectable at the highest particle concentration with conventional Raman spectroscopy while avoiding detector saturation for Raman measurements with active UPM. Each concentration was measured over three runs, where each measurement run consisted of acquiring a total of 42 spectra over 3 accumulation phases (ultrasound turned on) with 10 measurements each and 4×3 measurements with the ultrasound switched off. Between each run, the stirrer was set to maximum speed to counteract aggregation of particles and accumulation of analyte on the transducer surface.

Samples

Starch particles (ρ_{starch} = 1.5 g/cm^3, Merck KGaA, Germany) in an aqueous environment were chosen as the initial test system as starch is easy to handle, non-toxic, readily available, reasonably stable, and a good Raman scatterer. Additionally, the typical diameter of starch particles (roughly 10 µm) perfectly fits the size range (~1 µm up to some 100 µm) accessible with the frequency of ~2 MHz employed for particle trapping. Six starch concentrations ranging from 0.016 g/L to 0.5 g/L were investigated. Suspensions were prepared by weighing solid fractions of starch and adding 500 mL of deionized water before degassing the suspension in an ultrasound bath prior to Raman measurements. The band at 478 cm^{-1} was selected to monitor the effect of UPM on the Raman signal intensity; this is the most intense band in the spectral fingerprint region of starch and is attributed to C–C–C bend and C–O torsion vibrations.[16] Integration between 458 cm^{-1} and 498 cm^{-1} with 2-point baseline subtraction allowed estimation of the signal enhancement achieved via ultrasound-enhanced Raman spectroscopy.

Similar experiments were performed using smaller-diameter (≈3 µm) poly(methyl methacrylate) (PMMA) particles (ρ_{PMMA} = 1.2 g/cm^3, Polysciences GmbH, Germany) in deionized water, mainly to study the effect of particle size on the particle trapping efficiency of the ultrasound field, as the primary acoustic radiation force strongly depends on this parameter ($F_z^{rad} \sim r^3$, see Equation 1). PMMA also has several key properties such as (i) insolubility in water, (ii) good Raman scattering, and (iii) a narrow particle size distribution (3.36 µm ± 0.54 µm) in the lower µm range. The ν_s(C–O–C) vibration[17] at 818 cm^{-1} was selected as the PMMA marker band because it is one of the most intense bands in the spectral fingerprint of PMMA that experiences no spectral interference from water or the transducer material. Six PMMA concentrations ranging from 0.063 g/L to 2.0 g/L were investigated.

Data processing

iC Raman software (version 4.1, Kaiser Optical Systems Inc., an Endress+Hauser company, MI) was used for data acquisition and integration of marker bands with a 2-point baseline. Spectra were cut to focus on defined spectral regions and/or baseline corrected using the asymmetric least squares smoothing procedure of Eilers and Boelens[18] in Python 3.6.

DataLab (version 3.530, Epina GmbH, Pressbaum, Austria) and online calculators provided by Mathcrackers (https://mathcracker.com) were used for statistical evaluation of the ultrasound-enhanced Raman signal as a function of particle concentration.

Results and Discussion

To evaluate the effect of UPM on the Raman signal intensity and level of detection, single spectra were first recorded in stirred suspensions of starch and PMMA of different concentrations without ultrasound; Raman spectra with active UPM in the acoustic resonator were then recorded. Visual inspection shows distinct differences between the images with and without UPM for both particle systems in the parallel arrangement (see Figure 2a). In the absence of ultrasound manipulation, particles are homogenously distributed in the stirred suspension. Depending on the concentration, a particle occasionally passes in front of the probe such that interaction with the Raman laser is possible. The image of the PMMA suspension depicts the position of the laser focus in the lower half of the acoustic resonator (focal length of commercial probe: 2.4 mm). To exclude interference from the Macor bands in the spectral fingerprint of starch or PMMA particles, respectively, a greater distance is required between transducer and reflector, resulting in a weaker ultrasonic standing wave field. Balancing these two parameters (stability of the ultrasonic field vs. Macor interference in the Raman spectra) resulted in selection of a distance of 2.5 mm between the lens (reflector) and transducer. As soon as the ultrasound is turned on, particles are actively caught in the standing wave field and concentrated in front of the Raman probe. For starch, 0.5 g/L was determined as the LOD of the in-line Raman probe as a weak Raman signal could typically be obtained. In contrast, a pronounced spectrum of the same particle concentration is observed with ultrasound enhancement (Figure 2b). The LOD for the in-line probe with UPM was as low as 0.016 g/L, i.e., a 30-fold improvement is demonstrated. The limitation here is mostly the time required to collect particles in the nodal planes: Considering a stirred suspension with homogenously distributed particles, the number of particles in close proximity to the ultrasound standing wave field is significantly reduced for lower concentrations at constant vessel volume (here, 500 mL). Therefore, a particle must travel a greater distance before being close enough to the standing wave field to be caught in the nodal planes compared to suspensions with higher particle concentrations. Hence, longer particle collection times would be needed for lower concentrations before similarly strong Raman signal intensities with the same parameters (laser power, integration time) could be detected. Consecutive periods with and without UPM indicate reproducible results with a significant signal increase for ultrasound-enhanced Raman spectra. As can be seen in Figure 2c, an increase in signal intensity of the integrated marker band from 0 to values in the range of 10^4 is observed as soon as the ultrasonic field is formed and particles are drawn into the nodal planes of the standing wave field. Similar observations were made for PMMA suspensions. However, PMMA solutions required more time than starch solutions for the Raman signal to plateau with active UPM. This observation can be linked to the radius and the material properties of the particles: starch and PMMA differ in particle size (starch ≈ 10 µm, PMMA ≈ 3 µm) and density (ρ_{starch} = 1.5 g/cm^3, ρ_{PMMA} = 1.2 g/cm^3 according to data sheets), both of which affect the primary axial radiation force (see Equation 1 and 2). The main impact is attributed to particle size ($F_z^{rad} \sim r^3$); thus, a significantly higher force (roughly 37× higher) is acting on the starch particles as they are dragged into the nodal planes, resulting in quicker collection of particles in front of the Raman probe.

As mentioned above, six concentrations each of starch and PMMA were investigated. The highest particle concentration for each system represents the achieved LOD of the employed Raman probe/spectrometer without particle manipulation. The Raman signal collected with active UPM shows considerable improvement in signal intensity; however, the linear correlation between signal intensity and analyte concentrations is lost to a certain extent, as depicted in Figure 2d. For conventional Raman spectroscopy, no starch- or PMMA-specific signal was detected for concentrations below 0.5 g/L starch or 2 g/L PMMA. Hence, no linear dependency for the signal intensity as a function of particle concentration can be shown. Depending on the material properties of the particle system and carrier medium, a certain concentration dependency of the Raman signal with ultrasound active phases is possible – although with a significantly reduced dynamic range compared to conventional Raman spectroscopy – by balancing particle collection time, stirrer speed, and photon collection time on the CCD. Based on statistical tests (see Figures S1 and S2 in the Supporting Information), means/medians of the four lowest concentrations of each particle system are considered to be equal, whereas there is not enough evidence to assume that the means/medians of 0.25 g/L and 0.5 g/L starch or 1 g/L and 2 g/L PMMA, respectively, are equal. The results of the statistical evaluation are summarized in Figure 2d, in which statistically equal means/medians are framed in green. Hence, for very low particle concentrations, only qualitative detection is possible.

In some cases, a strong signal increase was observed within the first few minutes of ultrasound activation. To shed some light on this behavior, the spatial arrangement of the particles in the nodal planes was studied in more detail using a commercial video camera (Pi camera operated by a Raspberry Pi 3) without a near-infrared (NIR) filter. Videos were recorded while the Raman measurements were taken, using the Raman laser as the light source for the camera images. Three consecutive measurements with alternating phases with and without UPM are shown as examples in Figure 3a for 0.031 g/L starch in an aqueous environment. Here, a strong increase of at least 7-fold is observed in the Raman signal (see Figure 3b depicting the starch marker band at different points in time along the first "ultrasound on" phase) during the first two minutes of the first "ultrasound on"-phase (highlighted in grey in Figure 3a); this phenomenon could not be repeated for the subsequent periods with active UPM. Video images at distinct time points during the measurement sequence were selected for the first and third ultrasound-active phase (Figure 3c). Color-coded numbers in the intensity plot (Figure 3a) mark the time points at which the respective video image was recorded. Images 4 and 5 of both ultrasound-active phases look very similar: starch particles are concentrated in front of the sensor, yielding two contrasting effects: With more particles agglomerating in front of the Raman probe, a higher Raman signal is achieved. However, at the same time, more particles are blocking the backscattered photons, resulting in effective recording of a weaker Raman signal, although it is still significantly more intense than the measurements obtained without UPM (see Figure 3b). The two video images labeled 3 for both ultrasound-active phases are of particular interest: In both images, particles are concentrated in the focus point of the Raman probe. However, in the first ultrasound-active phase, fewer particles are blocking the backscattered photons in the upper area of the standing wave field (closer to the probe), which leads to a strong increase in the recorded Raman signal. In video image 4 of the first phase, particles are concentrated in all nodal planes

between the transducer and the Raman probe, thus resulting in a lower Raman signal, as recorded for most of the other ultrasound-active phases.

Arrangement of the laser and ultrasound wave propagation directions perpendicular to one another (see Figure 1b) allows not only increased signal sensitivity but also additional selectivity of in-line Raman measurements of suspensions. In the perpendicular arrangement, particles in the nodal planes are selectively moved in or out of the laser focus by changing the frequency of the ultrasonic wave, allowing selective investigation of either the liquid or the solid phase. The design of this arrangement to fit a D25 Ingold port requires a complex, refined design of the probe add-on; thus, limitations regarding strength and stability of the ultrasound standing wave field must be considered in the first iteration of this prototype. Before realizing this complex design, test measurements were performed using an experimental setup consisting of a UV/Vis cuvette filled with 6 g/L PMMA in water on a manually operated xyz-stage. Two piezoelectric elements were glued to two opposing sides of the cuvette to act as a transducer and reflector, respectively, thus forming an acoustic resonator within the cuvette. The experimental arrangement is shown in Figure 4a. In the final prototype, the particles accumulated in the nodal planes are moved in and out of the laser focus by changing the frequency of the ultrasonic waves. In the preliminary setup, the cuvette fixed on the xyz-stage was moved manually in the y-direction (perpendicular to the Raman laser direction but parallel to the ultrasonic wave propagation) to mimic the change in the frequency of the ultrasonic waves and to investigate how much selectivity can effectively be gained with this arrangement. Line scans across nodal and anti-nodal planes measured consecutively with and without active UPM, respectively, are shown in Figure 4b (additional data shown in Figure S4 in the Supporting Information). The intensity distribution of the integrated PMMA marker band (v_s(C–O–C) vibration at 818 cm^{-1}) along the 1-mm scanned area clearly illustrates the presence of three nodal planes, indicated by the significantly higher signal intensity in these areas. Comparison of the band areas of the nodal planes with the band areas of the stirred suspension without UPM indicates a 42-fold improvement of the signal. Enlargement of the baseline area in Figure 4b shows that the PMMA-specific signal is higher in stirred suspension without active UPM compared to the signal taken in areas between the nodal planes under active particle manipulation. A significant portion of the particles in the suspension are drawn into the nodal planes, leaving few particles in the areas between the planes; hence, a significantly lower or no PMMA-specific Raman signal is expected in these areas, as is clearly reflected in the line scans (Figure 4b, right-hand side). These line scans indicate that the nodal planes with agglomerated particles have a width of 100 to 150 µm and that the distance between the maximum of each nodal plane is 300 µm ± 50 µm, which correlates well with the expected distance based on the set frequency of the ultrasonic waves. Note that during measurements, rearrangement of particles in nodal planes and slight shifts of nodal planes as a consequence thereof were observed. On the one hand, this can be the result of temperature changes in the suspension due to energy input of the ultrasonic waves and a certain heat impact of the magnetic stirrer. For example, if the temperature of the medium increases from 20 °C to 25 °C, the temperature dependency of the speed of sound in water[19] results in a change of the ultrasonic wavelength of $\Delta\lambda = 7$ µm for a 2 MHz wave. This shows that system parameters must be well controlled to allow accurate

measurements between and on nodal planes for the perpendicular arrangement. Considering the small vessel volume of 3.5 mL of the UV/Vis cuvette, the heat impact is significantly higher here compared to the heat impact in a 500 mL beaker, and the heat impact should be insignificant in temperature-controlled vessels. On the other hand, constant particle rearrangement in the nodal planes due to the transverse primary radiation force F_{xy}^{rad} and the secondary radiation force F_{xyz}^{i} acting on the particles has an impact on the form of the aggregates in the nodal planes. Nevertheless, a significant gain in selectivity for in-line Raman measurements was observed. Therefore, the design of a second prototype with perpendicular propagation of the Raman laser and ultrasound wave was realized.

As for experiments with the parallel arrangement, starch in an aqueous environment was chosen as a test system for the perpendicular arrangement. Again, signal intensity was quantified by integration of the starch-specific band at 478 cm^{-1} with a 2-point baseline between the integration limits of 458 cm^{-1} and 498 cm^{-1}. As can be seen in Figure 5, the value of the integrated starch band for measurements on the nodal plane is the same order of magnitude (10^5) as was temporarily observed in the strong signal increase for the parallel arrangement (as shown in Figure 3a). In contrast to the parallel arrangement, the signal intensity in the perpendicular arrangement can be kept at this high level during active UPM and drops to zero as soon as the ultrasound is switched off. It is also noticeable that particles are caught within the nodal planes within seconds of switching the ultrasonic field on (grey area in Figure 5c), resulting in a detectable signal increase within the first minute (spectrum #2 in Figure 5a) of the ultrasound active-phase highlighted in grey in Figure 5c. Video images recorded simultaneously with the Raman spectra also depict this rapid accumulation of particles in the nodal planes (Figure 5b). As previously mentioned, in addition to increased signal intensity, the selectivity of the in-line Raman probe significantly increases in the perpendicular arrangement. In Figure 6, starch particles are selectively moved into or out of the probe's focus depending on the frequency f_1 or f_2 of the ultrasonic waves ($\Delta f \approx 30$ kHz). Based on theoretical considerations, a change in frequency of 30 kHz induces a shift of the agglomerated particles in the nodal planes of ≈ 14 µm. The custom-made probe in combination with the 785 nm Raman laser allows a laser spot size of ≈ 3µm and a spatial resolution of ≈ 1.4 µm. Hence, a shift of the agglomerated particles of 14 µm is sufficient to selectively measure the liquid phase between nodal planes. Additionally, the transverse primary radiation force F_{xy}^{rad} had an observable impact on the 3D arrangement of particles in the ultrasonic standing wave field. Changing the ultrasonic frequency from f_1 to f_2 led to a rearrangement of particles in the z-dimension, resulting in particles temporarily falling out of the laser focus point. Note that this effect is reversible (Figure 6a). The selectivity induced by the change in frequency is reflected in the information carried by the backscattered Raman photons: spectra recorded at f_1 (laser focus on nodal plane with accumulated starch particles) show the characteristic starch spectral fingerprint, which correlates well with the reference spectrum of starch powder (see Figure 6c), whereas no starch signal is detectable in the spectra recorded at f_2. The decrease and increase of the integrated starch marker band based on the frequency of the ultrasonic waves is demonstrated in Figure 6a. Video images at f_1 and f_2 (Figure 6b) highlight the laser focus on the line at f_1, as indicated by the intense scatter effect on concentrated starch particles, whereas no direct light scattering on starch particles is observed for f_2.

Conclusion

This work demonstrates the combination of in-line Raman spectroscopy with ultrasound particle manipulation. Two different arrangements of the laser propagation direction and ultrasonic wave propagation are realized. Increased sensitivity and selectivity are demonstrated in measurements of starch and PMMA suspensions at six different concentrations each. The parallel arrangement exhibited an ~30-fold improvement in the limit of detection of the recorded Raman spectra. Whereas the values of the integrated starch marker bands were typically on the scale of 10^4, the perpendicular arrangement promises even greater signal improvement (by an additional factor of ten). To achieve optimal signal sensitivity in Raman spectroscopy, lenses with a high numerical aperture are used. Usually, short focal lengths (for constant lens diameter) are preferred. Hence, future developments in the parallel arrangement will investigate better adaptation of the acoustic resonator's geometry and the Raman probe's focal length. The efficiency of the parallel arrangement can be substantially improved by designing a more compact system, for instance with a shorter-focal-length lens. Such a design would have two advantages: (i) The distance between transducer and reflector can be reduced, leading to a stronger and more stable standing wave field and hence more efficient particle manipulation. (ii) If the focus point is directly in front of the Raman probe (focal length of similar scale as the distance between nodal planes), then the negative impact of particles accumulating between the lens and the focus point and the resulting weakened recorded Raman signal can be circumvented.

The perpendicular arrangement additionally offers selective investigation of either the liquid or the solid phase of suspensions. However, further improvements are needed, such as enhanced stability of the ultrasonic standing wave field, e.g., by using a different amplifier or by increasing the size of the transducer surface. Also, until now, the frequency of the ultrasonic waves has been manually controlled for both arrangements. Hence, automated frequency regulation, allowing particles to be caught in the nodal planes without manual regulation, is desired to allow stable in-line measurements.

Having now introduced the general working principles of ultrasound-enhanced in-line Raman sensing, future work will concentrate on the investigation of products, by-products, or impurities in process analytical chemistry. Envisioned applications include crystallization processes, where the crystallization type can be determined by focusing on the crystals accumulating in the nodal planes and the composition of liquid phases can be accessed by changing the frequency of the ultrasonic waves in the acoustic resonator, allowing the laser to be focused between nodal planes. Other applications involve analysis of oil in water, wastewater treatment, and others where gains in sensitivity and/or selectivity will allow optimized, accurate, real-time process monitoring and control.

ASSOCIATED CONTENT

Supporting Information

The Supporting Information is available free of charge on the ACS Publications website.

Details on statistical evaluation of ultrasound-enhanced Raman signal as a function of particle concentration (PDF)

Comparison of cyclohexane Raman spectra recorded with commercial and custom-made probe (PDF)

Line scan parallel to the ultrasonic wave propagation direction in the cuvette (PDF)

AUTHOR INFORMATION

Corresponding Author

* Bernhard Lendl, Institute of Chemical Technologies and Analytics, TU Wien, Getreidemarkt 9/164, A-1060 Vienna, Austria

Email: bernhard.lendl@tuwien.ac.at

Author Contributions

All authors contributed to the writing of this manuscript. All authors have given approval to the final version of the manuscript.

REFERENCES

(1) De Beer, T. R. M.; Baeyens, W. R. G.; Ouyang, J.; Vervaet, C.; Remon, J. P. Raman Spectroscopy as a Process Analytical Technology Tool for the Understanding and the Quantitative In-Line Monitoring of the Homogenization Process of a Pharmaceutical Suspension. *Analyst* **2006**, 1137–1144.

(2) Li, Y.; Anderson, C. A.; Drennen, J. K.; Airiau, C. Method Development and Validation of an Inline Process Analytical Technology Method for Blend Monitoring in the Tablet Feed Frame Using Raman Spectroscopy. *Anal. Chem.* **2018**, *90*, 8436–8444.

(3) Matthiae, M.; Zhu, X.; Marie, R.; Kristensen, A. In-Line Whole Blood Fractionation for Raman Analysis of Blood Plasma. *Analyst* **2019**, *144*, 602–610.

(4) Hippler, M. Cavity-Enhanced Raman Spectroscopy of Natural Gas with Optical Feedback cw-Diode Lasers. *Anal. Chem.* **2015**, *87*, 7803–7809.

(5) Zhang, X.; Tan, Q.-H.; Wu, J.; Shi, W.; Tan, P.-H. Review on the Raman Spectroscopy of Different Types of Layered Materials. *Nanoscale* **2016**, *8*, 6435–6450.

(6) Wang, Q.; Li, Z.; Ma, Z.; Liang, L. Real Time Monitoring of Multiple Components in Wine Fermentation using an On-Line Auto-calibration Raman Spectroscopy. *Sensors Actuators B* **2014**, *202*, 426–432.

(7) Soares, F. L. F.; Carneiro, R. L. In-Line Monitoring of Cocrystallization Process and Quantification of Carbamazepine-Nicotinamide Cocrystal using Raman Spectroscopy and Chemometric Tools. *Spectrochim. Acta Part A Mol. Biomol. Spectrosc.* **2017**, *180*, 1–8.

(8) Csontos, I.; Pataki, H.; Farkas, A.; Bata, H.; Vajna, B.; Nagy, Z. K.; Keglevich, G.; Marosi, G. J. Feedback Control of Oximation Reaction by Inline Raman Spectroscopy. *Org. Process Res. Dev.* **2015**, *19*, 189–195.

(9) Koch, C.; Brandstetter, M.; Wechselberger, P.; Lorantfy, B.; Plata, M. R.; Radel, S.; Herwig, C.; Lendl, B. Ultrasound-Enhanced Attenuated Total Reflection Mid-infrared Spectroscopy In-Line Probe: Acquisition of Cell Spectra in a Bioreactor. *Anal. Chem.* **2015**, *87*, 2314–2320.

(10) Radel, S.; Schnöller, J.; Dominguez, A.; Lendl, B.; Gröschl, M.; Benes, E. Raman Spectroscopy of Particles in Suspension Concentrated by an Ultrasonic Standing Wave. *Elektrotechnik & Informationstechnik* **2008**, 82–85.

(11) Ruedas-Rama, M. J.; Domınguez-Vidal, A.; Radel, S.; Lendl, B. Ultrasonic Trapping of Microparticles in Suspension and Reaction Monitoring Using Raman Microspectroscopy. *Anal. Chem.* **2007**, *79*, 7853–7857.

(12) Gröschl, M. Ultrasonic Separation of Suspended Particles - Part I : Fundamentals. *Acta Acust.* **1998**, *84*, 432–447.

(13) Gröschl, M. Ultrasonic Separation of Suspended Particles - Part II: Design and Operation of Separation Devices. *Acta Acust.* **1998**, *84*, 632–642.

(14) Benes, E.; Gröschl, M.; Nowotny, H.; Trampler, F.; Radel, S.; Gherardini, L.; Hawkes, J. J.; König, R.; Delouvroy, C. Ultrasonic Separation of Suspended Particles. *Proc. IEEE Ultrason. Symp.* **2001**, 649–659.

(15) Settnes, M.; Bruus, H. Forces Acting on a Small Particle in an Acoustical Field in a Viscous Fluid. *Phys. Rev. E* **2012**, *85*, 1–12.

(16) Almeida, M. R.; Alves, R. S.; Nascimbem, L. B. L. R.; Stephani, R.; Poppi, R. J.; De Oliveira, L. F. C. Determination of Amylose Content in Starch using Raman Spectroscopy and Multivariate Calibration Analysis. *Anal. Bioanal. Chem.* **2010**, *397*, 2693–2701.

(17) Willis, H. A.; Zichy, V. J. I.; Hendra, P. J. The Laser-Raman and Infra-red Spectra of Poly (Methyl Methacrylate). *Polymer (Guildf).* **1969**, *10*, 737–746.

(18) Eilers, P. H. C.; Boelens, H. F. M. Baseline Correction with Asymmetric Least Squares Smoothing. **2005**, unpublished work.

(19) Greenspan, M.; Tschiegg, C. E. Speed of Sound in Water by a Direct Method. *J. Res. Natl. Inst. Stand. Technol.* **1957**, *59*, 249–254.
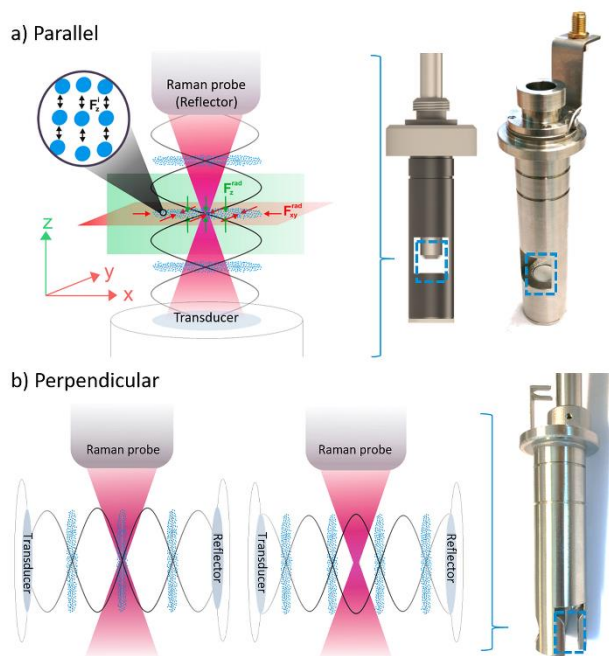
Figure 1. Two arrangements of the ultrasonic wave propagation direction with respect to the Raman excitation laser propagation direction: (a) in the parallel arrangement, particles are accumulated in the nodal planes of the standing wave in front of the probe, resulting in increased signal intensity. (b) In the perpendicular arrangement, the frequency of the ultrasonic wave can be shifted, allowing investigation of the solid (left) or liquid (right) phase of a suspension, thus resulting in increased selectivity as well as sensitivity.
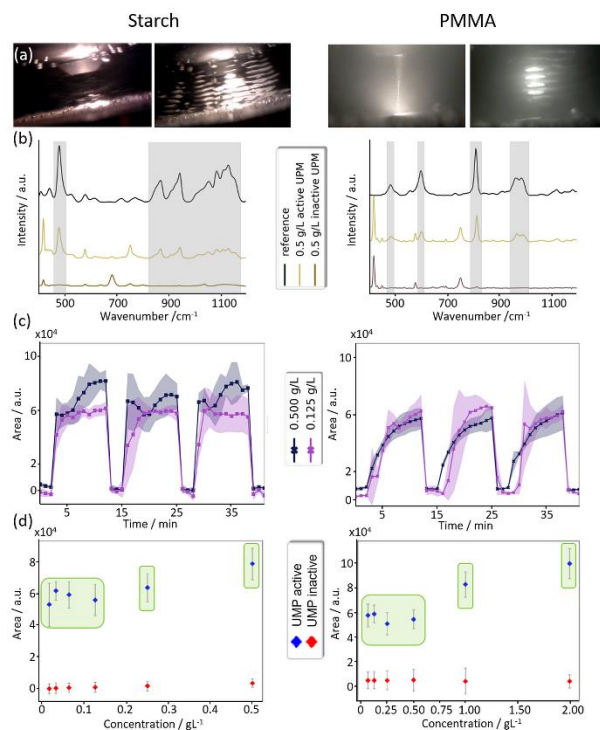
Figure 2. Two particle systems (starch and PMMA; primary difference is in particle size) were investigated with the parallel arrangement. (a) Video images with (right) and without (left) ultrasound particle manipulation (UPM), highlighting the effect of the primary axial radiation force on starch and PMMA particles, respectively. (b) Raman spectra of 0.5 g/L starch and PMMA extracted from phases with and without UPM are shown in comparison to a reference spectrum. Baseline-corrected spectra are normalized and offset for better comparison. (c) The integrated marker bands for two different concentrations of starch and PMMA as functions of time indicate different behaviors due to their different material properties (size, density). PMMA particles aggregate in the nodal planes more slowly than starch particles. Uncertainties are single standard deviations, indicated by the shaded, color-coded areas. (d) Six different concentrations of each particle system were investigated with (blue data points) and without (red data points) ultrasound. Statistically equal means/medians for ultrasound-active phases are framed in green.
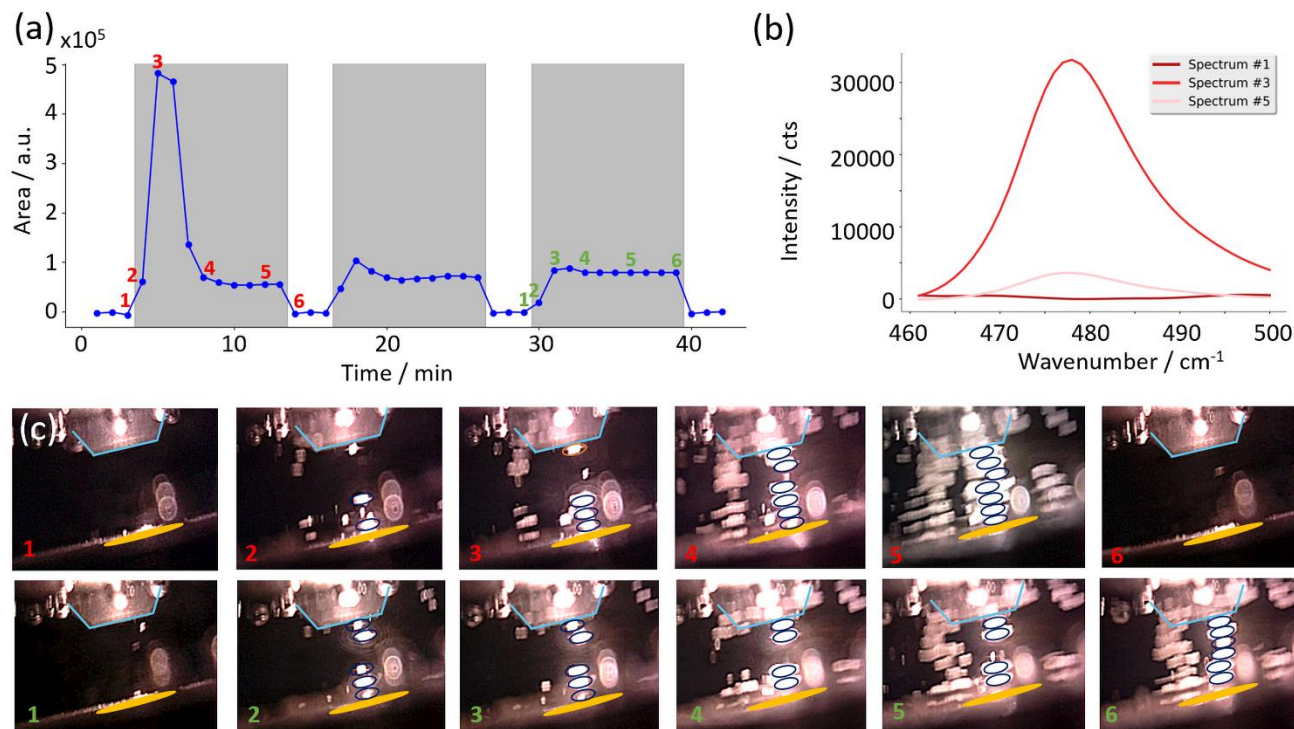
Figure 3. Ultrasound particle manipulation (UPM) of starch particles (0.031 g/L in a 500 mL vessel) using the parallel arrangement. (a) The intensity of the integrated starch marker band at 478 cm^{-1} (C–C–C bending, C–O torsion) increases significantly upon switching on the ultrasound (areas highlighted in grey) and drops to 0 as soon as the ultrasound is switched off. The first ultrasound-active phase (red numbers) differs from the following two phases. (b) As an example, the intensity of the starch marker band is shown for three different stages (1, 3, and 5) of the first ultrasound-active phase, as numbered in red in panel (a). (c) Video images of starch particles accumulating in the nodal planes of the ultrasound wave field with and without active UPM, corresponding to the numbered, color-coded events in panel (a), indicate different structures in the formation of the ultrasound standing wave field (images 2 and 3 colored in red and green) between the first and the following two ultrasound-active phases. The probe head is marked in light blue, the transducer is marked in yellow, and the particles in the nodal planes are marked in dark blue.

manually moving the cuvette in the y-direction. (b) Line scans along the y-axis with a step size of 50 µm with (blue) and without (red) active ultrasound particle manipulation (UPM). The Raman signal collected from particles in the nodal planes is significantly higher compared to the signal collected between nodal planes. Enlargement of the baseline shows that the PMMA-specific signal is higher in the stirred suspension without UPM compared to the Raman signal collected between nodal planes with UPM.

Figure 4. Experimental setup for test measurements with the Raman laser and ultrasonic wave propagation directions arranged perpendicularly. (a) Two piezoelectric elements acting as transducer and reflector are placed on opposite sides of a glass UV/Vis cuvette mounted on an xyz-stage. The PMMA particles agglomerated in the nodal planes of the ultrasonic standing wave field are moved in and out of the laser focus by

Figure 5. Ultrasound particle manipulation (UPM) of starch particles using the perpendicular arrangement. (a) The starch marker band at 478 cm^{-1} (C–C–C bending, C–O torsion) is clearly visible during UPM (spectra in the middle), while a flat line is recorded upon switching the ultrasound off (spectra on the left and right edge). (b) Video images of the acoustic resonator in front of the Raman probe with (images 2–4) and without (images 1 and 5) active UPM, corresponding to the numbered events in panel (c). (c) The starch marker band area increases significantly upon switching the ultrasound on (highlighted in grey), directly proportional to the intensity of scattered laser light in the video images, and drops upon switching the ultrasound off.
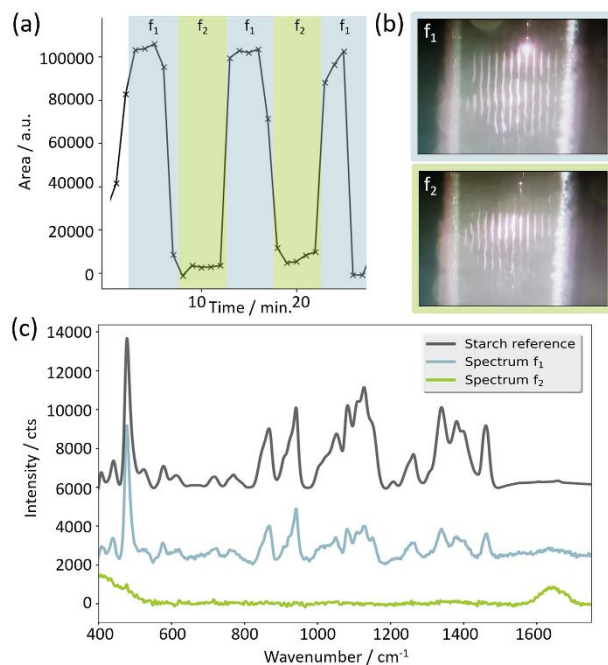
Figure 6. Starch particles are moved into and out of the laser focus point by changing the frequency of the ultrasonic waves in the kHz range. (a) The intensity of the integrated starch band [grey in panel (c)] changes significantly depending on the ultrasound frequency. (b) At f_1, the laser focus is on a nodal plane; accumulated starch particles are indicated by the bright point in the upper part of the image due to intense scattering effects. This intense scattering of the Raman laser is not observed when the laser is focused between nodal planes (f_2). (c) The selectivity based on the selected ultrasound frequency is reflected in the recorded Raman spectra, which carry starch-specific information for f_1 and lack the characteristic starch spectral fingerprint for f_2. Spectra are baseline corrected, scaled (1/40 of the intensity of the reference spectrum), and offset for better comparison.

For TOC only

9
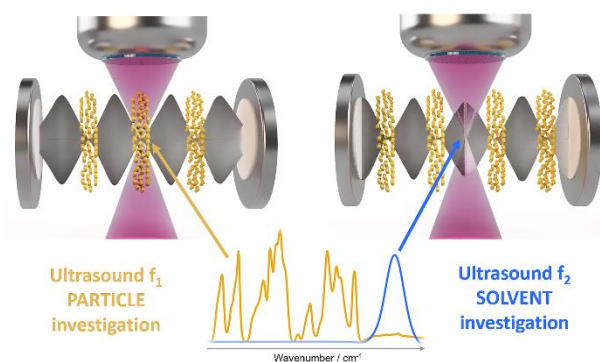
5.3   Publication III

Native Nano-electrospray Differential Mobility Analyzer (nES GEMMA) Enables Size Selection of Liposomal Nanocarriers Combined with Subsequent Direct Spectroscopic Analysis

Victur U. Weiss*, Karin Wieland*, Andreas Schwaighofer, Bernhard Lendl, Günter Allmaier; *Analytical Chemistry* 2019, 91, 3860-3868, 10.1021/acs.analchem.8b04252, CC-BY License (https://pubs.acs.org/page/policy/authorchoice_ccby_termsofuse.html)

*contributed equally

analytical chemistry

Article

ACS AuthorChoice

Native Nano-electrospray Differential Mobility Analyzer (nES GEMMA) Enables Size Selection of Liposomal Nanocarriers Combined with Subsequent Direct Spectroscopic Analysis

Victor U. Weiss,*,[†] Karin Wieland,[†] Andreas Schwaighofer, Bernhard Lendl, and Guenter Allmaier

Institute of Chemical Technologies and Analytics, Vienna University of Technology (TU Wien), A-1060 Vienna, Austria

S *Supporting Information*
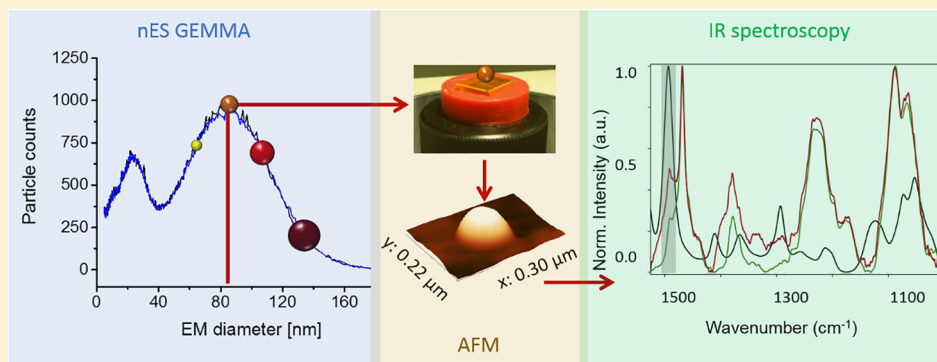
ABSTRACT: Gas-phase electrophoresis employing a nano-electrospray differential mobility analyzer (nES DMA), aka gas-phase electrophoretic mobility molecular analyzer (nES GEMMA), enables nanoparticle separation in the gas-phase according to their surface-dry diameter with number-based concentration detection. Moreover, particles in the nanometer size range can be collected after size selection on supporting materials. It has been shown by subsequent analyses employing orthogonal methods, for instance, microscopic or antibody-based techniques, that the surface integrity of collected analytes remains intact. Additionally, native nES GEMMA demonstrated its applicability for liposome characterization. Liposomes are nanometer-sized, biodegradable, and rather labile carriers (nanoobjects) consisting of a lipid bilayer encapsulating an aqueous lumen. In nutritional and pharmaceutical applications, these vesicles allow shielded, targeted transport and sustained release of bioactive cargo material. To date, cargo quantification is based on bulk measurements after bilayer rupture. In this context, we now compare capillary electrophoresis and spectroscopic characterization of vesicles in solution (bulk measurements) to the possibility of spectroscopic investigation of individual, size-separated/collected liposomes after nES GEMMA. Surface-dried, size-selected vesicles were collected intact on calcium fluoride (CaF$_2$) substrates and zinc selenide (ZnSe) prisms, respectively, for subsequent spectroscopic investigation. Our proof-of-principle study demonstrates that the off-line hyphenation of gas-phase electrophoresis and confocal Raman spectroscopy allows detection of isolated, nanometer-sized soft material/objects. Additionally, atomic force microscopy-infrared spectroscopy (AFM-IR) as an advanced spectroscopic system was employed to access molecule-specific information with nanoscale lateral resolution. The off-line hyphenation of nES GEMMA and AFM-IR is introduced to enable chemical imaging of single, i.e., individual, liposome particles.

Since its first appearance in literature,[1] gas-phase electrophoresis on a nES GEMMA (nano-electrospray gas-phase electrophoretic mobility molecular analysis) instrument has evolved to be a valuable tool for the characterization and analysis of a great variety of materials in the lower nanometer-size scale. nES GEMMA separates single-charged nanoparticles obtained from a nES process with subsequent charge equilibration. Analyte separation is based on the surface-dry nanoparticle size (electrophoretic mobility (EM) diameter) in a high laminar flow of dried air and a tunable electric field. By variation of the field strength, only particles of a certain EM diameter are capable to pass the size analyzer of the instrument toward a detector/collector. A corresponding setup (known as well as nES DMA, MacroIMS, ES SMPS, or LiquiScan ES) has

been shown to provide information for, e.g., proteins,[2,3] viruses and virus-like particles,[4,5] nanoparticles,[6–9] exosomes,[10] and liposomes.[11–13] Besides the information on surface-dry nanoparticle size with number-based concentration particle detection in accordance with the recommendation of the European Commission for nanoparticle analysis (2011/696/EU from October 18, 2011), a correlation between the EM diameter and the nanoparticle molecular weight based on well-defined standard material can be established. This correlation enables the assessment of the molecular weight of an analyte

based on its EM diameter as was shown by Bacher and colleagues for proteins in great detail in 2001.[2] In addition, even the molecular weight determination of larger proteinaceous complexes, for instance intact viruses, in a size and molecular weight range not easily accessible for classical mass spectrometric techniques[5] is possible. Conditions during the native nES process and gas-phase electrophoresis have recently been shown to be especially favorable for larger aggregates not even disrupting the noncovalent interactions between lectins and glycoproteins.[14]

In addition, nES GEMMA offers a size-selection step enabling the collection of nanoparticles of a defined size on flat surfaces for subsequent analysis via orthogonal methods. Electron microscopy of size-selected analytes was demonstrated, e.g., by Kallinger et al.[8] for silver nanoparticles and by Allmaier et al.[15] for tobacco mosaic virus. Likewise, atomic force microscopy (AFM) was successfully applied.[16] Furthermore, Havlik et al.[16] as well as Engel at al.[14] coupled nES GEMMA size separation off-line with dot blot analysis. Hence, it was demonstrated that nanoparticles remained identifiable for corresponding antibodies after gas-phase electrophoresis, proving that the surface structure of collected species was still intact after collection. Holder and Marr showed that silver nanoparticles can be directly sampled to cultured cells for subsequent cytotoxicity experiments.[17]

We now focus on the combination of nES GEMMA with spectroscopic techniques to gain additional, molecule-specific information on size-separated material in the nanometer-size range. Specifically, we use Raman and mid-infrared spectroscopy to perform chemical imaging of liposomes. In the methods, spectral features are evoked by molecular vibrations and can be assigned to specific functional groups. The spectrum represents the chemical fingerprint of the analyte, which is accessed in a direct, noninvasive way, providing information on chemical bonds as well as spatial arrangement and chemical interaction of molecules with the possibility of quantification.

Signal generation in Raman spectroscopy is based on an inelastic scattering process, i.e., the sample is illuminated with a short wavelength (VIS or NIR) light source and the light scattered off the sample contains additional wavelengths that are due to interaction with the sample. Given the short wavelength and using a confocal microscope, it should be possible to push the lateral resolution of Raman low enough to allow imaging of individual liposomes (here ~100 nm).

In contrast, infrared spectroscopy is based on an absorption process performed at wavelengths between 400 and 4000 cm^{-1} (mid-IR). The spatial resolution achievable with far-field mid-IR spectroscopy is diffraction-limited at 2−5 μm.[18,19] To achieve spatial resolution on the single-liposome scale, we employ a near-field detection technique based on photothermal induced resonance in an AFM cantilever. In short, the sample placed in an AFM is illuminated by a pulsed tunable infrared laser. Absorption of infrared radiation leads to rapid, local expansion of the absorber, which is transduced as a damped oscillation by the AFM cantilever positioned above the sample. This technique—called AFM-IR or photothermal induced resonance (PTIR)—has been demonstrated to give similar infrared spectra as far-field infrared spectroscopy, but with spatial resolutions down to 20 nm.[18,20] Increased signal sensitivity can be achieved using resonance-enhanced AFM-IR. Here, the repetition rate of the laser is set according to the frequency of the contact resonance of the AFM cantilever,

necessitating constant tracking thereof throughout the measurement.[20,21]

In our study we selected small unilamellar liposomes as model nanoparticle objects. These vesicles consist of a lipid bilayer encapsulating an aqueous volume. Hence, cargo compounds can be transported either in the lumen, the lipid bilayer, or the bilayer-associated layer according to the cargo hydrophobicity.[22] The cargo encapsulation efficiency of vesicles is usually assessed via chromatographic[23] or electrophoretic[24] assays. We employed capillary electrophoresis as well as spectroscopic bulk measurements prior to gas-phase electrophoresis to investigate cargo encapsulation. Subsequently, vesicles were size-separated/selected and collected on flat substrates to allow their microscopic and spectroscopic investigation. First, employing confocal Raman microscopy, we successfully demonstrated that Raman signals of liposomal structures collected on CaF$_2$ can be detected. However, facing limitations in signal sensitivity and lateral resolution (diffraction limit), in the second step, we opted for an advanced optical system to access chemical-specific information on individual liposomes beyond the diffraction limit. In our proof-of-principle study, we were able to show that AFM-IR is a promising method for destruction-free investigation of single, i.e., individual, nanocarriers, increasing the lateral resolution of obtained spectroscopic images. Our work indicates that off-line hyphenation of gas-phase electrophoresis and spectroscopy opens the avenue for thorough in-depth investigation of soft nanoparticle material in terms of size, shape, and chemical information. We believe that our method of off-line hyphenation will enable investigation of size-selected analytes from complex mixtures in the future, potentially resolving distributions of chemicals inside isolated nanocarriers.

■ MATERIALS AND METHODS

Additional detailed information on applied chemicals, liposome preparation, and instrumentation as well as sample preparation including AFM height maps of liposomes with different deposition methods can be found in the Supporting Information.

Liposome Preparation. In addition to liposomes similar to those employed in a previous study[12] (HSPC/Chol/DSPE-mPEG2000 in a 5.5:4.0:0.5 molar ratio, encapsulating a fluorophore at 10 μM concentration in 40 mM NH$_4$OAc, pH 8.4, from now on termed PEGylated liposomes), liposomes from HSPC/Chol/DSPE (5.7:3.8:0.5 molar ratio) were prepared according to the thin lipid film hydration technique.[25]

Instrumentation. Native nES GEMMA measurements were carried out on a TSI, Inc., instrument (Shoreview, MN, U.S.A.). It consists of a nES aerosol generator (model 3480) equipped with a ^{210}Po α-particle source, a nano differential mobility analyzer (nDMA) (model 3080) for separation, and a n-butanol-based ultrafine condensation particle counter (CPC) (model 3025A or model 3776C) for detection. A 25 μm inner diameter, fused silica capillary with a homemade tip[26] was used for generation of a stable Taylor cone. A fresh capillary was employed for each day of measurement to exclude cross-contamination. Liposomes were collected on calcium fluoride (CaF$_2$) or zinc selenide (ZnSe) prisms for subsequent AFM and spectroscopic imaging after particle passage through the nDMA and applying an electrostatic nanometer aerosol sampler (ENAS, model 3089, TSI, Inc.) at −3 to −3.1 kV
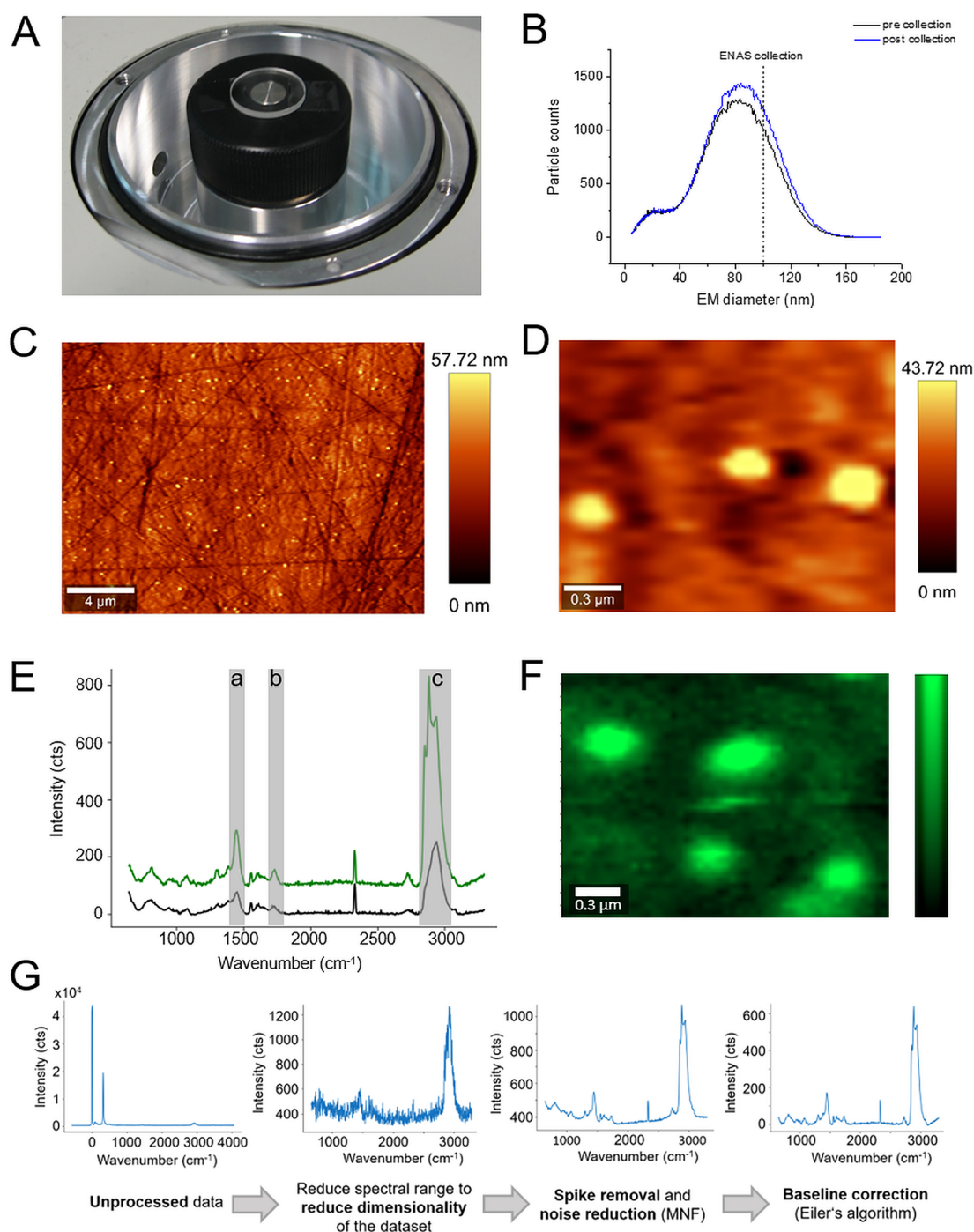
Figure 1. CaF_2 substrate was placed on top of the electrode in the ENAS unit of the nES GEMMA instrument (A) to size-select liposomes for Raman spectroscopy. After collection of intact liposomal nanocarriers at 100 nm EM diameter (B), the distribution of single vesicles was investigated via AFM height maps (C). The stability of the nES GEMMA instrument during particle collection is demonstrated by the very similar spectra measured prior to and after particle collection (B). A closer look at the AFM height map indicates elliptical structures on the substrate with a width between 200 and 250 nm and a height of 40−45 nm (D). Raman spectra collected on (green) and between (black) these elliptical structures show a similar spectral fingerprint but exhibit different signal intensity with the liposome signal (green) being significantly higher (E). The intensity distribution of the integrated CH stretching vibration ($\sim$2920 cm^{-1}) depicts similar structures as observed in the AFM height map; however, the elliptical structures in the Raman map are blurred and measure a width of 300−350 nm, indicating insufficient lateral resolution (F). Data processing scheme (G).

and 1.5 L per minute (Lpm) air flow for 120 min at 85 nm EM diameter.

A custom-made, 3D-printed holder was designed for stable ZnSe prism montage in the ENAS. Polylactic acid (PLA)-based fused deposition modeling (FDM) was employed using a self-built 3D printer with a nozzle diameter of 0.4 mm. Capillary electrophoresis was performed with an Agilent 3D CE instrument (Agilent Technologies, Waldbronn, Germany) employing 200 mM sodium borate, pH 8.4, as background electrolyte (BGE).

Nonencapsulated material was removed from vesicles via spin filtration.[9] On the basis of the weighed initial liposome amount (of a 10 μL volume) and the weighed liposome material after buffer exchange, a 1:10 [v/v] dilution of the initial stock (i.e., final 1 mM lipid concentration in samples) was achieved.

AFM measurements in contact mode (WITec AFM Arrow Cantilever reflex-coated: 0.2 N/m, 14 kHz) were performed of liposomes with and without encapsulated drug deposited on either ZnSe or CaF$_2$ substrates using a WITec alpha 300 RSA+ confocal microscope (Ulm, Germany). The microscope was equipped with a 20× magnification objective (Zeiss EC Epiplan, NA 0.4, Zeiss, Jena, Germany) and an internal cantilever drive mount. Project FIVE (WITec) and Gwyddion 2.44 software were used for subsequent data analysis.

A WITec alpha 300 RSA+ confocal Raman microscope equipped with a 488 nm excitation laser (DPSS laser, <50 mW, laser class 3B) was used for Raman imaging of liposomes. The laser was focused onto the sample through a 100× objective (Zeiss, NA 0.9). Backscattered photons were collected in reflection mode with the same objective, resulting in a lateral resolution of 220 nm based on the diffraction limit for confocal microscopes. The Stokes signal (anti-Stokes and Rayleigh light is removed via an edge filter) is detected with a fiber coupled spectrometer (UHTS 300 spectrometer VIS, f/4 300 mm focal length) equipped with a 600 grooves/mm grating (blaze wavelength = 500 nm) and a highly sensitive, thermoelectrically cooled electron-multiplying charged-coupled device (EMCCD) camera allowing a spectral resolution of 2−3 cm^{-1}. After nES GEMMA separation/collection on flat CaF$_2$ substrates (Raman grade, Crystran, Poole, U.K.), the sample was fixed on a piezo-stage on top of a motorized sample stage enabling a lateral positioning accuracy of <2 nm. Balancing signal intensity and thermal stress exerted onto the sample, Raman images were collected with a laser power of 43 mW and 1 s of integration time covering an area of 10 × 10 μm^2 with 50 nm step size in x- and y-direction. Control FOUR (WITec) software was used for data acquisition.

Raman images were processed (see Figure 1G) using ImageLab (Epina, Pressbaum, Austria). First, the data matrix was reduced by selecting the spectral range between 650 and 3290 cm^{-1} for each spectrum/pixel to reduce the dimensionality of the data cube and speed up calculation time for subsequent processing steps. After spike removal, maximum noise fraction (MNF, noise structure: horizontal stripes) was performed to reduce noise in the spectra. As a last step, the spectra were baseline-corrected using Eiler's algorithm ($\lambda = 10^5$, $p = 0.0020$, 7 iterations).[27]

AFM-IR measurements were performed using a NanoIR 1 system (Anasys Instruments, Santa Barbara, CA, U.S.A.) operated in bottom-up illumination equipped with a pulsed tunable IR source (MIRcat, Daylight Solutions, San Diego, CA, U.S.A.) covering the spectral range from 789 to 1763 cm^{-1}.

AFM-IR spectra were processed using Solo+MIA software (Eigenvector Research, Inc., Manson, WA, U.S.A., release 8.1.1). To increase the signal-to-noise ratio, Savitzky Golay smoothing (window size: 11, zeroth order polynomial) was applied before cutting the data set selecting the spectral range between 1200 and 1770 cm^{-1}. For better comparison, baseline-corrected spectra (Automatic Whittaker Filter: $\lambda = 1000$, $p = 0.000001$) were scaled between 0 and 1.

■ RESULTS AND DISCUSSION

Within the last few years, gas-phase electrophoresis on a native nES GEMMA instrument evolved as a valuable analysis method for the characterization of nanoparticle material. Especially the collection of size-selected material for subsequent analysis employing orthogonal methods enables in-depth nanoparticle characterization. Here, we focus on spectroscopic techniques to gain additional, molecule-specific information on size-separated material in the lower nanometer-size range (i.e., below 100 nm surface-dry EM particle diameter).

Native nES GEMMA Collection of Size-Selected Liposomes Followed by Their Raman Spectroscopic Investigation. Following our findings in 2016,[12,13] we investigated the collection of size-selected PEGylated liposomal vesicles on supporting materials suitable for subsequent spectroscopic analysis. The simplest approach for deposition of particles from suspensions on substrates would be dropping the sample solution onto the substrate and letting it dry in an unforced way at room temperature. This approach, however, does not allow homogeneous particle distribution on the substrate. Furthermore, fragile particles such as liposomes have the tendency to burst during the drying process (see Figure S1 of the Supporting Information). nES GEMMA, besides yielding information on the analyte size distribution and the particle number concentration, allows collection of particles from suspension in a dry and intact form and offers additional features such as a customizable particle distribution density on the substrate and a size-selection step. For initial AFM and Raman measurements, we opted for vesicles similar in lipid composition and cargo material to those originally analyzed via nES GEMMA. Infrared microscopy with a lateral resolution of roughly 5 μm[18,19] is not applicable to spatially resolve individual PEGylated liposomes, which are in the size range of roughly 200 nm once collected on a substrate (see below). Therefore, because the diffraction limit is directly proportional to the wavelength of the emitting light source, we opted for confocal Raman spectroscopy/imaging. Corresponding laser sources emit light in the visible region with a lateral resolution of 220 nm for a confocal system with 488 nm laser excitation wavelength and 100× magnification (NA = 0.9). CaF$_2$ was used as supporting material (Figure 1A) because it exhibits a flat baseline in the spectral region of interest.[28,29] Native nES GEMMA spectra were collected prior to and post sample collection to check for stability of the system (Figure 1B). Prior to spectroscopic analysis, AFM images of PEGylated liposomes on CaF$_2$ with a sampling diameter of 100 nm (EM diameter) were recorded (i) to investigate the spatial distribution of the PEGylated liposomes on the substrate and (ii) to check if PEGylated liposomes were collected in an intact form on the substrate. Once PEGylated liposomes are collected on the substrate, their original spherical shape in solution changes to an ellipsoid one upon contact with the solid sample support. A width of ∼200−250 nm and a height in the range of 25−35 nm (Figure 1C and D) as detected via AFM lead to a particle volume of collected vesicles similar to values obtained for liposomes in the gas/liquid phase. Besides vesicle/substrate interaction, this deformation also results from the force exerted by the AFM tip. Investigation by Raman spectroscopy of the particles successfully revealed typical bands evoked by lipids such as the CH stretching vibration at ∼2920 cm^{-1}, the C=O stretching vibration at 1740 cm^{-1}, or the CH$_2$
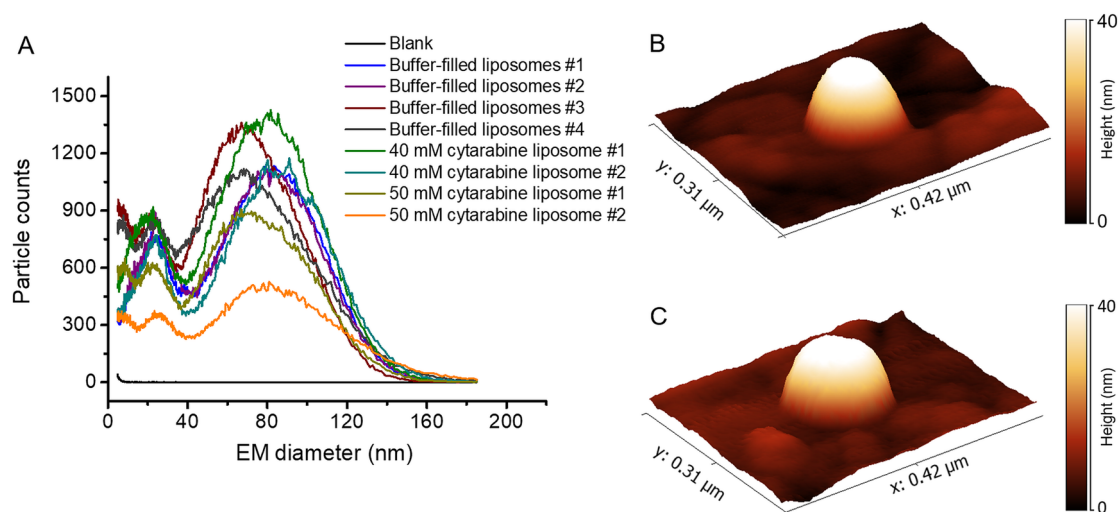
Figure 2. Native nES GEMMA data (A) of buffer-filled as well as cytarabine-encapsulating liposomes. No significant difference between these two vesicle types is detectable. This finding was also corroborated by AFM results in contact mode of buffer-filled liposomes (B) as well as vesicles encapsulating cytarabine cargo (C, preparation of vesicles in 40 mM cytarabine solution).
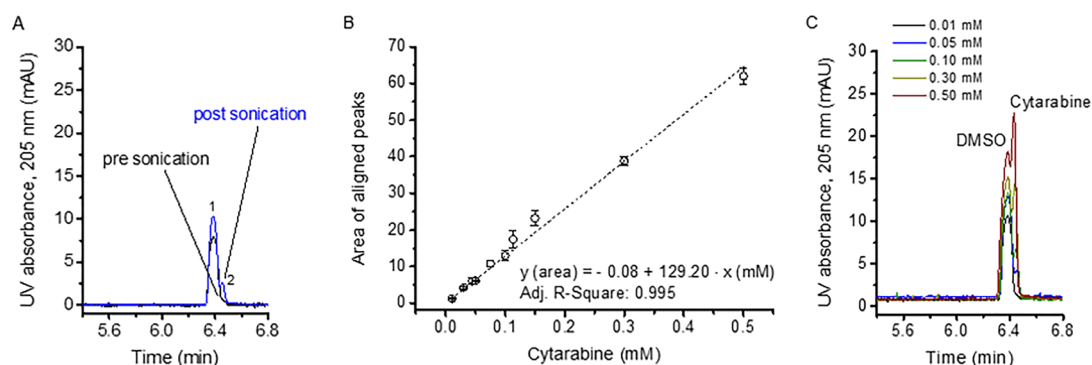
Figure 3. Amount of cytarabine encapsulated in vesicles being released upon liposome sonication (A) was determined via correlation of the analyte concentration and the obtained peak area (B) by measurement of cytarabine standards (C). CE with UV absorption detection at 205 nm was employed. Peak 1 corresponds to dimethylsulfoxide (DMSO) employed as internal standard, and peak 2 corresponds to cytarabine.

deformation vibration at 1440 cm^{-1}.[30] The intensity distribution of the integrated CH stretching vibration (2821 to 3056 cm^{-1}) as the most intense band in the Raman spectrum (Figure 1E) indicates that ellipsoid structures are indeed detected based on their lipid-specific spectral fingerprint. However, (i) the structures seem blurred and measure 300−350 nm in width, which is significantly broader than in AFM images of the same sample. Hence, while we successfully verify via AFM that only single liposomes are present on the substrate, chemical differences within a single liposome cannot be measured spectroscopically due to the diffraction limit of confocal Raman spectroscopy. Also, (ii) a very similar spectral fingerprint—although with significantly lower intensity—could be recorded from areas between PEGylated liposomes (black spectrum in Figure 1E). These two observations are most likely attributed to insufficient lateral resolution of the employed spectroscopic method. Furthermore, (iii) the original spectra of PEGylated liposomes before the processing steps show poor signal-to-noise ratios in the range of 2−6 (Figure 1G). (iv) We used CaF$_2$ as substrate for Raman spectroscopy, even though the surface of the substrate is rough, making it less suitable for AFM investigations. Considering that we ultimately want to develop a method that allows detection of the encapsulated cargo at even lower concentration compared to the lipid

vesicles, Raman spectroscopy appears not to offer this possibility in terms of signal sensitivity and lateral resolution at the moment. Hence, we assessed the applicability of another spectroscopic method for our purpose and at the same time adapted the liposome system from our initial study[12,13] to a vesicle system encapsulating a chemotherapeutic drug.

Preparation and Characterization of Drug-Loaded Liposomes. For investigation of liposomes encapsulating a pharmacologically active compound, we opted for cytarabine—also known as cytosine arabinoside (ara-C) or 1β-arabinofuranosylcytosine. Cytarabine, employed, e.g., for leukemia treatment, was FDA approved already in April 1999. Only recently, a novel combination of cytarabine and daunorubicin in liposomes has been reported for treatment of acute myeloid leukemia with a corresponding pharmacological investigation published in 2018.[31]

After preparation, liposomes were analyzed via gas-phase electrophoresis on a nES GEMMA instrument according to an already established protocol.[12,13] Our analysis yielded liposome preparations with vesicles of 78.4 ± 6.5 nm surface-dry particle diameter at the peak apex and an average full peak width of 66.9 ± 7.3 nm at half peak height (Figure 2A). Note that filling of liposomes with cytarabine cargo had no impact on the vesicle appearance upon nES GEMMA analysis—vesicles were
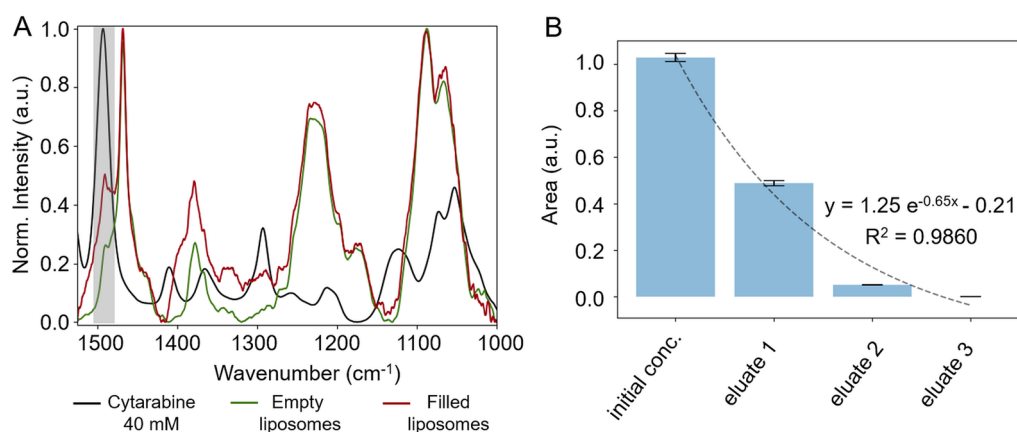
Figure 4. FTIR spectra of liposomes in plain buffer or encapsulating cytarabine measured in a transmission flow cell after exchange of nonencapsulated buffer material. For comparison, the FTIR spectrum of 40 mM cytarabine is shown. Cytarabine can be detected at 1494 cm^{-1} (highlighted in gray) besides signals originating from lipids (A). Removal of nonencapsulated cytarabine during spin-filtration can be followed by FTIR measurements (B).

prepared in the absence as well as in the presence of 40 and 50 mM cytarabine, respectively. Likewise, AFM data corroborates this finding (Figure 2B and C). Despite differences in obtained nanoparticle height and width values and their respective standard deviations (probably due to interactions of the AFM tip with soft matter analytes, i.e., liposomes, especially for vesicles not filled with corresponding cargo molecules), similar values for vesicle dimensions were obtained: buffer-filled liposomes (Figure 2B) were 160 ± 59 nm in width and 36 ± 15 nm in height (*n* = 20 individual particles), whereas vesicles encapsulating cytarabine (Figure 2C) were 158 ± 26 nm in width and 26 ± 10 nm in height (*n* = 21 individual particles).

It is of note that, in order to remove nonencapsulated cytarabine from individual preparations, vesicles were subjected to spin filtration.[9] Despite this purification step, still some low EM diameter material was detectable for our preparations; this material previously was assigned to unspecific aggregates of material employed during the vesicle-formation process, possibly lipid micelles or similar.[12,13] However, in relation to the main vesicle peak at 78.4 ± 6.5 nm EM diameter, the amount of this smaller-sized material seemed negligible for the experiments presented in this work (note, however, that the low EM diameter material had been shown to influence cell viability in a previous study).[12]

Applying capillary electrophoresis (CE) to such preparations after desalting allowed us to subsequently assess the amount of the encapsulated drug within vesicles similar to studies found in the literature.[32,33] CE of cytarabine-containing vesicles after desalting did not yield a peak for cytarabine (Figure 3A). Only after sonication, which had already been shown to disrupt vesicles and to release the vesicle cargo as seen due to the increase of smaller-sized sample components,[13] significant amounts of the employed drug were detectable (Figure 3A). Comparing the obtained peak area to the correlation between peak areas and sample concentrations of cytarabine standards with known analyte concentration (Figure 3B, at least *n* = 2 measurements per data point) analyzed via CE (Figure 3C) allows calculation of the analyte concentration within vesicles based on the following simplifications and assumptions: (i) 80 nm surface-dry liposome particle diameter as found approximately upon native nES GEMMA analysis of a corresponding sample (Figure 1), (ii) 10 mM overall lipid concentration

based on the lipid amount employed in the vesicle-preparation process, (iii) the molar lipid ratio, and (iv) a phospholipid headgroup projected area of ~0.7 nm^2 for phosphatidylcholine (PC),[34] 0.6 nm^2 for phosphatidylethanolamine (PE),[35] and 0.4 nm^2 for cholesterol.[36] Combining these numbers, a liposome concentration of ~40 nM was determined. Taking into account this value as well as the volume of corresponding spheres based on approximation of the surface-dry particle diameter, a total liposome volume of ~6 mL/L solution was obtained. Relating the liposome volume to the increase of analyte concentration upon vesicle sonication (~0.04 mM) yielded the concentration of cytarabine inside vesicles (~5 mM for various liposome preparations).

In a next step, we performed bulk Fourier transform infrared (FTIR) measurements of liposomes encapsulating cargo molecules. Employing a flow cell setup for transmission FTIR measurements, we successfully identified a characteristic band (evoked by C=C and C=N stretch vibrations[37]) for the detection of cytarabine in solution at 1494 cm^{-1} (Figure 4A). This characteristic band even allowed us to follow the removal of nonencapsulated cytarabine via spin-filtration by measurement of solutions that had passed the spin-filter membrane (Figure 4B). From the first to the second spin-filtration step (eluate 1 vs eluate 2), a significant reduction in cytarabine content of the eluate is demonstrated, indicating that most of the nonencapsulated cytarabine is removed in the first spin filtration step. Nevertheless, a second washing step is necessary because cytarabine can still be detected by transmission FTIR spectroscopy after the second spin-filtration step, whereas no cytarabine was detectable after the third spin-filtration (eluate 3), proving successful removal of nonencapsulated cytarabine. This also means that any cytarabine signal detectable with FTIR spectroscopy of liposomes after spin-filtration is most certainly evoked by cytarabine vibrations inside the nano-carrier. Furthermore, as depicted by the small band at 1494 cm^{-1} in Figure 4A, besides IR bands that can be related to lipid building blocks, cytarabine is detectable in samples containing vesicle-encapsulated cargo after spin-filtration. After calculating the difference spectrum of filled and empty liposomes, the concentration of encapsulated cytarabine can be estimated based on the area ratio of the characteristic cytarabine band in the difference spectrum and the FTIR spectrum of 40 mM cytarabine. Hence, a cytarabine concentration of roughly 1
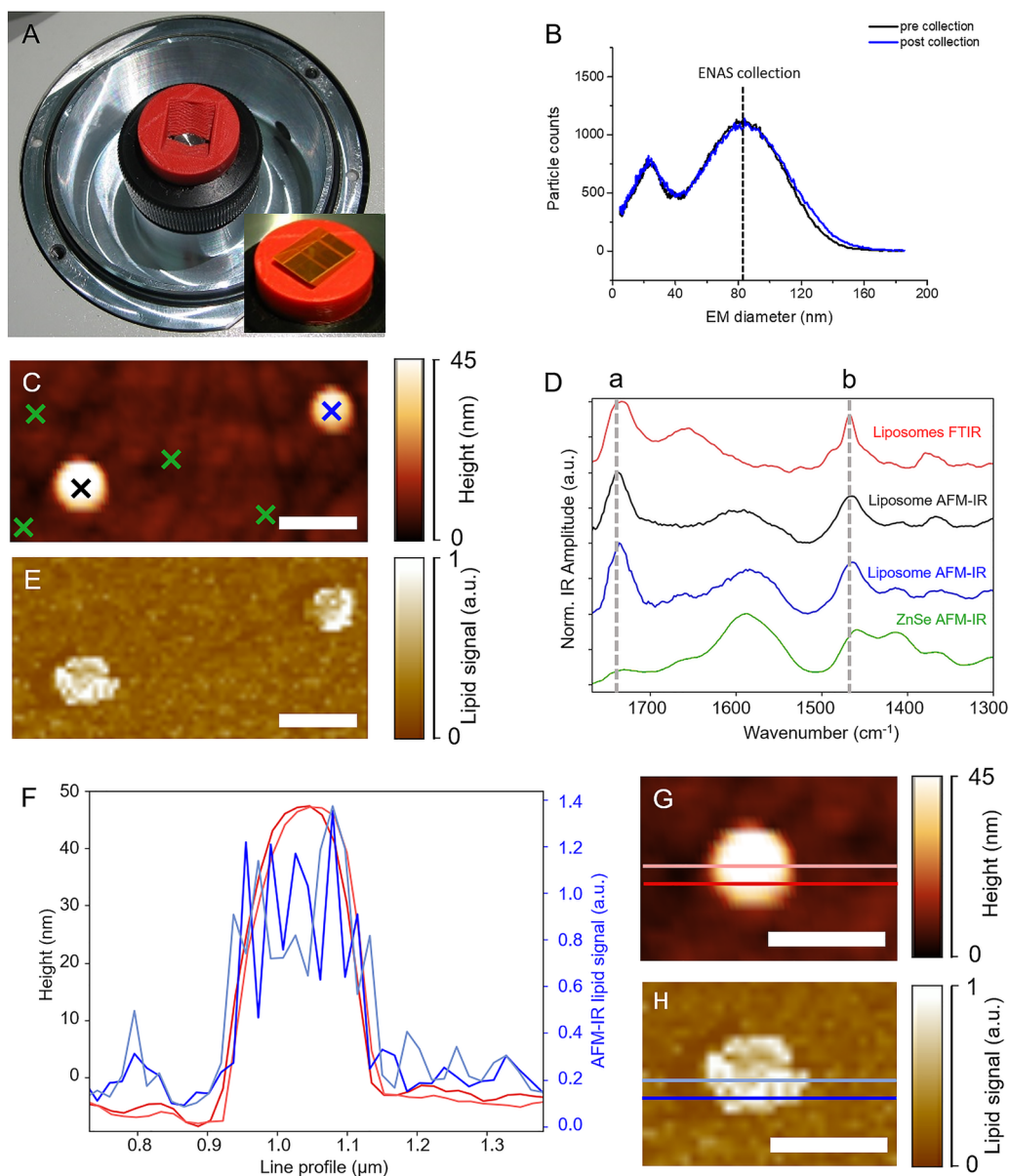
Figure 5. AFM-IR spectroscopy of individual, size-selected liposomes collected on ZnSe prisms. Application of a 3D-printed support enabled positioning of prisms in the nES GEMMA ENAS unit (A). Liposomes were size-collected at 85 nm EM diameter from a liposome batch with heterogeneous size distribution. No significant differences in obtained spectra prior to and after size collection were detected (B). Single liposomes were selected based on the AFM height map depicting structures with a width of ~150 nm and a height of 45−50 nm (C). AFM-IR spectra of individual liposomes with buffer as encapsulated cargo collected on positions indicated by color-coded crosses (e.g., blue cross in (C) corresponds to blue spectrum in (D)) in (C) are in good agreement with far-field FTIR-ATR spectra (red) of the same sample system. Typical vibrational bands such as (a) the carbonyl band at 1735 cm^{-1} or (b) the CH$_2$ deformation vibration at 1467 cm^{-1} evoked by lipids are marked by the dashed gray line. Spectra are normalized and offset for clarity (D). Tuning the laser to the carbonyl band (1735 cm^{-1}) results in a map depicting the spatial distribution of lipids with 17.5 nm step size in *x*- and *y*-direction (E). The lipid signal was referenced to the SiO$_2$ cantilever signal for reasons of better visualization. Line profiles (F) taken from the height map of a single liposome (G) compared to the lipid signal of the same liposome (H) outline that AFM-IR imaging provides sufficient lateral resolution to resolve a single liposome. The scale bar is 250 nm.

mM was determined that is in good agreement with the results obtained by CE measurements (roughly 5 mM). However, like CE, the application of this spectroscopic setup only allows bulk measurements; hence, only a calculated average drug concentration per liposomal vesicle can be obtained.

To conclude, gas-phase electrophoretic analysis for collection of size-selected cytarabine-filled vesicles in an intact form was demonstrated. The size and shape of isolated liposomes were investigated by AFM measurements. CE measurements confirmed that liposomes encapsulating cytar-

abine were successfully prepared, which was additionally verified by FTIR measurements. However, all these methods yielded information on the carrier itself or bulk analysis of the chemotherapeutic drug in general—no information on encapsulation efficiency and the cargo content of individual nanocarriers was obtainable.

Spectroscopic Investigation of Single Liposomal Nanocarriers. On the basis of our Raman spectroscopy results, we wanted to improve our method in terms of lateral resolution, signal sensitivity, and AFM image quality. In doing

so, we opted for resonance-enhanced AFM-IR spectroscopy promising a lateral resolution of 20 nm and a signal sensitivity that allows monolayer detection.[38,39]

In terms of substrate, we opted for ZnSe prisms as supporting material due to their good spectroscopic characteristics as well as surface smoothness necessary for AFM analysis. A ZnSe prism support was 3D-printed, allowing for prisms to be placed into the nES GEMMA ENAS unit. The 3D-printed support was fixed in the ENAS unit via double-sided tape, and the ZnSe prism was placed in the printed cavity without any additional support. An opening in the bottom of the 3D-printed support allowed contact between the electrode of the ENAS unit and the ZnSe prisms (Figure 5A).

Liposomes filled with buffer were collected at 85 nm EM diameter on ZnSe substrates. To check for stability of the nES GEMMA system, spectra prior to and post sampling were recorded and compared (Figure 5B). No significant differences between these two spectra could be observed, indicating a stable collection of particles over time.

Following ENAS collection, AFM analysis of collected vesicles was performed. After microscopic determination of the position of a vesicle on the ZnSe surface (Figure 5C), AFM-IR spectra were collected of individual liposomes with a collection diameter of roughly 100 nm (Figure 5D). Comparison of the near-field IR spectra with far-field FTIR-ATR spectra of the identical liposomal drug-delivery system shows that the spectra correspond well with each other. Both methods show characteristic bands evoked by molecule-specific vibrations of lipids such as the carbonyl band at 1735 cm^{-1} or the CH_2 deformation vibration at 1467 cm^{-1} wavenumbers.[40,41] Additionally, AFM-IR spectra of the ZnSe substrate were collected on different positions between single liposomes (Figure 5D). The average spectrum of four different measurement positions is depicted in Figure 5D and—compared to the AFM-IR spectra of single liposomes—does not exhibit any characteristic lipid bands. The AFM-IR map of the lipid signal (Figure 5E and H) indicates a similar shape as the height map of the same liposome (Figure 5C and G). For better visualization, the lipid AFM-IR signal was referenced to an internal standard (SiO_2 signal of the cantilever recorded at 1260 cm^{-1}). To demonstrate the lateral resolution that can be achieved with AFM-IR imaging, profile lines of the height image and the lipid map of the same liposome were compared (Figure 5F), highlighting the ability of AFM-IR to spatially resolve an individual, single liposome. Both maps show sharp features at the edge of the liposome and indicate the same liposome width of roughly 200 nm.

Identical collection and analysis steps were repeated for liposomes filled with cytarabine. However, so far, we have not been able to identify the encapsulated cargo based on the AFM-IR signal. This might be improved using a different geometric arrangement in the sample-light interaction. In the setup used in this work, the IR laser is focused onto the sample via bottom illumination. A higher AFM-IR signal intensity is to be expected using the top illumination arrangement, which would allow increased signal intensity due to the possibility of plasmonic enhancement using gold-coated tips and substrates. We concentrate on this setup in another study.[42]

To conclude, we were able to collect the spectral fingerprint of size-selected single liposomes employing AFM-IR spectroscopy. Nevertheless, despite our advance in lateral resolution upon switching from Raman to AFM-IR spectroscopy, we were still not able to extract spectroscopic information on the encapsulated cargo material inside liposomal vesicles.

CONCLUSIONS

With the current work we focus on the collection of liposomes after size-separation on a nES GEMMA instrument on a suitable analyte support for subsequent spectroscopic characterization. Prior to gas-phase electrophoresis, deployed liposomes were characterized via CE, AFM, and FTIR spectroscopy, especially concerning their encapsulated cargo in bulk measurements. Going one step further, we intended to access similar information but from individual nanocarriers. For this purpose, collection of size-selected, individual liposomal vesicles followed by spectroscopy-based identification of single nanocarriers was shown based on the application of our native nES GEMMA/spectroscopy off-line hyphenation.

Using Raman spectroscopy, we are able to demonstrate spectroscopy of individual liposomes. While the lateral resolution of confocal Raman microscopy per se is not sufficient to resolve individual liposomes, AFM microscopy can be used to ensure that only individual liposomes are evaluated. The combination of native nES GEMMA with AFM-IR spectroscopy is shown to give access to chemical information on single, nanosized vesicles. For both techniques, further improvements can be envisioned, such as using surface-enhanced Raman effects to improve the confocal Raman signal or using plasmonic enhancement in top illumination for AFM-IR.[38]

To conclude, native nES GEMMA/AFM-IR spectroscopy off-line hyphenation has been demonstrated to be a promising approach for label-free, nondestructive investigation of nanocarriers with sufficient nanoscale lateral resolution. We believe that, especially for drug as well as other bioactive ingredient-delivery nanoparticles in pharmaceutical, cosmetic, and food applications or naturally occurring material, e.g., exosomes, the noninvasive characterization of material via spectroscopic methods will yield valuable additional information on analytes.

ASSOCIATED CONTENT

Ⓢ Supporting Information

The Supporting Information is available free of charge on the ACS Publications website at DOI: 10.1021/acs.analchem.8b04252.

> Chemicals, liposome preparation, native nES GEMMA measurements, CE measurements, buffer exchange of samples, instrumentation, and AFM height maps (PDF)

AUTHOR INFORMATION

Corresponding Author
*E-mail: victor.weiss@tuwien.ac.at. Tel.: +43 1 58801 151611. Fax: +43 1 58801 16199.

ORCID ⊙
Victor U. Weiss: 0000-0002-0056-6819
Andreas Schwaighofer: 0000-0003-2714-7056

Author Contributions

†V.U.W. and K.W. contributed equally to the manuscript. Initial idea: V.U.W., G.A., B.L.; liposome preparation, nES GEMMA, and CE measurements: V.U.W.; spectroscopic and AFM measurements: K.W., A.S.; instrumentation: G.A., B.L.; funding: B.L., G.A., V.U.W.; guidance: G.A., B.L.; all authors contributed to the manuscript.

■ REFERENCES

(1) Kaufman, S. L.; Skogen, J. W.; Dorman, F. D.; Zarrin, F.; Lewis, K. C. *Anal. Chem.* **1996**, *68* (11), 1895−904.

(2) Bacher, G.; Szymanski, W. W.; Kaufman, S. L.; Zollner, P.; Blaas, D.; Allmaier, G. *J. Mass Spectrom.* **2001**, *36* (9), 1038−52.

(3) de la Mora, J. F.; Ude, S.; Thomson, B. A. *Biotechnol. J.* **2006**, *1* (9), 988−97.

(4) Kaddis, C. S.; Lomeli, S. H.; Yin, S.; Berhane, B.; Apostol, M. I.; Kickhoefer, V. A.; Rome, L. H.; Loo, J. A. *J. Am. Soc. Mass Spectrom.* **2007**, *18* (7), 1206−16.

(5) Weiss, V. U.; Bereszcazk, J. Z.; Havlik, M.; Kallinger, P.; Gosler, I.; Kumar, M.; Blaas, D.; Marchetti-Deschmann, M.; Heck, A. J.; Szymanski, W. W.; Allmaier, G. *Anal. Chem.* **2015**, *87* (17), 8709−17.

(6) Dudkiewicz, A.; Wagner, S.; Lehner, A.; Chaudhry, Q.; Pietravalle, S.; Tiede, K.; Boxall, A. B.; Allmaier, G.; Tiede, D.; Grombe, R.; von der Kammer, F.; Hofmann, T.; Molhave, K. *Analyst* **2015**, *140* (15), 5257−67.

(7) Hinterwirth, H.; Wiedmer, S. K.; Moilanen, M.; Lehner, A.; Allmaier, G.; Waitz, T.; Lindner, W.; Laemmerhofer, M. *J. Sep Sci.* **2013**, *36* (17), 2952−61.

(8) Kallinger, P.; Weiss, V. U.; Lehner, A.; Allmaier, G.; Szymanski, W. W. *Particuology* **2013**, *11* (1), 14−19.

(9) Weiss, V. U.; Lehner, A.; Kerul, L.; Grombe, R.; Kratzmeier, M.; Marchetti-Deschmann, M.; Allmaier, G. *Electrophoresis* **2013**, *34* (24), 3267−76.

(10) Chernyshev, V. S.; Rachamadugu, R.; Tseng, Y. H.; Belnap, D. M.; Jia, Y.; Branch, K. J.; Butterfield, A. E.; Pease, L. F., 3rd; Bernard, P. S.; Skliar, M. *Anal. Bioanal. Chem.* **2015**, *407* (12), 3285−301.

(11) Epstein, H.; Afergan, E.; Moise, T.; Richter, Y.; Rudich, Y.; Golomb, G. *Biomaterials* **2006**, *27* (4), 651−9.

(12) Urey, C.; Weiss, V. U.; Gondikas, A.; von der Kammer, F.; Hofmann, T.; Marchetti-Deschmann, M.; Allmaier, G.; Marko-Varga, G.; Andersson, R. *Int. J. Pharm.* **2016**, *513* (1−2), 309−318.

(13) Weiss, V. U.; Urey, C.; Gondikas, A.; Golesne, M.; Friedbacher, G.; von der Kammer, F.; Hofmann, T.; Andersson, R.; Marko-Varga, G.; Marchetti-Deschmann, M.; Allmaier, G. *Analyst* **2016**, *141* (21), 6042−6050.

(14) Engel, N. Y.; Weiss, V. U.; Marchetti-Deschmann, M.; Allmaier, G. *J. Am. Soc. Mass Spectrom.* **2017**, *28* (1), 77−86.

(15) Allmaier, G.; Laschober, C.; Szymanski, W. W. *J. Am. Soc. Mass Spectrom.* **2008**, *19* (8), 1062−8.

(16) Havlik, M.; Marchetti-Deschmann, M.; Friedbacher, G.; Winkler, W.; Messner, P.; Perez-Burgos, L.; Tauer, C.; Allmaier, G. *Anal. Chem.* **2015**, *87* (17), 8657−64.

(17) Holder, A. L.; Marr, L. C. *BioMed Res. Int.* **2013**, *2013*, 328934.

(18) Dazzi, A.; Prater, C. B.; Hu, Q.; Chase, D. B.; Rabolt, J. F.; Marcott, C. *Appl. Spectrosc.* **2012**, *66* (12), 1365−84.

(19) Nasse, M. J.; Walsh, M. J.; Mattson, E. C.; Reininger, R.; Kajdacsy-Balla, A.; Macias, V.; Bhargava, R.; Hirschmugl, C. J. *Nat. Methods* **2011**, *8* (5), 413−416.

(20) Centrone, A. *Annu. Rev. Anal. Chem.* **2015**, *8*, 101−26.

(21) Ramer, G.; Reisenbauer, F.; Steindl, B.; Tomischko, W.; Lendl, B. *Appl. Spectrosc.* **2017**, *71* (8), 2013−2020.

(22) Gomez-Hens, A.; Fernandez-Romero, J. M. *TrAC, Trends Anal. Chem.* **2005**, *24* (1), 9−19.

(23) Xuan, T.; Zhang, J. A.; Ahmad, I. *J. Pharm. Biomed. Anal.* **2006**, *41* (2), 582−8.

(24) Franzen, U.; Nguyen, T. T.; Vermehren, C.; Gammelgaard, B.; Ostergaard, J. *J. Pharm. Biomed. Anal.* **2011**, *55* (1), 16−22.

(25) Bangham, A. D.; Standish, M. M.; Watkins, J. C. *J. Mol. Biol.* **1965**, *13* (1), 238−52.

(26) Tycova, A.; Prikryl, J.; Foret, F. *Electrophoresis* **2016**, *37* (7−8), 924−30.

(27) Eilers, P. H. C.; Boelens, H. F. M. *Baseline Correction with Asymmetric Least Squares Smoothing*; **2005**.

(28) Wieland, K.; Kuligowski, J.; Ehgartner, D.; Ramer, G.; Koch, C.; Ofner, J.; Herwig, C.; Lendl, B. *Appl. Spectrosc.* **2017**, *71* (12), 2661−2669.

(29) Schuster, K. C.; Reese, I.; Urlaub, E.; Gapes, J. R.; Lendl, B. *Anal. Chem.* **2000**, *72* (22), 5529−34.

(30) Huang, W. E.; Li, M.; Jarvis, R. M.; Goodacre, R.; Banwart, S. A. *Adv. Appl. Microbiol.* **2010**, *70*, 153−86.

(31) Nikanjam, M.; Capparelli, E. V.; Lancet, J. E.; Louie, A.; Schiller, G. *Cancer Chemother. Pharmacol.* **2018**, *81* (1), 171−178.

(32) Chen, D.; Cole, D. L.; Srivatsa, G. S. *J. Pharm. Biomed. Anal.* **2000**, *22* (5), 791−801.

(33) Perjesi, P.; Kim, T.; Zharikova, A. D.; Li, X.; Ramesh, T.; Ramasubbu, J.; Prokai, L. *J. Pharm. Biomed. Anal.* **2003**, *31* (5), 929−35.

(34) Dickey, A.; Faller, R. *Biophys. J.* **2008**, *95* (6), 2636−46.

(35) Murzyn, K.; Rog, T.; Pasenkiewicz-Gierula, M. *Biophys. J.* **2005**, *88* (2), 1091−103.

(36) Edholm, O.; Nagle, J. F. *Biophys. J.* **2005**, *89* (3), 1827−32.

(37) El-Subbagh, H. I.; Al-Badr, A. A. Chapter 2—Cytarabine. In *Profiles of Drug Substances, Excipients and Related Methodology*; Brittain, H. G., Ed.; Academic Press: 2009; Vol. 34, pp 37−113.

(38) Lu, F.; Jin, M. Z.; Belkin, M. A. *Nat. Photonics* **2014**, *8* (4), 307−312.

(39) Ramer, G.; Aksyuk, V. A.; Centrone, A. *Anal. Chem.* **2017**, *89* (24), 13524−13531.

(40) Lewis, R. N. A. H.; Mcelhaney, R. N.; Pohle, W.; Mantsch, H. H. *Biophys. J.* **1994**, *67* (6), 2367−2375.

(41) Movasaghi, Z.; Rehman, S.; ur Rehman, I. *Appl. Spectrosc. Rev.* **2008**, *43* (2), 134−179.

(42) Wieland, K.; Ramer, G.; Weiss, V. U.; Allmaier, G.; Lendl, B.; Centrone, A. *Nano Res.* **2019**, *12* (1), 197−203.

5.4   Publication IV

Nanoscale Chemical Imaging of Individual, Chemotherapeutic Cytarabine-Loaded Liposomal Nanocarriers

Karin Wieland, Georg Ramer, Victor U. Weiss, Günter Allmaier, Bernhard Lendl, Andrea Centrone; Nano Research 2019, 12, 197-203

Nanoscale chemical imaging of individual chemotherapeutic cytarabine-loaded liposomal nanocarriers

Karin Wieland[1], Georg Ramer[2,3], Victor U. Weiss[4], Guenter Allmaier[4], Bernhard Lendl[1], and Andrea Centrone[2] (✉)

[1] Institute of Chemical Technologies and Analytics, Research Division Environmental, Process Analytics and Sensors, TU Wien, Vienna 1060, Austria
[2] Center for Nanoscale Science and Technology, National Institute of Standards and Technology, Gaithersburg, MD 20899, USA
[3] Institute for Research in Electronics and Applied Physics, University of Maryland, College Park, MD 20742, USA
[4] Institute of Chemical Technologies and Analytics, Research Division Instrumental and Imaging Analytical Chemistry, TU Wien, Vienna 1060, Austria

ABSTRACT

Dosage of chemotherapeutic drugs is a tradeoff between efficacy and side-effects. Liposomes are nanocarriers that increase therapy efficacy and minimize side-effects by delivering otherwise difficult to administer therapeutics with improved efficiency and selectivity. Still, variabilities in liposome preparation require assessing drug encapsulation efficiency at the single liposome level, an information that, for non-fluorescent therapeutic cargos, is inaccessible due to the minute drug load per liposome. Photothermal induced resonance (PTIR) provides nanoscale compositional specificity, up to now, by leveraging an atomic force microscope (AFM) tip contacting the sample to transduce the sample's photothermal expansion. However, on soft samples (e.g., liposomes) PTIR effectiveness is reduced due to the likelihood of tip-induced sample damage and inefficient AFM transduction. Here, individual liposomes loaded with the chemotherapeutic drug cytarabine are deposited intact from suspension via nano-electrospray gas-phase electrophoretic mobility molecular analysis (nES-GEMMA) collection and characterized at the nanoscale with the chemically-sensitive PTIR method. A new tapping-mode PTIR imaging paradigm based on heterodyne detection is shown to be better adapted to measure soft samples, yielding cytarabine distribution in individual liposomes and enabling classification of empty and drug-loaded liposomes. The measurements highlight PTIR capability to detect ~ 10^3 cytarabine molecules (~ 1.7 zmol) label-free and non-destructively.

KEYWORDS

tapping PTIR, nanoscale chemical imaging, liposomes, cytarabine, drug delivery, nanocarriers

1 Introduction

Efforts to develop novel nanoparticle-based therapeutic paradigms to provide selective drug delivery, disease diagnosis and monitoring of the therapeutic response [1–4] have yielded several clinically approved formulations, particularly for theranostic applications [5]. For example, liposomes [6, 7] consist of spherical lipid bilayers that are effective in encapsulating and transporting hydrophilic cargos. The liposomes' lipid composition can be easily customized while their surface can be functionalized with a variety of ligands/adjuvants like antibodies, polyethylene glycol (PEG), carbohydrates, etc., that enhance bloodstream stability and/or add chemical functions tailored towards clinical targets [8, 9]. Liposomes' chemical versatility, biocompatibility and biodegradability, make them ideal carriers for transporting and delivering otherwise difficult to administer therapeutics [10–16], such as short-lived compounds [15], toxic anticancer drugs [14, 17, 18], vaccines [19], genes [20, 21] etc., as highlighted by the growing number of clinically approved formulations [22]. For example, liposomal cytarabine is clinically approved for treating of lymphomatous meningitis [23]. Cytarabine – or cytosine arabinoside (ara-C) - is a chemotherapeutic drug that stops cancer growth by interfering with DNA synthesis by virtue of its close structural/chemical similarity to the DNA nucleoside cytosine deoxyribose [24]. Because liposomes increase the delivery precision of toxic compounds to cancer sites with respect to disease-free tissues, one of their primary benefits is the reduction of side effects [25]. The synergistic interaction with other nanoparticles *in vivo* [3, 26], can even further augment liposomal drug delivery precision. Ultimately, delivering anticancer drugs with greater specificity enables reduction of the therapeutic dose significantly, provided that the drug encapsulation efficacy in the carrier is known. Batch to batch reproducibility of nanoparticle properties and composition is critically important for their approval and efficacy in clinical applications, requiring both high throughput and single particle composition-sensitive characterization methods [27–29]. Bulk assays such as high pressure liquid chromatography [30], nuclear magnetic resonance [31] or capillary electrophoresis [32] are commonly employed to assess encapsulation efficiency. However, measurements on single vesicles typically require labelling with fluorescent dyes [28, 33]. Consequently, there is an unfulfilled need for label-free methods capable of measuring the composition of small (typically < 100 nm) individual liposomes with high spatial resolution. Here, we leverage the photothermal induced resonance (PTIR) technique, a near-field infrared (IR) spectroscopic method, to obtain chemical images and spectra of individual cytarabine-loaded liposomes with nanoscale resolution. PTIR experiments in contact mode, the legacy implementation of this technique, are compared with PTIR experiments leveraging a novel heterodyne detection scheme and AFM tapping-mode operation. Both methods enable discrimination of cytarabine-loaded and empty liposomes as well as the visualization

---

of the cytarabine nanoscale distribution in individual liposomes. However, because liposomes are very soft, they can be easily damaged in contact-mode and expert supervision is necessary to exclude imaging artefacts due to heterogeneities in the local PTIR transduction efficiency. In contrast, we find that the new tapping-mode PTIR imaging method is better adapted for characterizing mechanically compliant (soft) samples, extending the boundaries of this versatile characterization technique. PTIR's exceptional sensitivity is highlighted by the ability to detect ~ 1.7 zmol of cytarabine (~ 10^3 molecules) label-free and non-destructively.

2 Experimental

2.1 Liposome preparation

All the chemicals were used as received from commercial sources. Liposomes composed of hydrogenated L-α-phosphatidylcholine (HSPC), cholesterol (Chol) and 1,2-dioctadecanoyl-sn-glycero-3-phosphoethanolamine (PE (18:0/18:0), DSPE) with 5.7:3.8:0.5 (HSPC:Chol:DSPE) molar ratio were prepared according to the thin lipid film hydration technique [34–36]. Sodium phosphate (≥ 99.5%; 15 mmol·L^{-1}, pH 7.4) and NH$_4$OAc (≥ 99.99 %; 40 mmol·L^{-1}, pH 8.4) filtered through a 0.2 μm pore size syringe filter were used for vesicle preparation. Cytarabine (cytosine β-D-arabinofuranoside, ≥ 90 %) from a 40 mmol·L^{-1} stock in 40 mmol·L^{-1} NH$_4$OAc (pH 8.4) or 50 mmol·L^{-1} stock in 15 mmol·L^{-1} sodium phosphate (pH 7.4) was used. Hydration of the lipid film was either performed with (i) 1 mL NH$_4$OAc, (ii) 1 mL NH$_4$OAc including cytarabine (40 mmol·L^{-1}), (iii) 1 mL sodium phosphate or (iv) 1 mL sodium phosphate including cytarabine (50 mmol·L^{-1}). The hydration procedure yielded dispersions of 10 mmol·L^{-1} total lipid concentration, which were extruded 21 times through two pre-wetted polycarbonate membranes (100 nm nominal pore size) to obtain small unilamellar liposomes.

Prior to the nano-electrospray gas-phase electrophoretic mobility molecular analysis (nES-GEMMA) separation and collection on the substrate, all non-encapsulated material was removed from the vesicles via spin filtration [37] employing a polyethersulfone membrane (10 kDa molecular weight cut-off spin filter). Based on the measured weights prior to and post spin filtration, a 1:10 (v:v) dilution of the initial stock was achieved (i.e., the samples had a final lipid concentration of 1 mmol·L^{-1}).

2.2 nES-GEMMA collection

The nES-GEMMA set-up [38] consists of a commercially available nES aerosol generator equipped with a ^{210}Po α-particle source, a nano differential mobility analyzer (nDMA) and a n-butanol-based ultrafine condensation particle counter (CPC). A 25 μm inner diameter, fused silica capillary with a homemade tip [39] was used for generation of a stable Taylor cone. A fresh capillary was employed for each day of measurement to preclude cross-contamination of the liposome samples. 0.1 L·min^{-1} CO$_2$ and 1 L·min^{-1} compressed, particle-free air at a pressure difference of 28 kPa (4 PSId) were employed for transporting the analytes via the capillary through the neutralization chamber and to the nDMA unit. Particle-free air was additionally dried prior to application. Size-selected liposomes were collected on substrates after particle passage through the nDMA via an electrostatic nanometer aerosol sampler (ENAS) at −3 to −3.1 kV voltage on the inner collector rod and 1.5 L·min^{-1} sheath air flow rate for 120 min (liposomes with acetate buffer) selecting an EM diameter of 85 nm. Collection of liposomes with phosphate buffer was done similarly but the air flow was held for 180 min (80 nm of EM diameter).

2.3 PTIR measurements

The setup used in this work consists of a commercial PTIR instrument coupled to a commercial external cavity quantum cascade laser array tunable from 1,130 to 1,930 cm^{-1}. Contact-mode PTIR experiments were carried out using gold coated cantilevers with 13 ± 4 kHz nominal resonance frequency and with a nominal spring constant between 0.07 and 0.4 N·m^{-1}. Contact-mode spectra were obtained by matching the laser repetition rate to the cantilever second contact resonance frequency by sweeping the laser wavelength at 2 cm^{-1} intervals while maintaining the probe position fixed. Contact-mode maps were obtained by raster scanning the probe while illuminating the sample with a fixed wavelength and using a phase locked loop (PLL) to maintain the resonance excitation condition on the second or third cantilever mode.

For tapping-mode PTIR experiments, a commercial digital lock-in amplifier interfaced with the PTIR instrument was used to demodulate the amplitude at $|f_1 \pm f_{\text{laser}}|$ from the cantilever deflection signal. First, using a piezoelectric actuator the cantilever was shaken to identify the first (f_1) and second (f_2) cantilever modes (Fig. 3(a)). The laser frequency was first set tentatively as $f_{\text{laser}} = f_2 - f_1$. The laser repetition rate in the tapping-mode PTIR experiments was refined by determining the maximum of the lock-in amplifier demodulated output (at f_2) when sweeping it across a frequency range centered around the f_{laser} first guess value. Tapping-mode PTIR experiments were obtained using gold coated cantilevers with 75 ± 15 kHz nominal resonance frequency and a nominal spring constant between 1 and 7 N·m^{-1}.

2.4 ATR FTIR reference measurements

A commercially available FTIR spectrometer equipped with a DLaTGS (deuterated L-alanine doped triglycerine sulfate) detector and a commercial diamond ATR element (single reflection) was employed for ATR FTIR reference measurements. Spectra were recorded as co-addition of 100 scans with a spectral resolution of 2 cm^{-1}.

2.5 FTIR transmission measurements

A commercially available spectrometer equipped with a liquid nitrogen cooled MCT (mercury cadmium telluride) detector was employed for transmission measurements in a flow cell (27 μm path length) connected to a commercial syringe pump with a 500 μL glass syringe. For all spectra, 100 scans were co-added with a spectral resolution of 2 cm^{-1}.

3 Results and discussion

The liposomes investigated here are composed of three different lipids: hydrogenated L-α-phosphatidylcholine (HSPC), cholesterol (Chol) and 1,2-dioctadecanoyl-sn-glycero-3-phosphoethanolamine (DSPE) with 5.7:3.8:0.5 HSPC:Chol:DSPE molar ratio. Liposomes loaded with cytarabine and buffer solution (either ammonium acetate or phosphate buffer), or liposome filled with buffer solution only (hereafter buffer-loaded liposomes) were prepared according to a thin film hydration method [34, 40] followed by an extrusion step (polycarbonate filter, 100 nm nominal pore size) to generate small unilamellar liposomes. Ammonium acetate buffer was used for the first set of experiments (Figs. 1 and 2) as part of an established protocol [35, 36], but was substituted later with phosphate buffer because of its transparency in the IR range (see Fig. S1 in the Electronic Supplementary Material (ESM)). Size-selected liposomes (85 ±3 nm or 80 ± 2 nm particle diameter loaded with ammonium acetate and phosphate buffer respectively) were collected on ZnSe and template stripped gold substrates via nES-GEMMA [38] for subsequent PTIR measurements. In the collection and size selection process, the particles are injected via electrospray ionization and separated according to their electrophoretic mobility (proportional to the particle size) in a tunable electric field [41]. Throughout the manuscript, the uncertainties in the liposomes' diameters represent

a single standard deviation based on the nES-GEMMA manufacturer specifications which are in good agreement with previous reports [41]. This liposome production method was chosen to ensure the deposition of intact liposomal nanocarriers, which have otherwise the tendency to burst when deposited on a substrate with other methods [35]. After deposition, the liposome shape typically changes from spherical to ellipsoidal (Figs. 1(c) and 2(a)) with ~ 100 to ~ 200 nm widths and ~ 35 to ~ 50 nm thicknesses, as measured by AFM.

First, FTIR and PTIR reference spectra of buffer-loaded liposomes and pure cytarabine in various forms (see Fig. S2 in the ESM) were used to identify chemically representative marker bands for cytarabine and liposomes. The C=O stretch vibration (1,734 cm^{-1}) [42] of the liposome constituent lipids was chosen as the liposome marker band because of its strong intensity and because it does not spectrally overlap with the IR bands of cytarabine and buffer. Similarly, the band at 1,528 cm^{-1} (C=N and C=C vibration of pyrimidines [24, 43]) was selected as the cytarabine marker band.

By combining IR spectroscopy composition sensitivity with atomic force microscopy (AFM) resolution, PTIR, also known as AFM-IR, provides direct and label-free access to molecule-specific information at the nanoscale [44, 45]. In PTIR, a portion of the analyte, centered around the AFM tip, is illuminated by a pulsed wavelength-tunable laser (Fig. 1(a)). The absorption of a light pulse in the sample prompts its fast thermal expansion and induces cantilever oscillations with an amplitude (measured by the AFM deflection sensor) proportional to the absorbed energy [46, 47]. In PTIR the AFM probe serves as a near-field mechanical detector, enabling nanoscale spectroscopy from the IR to the visible range [48]. Although, the PTIR spatial resolution is typically a weak function of the sample thermomechanical properties, a spatial resolution below 50 nm is routinely obtained [45, 48, 49]; with resolution down to ~ 20 nm in contact-mode PTIR [48]. The tapping-mode PTIR experiments reported here indicate a spatial
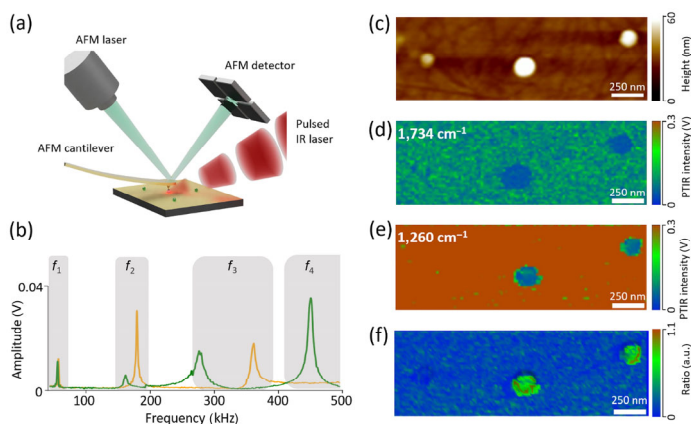
resolution of ~ 10 nm (see below). In principle, the PTIR technique is of broad applicability because of the demonstrated proportionality between the PTIR signal and the absorption coefficient [46], as in FTIR. PTIR has successfully characterized a wide range of materials e.g., solar cells [50, 51], photodetectors [52], pharmaceutics [53], art conservation [54], polymers [55–57], plasmonic structures [58–60], metal-organic frameworks [61] and 2D materials [62, 63]. In life sciences applications, PTIR has enabled the investigation of protein secondary structure [64, 65], single cells [66], lipids [67, 68] and recently, polymeric nanoparticles [69] and hybrid lipid-polymer films [70, 71] for drug delivery. Furthermore, PTIR operation in water has been recently demonstrated [72, 73], enabling conformational analysis of molecules at the nanoscale and in their native environment [72]. Recent reviews comparing PTIR with other near-field techniques, such as scattering scanning near field microscopy (s-SNOM) and tip-enhanced Raman spectroscopy (TERS) are available elsewhere [44, 74]. Briefly, in contrast with TERS and s-SNOM, which are primarily surface sensitive techniques, PTIR probes samples throughout their thicknesses even in excess of 1 µm [47, 75] and it necessitates the probe's plasmonic enhancement only to measure very thin (< 50 nm) samples. This PTIR characteristic, for example, has enabled characterization of live cells [75] and visualizing viral infection at various stages in single bacteria [76].

Dazzi et al. developed a theory for the PTIR signal (S_{PTIR}) generation, that factorizes the PTIR signal transduction into a series of multiplicative contributions [46]; rewritten here, for convenience, using the notation of Ramer et al. [77]

$$S_{PTIR}(\lambda) \propto H_{AFM}H_mH_{th}H_{opt}(\lambda)I_{inc}(\lambda) \qquad (1)$$

Where H_{AFM} is the cantilever contribution (a function of the cantilever modal stiffness, frequency, etc.), $H_m = k_{t-s} \cdot \alpha \cdot z$ is the mechanical contribution (a function of the tip-sample contact stiffness – k_{t-s}, of the sample thermal expansion coefficient – α and thickness – z), H_{th} is the thermal contribution, (a function of the sample thermal properties), H_{opt} is the optical contribution (due to the sample absorptance, i.e., a function of the sample complex refractive index) and I_{inc} is the laser incident power, typically measured in a background spectrum. Although the shape of PTIR spectral profiles is determined by the sample optical properties (H_{opt}), the thermo-mechanical properties of sample and AFM probe ($H_{AFM}H_mH_{th}$) influence the overall PTIR signal intensity [77] making some samples (i.e., with small z or low α or low k_{t-s}) more challenging to measure [78, 79]. For example, Barlow et al. observed that for stiffer bacteria on top of softer and more damping polymer layer the PTIR amplitude due to the polymer absorption was stronger when the tip was above the bacteria than when directly over the polymer layer. Since the $H_{AFM}H_mH_{th}$ term in Eq. (1) is wavelength independent (i.e., has the same value in a given location in subsequent PTIR images), ratios of PTIR images can obviate this PTIR mechanical transduction artefact [79].

The liposomes' very low stiffness hampers the PTIR signal transduction and predisposes them to tip damage in contact-mode. The low stiffness in combination with the liposome small thickness makes these samples challenging to measure with PTIR. Here, we leverage resonance-enhanced PTIR (RE-PTIR) [49] to increase the PTIR sensitivity. Although, RE-PTIR was originally developed for contact-mode AFM, a novel heterodyne detection scheme (explained below) allows resonance enhancement in tapping mode (tapping-mode PTIR).

In contact-mode PTIR experiments [49], the legacy implementation of the technique, the laser repetition rate was tuned to match the frequency of one of the cantilever oscillation modes (~ 160 kHz, Fig. 1(b)). Because for a given cantilever spring constant (k_C) and free resonance frequency (f_0), the cantilever contact resonance frequencies (f_{res}) depend on the local tip-sample contact stiffness (k_{t-s})

Figure 1 Contact-mode RE-PTIR measurement schematic and characterization of buffer-loaded liposomes. (a) PTIR measurement schematic: the sample is illuminated from the air side by a pulsed, wavelength-tunable mid-IR laser with tunable repetition rate (red). The IR absorption is detected locally via the cantilever deflection signal. (b) Contact-mode PTIR signal (frequency domain) displaying the intensity of the cantilever resonances excited by the absorption of light pulses when the cantilever is in contact with the sample (green) or the substrate (yellow). In contact-mode RE-PTIR experiments, the laser frequency was set to match either the second (~ 160 kHz) or third (~ 270 kHz) cantilever resonance. (c) AFM topography map, (d) PTIR map at 1,734 cm^{-1} (liposome marker band), (e) PTIR map at 1,260 cm^{-1} (non-specific background) of liposomes loaded with ammonium acetate buffer solution. (f) Because the soft liposomes hamper PTIR signal transduction, the correct distribution of analytes (lipids) is obtained by calculating PTIR ratio maps (1,734 cm^{-1} vs. 1,260 cm^{-1}). The images (0.2 Hz scan rate) were acquired with a PLL bandwidth of ± 8 kHz centered around the cantilever second resonance mode. The pixel size was 17.5 nm in x- and y-directions.

according to the following (simplified) relationship [80]

$$\frac{f_{\text{res}}}{f_0} = \sqrt{\frac{k_{\text{C}} + k_{\text{t-s}}}{k_{\text{C}}}} \qquad (2)$$

methods, such as a phase locked loop (PLL), are necessary to maintain the resonance enhanced condition throughout the scans [81]. For PTIR tapping-mode experiments, which reduce the likelihood of tip-sample damage, resonant excitation was obtained using a heterodyne detection scheme (see below) which doesn't require resonance tracking because of the weak dependence of the tapping-mode resonance frequencies on the sample's mechanical properties. All the PTIR experiments were obtained by illuminating the sample from the air side (∼ 20° from the sample plane) using p-polarization and gold-coated Si probes.

To illustrate the challenges provided by the liposome samples to PTIR measurements when the tip is in contact, we first measured liposomes containing only the ammonium acetate buffer solution, Fig. 1. Counterintuitively, the PTIR image of the liposome marker band (1,734 cm^{-1}, Fig. 1(d)) displays lower signal intensity in the liposome locations than on the substrate. This effect is attributed to the inefficiency of PTIR signal transduction due to the weaker sample-tip force transfer and higher damping on the liposomes (Fig. 1(b)), similarly to what previously observed by Barlow et al. [79]. Since the ZnSe substrate is transparent, to calculate image ratios (Fig. 1(f)) we reference our measurements to the spatially unspecific background absorption at 1,260 cm^{-1} attributed to SiO$_2$ absorption [82] in the AFM cantilever (Fig. 1(e)). Although this operation is relatively straightforward in non-resonantly excited PTIR experiments [79], its implementation with RE-PTIR requires careful supervision, because of the abrupt f_{res} variations observed when the tip is in contact with the liposomes or substrate. While the PLL does not compensate for Q-factor variations, it is effective to maintain the cantilever resonant excitation by adjusting the laser repetition rate, provided that the PTIR signal is well above the noise level – a condition difficult to achieve on these liposome samples. If tracking is lost, the PTIR signal is not properly scaled making the PTIR map not suitable for the image ratio procedure (at least for the pixels where the PLL is ineffective).

Next, we measure liposomes loaded with cytarabine (Fig. 2). On this sample, the low PTIR signal intensity at 1,528 cm^{-1} (cytarabine marker), makes resonance tracking particularly hard to maintain throughout an image. However, this problem can be obviated in part by restricting the PLL tracking range to include the liposome contact resonance frequency but exclude the substrate contact resonance frequency. Because the $k_{\text{t-s}}$ dependence of the contact resonance is stronger for higher order modes [80], the third cantilever mode was used for these measurements to ensure that the contact resonance frequency of substrate and liposomes were sufficiently separated. This scheme enables reliable frequency tracking on the liposome (the sample of interest) and reaches the upper limit of the PLL range on the ZnSe substrate (see Figs. 2(d) and 2(e)). Subsequently, the ZnSe areas, identified by the frequency map, are carefully excluded from data processing and interpretation.

Using the range-restricted contact resonance tracking the PTIR images at 1,528 cm^{-1} (cytarabine marker band; see Fig. 2(b)) and at 1,734 cm^{-1} (liposome band; see Fig. 2(c)) highlight cytarabine distribution in the liposome center. This interpretation is confirmed by the PTIR spectra (Fig. 2(g)). Consistently, the spectrum in the liposome periphery displays only the spectral features of the lipids, while the spectrum in the center of the liposome shows additional cytarabine bands. Such heterogeneity is further evidenced by the contact resonance image (see Fig. 2(d)) which shows higher frequencies on the substrate, lower frequencies on the soft liposome periphery and intermediate frequencies in the middle of the liposome (see Fig. 2(e)); indicating that the central region is harder than the
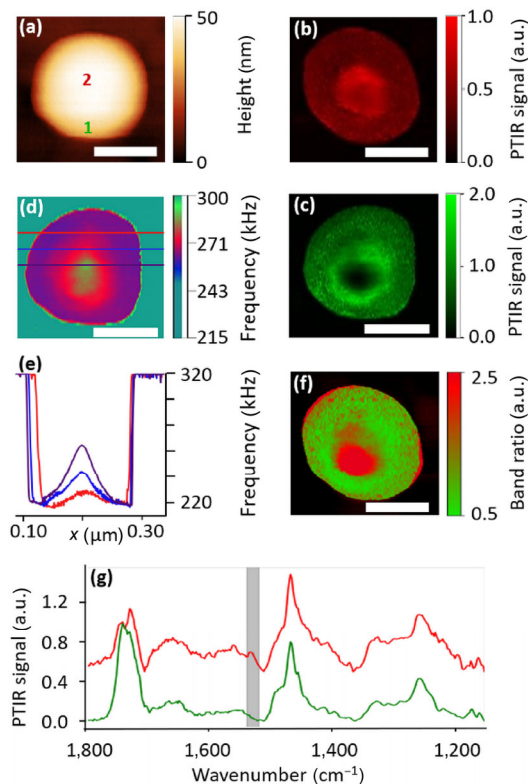
Figure 2 Contact-mode RE-PTIR characterization of cytarabine-loaded liposomes. (a) AFM topography map, (b) PTIR map at 1,528 cm^{-1} (cytarabine), (c) PTIR map at 1,734 cm^{-1} (liposome) and (d) contact frequency map (5 parallel lines average) of cytarabine-loaded liposomes. (e) Color-coded line profiles extracted in the marked locations in panel (d) showing higher contact resonance frequencies in the center of the liposome. (f) 1,528 cm^{-1} vs. 1,734 cm^{-1} PTIR image ratio (i.e., cytarabine vs. lipid). Red and green highlight cytarabine rich and lipid rich regions respectively. The images (0.1 Hz scan rate) were acquired using a PLL to track the position of the cantilever's third resonance mode (∼ 270 kHz) in the range between 210 and 320 kHz. The pixel size was 0.75 and 3 nm in x- and y-directions respectively. (g) PTIR spectra obtained from the color-coded locations in panel (a). The spectrum closer to the liposome center (red) shows the cytarabine characteristic peak (1,528 cm^{-1}, highlighted in gray) which is absent in the spectrum closer to the liposome edge (green). The spectra are displayed with an offset for clarity. The scale bars are 100 nm.

liposome shell. Because the soft liposome is deformed by consecutive contact-mode images (see changes of liposome contour in Figs. 2(b) and 2(c) and Fig. S3 in the ESM) the edges of the liposomes have been excluded from the estimation of the PTIR image ratio (Fig. 2(f)) which, once again, reveals the cytarabine distribution inside a single liposome.

AFM measurements of soft samples are often carried out in tapping mode to avoid sample deformation and/or irreversible sample damage [83]. Therefore, next we leverage the new tapping-mode PTIR method to characterize optimized liposomal nanocarriers (phosphate buffer instead of ammonium acetate buffer, see ESM) deposited on a gold substrate to augment the PTIR signal intensity [49]. Tapping mode PTIR images were obtained with heterodyne detection (a measurement scheme that enables resonant excitation by non-linear mixing of the cantilever oscillation modes) [84] by setting the laser repetition rate ($f_{\text{laser}} \approx 290$ kHz) to match the difference between the second ($f_2 \approx 344$ kHz) and first ($f_1 \approx 54$ kHz) bending modes of the AFM cantilever (Fig. 3(a)). In practice, the cantilever tapping frequency was f_1 and the heterodyne detection was measured at f_2. The tapping-mode PTIR image ratios (Fig. 3(c)) of the chemically specific marker bands (cytarabine: 1,528 cm^{-1}; liposome: 1,734 cm^{-1}) clearly highlight cytarabine localization at the center of the nanocarrier but not in the controls containing only the buffer (Fig. 3(e)), indicating that tapping-mode PTIR can successfully classify drug-free

and drug-loaded liposomes. An additional representative PTIR image of a cytarabine loaded liposome is reported in Fig. S4 in the ESM. Figure S5 in the ESM highlights the good reproducibility of the PTIR images obtained in tapping-mode, even for samples that are easily damaged in contact mode (see Fig. S3 in the ESM). Furthermore, the tapping-mode PTIR images reveal a spatial resolution of ~ 10 nm, defined as the distance (Δx) over which the PTIR signal changes from 80%(B) to 20%(A) of the maximum value (Fig. 3(f)), which is better than the highest spatial resolution reported for contact-mode PTIR (~ 20 nm) [48]. Based on capillary electrophoresis bulk measurements of the cytarabine concentration inside the liposomes (see ESM) we estimate an average cytarabine concentration of ~ 1.7×10^{-21} mol or ~ 10^3 molecules inside a single nanocarrier. The PTIR measurements presented here are close to the limit of what currently possible; however, the ultimate PTIR limit of detection for cytarabine molecules cannot be obtained with precision because of the uncertainty on the number of cytarabine molecules encapsulated in any given nanocarrier (see Table S1 in the ESM). Nevertheless, these measurements demonstrate an impressive sensitivity, comparable to the lowest PTIR detection limit (~ 300 molecules), reported for self-assembled monolayers [49], which however, are characterized by a much higher tip-sample contact stiffness (i.e., more amenable to PTIR characterization).
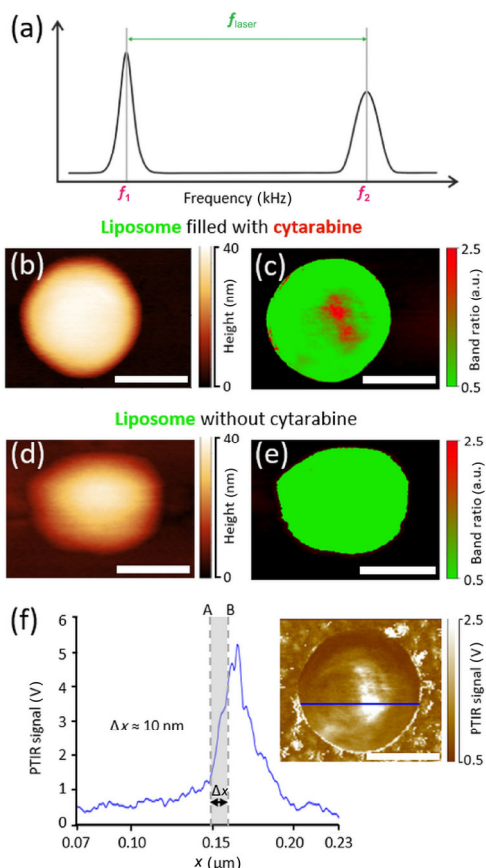
Figure 3 Tapping-mode PTIR measurements of cytarabine-loaded liposomes and buffer-loaded liposomes. (a) In tapping-mode PTIR experiments, the laser frequency ($f_{laser} \approx 290$ kHz) was set to match the difference between the second ($f_2 \approx 344$ kHz) and first ($f_1 \approx 54$ kHz) bending modes of the AFM cantilever. (b) AFM topography map and (c) 1,528 cm^{-1} vs. 1734 cm^{-1} PTIR image ratio (i.e., cytarabine vs. lipid) of a cytarabine-loaded liposome. (d) AFM topography map and (e) 1,528 cm^{-1} vs. 1,734 cm^{-1} PTIR image ratio of a liposome loaded with phosphate buffer only. Red and green colors in the PTIR ratio maps highlight cytarabine rich and lipid rich regions, respectively. (f) Line profile from the 1,528 cm^{-1} tapping-mode PTIR map (blue line in the inset) highlighting the high spatial resolution (~ 10 nm) of this method. The images (0.5 Hz scan rate) have a pixel size of 0.6 nm in the *x*-direction and 2 nm (c) or 3 nm (e) in the *y*-direction respectively. The scale bars are 100 nm.

4   Conclusion

In summary, resonance enhanced contact-mode PTIR imaging of soft samples is challenging because of the inefficient PTIR signal transduction, difficulty to maintain resonance excitation and risk for sample damage or deformation. However, careful adaptation of parameter settings and data processing based on detailed understanding of the tip-sample interaction can yield suitable PTIR images that enable the visualization of the cytarabine distribution inside individual liposomes. In contrast, by avoiding sample damage and mechanical artefacts the novel ability to measure PTIR images in tapping-mode can more easily and clearly classify empty and drug loaded liposomes, with the added benefit of increased (~ 2- to ~ 5-fold) measurement throughput, based on the scan rate practically achievable. The detection of an estimated ~ 1.7 zmol of cytarabine inside individual liposomes highlights the impressive PTIR sensitivity and enables, for the first time, measuring the drug distribution inside a single nanocarrier directly (i.e., label free) with a chemically sensitive spectroscopic method, non-destructively and at room temperature. Beyond the proof of concept presented here, extensive studies to determine the distribution and quantification of chemotherapeutic drug-loading in liposomal nanocarriers will benefit from improvements in the PTIR signal-to-noise ratio and throughput. Incremental advances could be obtained by leveraging different combinations of cantilever modes for PTIR heterodyne detection. Alternatively, a more disruptive approach involves the use of novel nanoscale optomechanical AFM transducers [85] that have been shown to increase the PTIR sensitivity (50-fold) and throughput (> 2,500-fold) compared to conventional AFM cantilevers without the need for resonant excitation [85]. We believe that such transducers hold great promise to further aid the development of liposome formulations towards clinical applications. This study lays the foundation for the quantification of drug-loading in single liposomes; a longstanding goal that could potentially improve the quality control for drug delivery systems and ultimately contribute to minimize side effects of highly toxic drugs.

References

[1]   Boisselier, E.; Astruc, D. Gold nanoparticles in nanomedicine: Preparations, imaging, diagnostics, therapies and toxicity. *Chem. Soc. Rev.* **2009**, *38*, 1759–1782.

[2] Ding, J.; Liang, T.; Zhou, Y.; He, Z.; Min, Q.; Jiang, L.; Zhu, J. Hyaluronidase-triggered anticancer drug and siRNA delivery from cascaded targeting nanoparticles for drug-resistant breast cancer therapy. *Nano Res.* **2017**, *10*, 690–703.

[3] Von Maltzahn, G.; Park, J. H.; Lin, K. Y.; Singh, N.; Schwöppe, C.; Mesters, R.; Berdel, W. E.; Ruoslahti, E.; Sailor, M. J.; Bhatia, S. N. Nanoparticles that communicate *in vivo* to amplify tumour targeting. *Nat. Mater.* **2011**, *10*, 545–552.

[4] Lee, D. E.; Koo, H.; Sun, I. C.; Ryu, J. H.; Kim, K.; Kwon, I. C. Multifunctional nanoparticles for multimodal imaging and theragnosis. *Chem. Soc. Rev.* **2012**, *41*, 2656–2672.

[5] Thakor, A. S.; Gambhir, S. S. Nanooncology: The future of cancer diagnosis and therapy. *CA: A Cancer J. Clin.* **2013**, *63*, 395–418.

[6] Senapati, S.; Mahanta, A. K.; Kumar, S.; Maiti, P. Controlled drug delivery vehicles for cancer treatment and their performance. *Signal Transduct. Target. Ther.* **2018**, *3*, 7.

[7] Lammers, T.; Hennink, W. E.; Storm, G. Tumour-targeted nanomedicines: Principles and practice. *Br. J. Cancer* **2008**, *99*, 392–397.

[8] Peer, D.; Karp, J. M.; Hong, S.; Farokhzad, O. C.; Margalit, R.; Langer, R. Nanocarriers as an emerging platform for cancer therapy. *Nat. Nanotechnol.* **2007**, *2*, 751–760.

[9] Torchilin, V. P. Recent advances with liposomes as pharmaceutical carriers. *Nat. Rev. Drug Discov.* **2005**, *4*, 145–160.

[10] Morton, S. W.; Lee, M. J.; Deng, Z. J.; Dreaden, E. C.; Siouve, E.; Shopsowitz, K. E.; Shah, N. J.; Yaffe, M. B.; Hammond, P. T. A nanoparticle-based combination chemotherapy delivery system for enhanced tumor killing by dynamic rewiring of signaling pathways. *Sci. Signal.* **2014**, *7*, ra44.

[11] Zhang, Y.; Chan, H. F.; Leong, K. W. Advanced materials and processing for drug delivery: The past and the future. *Adv. Drug Deliv. Rev.* **2013**, *65*, 104–120.

[12] Venditto, V. J.; Szoka Jr, F. C. Cancer nanomedicines: So many papers and so few drugs! *Adv. Drug Deliv. Rev.* **2013**, *65*, 80–88.

[13] Allen, T. M.; Cullis, P. R. Liposomal drug delivery systems: From concept to clinical applications. *Adv. Drug Deliv. Rev.* **2013**, *65*, 36–48.

[14] Sercombe, L.; Veerati, T.; Moheimani, F.; Wu, S. Y.; Sood, A. K.; Hua, S. S. Advances and challenges of liposome assisted drug delivery. *Front. Pharmacol.* **2015**, *6*, 286.

[15] Young, S. A.; Smith, T. K. Lipids and liposomes in the enhancement of health and treatment of disease. In *Drug Discovery and Development - From Molecules to Medicine*. Vallisuta, O.; Olimat, S., Eds.; InTech: Croatia, 2015; pp 133–162.

[16] Bozzuto, G.; Molinari, A. Liposomes as nanomedical devices. *Int. J. Nanomedicine* **2015**, *10*, 975–999.

[17] de Araújo Lopes, S. C.; dos Santos Giuberti, C.; Rocha, T. G. R.; dos Santos Ferreira, D.; Leite, E. A.; Oliveira, M. C. Liposomes as carriers of anticancer drugs. In *Cancer Treatment - Conventional and Innovative Approaches*. Rangel, L., Ed.; InTech: Rijeka, 2013; pp 85–124.

[18] Çağdaş, M.; Sezer, A. D.; Bucak, S. Liposomes as potential drug carrier systems for drug delivery. In *Application of Nanotechnology in Drug Delivery*. Sezer, A. D., ed.; InTech: Rijeka, 2014; pp 1–50.

[19] Schwendener, R. A. Liposomes as vaccine delivery systems: A review of the recent advances. *Ther. Adv. Vaccines* **2014**, *2*, 159–182.

[20] Rasoulianboroujeni, M.; Kupgan, G.; Moghadam, F.; Tahriri, M.; Boughdachi, A.; Khoshkenar, P.; Ambrose, J. J.; Kiaie, N.; Vashaee, D.; Ramsey, J. D. et al. Development of a DNA-liposome complex for gene delivery applications. *Mater. Sci. Eng. C* **2017**, *75*, 191–197.

[21] Saffari, M.; Moghimi, H. R.; Dass, C. R. Barriers to liposomal gene delivery: From application site to the target. *Iran. J. Pharm. Res.* **2016**, *15*, 3–17.

[22] Bulbake, U.; Doppalapudi, S.; Kommineni, N.; Khan, W. Liposomal formulations in clinical use: An updated review. *Pharmaceutics* **2017**, *9*, 12.

[23] Pillai, G. Nanomedicines for cancer therapy: An update of fda approved and those under various stages of development. *Pharm. Pharm. Sci.* **2014**, *1*, 13.

[24] El-Subbagh, H. I.; Al-Badr, A. A. Cytarabine. In *Profiles of Drug Substances, Excipients, and Related Methodology*. Brittain, H. G., ed.; Elsevier: Amsterdam, 2009; pp 37–113.

[25] Germain, M.; Meyre, M. E.; Poul, L.; Paolini, M.; Berjaud, C.; Mpambani, F.; Bergere, M.; Levy, L.; Pottier, A. Priming the body to receive the therapeutic agent to redefine treatment benefit/risk profile. *Sci. Rep.* **2018**, *8*, 4797.

[26] Park, B. H.; von Maltzahn, G.; Ong, L. L.; Centrone, A.; Hatton, T. A.; Ruoslahti, E.; Bhatia, S. N.; Sailor, M. J. Cooperative nanoparticles for tumor detection and photothermally triggered drug delivery. *Adv. Mater.* **2010**, *22*, 880–885.

[27] Mullen, D. G.; Holl, M. M. B. Heterogeneous ligand–nanoparticle distributions: A major obstacle to scientific understanding and commercial translation. *ACC. Chem. Res.* **2011**, *44*, 1135–1145.

[28] Lohse, B.; Bolinger, P. Y.; Stamou, D. Encapsulation efficiency measured on single small unilamellar vesicles. *J. Am. Chem. Soc.* **2008**, *130*, 14372–14373.

[29] Ernsting, M. J.; Murakami, M.; Roy, A.; Li, S. D. Factors controlling the pharmacokinetics, biodistribution and intratumoral penetration of nanoparticles. *J. Control. Release* **2013**, *172*, 782–794.

[30] Ohnishi, N.; Yamamoto, E.; Tomida, H.; Hyodo, K.; Ishihara, H.; Kikuchi, H.; Tahara, K.; Takeuchi, H. Rapid determination of the encapsulation efficiency of a liposome formulation using column-switching HPLC. *Int. J. Pharm.* **2013**, *441*, 67–74.

[31] Zhang, X. M.; Patel, A. B.; de Graaf, R. A.; Behar, K. L. Determination of liposomal encapsulation efficiency using proton NMR spectroscopy. *Chem. Phys. Lipids* **2004**, *127*, 113–120.

[32] Franzen, U.; Nguyen, T. T. T. N.; Vermehren, C.; Gammelgaard, B.; Østergaard, J. Characterization of a liposome-based formulation of oxaliplatin using capillary electrophoresis: Encapsulation and leakage. *J. Pharm. Biomed. Anal.* **2011**, *55*, 16–22.

[33] Chen, C. X.; Zhu, S. B.; Wang, S.; Zhang, W. Q.; Cheng, Y.; Yan, X. M. Multiparameter quantification of liposomal nanomedicines at the single-particle level by high-sensitivity flow cytometry. *ACS Appl. Mater. Interfaces* **2017**, *9*, 13913–13919.

[34] Jesorka, A.; Orwar, O. Liposomes: Technologies and analytical applications. *Annu. Rev. Anal. Chem.* **2008**, *1*, 801–832.

[35] Weiss, V. U.; Urey, C.; Gondikas, A.; Golesne, M.; Friedbacher, G.; von der Kammer, F.; Hofmann, T.; Andersson, R.; Marko-Varga, G.; Marchetti-Deschmann, M. et al. Nano electrospray gas-phase electrophoretic mobility molecular analysis (nES-GEMMA) of liposomes: Applicability of the technique for nano vesicle batch control. *Analyst* **2016**, *141*, 6042–6050.

[36] Urey, C.; Weiss, V. U.; Gondikas, A.; von der Kammer, F.; Hofmann, T.; Marchetti-Deschmann, M.; Allmaier, G.; Marko-Varga, G.; Andersson, R. Combining gas-phase electrophoretic mobility molecular analysis (GEMMA), light scattering, field flow fractination and cryo electron microscopy in a multidimensional approach to characterize liposomal carrier vesicles. *Int. J. Pharm.* **2016**, *513*, 309–318.

[37] Weiss, V. U.; Lehner, A.; Kerul, L.; Grombe, R.; Kratzmeier, M.; Marchetti-Deschmann, M.; Allmaier, G. Characterization of cross-linked gelatin nanoparticles by electrophoretic techniques in the liquid and the gas phase. *Electrophoresis* **2013**, *34*, 3267–3276.

[38] Kaufman, S. L.; Skogen, J. W.; Dorman, F. D.; Zarrin, F. Macromolecule analysis based on electrophoretic mobility in air: Globular proteins. *Anal. Chem.* **1996**, *68*, 1895–1904.

[39] Tycova, A.; Prikryl, J.; Foret, F. Reproducible preparation of nanospray tips for capillary electrophoresis coupled to mass spectrometry using 3D printed grinding device. *Electrophoresis* **2016**, *37*, 924–930.

[40] Bangham, A. D.; Standish, M. M.; Watkins, J. C. Diffusion of univalent ions across the lamellae of swollen phospholipids. *J. Mol. Biol.* **1965**, *13*, 238–252.

[41] Kinney, P. D.; Pui, D. Y. H.; Mulliolland, G. W.; Bryner, N. P. Use of the electrostatic classification method to size 0.1 μm SRM particles—a feasibility study. *J. Res. Natl. Inst. Stand. Technol.* **1991**, *96*, 147–176.

[42] Lewis, R. N.; McElhaney, R. N.; Pohle, W.; Mantsch, H. H. Components of the carbonyl stretching band in the infrared spectra of hydrated 1,2-diacylglycerolipid bilayers: A reevaluation. *Biophys. J.* **1994**, *67*, 2367–2375.

[43] Socrates, G. *Infrared and Raman Characteristic Group Frequencies: Tables and Charts*; 3rd ed. John Wiley and Sons: Chichester, 2001.

[44] Centrone, A. Infrared imaging and spectroscopy beyond the diffraction limit. *Annu. Rev. Anal. Chem.* **2015**, *8*, 101–126.

[45] Dazzi, A.; Prater, C. B. AFM-IR: Technology and applications in nanoscale infrared spectroscopy and chemical imaging. *Chem. Rev.* **2017**, *117*, 5146–5173.

[46] Dazzi, A.; Glotin, F.; Carminati, R. Theory of infrared nanospectroscopy by photothermal induced resonance. *J. Appl. Phys.* **2010**, *107*, 124519.

[47] Lahiri, B.; Holland, G.; Centrone, A. Chemical imaging beyond the diffraction limit: Experimental validation of the PTIR technique. *Small*

2013, *9*, 439–445.

[48] Katzenmeyer, A. M.; Holland, G.; Kjoller, K.; Centrone, A. Absorption spectroscopy and imaging from the visible through mid-infrared with 20 nm resolution. *Anal. Chem.* **2015**, *87*, 3154–3159.

[49] Lu, F.; Jin, M. Z.; Belkin, M. A. Tip-enhanced infrared nanospectroscopy via molecular expansion force detection. *Nat. Photonics* **2014**, *8*, 307–312.

[50] Strelcov, E.; Dong, Q. F.; Li, T.; Chae, J.; Shao, Y. C.; Deng, Y. H.; Gruverman, A.; Huang, J. S.; Centrone, A. CH₃NH₃PbI₃ perovskites: Ferroelasticity revealed. *Sci. Adv.* **2017**, *3*, e1602165.

[51] Chae, J.; Dong, Q. F.; Huang, J. S.; Centrone, A. Chloride incorporation process in CH₃NH₃PBI₃₋ₓClₓ perovskites via nanoscale bandgap maps. *Nano Lett.* **2015**, *15*, 8114–8121.

[52] Dong, R.; Fang, Y. J.; Chae, J.; Dai, J.; Xiao, Z. G.; Dong, Q. F.; Yuan, Y. B.; Centrone, A.; Zeng, X. C.; Huang, J. High-gain and low-driving-voltage photodetectors based on organolead triiodide perovskites. *Adv. Mater.* **2015**, *27*, 1912–1918.

[53] van Eerdenbrugh, B.; Lo, M.; Kjoller, K.; Marcott, C.; Taylor, L. S. Nanoscale mid-infrared imaging of phase separation in a drug–polymer blend. *J. Pharm. Sci.* **2012**, *101*, 2066–2073.

[54] Morsch, S.; van Driel, B. A.; van den Berg, K. J.; Dik, J. Investigating the photocatalytic degradation of oil paint using ATR-IR and AFM-IR. *Appl. Mater. Interfaces* **2017**, *9*, 10169–10179.

[55] Ghosh, S.; Kouamé, N. A.; Ramos, L.; Remita, S.; Dazzi, A.; Deniset-Besseau, A.; Beaunier, P.; Goubard, F.; Aubert, P. H.; Remita, H. Conducting polymer nanostructures for photocatalysis under visible light. *Nat. Mater.* **2015**, *14*, 505–511.

[56] Tri, P. N.; Prud'homme, R. E. Nanoscale lamellar assembly and segregation mechanism of poly (3-hydroxybutyrate)/poly(ethylene glycol) blends. *Macromolecules* **2018**, *51*, 181–188.

[57] Morsch, S.; Liu, Y. W.; Lyon, S. B.; Gibbon, S. R. Insights into epoxy network nanostructural heterogeneity using AFM-IR. *Appl. Mater. Interfaces* **2016**, *8*, 959–966.

[58] Chae, J.; Lahiri, B.; Centrone, A. Engineering near-field SEIRA enhancements in plasmonic resonators. *ACS Photonics* **2016**, *3*, 87–95.

[59] Lahiri, B.; Holland, G.; Aksyuk, V.; Centrone, A. Nanoscale imaging of plasmonic hot spots and dark modes with the photothermal-induced resonance technique. *Nano Lett.* **2013**, *13*, 3218–3224.

[60] Katzenmeyer, A. M.; Chae, J.; Kasica, R.; Holland, G.; Lahiri, B.; Centrone, A. Nanoscale imaging and spectroscopy of plasmonic modes with the PTIR technique. *Adv. Opt. Mater.* **2014**, *2*, 718–722.

[61] Katzenmeyer, A. M.; Canivet, J.; Holland, G.; Farrusseng, D.; Centrone, A. Assessing chemical heterogeneity at the nanoscale in mixed-ligand metal-organic frameworks with the PTIR technique. *Angew. Chem., Int. Ed.* **2014**, *53*, 2852–2856.

[62] Brown, L. V; Davanco, M.; Sun, Z. Y.; Kretinin, A.; Chen, Y. G.; Matson, J. R.; Vurgaftman, I.; Sharac, N.; Giles, A. J.; Fogler, M. M. et al. Nanoscale mapping and spectroscopy of nonradiative hyperbolic modes in hexagonal boron nitride nanostructures. *Nano Lett.* **2018**, *18*, 1628–1636.

[63] Rosenberger, M. R.; Wang, M. C.; Xie, X.; Rogers, J. A.; Nam, S.; King, W. P. Measuring individual carbon nanotubes and single graphene sheets using atomic force microscope infrared spectroscopy. *Nanotechnology* **2017**, *28*, 355707.

[64] Ramer, G.; Balbekova, A.; Schwaighofer, A.; Lendl, B. Method for time-resolved monitoring of a solid state biological film using photothermal infrared nanoscopy on the example of poly-L-lysine. *Anal. Chem.* **2015**, *87*, 4415–4420.

[65] Ruggeri, F. S.; Habchi, J.; Cerreta, A.; Dietler, G. AFM-based single molecule techniques: Unraveling the amyloid pathogenic species. *Curr. Pharm. Des.* **2016**, *22*, 3950–3970.

[66] Dazzi, A.; Prater, C. B.; Hu, Q. C.; Chase, D. B.; Rabolt, J. F.; Marcott, C. AFM–IR: Combining atomic force microscopy and infrared spectroscopy for nanoscale chemical characterization. *Appl. Spectrosc.* **2012**, *66*, 1365–1384.

[67] Marcott, C.; Lo, M.; Kjoller, K.; Fiat, F.; Baghdadli, N.; Balooch, G.; Luengo, G. S. Localization of human hair structural lipids using nanoscale infrared spectroscopy and imaging. *Appl. Spectrosc.* **2014**, *68*, 564–569.

[68] Yarrow, F.; Kennedy, E.; Salaun, F.; Rice, J. H. Sub-wavelength infrared imaging of lipids. *Biomed. Opt. Express*, **2011**, *2*, 37–43.

[69] Pancani, E.; Mathurin, J.; Bilent, S.; Bernet‑Camard, M. F.; Dazzi, A.; Deniset-Besseau, A.; Gref, R. High-resolution label-free detection of biocompatible polymeric nanoparticles in cells. *Part. Part. Syst. Charact.* **2018**, *35*, 1700457.

[70] Kang, M.; Tuteja, M.; Centrone, A.; Topgaard, D.; Leal, C. Nanostructured lipid-based films for substrate-mediated applications in biotechnology. *Adv. Funct. Mater.* **2018**, *28*, 1704356.

[71] Tuteja, M.; Kang, M.; Leal, C.; Centrone, A. Nanoscale partitioning of paclitaxel in hybrid lipid–polymer membranes. *Analyst* **2018**, *143*, 3808–3813.

[72] Ramer, G.; Ruggeri, F. S.; Levin, A.; Knowles, T. P. J.; Centrone, A. Determination of polypeptide conformation with nanoscale resolution in water. *ACS Nano* **2018**, *12*, 6612–6619.

[73] Jin, M. Z.; Lu, F.; Belkin, M. A. High-sensitivity infrared vibrational nanospectroscopy in water. *Light Sci. Appl.* **2017**, *6*, e17096.

[74] Xiao, L. F.; Schultz, Z. D. Spectroscopic imaging at the nanoscale: Technologies and recent applications. *Anal. Chem.* **2018**, *90*, 440–458.

[75] Mayet, C.; Dazzi, A.; Prazeres, R.; Allot, F.; Glotin, F.; Ortega, J. M. Sub-100 nm IR spectromicroscopy of living cells. *Opt. Lett.* **2008**, *33*, 1611–1613.

[76] Dazzi, A.; Prazeres, R.; Glotin, F.; Ortega, J. M.; Al-Sawaftah, M.; de Frutos, M. Chemical mapping of the distribution of viruses into infected bacteria with a photothermal method. *Ultramicroscopy* **2008**, *108*, 635–641.

[77] Ramer, G.; Aksyuk, V. A.; Centrone, A. Quantitative chemical analysis at the nanoscale using the photothermal induced resonance technique. *Anal. Chem.* **2017**, *89*, 13524–13531.

[78] Katzenmeyer, A. M.; Holland, G.; Chae, J.; Band, A.; Kjoller, K.; Centrone, A. Mid-infrared spectroscopy beyond the diffraction limit via direct measurement of the photothermal effect. *Nanoscale* **2015**, *7*, 17637–17641.

[79] Barlow, D. E.; Biffinger, J. C.; Cockrell-Zugell, A. L.; Lo, M.; Kjoller, K.; Cook, D.; Lee, K. W.; Pehrsson, P. E.; Crookes-Goodson, W. J.; Hung, C. S. et al. The importance of correcting for variable probe–sample interactions in AFM-IR spectroscopy: AFM-IR of dried bacteria on a polyurethane film. *Analyst* **2016**, *141*, 4848–4854.

[80] Rabe, U.; Janser, K.; Arnold, W. Vibrations of free and surface-coupled atomic force microscope cantilevers: Theory and experiment. *Rev. Sci. Instrum.* **1996**, *67*, 3281–3293.

[81] Ramer, G.; Reisenbauer, F.; Steindl, B.; Tomischko, W.; Lendl, B. Implementation of resonance tracking for assuring reliability in resonance enhanced photothermal infrared spectroscopy and imaging. *Appl. Spectrosc.* **2017**, *71*, 2013–2020.

[82] Hu, S. M. Infrared absorption spectra of SiO₂ precipitates of various shapes in silicon: Calculated and experimental. *J. Appl. Phys.* **1980**, *51*, 5945–5948.

[83] Last, J. A.; Russell, P.; Nealey, P. F.; Murphy, C. J. The applications of atomic force microscopy to vision science. *Invest. Ophthalmol. Vis. Sci.* **2010**, *51*, 6083–6094.

[84] Tetard, L.; Passian, A.; Farahi, R. H.; Thundat, T.; Davison, B. H. Opto-nanomechanical spectroscopic material characterization. *Nat. Nanotechnol.* **2015**, *10*, 870–877.

[85] Chae, J.; An, S. M.; Ramer, G.; Stavila, V.; Holland, G.; Yoon, Y.; Talin, A. A.; Allendorf, M.; Aksyuk, V. A.; Centrone, A. Nanophotonic atomic force microscope transducers enable chemical composition and thermal conductivity measurements at the nanoscale. *Nano Lett.* **2017**, *17*, 5587–5594.

5.5   Publication V

Phosphonate Coating of SiO₂ Nanoparticles Abrogates Inflammatory Effects and Local Changes of the Lipid Composition in the Rat Lung: A Complementary Bioimaging Study

Mandy Großgarten*, Matthias Holzlechner*, Antje Vennemann, Anna Balbekova, Karin Wieland, Michael Sperling, Bernhard Lendl, Martina Marchetti-Deschmann, Uwe Karst, Martin Wiemann; *Particle and Fibre Toxicology* 2018, 15, 1-16, 10.1186/s12989-018-0267-z, CC-BY License (https://creativecommons.org/licenses/by/4.0/)

*contributed equally

RESEARCH

Phosphonate coating of SiO$_2$ nanoparticles abrogates inflammatory effects and local changes of the lipid composition in the rat lung: a complementary bioimaging study

Mandy Großgarten[1†], Matthias Holzlechner[2†], Antje Vennemann[3], Anna Balbekova[2], Karin Wieland[2], Michael Sperling[1], Bernhard Lendl[2], Martina Marchetti-Deschmann[2], Uwe Karst[1] and Martin Wiemann[3*]

Abstract

Background: The well-known inflammatory and fibrogenic changes of the lung upon crystalline silica are accompanied by early changes of the phospholipid composition (PLC) as detected in broncho-alveolar lavage fluid (BALF). Amorphous silica nanoparticles (NPs) evoke transient lung inflammation, but their effect on PLC is unknown. Here, we compared effects of unmodified and phosphonated amorphous silica NP and describe, for the first time, local changes of the PLC with innovative bioimaging tools.

Methods: Unmodified (SiO$_2$-n), 3-(trihydroxysilyl) propyl methylphosphonate coated SiO$_2$-n (SiO$_2$-p) as well as a fluorescent surrogate of SiO$_2$-n (SiO$_2$-FITC) nanoparticles were used in this study. In vitro toxicity was tested with NR8383 alveolar macrophages. Rats were intratracheally instilled with SiO$_2$-n, SiO$_2$-p, or SiO$_2$-FITC, and effects on lungs were analyzed after 3 days. BALF from the right lung was analyzed for inflammatory markers. Cryo-sections of the left lung were subjected to fluorescence microscopy and PLC analyses by matrix-assisted laser desorption/ ionization mass spectrometry imaging (MALDI-MS), Fourier transform infrared microspectroscopy (FT-IR), and tandem mass spectrometry (MS/MS) experiments.

Results: Compared to SiO$_2$-p, SiO$_2$-n NPs were more cytotoxic to macrophages in vitro and more inflammatory in the rat lung, as reflected by increased concentration of neutrophils and protein in BALF. Fluorescence microscopy revealed a typical patchy distribution of SiO$_2$-FITC located within the lung parenchyma and alveolar macrophages. Superimposable to this particle distribution, SiO$_2$-FITC elicited local increases of phosphatidylglycerol (PG) and phosphatidylinositol (PI), whereas phoshatidylserine (PS) and signals from triacylglyceride (TAG) were decreased in the same areas. No such changes were found in lungs treated with SiO$_2$-p or particle-free instillation fluid.

Conclusions: Phosphonate coating mitigates effects of silica NP in the lung and abolishes their locally induced changes in PLC pattern. Bioimaging methods based on MALDI-MS may become a useful tool to investigate the mode of action of NPs in tissues.

Keywords: Lung surfactant, Silica nanoparticles, In vitro and in vivo lung toxicity, MALDI-MS imaging, Phospholipids, Phosphonate coating, PI/PG ratio, Fourier transform infrared microspectroscopy imaging

* Correspondence: martin.wiemann@ibe-ms.de
[†]Mandy Großgarten and Matthias Holzlechner contributed equally to this work.
[3]IBE R&D Institute for Lung Health gGmbH, Mendelstraße 11, 48149 Münster, Germany
Full list of author information is available at the end of the article

Großgarten *et al. Particle and Fibre Toxicology* (2018) 15:31

Page 2 of 16

Background

Nanoparticles (NPs) consisting of silica are among the most common materials of everyday life. Besides other applications, silica NPs act as bulking agent in car wheels, as drug delivery system in cancer therapy or as food additive (E551) to prevent pulverulent foodstuffs from agglutinating. Respirable airborne silica may enter the lungs in special workplace situations and it is known for crystalline silica particles (quartz, cristobalite) that they elicit strong adverse health effects such as neoplastic transformation, progressive fibrosis or even cancer [1]. Amorphous nanosized silica particles are of less concern. They are produced by different production processes such that precipitated, fumed, or colloidal silica qualities are to be distinguished. From a toxicological point of view, most amorphous nanosized silica particles, at least above a certain dose, have been shown to cause acute pulmonary inflammation, but no progressive lung fibrosis [2–4]. Also, genotoxic or mutagenic effects, both of which had been described for cells in vitro mostly at high concentrations, have not been identified in the lung or secondary target organs [5]. This holds true also for comparatively high dose rates and even under conditions which increase the population of neutrophilic granulocytes inside the lung to extreme values [3].

The mechanisms underlying the cytotoxic, membrane disrupting or hemolytic potential of amorphous silica seem to involve silanol groups which are present at the particles' surface and may interact with biological molecules such as proteins [6–9]. Accordingly, the biologic activity of amorphous silica NPs correlates largely with the overall size of the silica surface [10, 11] and modification of the chemical surface structures of silica NPs may alter their bioactivity. Effects of SiO_2-n and SiO_2-p used in this study have been investigated previously: coating of SiO_2-n (diameter: 15 nm, BET surface: 200 $m^2 \cdot g^{-1}$) with 3-(trihydroxysilyl) propyl methylphosphonate (TPMP), which led to SiO_2-p, largely abrogated the typical signs of inflammation elicited by the unmodified SiO_2-n [12, 13]. The effect was not attributable to altered particle properties in general, as the TPMP coating had no or only minor effects on particle properties or agglomeration in biological media [12]. Interestingly, the in vitro binding of phospholipids from lung surfactant to SiO_2-n and SiO_2-p (both negatively charged) was similarly low, but increased in the presence of surfactant proteins A and D [14]. However, the binding of lung surfactant components to SiO_2-n and SiO_2-p under in vivo conditions has not yet been explored.

Lung surfactant is produced by alveolar type II cells and is released in the form of lamellar bodies which consist of 90% phospholipids and 10% surfactant proteins [15]. The unfolded lipid layer covers the inner surface of the lung and decreases the surface tension of the

air-liquid interface [16]. The surfactant proteins A and D (so called collectins) are immunologically relevant as they can bind to microorganisms or foreign material such as (nano) particles, thus augmenting their uptake by alveolar macrophages [17–19]. For micron-sized crystalline silica and also for other particles it is known that they change the phospholipid composition (PLC) of the broncho-alveolar lavage fluid (BALF) in a time- and dose-dependent manner [20–22]: while the overall concentration of phosphatidylcholine (the major constituent of lung surfactant) increases, fractions of phosphatidylglycerol (PG) and phosphatidylinositol (PI) de- and increase, respectively [20]. Due to these opposed changes, the ratio PI/PG has been used as a sensitive tool to describe impairments of the lung. Of note, changes in PI/PG were observed during bleomycin- or quartz-induced lung fibrosis [20, 23], and also in humans suffering from the acute respiratory distress syndrome or other lung diseases such as cystic fibrosis [24, 25]. However, the impact of amorphous silica on the composition of the PLC of the lung is still unknown.

In contrast to previous studies on the composition of phospholipids in BALF, here we apply bioimaging methods to cryo-sections of the rat lung to demonstrate local lipid changes upon intratracheal instillation caused by amorphous silica NP in a laterally resolved manner. It is to be expected that allocation of changes in PI and PG to the presence of particles in the lung will improve our understanding of biological processes elicited by nanoparticles. To this aim, matrix-assisted laser desorption/ionization mass spectrometry imaging (MALDI-MS) and Fourier transform infrared (FT-IR) microspectroscopy imaging were applied to cryo-conserved lung sections to localize changes in the phospholipid composition secondary to the application of SiO_2-n, SiO_2-p and SiO_2-FITC. With these methods, we found typical changes of distinct phospholipids to be co-localized with the distribution pattern of SiO_2-FITC, whereas SiO_2-p NP evoked no such changes.

Results

In vitro and in vivo toxicity study

To demonstrate the differential toxicity of the three SiO_2 nanoparticle varieties, in vitro testing with a rat alveolar macrophage cell line was carried out with increasing concentrations of the particles (22.5, 45, 90, and 180 $\mu g \cdot mL^{-1}$). Exposure to the pristine material SiO_2-n for 16 h (Fig. 1a-d) led to dose-dependent increases in the cell culture supernatant of lactate dehydrogenase (LDH, a), glucuronidase (Glu, b), and TNF-α (d), mostly beginning at a concentration of 22.5 $\mu g \cdot mL^{-1}$. These cytotoxic and inflammatory effects were far less pronounced upon SiO_2-p, while the release of H_2O_2 from NR8383 cells, as measured during a 90 min incubation period, was augmented (c).

Großgarten *et al. Particle and Fibre Toxicology* (2018) 15:31

Page 3 of 16

Fig. 1 Effects of SiO$_2$-n and SiO$_2$-p NPs in vitro. **a-d** Dose dependent effects of SiO$_2$-n and SiO$_2$-p (22.5, 45, 90, and 180 µg·mL^{-1}) on NR8383 cells, taken from [54]. Release of **a** lactate dehydrogenase (LDH), **b** glucuronidase (Glu), **c** H$_2$O$_2$, and **d** tumor necrosis factor α (TNF-α). LDH and Glu activities were measured relative to positive control (Triton X-100-lysed cells) after 16 h. The H$_2$O$_2$ concentration was measured in µmol·L^{-1} after 90 min, and bioactive TNF-α was measured after 16 h as lysis of TNF-α responsive L-929 cells. All columns represent mean values ± standard deviation of 3 independent experiments. Untreated cells served as controls ($n = 3$) whose mean values are indicated by dashed lines. Significance was tested by two-way ANOVA and post-hoc Dunnett's multiple comparison test (*: $p \leq 0.05$, **: $p \leq 0.01$, ***: $p \leq 0.001$)

In vivo tests were carried out with SiO$_2$-n, and SiO$_2$-p. The fluorescence surrogate SiO$_2$-FITC was used to demonstrate particle distribution in the left lung lobe secondary to intratracheal instillation which was carried out with a micro-sprayer device. In all tests, a concentration of 0.36 mg per rat lung was used to match the lung burden achieved in a previous inhalation study [13]. BALF analysis was conducted 3 days after intratracheal instillation of the NPs in order to examine their effect on cell counts and total protein content. SiO$_2$-n and SiO$_2$-FITC both increased the numbers of alveolar macrophages (AM) and polymorphonuclear leukocytes (PMN) as well as the concentration of total protein in BALF compared to the vehicle-treated control (Fig. 2a, b). Based on these biological effects, no difference was found between SiO$_2$-FITC and SiO$_2$-n NPs. Spray application of particles resulted in a patchy distribution pattern of particles inside the lung typically found upon intratracheal instillation (Fig. 2c) [26]. Higher magnification revealed many condensed fluorescent NP agglomerates alongside the alveolar septa after 30 min. After 3 d, the majority of this material had disappeared from alveolar walls but occurred within alveolar macrophages (Fig. 2d, e), whose overall distribution was still detectable by fluorescent microscopy and reflected the original sites of particle deposition. On hematoxylin-eosin stained lung cryo-sections SiO$_2$-n or SiO$_2$-p nanoparticle (or agglomerates thereof) were not detectable with bright field optics. However, SiO$_2$-n or SiO$_2$-FITC-treated lungs showed regions with increased macrophage numbers, slightly deteriorated structure and beginning hypercellularity. These changes were absent in lungs treated with SiO$_2$-p and in vehicle-treated control lungs (Additional file 1: Figure S1).

Identification of phospholipid species with MALDI-MS

To get information about particle-related changes of the local PLC we analyzed representative cryo-sections of the lung from a vehicle-treated control animal for phospholipid distribution by MALDI-MS and secondary to the application of inflammatory SiO$_2$-n or SiO$_2$-FITC, as well as non-inflammatory SiO$_2$-p NPs. Figure 3 shows low power micrographs of the sections and respective MALDI-MS ion images for mass-to-charge ratio (m/z) of 835.9 assigned to PI (34:1). This molecule gave a sufficient contrast in the negative ion mode and was selected as a starting point to highlight the distributional disparities between the three surveyed nanoparticle species. The lateral resolution (50 µm) of the method allowed to visualize major tissue components such as large and medium-sized bronchi.

The vehicle-treated control lung (Fig. 3a, b) exhibited a largely homogeneous distribution of PI (34:1) and all other detected m/z (Additional file 1: Figure S4). Signal inhomogeneity in this case was attributable to compression artifacts (lower right margin) or to a partial loss of the tissue (left hand side), as was evident from the low-power micrograph (Fig. 3a). Of note, as the pseudocolor scale reflects relative intensity values and spreads the complete set of data from 0 to 100%, a comparison of absolute values cannot be made for different treatments, i.e., between different tissue sections. Yet, absolute intensity values within one tissue section can be compared.

Particle treatment could change the homogeneous lipid distribution pattern in a striking manner: While SiO$_2$-p had no influence on the lipid distribution (Fig. 3d), SiO$_2$-FITC NPs induced round-shaped patchy regions within which the PI (34:1) signal was

Großgarten *et al. Particle and Fibre Toxicology* (2018) 15:31

Page 4 of 16
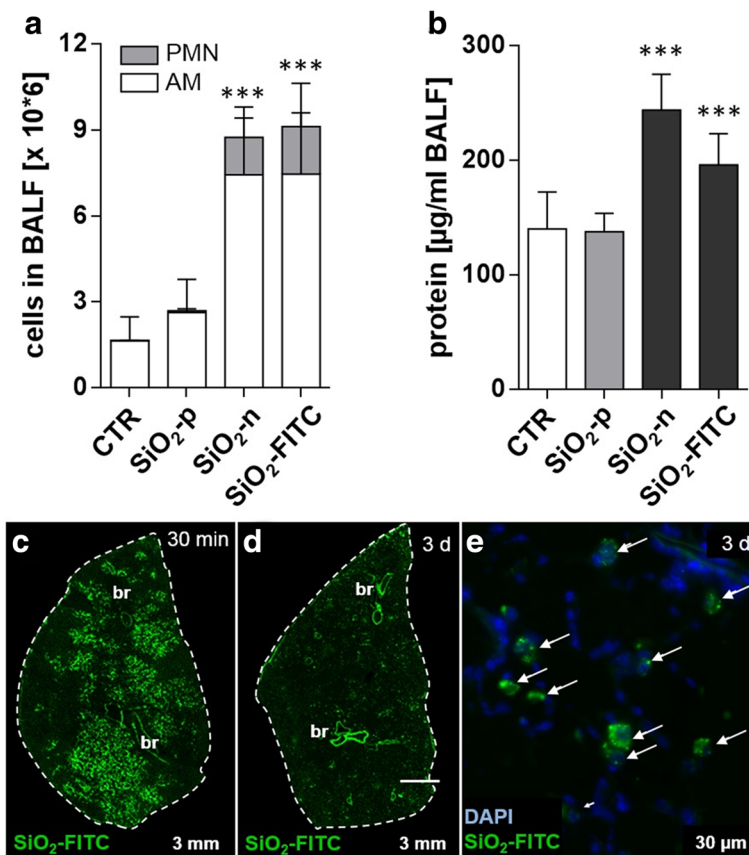
Fig. 2 Effects of SiO$_2$-n, SiO$_2$-FITC, and SiO$_2$-p in vivo and distribution of SiO$_2$-FITC in the lung. SiO$_2$-n, SiO$_2$-p, SiO$_2$-FITC NPs were intratracheally instilled into rat lungs (0.36 mg per animal, $n = 5$ animals per group) and compared to vehicle-treated controls (CTR). **a, b** Analysis of broncho-alveolar lavage fluid 3 d post instillation: **a** alveolar macrophages (AM) and polymorphonuclear leukocytes (PMN); **b** total protein concentration. Columns represent means ± standard deviation; significance was tested by ANOVA and post-hoc Dunnett's multiple comparison test (***: $p \leq$ 0.001). **c-e** Fluorescence micrographs of transversal cryo-sections of the left lung resected 30 min (**c**), and 3 d (**d, e**) after intratracheal instillation of SiO$_2$-FITC. Dashed lines mark the outer rim of each section. Large bronchi (br) appear as strongly autofluorescent structures. **e** Detail of the section shown in (**d**); nuclei of lung cells were visualized with 4′, 6-diamidin-2-phenylindol (DAPI). Note that the fluorescent signal is confined to phagocytic cells (arrows) which were identified as alveolar macrophages in preceding studies

strongly increased (Fig. 3h). Similarly, but with larger heterogeneity, SiO$_2$-n induced several regions with increased PI (34:1) (Fig. 3f).

To analyze whether there is a congruency of particle distribution and the pattern of increased PI (34:1) intensity, we compared serial sections of the same lung for their distribution patterns of FITC fluorescence and PI (34:1). Figure 4 shows the overview distribution of FITC fluorescence and the PI (34:1) signal: Hand-drawn regions demarcating PI (34:1)-enriched regions were transferred from Fig. 4b to the fluorescent image of Fig. 4a. Although connective tissue around bronchiolar structures and blood vessels stands out clearly due to considerable autofluorescence, fluorescent dots in PI (34:1)-enriched regions are far more numerous. At higher magnification these fluorescent signals represent SiO$_2$-FITC-laden cells (compare Fig. 2e) which have gathered the fluorescent material.

In the next step we imaged further (phospho) lipids and analyzed if distribution changes were congruent to the patchy PI (34:1) signal elicited by SiO$_2$-n and SiO$_2$-FITC. These in-depth analyses were carried out on sections of lungs instilled with SiO$_2$-FITC (Fig. 5), particle-free instillation fluid (Additional file 1: Figure 4S), and SiO$_2$-p (Additional file 1: Figure 5S). Figure 5 displays the MALDI-MS ion images of distinct m/z representing a variety of phospholipids detected in negative ion mode in the lung section originating from a rat instilled with SiO$_2$-FITC NPs. Detected m/z were classified as phosphatidylglycerol (Fig. 5b, c), phosphatidylinositol (Fig. 5d-f) and phosphatidylserine (PS) (Fig. 5g), each featuring two fatty acyl residues. The assignment of m/z 966.1 (Fig. 4h) as triacylglycerine (TAG) will be discussed below. Shorthand designations, which will be used in the next section, represent the length of the carbon chains summarizing all fatty acyl

Großgarten *et al. Particle and Fibre Toxicology* (2018) 15:31

Page 5 of 16
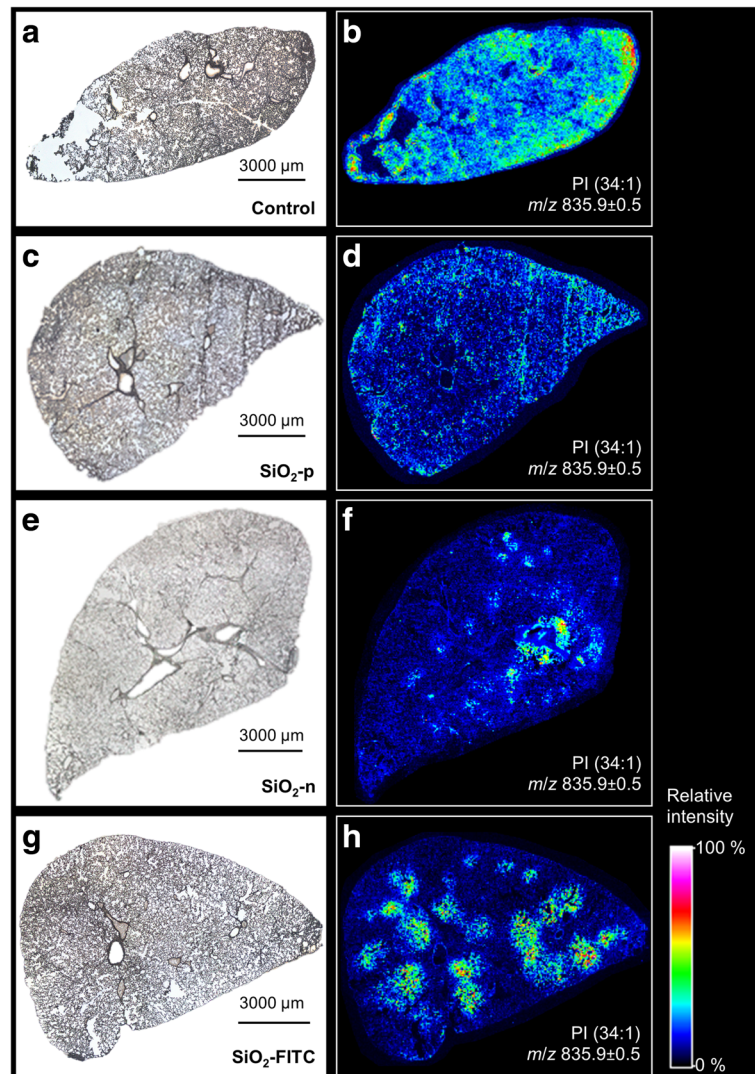
Fig. 3 Local increases of PI concentration in the rat lung upon SiO$_2$ NP treatment are abrogated by phosphonate coating. Distribution of phosphatidylinositol PI (34:1) 3 d after instillation of SiO$_2$-n, SiO$_2$-p, or SiO$_2$-FITC (0.36 mg/lung): Microscopic images of the investigated cryo-sections (left) and corresponding MALDI-MS ion images of *m/z* 835.9 (right, detected as [M-H]$^-$ in negative ion mode) of rat lung treated with **a**, **b** vehicle, **c**, **d** SiO$_2$-p, **e**, **f** SiO$_2$-n, or **g**, **h** SiO$_2$-FITC. Note the patchy occurrence of PI upon SiO$_2$-n and SiO$_2$-FITC, but not upon SiO$_2$-p. The seemingly high signal of the vehicle-treated control section results from automated scaling of the relative signal intensity

residues and the degree of unsaturation, i.e. the number of double bonds within fatty acid chains. Most striking, the round-shaped regional overexpression of the previously mentioned PI (34:1) with a *m/z* of 835.9 (Fig. 5d) was largely colocalized with *m/z* which can be assigned to [M-H]$^-$ ions of PI (36:2) (*m/z* 861.9), and PI (38:4) (*m/z* 885.9, Fig. 5e, f). Interestingly, highest concentration of PI (38:4) apparently lined the larger bronchi. The pattern of round-shaped regional increases was found, to a lesser extent, also for *m/z* corresponding to phospholipids of the phosphatidylglycerol (PG) class (Fig. 5b, c), such that the overexpression patterns of PIs and PGs were highly co-located.

Compared to PIs and PGs, a mild inversely correlating distribution was found for *m/z* 788.9 assigned to PS (36:1) (Fig. 5g), and in an even more pronounced manner also for *m/z* 966.1 (Fig. 5h). The contrastive distribution of different phospholipids is further shown in an overlay image of *m/z* 788.9 and *m/z* 835.9 (Fig. 5i).

For verification purposes, two exemplary *m/z*, namely, *m/z* 721.4 assigned to PG (32:0) and *m/z* 861.5 assumed to be PI (36:2) were selected as precursor ions for tandem mass spectrometry (MS/MS) experiments. Mass spectra of their characteristic fragments (Additional file 1: Figures S2 and S3) confirm the abundance of PIs and PGs as the major phospholipid classes detected in the negative ion
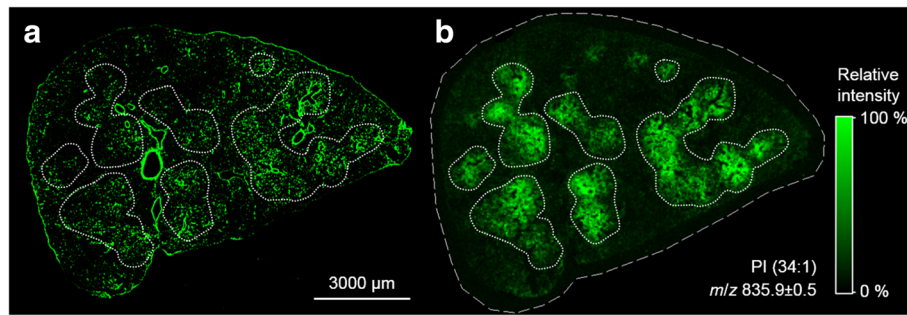
Fig. 4 Correlation of nanoparticle distribution and local PI overexpression. Cryo-section 3 d post instillation of SiO_2-FITC NPs. **a** Fluorescence overview image visualizing the principal distribution of NPs mainly located in alveolar macrophages. **b** MALDI-MS ion image of PI (34:1) ([M-H]$^-$) in a parallel tissue section (bordered by a dashed line). The fine dotted lines demarcate seven main areas of PI overexpression. These areas were transferred to the fluorescence image in (**a**) to show the co-localization with FITC fluorescence. Large blood vessels and bronchioli show strong autofluorescence, but no PI signal
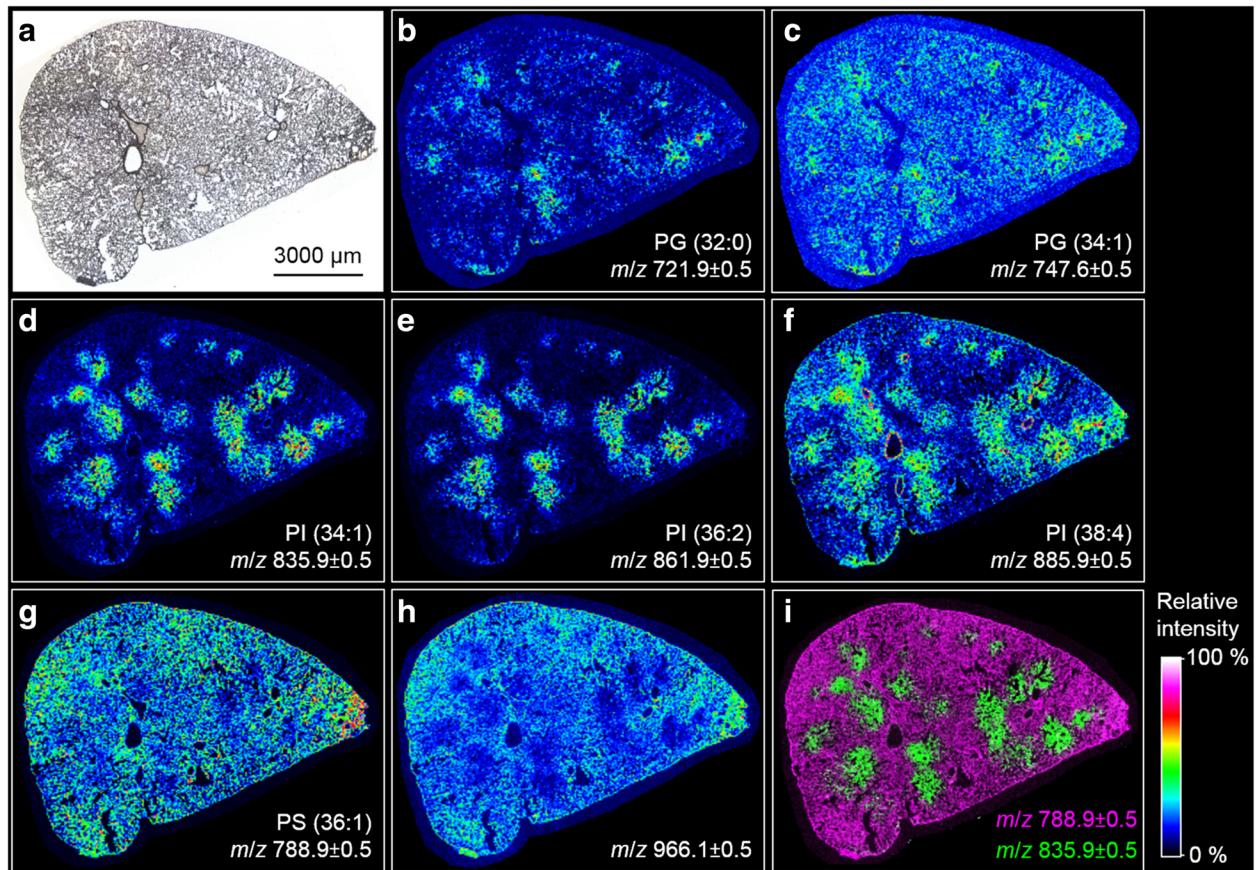
Fig. 5 MALDI-MS ion images of local changes of lipid concentration in the SiO_2-FITC laden rat lung. Cryo-section from an animal 3 d after intratracheal instillation of 0.36 mg SiO_2-FITC NPs. **a** Microscopic image of investigated cryo-section. **b, c** Ion images indicating a minor local overexpression of PGs. **d**-**f** Ion images with pronounced local overexpression of PIs. **g, h** Ion images of m/z 788.0 ± 0.5 and 966.1 ± 0.5 revealing an inversely correlating distribution of PS and TAG compared to the PIs shown in (**d, e**) and (**f**). **i** Overlay of MS ion images shown in (**d** and **g**); m/z are assigned to ion [M-H]$^-$

Großgarten *et al. Particle and Fibre Toxicology* (2018) 15:31

Page 7 of 16

mode. They further indicate that PG (32:0) consists of two (16:0) chains (Additional file 1: Figure S4), while for PI (36:2) both fatty acyl compositions, PI (18:1|18:1) and PI (18:0|18:2), are deduced (Additional file 1: Figure S5).

Since especially the ratio PI/PG is a well-known marker of lung affection in BALF, we calculated a local PI/PG on the basis of absolute intensity data. Regions of interest (ROIs) were defined on sections of SiO$_2$-FITC-treated and vehicle-treated lungs, within which the signal intensities of PI (34:1) (*m/z* 835.9) and PG (34:1) (*m/z* 747.6) were integrated from 600 spectra. On an untreated lung tissue section, where phospholipids appeared evenly distributed, a control ROI was chosen randomly. Its absolute intensity values were 0.67 a.u. (arbitrary units) for PI (34:1) and 0.36 a.u. for PG (34:1), resulting in a PI/PG of 1.9. On a lung section from a SiO$_2$-FITC instilled animal, a ROI with an apparent local PI overexpression was chosen. The absolute intensities therein were calculated as to be 2.15 a.u. for PI (34:1) and 0.38 a.u. for PG (34:1) resulting in a high local PI/PG ratio of 5.7. Together with the localization of SiO$_2$-FITC the result shows that the PI/PG was locally increased in SiO$_2$-FITC-laden regions.

In contrast to PI and PG, we found *m/z* 966.1 and other closely related masses to be lowered in particle-laden regions (Fig. 5h). Results obtained by MALDI-MS suggest that *m/z* 966.1 represents a triacylglyceride TAG (60:4). Interestingly, the signal was co-distributed with closely related molecules whose peaks showed mass differences of two mass units (*m/z* 964.0, 966.0 and 968.0, see Fig. 6) and,

therefore, might correspond to related TAGs whose number of double bonds range from 3 to 5. Further evidence for the correct detection of TAG comes from the co-distribution of a DAG-like derivative *m/z* 605.7 (Fig. 6a) because this fragment is derived from TAG in tissue by cleavage of a fatty acyl residue [27].

None of the aforementioned patchy irregularities of the PLC was observed in the vehicle-treated or SiO$_2$-p--treated animals, as is shown in Additional file 1: Figures S4 and S5 of the Supplementary Information.

Fourier transform infrared microspectroscopy and hierarchical cluster analysis

Unlike MALDI-MS Fourier transform infrared (FT-IR) microspectroscopy provides molecule specific information based on the investigation of spectral fingerprints consisting of vibrations which can be assigned to functional groups of the building blocks of biological tissues, such as lipids, proteins, carbohydrates, and nucleic acids. To test whether lipid-enriched areas seen with MALDI-MS could be verified with another independent technique, FT-IR microspectroscopy was carried out on parallel sections of the SiO$_2$-FITC laden rat lung tissue, i.e. adjacent to the sections investigated with MALDI-MS. The pre-processed spectral data generated by means of FT-IR imaging were subjected to a hierarchical cluster analysis (HCA), which is a powerful tool to statistically validate the spectral disparities between the pixels within an image. Figure 7 shows average spectra of two ascertained clusters (cluster
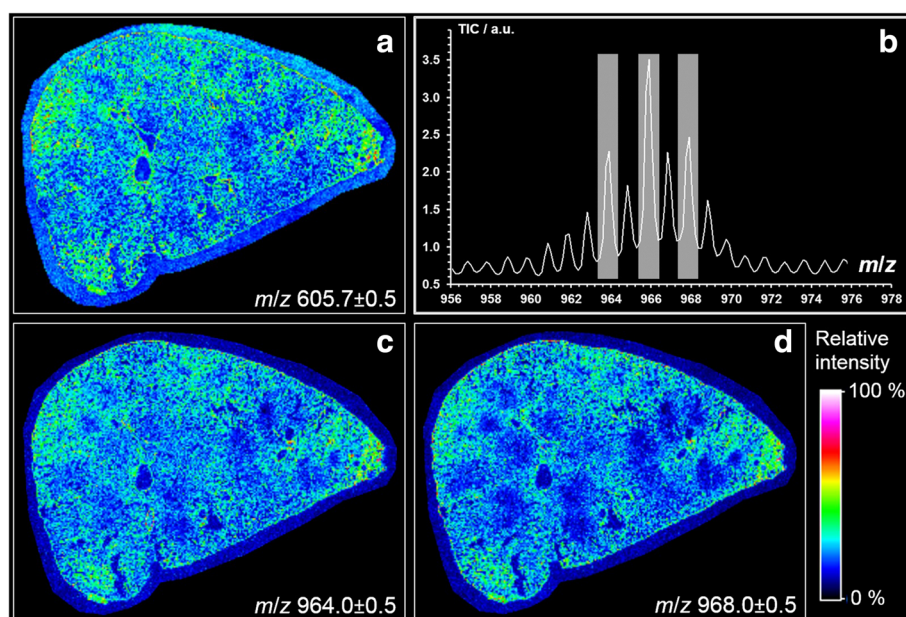
Fig. 6 MALDI-MS ion images showing the local distribution of TAG and DAG-like molecules in a SiO$_2$-FITC laden rat lung. Cryo-section from an animal 3 d after intratracheal instillation of 0.36 mg SiO$_2$-FITC NPs. Ion images of **a** *m/z* 605.7 from DAG-like fragment (36:1) as [M–H$_2$O + H]$^+$ detected in the positive ion mode, **c** *m/z* 964.0 assumed to be TAG (60:5), **d** *m/z* (968.0) assumingly from TAG (60:3). **b** Relevant section of the average MALDI-MS spectrum (negative ion mode) of the analysis of the rat lung tissue shown in (**c** and **d**)

Großgarten *et al. Particle and Fibre Toxicology* (2018) 15:31

Page 8 of 16
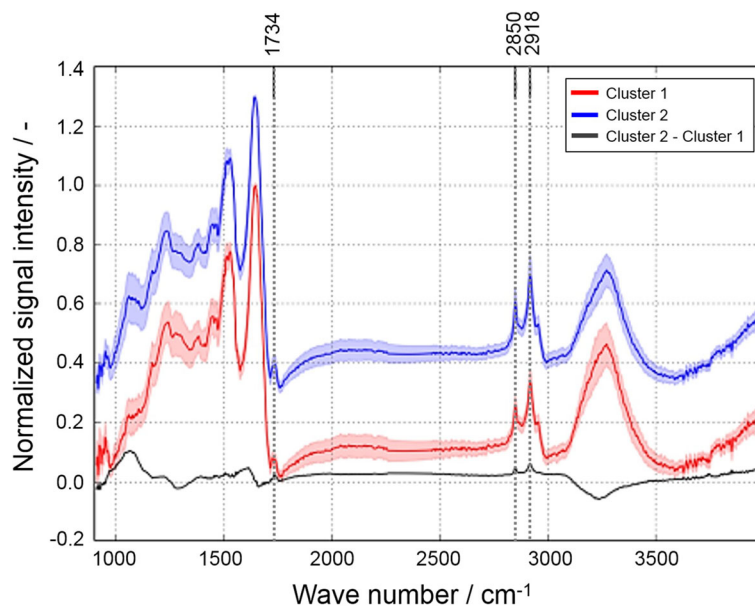
Fig. 7 FT-IR microspectroscopy of a cryo-section from a SiO$_2$-FITC-laden rat lung. Average spectra and standard deviation from hierarchical cluster analysis. Red spectrum: cluster 1; blue spectrum: cluster 2 (an offset was added to cluster 2 for better visualization); black spectrum: difference spectrum (cluster 2 - cluster 1). Dashed lines mark wavenumbers identifying lipids. Protein bands are highlighted in grey

1: red line; cluster 2: blue line) along with their difference spectrum (cluster 2 - cluster 1: black line). Three positive deviations at defined position of this difference spectrum (arrows in Fig. 7) indicate that the blue cluster pixels have more intense vibrations resulting from lipids (CH$_2$ asymmetric stretching vibration at 2918 cm^{-1} and CH$_2$ symmetric stretching vibration at 2850 cm^{-1}) and esters of free fatty acids (C=O stretching vibration at 1734 cm^{-1}). In contrast, the red cluster pixels show increased signal intensities for bands in the spectral ranges of 1695–1620 cm^{-1}, 1580–1480 cm^{-1}, and 3290 cm^{-1} (grey areas in Fig. 7) which can be assigned to peptide groups termed Amide I, Amide II and Amide A, respectively. It can thus be concluded that the red cluster 1 indicates areas of higher protein signal, while the blue cluster 2 corresponds to areas with higher lipid content.

Figures 8a-d show the superposition of the spatially resolved images of clusters 1 and 2 to the MALDI-MS image of PI (34:1, *m/z* 835.9), and the optical image of the SiO$_2$-FITC laden lung tissue section from Fig. 8b. Comparing the color-coded regions it can be seen that the lipid-enriched cluster 2 pixels (blue) were largely co-localized with PI (34:1) (Fig. 8d), whereas protein-enriched cluster 2 pixels (red) were evenly distributed throughout the lung parenchyma but were lowered in PI (34:1) enriched regions (Fig. 8c). Thus, the detection of lipid enrichment by FT-IR microspectroscopy confirms results from MALDI-MS studies on adjacent sections.

Discussion

This study has shown that the cytotoxicity and acute inflammation typically induced by SiO$_2$-n or SiO$_2$-FITC NP was not elicited by SiO$_2$-p, whose surface is modified by phosphonate residues. The primary distribution of SiO$_2$-FITC administered to the lung was mirrored by local changes of PI, PG, PS and TAG as measured for the first time by MALDI-MS and confirmed by FT-IR spectroscopy. A similar patchy distribution of phospholipids was obtained in SiO$_2$-n-treated, but not in vehicle-treated lungs. Importantly, SiO$_2$-p evoked no such changes in the local (phospho) lipid composition pattern. Together the findings suggest that alterations in PLC were secondary to local inflammatory processes.

Effects of phosphonate coating on bioactivity of SiO$_2$

The cytotoxic, membrane disrupting and/or hemolytic potential of amorphous silica has been attributed to silanol groups at the particle surface [6–9]. Pandurangi et al. observed a correlation between the concentration of surface silanol groups determined by means of FT-IR spectroscopy and the hemolytic activity of silica particles expressed as enhanced cell lysis of sheep blood erythrocytes [8]. Adverse effects of silica may, therefore, be reduced by modifying surface silanol groups, as shown for cristobalite which lost its cytotoxicity upon heating to 1300 °C, a treatment which condenses silanol groups to siloxane bridges [9]. Cytotoxic and inflammatory effects of silica may also be suppressed by coating with hydrophobic substances [28], polyvinylpyridine-N-oxide [29], or amino
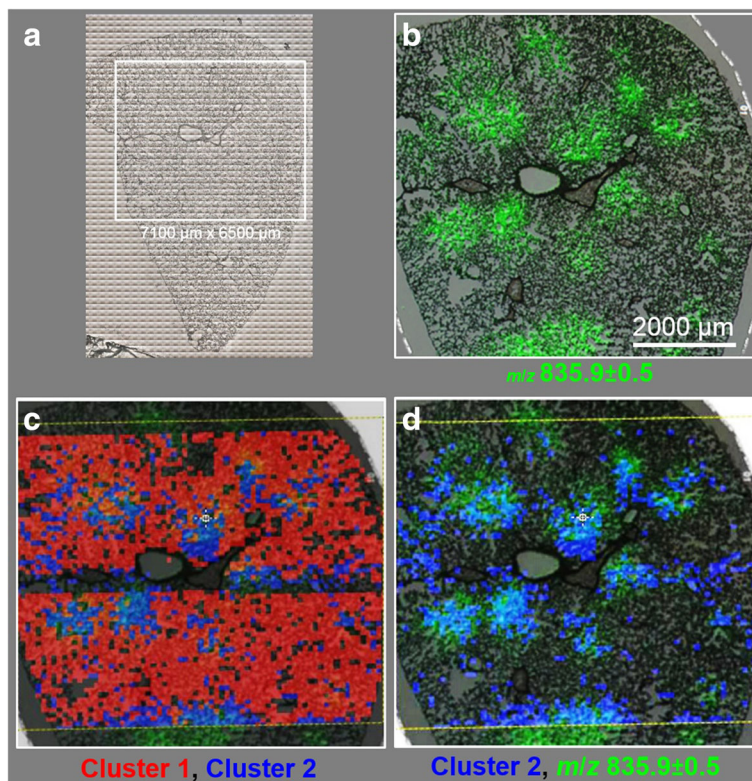
Fig. 8 Comparison of MALDI-MS imaging with FT-IR spectroscopy followed by add-on hierarchical cluster analysis. **a** Optical image of lung cryo-section. Region inside the white box was analyzed by means of FT-IR imaging. **b** Overlay of optical image with MALDI-MS ion image of PI 34:1 of the marked area. **c** Overlay of (**b**) with cluster 1 (red) and cluster 2 pixels (blue), as derived from HCA of FT-IR data analysis (Fig. 6). **d** Overlay of (**b**) with cluster 2 pixels (blue), indicating that their positions are largely co-located with regions of PI overexpression

groups [12]. As the TPMP coating of SiO_2-n, which generated the SiO_2-p used in this study, largely reduced cytotoxic and inflammatory properties, phosphonate residues appear well suited to protect cell and tissue components against effects of silanol groups or other types of surface reactivity. Interestingly, a reduction of particle reactivity in vitro and in vivo has also been achieved for NP composed of rare earth elements [30] or of partially soluble metals such as Ni, Co, and Cu [31] using ethylenediamine tetra (methylene phosphonic acid) (EDTMP) as a coating agent. However, EDTMP can chelate metal ions released from NP surface [31] and this mode of action may underlie the beneficiary effect of EDTMP which, therefore, differs from that of TPMP. Nevertheless the outwardly directed phosphonate residues of both, EDTMP and TPMP, seem to confer a high degree of biocompatibility to NPs.

Although phosphonate coating lowered the cytotoxicity of SiO_2-n, SiO_2-p dose-dependently increased the release of H_2O_2 from alveolar macrophages in vitro (Fig. 1c). Similar to primary alveolar macrophages, NR8383 cells respond to specific stimuli such as the non-cytotoxic zymosan with an oxidative burst [32]. However, the mechanism underlying the augmented induction of H_2O_2 by SiO_2-p is

unknown. At least for high concentrations of SiO_2-n (and also for other nano-sized amorphous silica materials, own unpublished observations) there is a tendency to induce a release of H_2O_2 from NR8383 cells but this effect may be counteracted by the cytotoxicity of SiO_2-n under serum-free conditions. The enhanced formation of H_2O_2 upon SiO_2-p may, therefore, be favored by the low cytotoxicity of the phosphonated material, although a more direct stimulation of H_2O_2 generating processes cannot be excluded. Of note, the comparatively low dose of SiO_2-p had no obvious effect on the lung as it elicited neither signs of tissue damage, nor did it increase inflammatory cell counts in the lavage fluid.

Methodological considerations of MALDI-MS
MALDI-MS is most commonly used for the spatially resolved determination of biomolecules such as lipids and proteins as well as drugs and their metabolites [33–35]. Due to fast laser scan speed and high sensitivity, while covering a broad mass range, MALDI-MS provides high potential for the determination of lipids and has successfully been applied to study the composition of broncho-alveolar lavage fluid [36, 37]. In the lung a fairly even distribution of phospholipids has been shown for the lung parenchyma by

Großgarten *et al. Particle and Fibre Toxicology* (2018) 15:31

Page 10 of 16

MALDI-MS, whereas there was a differential overexpression of arachidonate/docosahexaenoate phospholipids and sphingomyelin molecular species lining the profiles of larger bronchioli and blood vessels, respectively [35].

Surprisingly, no information is available on the influence of nanoparticles on the spatial distribution of phospholipids in lung tissue [35]. By weight, ~ 90% of the lung surfactant consists of lipids, from which phosphatidylcholine (PC) is the major component (70–80%). In addition, variable amounts of phosphatidylglycerols (7–18%), phosphatidylinositols (2–4%), and phosphatidylethanolamines (2–3%) are contained [38]. As the MALDI-MS analyses presented here were conducted in the negative ion mode, acidic phospholipids such as the low abundance PIs and PGs are preferably detected and this is in contrast to PCs, which are rather ionized in positive mode. To properly assign the detected m/z to corresponding (phospho) lipid species, we first analyzed published MALDI-MS analyses of rat BALF for respective phospholipid classes [35, 39, 40]. Next, we compared experimental and theoretical m/z values from the Metabolomics Workbench Metabolite Database and the LIPID MAPS Structure Database to assign the m/z detected during MALDI-MS to distinct phospholipid species. To finally confirm the assignments and deduce the composition of the individual fatty acyl residues, MS/MS experiments were conducted regarding distinct m/z. Phospholipid species were identified via characteristic fragment ions. With this strategy phosphatidylglycerols PG (32:0) and PG (34:1) as well as the phophatidylinositols PI (34:1), PI (36:2), and PI (38:4) were confirmed in the rat lung. It could also be shown by MS/MS experiments (Additional file 1: Figure S2) that PG (32:0) is composed of PG (16:0|16:0). This finding is in accord with a previous study on the composition of BALF phospholipids [40], which also suggests that PG (34:1) is composed of a 16:0 and an 18:1 fatty acyl residue. With respect to PI species the same study on BALF composition showed that PI (34:1) is PI (16:0|18:1), and PI (38:4) is PI (18:0|20:4). For PI (36:2) it was found that it is build up from two 18:1 chains [40]. This finding was also confirmed by MS/MS experiments (Additional file 1: Figure S3), which furthermore identified PI as to be composed of (18:0|18:2). In general, PI species with highly unsaturated acyl residues are highly abundant in BALF and, therefore, seem to be characteristic components of the rodent lung surfactant [40].

Although MALDI-MS is a highly reliable technique one should keep in mind that the detection of distinct phospholipid species is not only concentration-dependent, but also a matter of accessibility to ionization. Intensity differences observed for specific ions likely show differences in amounts of lipids within the sample, however, the final estimation is subject to some limitations [41]. More specifically, experimental and theoretical m/z ratios showed a systematic bias ($\Delta = -0.3$ Da) possibly caused by the topographical structure of the cryo-section and/or the small height difference of the calibration standard, which had to be pipetted onto the sample target as a small droplet. Notably different starting locations of desorbed ions at the time of acceleration lead to a deviation in the drift time, thus negatively affecting mass resolution. We are aware that all these restrictions make MALDI-MS a semi-quantitative method. Nevertheless, the changes of PI and PG in SiO_2–n and SiO_2-FITC NP laden areas, which were imaged with MALDI-MS and confirmed by MALDI MS/MS for the first time, are highly plausible and especially the locally observed increases in PI/PG ratio are in accordance with previous particle-elicited changes of PI and PG in BALF of animals treated with crystalline silica [20].

Specific changes of phospholipids in the lung

As outlined above, many amorphous SiO_2 particles and especially crystalline quartz elicit strong inflammation which, in case of quartz, progressively develops into lung fibrosis, accompanied or proceeded by an increased PI/PG ratio [20–22, 42]. The mechanisms underlying these changes in lipid composition are not fully understood. With respect to the local accumulation of PI and other phospholipids (see Figs. 3 and 4) a simple binding to the large surface of deposited SiO_2-n or SiO_2-FITC can be ruled out, because phosphonate coating had neither a major effect on polarity or surface charge of SiO_2-n NP, nor had it an influence on the binding of native surfactant, at least under in vitro conditions [14]. It has been suggested that silica acts on alveolar type 2 cells and induces a switchover in the biosynthesis of phospholipids from the same precursor, thus enhancing PI and suppressing PG synthesis [21]. Further mechanisms may involve a release of ATP from damaged cells followed by an ATP-stimulated secretion by type 2 epithelial cells [43] and/or changes of the activity of specific cleaving enzymes such as phospholipase A2 or phospholipase C [24]. Furthermore, phospholipids are differentially taken up by alveolar type 2 cells and/or macrophages with PI being ingested to a lesser extent both in vitro and in vivo [44, 45]. Based on these studies it appears plausible that more than one mechanism contributes to the local changes of (phospho) lipid concentration elicited by SiO_2-FITC or SiO_2-n.

An increased PI/PG increases the rigidity and lowers the surface activity of the surfactant [25] which might be beneficial e.g. for the repair of local tissue damage. Concerning an impact on local inflammation, in vitro experiments suggest that elevated concentrations of PI attenuate the non-specific inflammatory reaction via a reduced production of nitric oxide and tumour necrosis factor alpha (TNF-α) from alveolar macrophages [46]. Considering these findings and the fact that SiO_2-FITC NPs were mainly localized in alveolar macrophages but not within alveolar type-2 cells led us to suggest that the locally increased ratio PI/PG may originate, at least in part, from the population of NP-affected

alveolar macrophages. These cells, when sufficiently loaded with particles, have been shown to release mediators or signalling molecules, which might act on alveolar type-2 cells via specific pathways. This interpretation appears in line with the striking reduction of cytotoxic SiO_2-n effects on NR8383 macrophages in vitro and the abrogation of inflammation in vivo upon phosphonate coating (see Figs. 1 and 2). A role of macrophages or other inflammatory cells such as neutrophilic granulocytes may also be suspected from a work describing dose-dependent changes of PI/PG in BALF from rat lung upon quartz DQ12: In that study PI/PG developed along with the numbers of cells in BALF, the majority of which were macrophages [20, 47]. In the present study we found that SiO_2-n and SiO_2-FITC but not SiO_2-p led to focal assemblies of macrophages in the lung parenchyma, intermingled with regions of beginning hypercellularity and some structural loss of alveolar septa (Additional file 1: Figure S1). It appears likely that these regions are structural correlates of the patchy areas with increased PI/PG ratio in SiO_2-n and SiO_2-FITC treated lungs. Future imaging studies with increased resolution are needed to shed more light on the cellular components involved in particle-induced (phospho) lipid changes in lung tissue.

Apart from the changes in phospholipids there was a decrease in TAG in regions where SiO_2-FITC was accumulated. Although the final identification of these TAG species awaits further experiments (e.g. tandem MS and high-energy collision induced dissociation and/or high-resolution mass analysis), their presence is highly likely due to the congruent distribution of the DAG-like derivative m/z 605.7 (Fig. 5) which are derived from TAG in tissue by cleavage of a fatty acyl residue [27]. The local diminution of TAG concentration may reflect its consumption for phospholipid production: TAG is utilized for the formation of dipalmitoyl lecithin, which is the principal lipid in the lung surfactant [48] and which dose-dependently increases in BALF e.g. upon application of quartz to the lung [47]. A lowering of TAG might, therefore, mirror e.g. the new formation of lung surfactant. A decrease of TAG was also found for homogenates of quartz-treated silicotic rat lungs, if values were normalized to the treatment-increased lung weights [48]. As MALDI-MS reports on the concentration of a metabolite in tissue, local decreases of TAG in SiO_2-FITC laden regions are in line with these findings.

Unlike MALDI-MS, with FT-IR imaging methods molecular information is not generated instantaneously, but through the determination of spectral fingerprints, which can be assigned to particular functional groups in the building blocks of biological tissues, such as lipids, proteins, carbohydrates, and nucleic acids. Besides these building blocks, characteristic biochemical markers of disease are detected and identified. Thus, although FT-IR imaging enables the distinction between healthy

and initial-to-advanced states of disease [49], the method has not yet been applied for the examination of nanoparticle-affected lung tissues. Results obtained here appear, however, highly plausible as they showed accumulated lipids, which were confirmed by MALDI-MS as to be mainly related to PI and PG. Furthermore FT-IR spectroscopy revealed a local decrease in protein. Other infrared spectroscopic studies similarly demonstrated an increase in the overall lipid concentration accompanied by a decrease in protein concentration and suggested these changes as suitable markers for cytotoxic [50] or apoptotic changes in cells [51, 52]. With respect to the whole lung, an increase in total phospholipid lung content was observed several days after administration of silica [53], and this effect may involve a transport of de novo formed lipids from liver to lung [48]. As a whole, the locally enhanced lung lipid content in SiO_2-NP laden areas observed here by means of FT-IR analysis appears to be in line with older results. Application of FT-IR spectroscopy therefore may become important in the field of lung toxicology and histology [54].

Conclusions

In this study, laterally resolved information on changes in phospholipid and distribution upon SiO_2-n and SiO_2-p NPs instilled into the rat lung were demonstrated for the first time by utilizing two powerful bioimaging techniques. MALDI-MS analysis of rat lung tissue sections revealed a local overexpression of PIs and, to a lesser extent, PGs. The pattern of changes was largely congruent with the distribution pattern of SiO_2-FITC in the lung tissue. FT-IR analyses of a neighboring cryo-sections combined with a subsequent hierarchical cluster analysis revealed regions representing enhanced lipid content, which corresponded invariably with the PI pattern. Notably, these observations were true only for lungs treated with SiO_2-FITC and SiO_2-n nanoparticles, but not for lungs which received SiO_2-p, or for vehicle-treated controls. This disparity was in excellent accordance with in vitro and in vivo toxicity studies which showed that SiO_2-n or SiO_2-FITC but not SiO_2-p induced cytotoxicity and lung inflammation. As the in vitro binding of major surfactant lipids to SiO_2-n and SiO_2-p is virtually equal [14], we conclude that the locally increased PI/PG ratio is primarily due to early cytotoxic effects of instilled SiO_2-n or SiO_2-FITC.

In sum, bioimaging revealed spatially resolved tissue remodeling of nanoparticle-affected tissue. The results show that changes in phospholipid composition depend on particle surface coating and are related to the particle distribution in the tissue. Therefore, the complementary use of MALDI-MS and FT-IR imaging is assumed to hold a great potential for the examination of health and disease states in biological tissue samples.

Großgarten *et al. Particle and Fibre Toxicology* (2018) 15:31

Page 12 of 16

Table 1 Particle characterization and properties under study conditions (taken from [55])

	SiO$_2$-n	SiO$_2$-FITC	SiO$_2$-p
Primary particle size (TEM)	5–50 nm	23–30 nm	5–50 nm
Average size (AUC)	19 nm	25 nm	19 nm
Zeta potential, pH 7.4	−39 mV	− 39 mV	− 42.9 mV
BET surface	200 m^2·g^{-1}	178 m^2·g^{-1}	200 m^2·g^{-1}
Crystallinity (XRD)	Amorphous	Amorphous	Amorphous
Morphology	Mostly spherical	Mostly spherical	Mostly spherical
Surface chemistry in XPS	O: 66 at.% Si: 29 at.% C: 4 at.% Na: 1 at.%	O: 63 at.% Si: 29 at.% C: 8 at.%	O: 66 at.% Si: 29 at.% C: 5 at.% Na: 0.5 at.% PO$_2$, PO$_3$: 0.5 at.%
pH of stock suspension	10.2	8.7	10.8
d$_{50}$ in H$_2$O (NTA)	47.5 ± 0.7 nm	n.m.	64.5 ± 10.6 nm
d$_{50}$ in KRPG buffer (NTA)	65.3 ± 7.5 nm	n.m.	60.7 ± 7.8 nm
d$_{50}$ in F-12 K medium (NTA)	73.3 ± 14 nm	n.m.	59.3 ± 8.1 nm
d$_{50}$ in instillation fluid (NTA)	61.5 ± 7.8 nm	51.0 ± 4.2 nm	50.0 ± 17.0 nm

TEM Transmission electron microscopy, *AUC* analytical ultracentrifugation, *XRD* X-ray diffraction, *XPS* X-ray photoelectron spectroscopy, *NTA* NanoSight tracking analysis, *KRPG* Krebs-Ringer phosphate glucose, *d$_{50}$* median diameter, *n.m.* not measured

Methods

Nanoparticle characterization

Colloidal SiO$_2$ NPs, the TPMP-treated modification thereof, and fluorescein isothiocyanate-labeled SiO$_2$ NPs were provided by project partners of the NanoGEM project and have been extensively characterized before [13, 55]. Additionally, particle suspensions were investigated with a NanoSight instrument (LM-10, Malvern Instruments Ltd., Worcestershire, UK), equipped with a LM14 laser device (535 nm) and NTA software 2.1 to 2.3. All data are summarized in Table 1. The particles showed a similar size under conditions of in vitro (serum-free F-12 K medium and KRPG buffer) and in vivo testing.

In vitro toxicity study

The rat alveolar macrophage cell line NR8383 was cultured in 175 cm^2 culture flasks in F-12 K medium (Biochrom GmbH, Berlin, Germany) supplemented with 15% heat inactivated standardized fetal calf serum at 37 °C and 5% CO$_2$. Cell culture testing of SiO$_2$ NPs was carried out as described by Wiemann et al. [56]. In brief, NR8383 alveolar macrophages were incubated with ascending concentrations of particles in F-12 K medium under serum-free conditions. Assays were run in triplicates in 96-well plates (with 3×10^5 cells per well) and 3 independent experiments were conducted. Untreated cells were used as negative controls. Macrophage supernatants were analysed for typical signs of inflammation indicated by the release of lactate dehydrogenase, glucuronidase, and TNF-α 16 h after addition of the particles. LDH and Glu activities were expressed as % of the positive control value, which was obtained by adding 0.1% Triton X-100. The concentration of TNF-α was

measured using 50 μL of the supernatant from each well for inducing apoptosis in L-929 fibroblasts in the presence of actinomycin D and expressed as % killing activity. To measure the release of H$_2$O$_2$, cells and particles were prepared in Krebs-Ringer phosphate glucose (KRPG) buffer. Quantitative measurements were carried out in the presence of horseradish peroxidase using resorufin as a detection reagent, which was added for 90 min during application of the particles. In all assays cell-free controls were run in parallel to test for particle interferences with the assays.

Animal study

Female rats (Wistar strain WU, 200–250 g, Charles River Laboratories, Sulzfeld, Germany) were maintained with a 12 h lights-on lights-off cycle with food and water being provided ad libitum. Animals were housed at least 14 d before the experiments were commenced. All animal experiments were ethically approved by local authorities (LANUV, Dortmund, Germany) and were carried out in the animal facility at the University Clinics of Essen, Germany.

Instillation fluid was prepared using a sterile mixture of 0.9% NaCl (9 parts by volume) and sodium buffered phosphate buffer, pH 7.3 (one part by volume). Phosphate concentration was 1 mmol·L^{-1} and maintained a pH of the instillation fluid in the physiologic range. SiO$_2$-n, SiO$_2$-p and SiO$_2$-FITC particles were diluted from respective stock solutions to a final concentration of 0.72 mg·mL^{-1}. Particle-free instillation fluid was administered to control animals thus generating vehicle-treated controls. For intratracheal instillation, rats were briefly anaesthetized with isoflurane. A total amount of 0.36 mg in 500 μL instillation

Großgarten *et al. Particle and Fibre Toxicology* (2018) 15:31

Page 13 of 16

fluid was intratracheally instilled per animal using a Penn Century Microsprayer inserted into the trachea under visual control. This mass of particles was considered equivalent to the lung burden obtained for SiO_2-n upon short term inhalation conditions [13]. After 3 d rats were deeply anaesthetized with a mixture of ketamine and xylazine and sacrificed by bleeding from the *Aorta descendens*. A cannula was inserted into the trachea and, while the left bronchus was transiently closed with a Diefenbach clamp, the right lung was lavaged five times with 3 mL, yielding a total of approx. 14 mL BALF per animal for further analyses. Then the right bronchus was clamped and the left lung was inflated with 3 mL Cryomatrix (Thermo Shandon Ltd., Runcorn, UK). The left lung was then resected, snap frozen in liquid nitrogen, and stored at − 80 °C until further processing.

BALF analysis
Cells from pooled BALF preparations were collected at the bottom of a centrifuge vial (200 × g, 4 °C, 10 min). The supernatant was centrifuged again and the final supernatant was used for protein determination according to the Lowry method [57]. Final numbers of cells were determined with a coulter counter (model Z2, Beckman Coulter GmbH, Krefeld, Germany) and the proportion of dead cells was determined by trypan blue testing. Differential cell counting was carried out with cytospin preparations stained with May-Grünewald or Giemsa dyes. At least 400 cells per animal were evaluated under the light microscope.

Preparation of lung tissue for fluorescence microscopy
Transverse sections were cut from the hilar region of the left lung with a cryo-microtome (Microtome Cryostsat HM 500, MICROM International GmbH, Walldorf, Germany). Seven μm thick sections were dried onto glass slides and stored under a nitrogen atmosphere at − 20 °C until further processing. To visualize the distribution of fluorescent SiO_2-FITC NPs, sections were taken from the freezer, fixed with 4% buffered formaldehyde, rinsed thoroughly in phosphate buffered saline (PBS), and covered with a coverslip using Roti-Mount FluorCare (Carl Roth, Karlsruhe, Germany) to stain cell nuclei with the contained 4′,6-diamidin-2-phenylindol (DAPI). Sections were viewed with an inverted fluorescence microscope (Olympus IX51, Olympus Deutschland GmbH, Hamburg, Germany), equipped with a 20× objective and conventional filter sets for DAPI and FITC. In some cases, an antibody labeling of CD68-positive alveolar macrophages was performed as described [58]. Images were taken with a charge-coupled device camera connected to a Nikon Lucia system.

Sample preparation for bioimaging
For each group the left lung from one animal was chosen for MALDI-MS and FT-IR imaging analyses; selection was based on the protein concentration of BALF as to be typical for the group. In case of SiO_2-FITC, selection was also based on the distribution of fluorescence which was regarded typical for an intratracheal instillation. Cryo-sections (8 and 10 μm thick) were prepared as described above. The sections were thaw-mounted on indium tin oxide coated glass slides (for MALDI-MS imaging) and calcium fluoride targets (for FT-IR imaging), respectively. Prior to MALDI-MS imaging analysis, frozen tissue sections were allowed to equilibrate to room temperature in a desiccator for ≥2 h. Samples were subsequently washed by submerging the glass slides in 50 mM ammonium acetate buffer (pH 6.7, 4 °C) 4 times, 5 s each, without agitation, to remove the cryo-compound. After each washing step, tissues were dried in a gentle stream of N_2. After drying the tissues for ≥15 min under vacuum, matrix deposition was performed using a home-built sublimation apparatus. In a vacuum-sealed and pressure-controlled deposition chamber, 25.5 mg of 2, 5-dihydroxybenzoic acid (2, 5-DHB, Sigmal-Aldrich, St. Louis, MO, USA) were quantitatively vaporized and sublimed onto the tissue at 155 °C and 4.7 Pa forming a homogenous layer (0.23 mg·cm^{-2}) of crystals. Before FT-IR imaging the cryo-sections were thawed in a darkened desiccator for 1 h and subsequently washed three times, 5 s each, in *aqua dest.*, followed by a second drying step in a desiccator. As FT-IR imaging provides direct molecular specific information in a non-destructive way, no application of a special matrix is needed.

MALDI-MS
MALDI-MS measurements were performed using a MALDI-TOF/TOF mass spectrometer (ultrafleXtreme, Bruker Daltonics, Bremen, Germany) operated in reflectron mode. MSI data were acquired using flexControl software v3.4 (Bruker Daltonics). The attenuator offset of the laser (smartbeam-II, wavelength 355 nm) was adjusted to 65% and the laser fluence was set to 45%. For lipid analysis, the mass range was set from 440 to 1700 Da with ion suppression for analytes below 340 Da. Imaging data were acquired in the negative ion mode with a lateral resolution of 50 μm by summing up 100 shots per array position (without intra-spot rastering) using a laser repetition rate of 1 kHz. The sample originating from the rat instilled with SiO_2-FITC NPs was subsequently rastered in the positive ion mode. Extraction voltage was set to 17.95 kV and lens voltage to 7.50 kV. Mass spectra were calibrated externally using the cubic enhanced algorithm on singly charged ions of bovine cardiolipin disodium salt (Sigma-Aldrich, St. Louis, MO, USA). Data acquisition and image representation were carried out with flexImaging software v3.0 (Bruker Daltonics). Acquired imaging data were normalized to the total ion current (TIC). Lipid identification was based on the comparison of the experimental with the theoretical *m/z* values according to the Metabolomics Workbench

Großgarten *et al. Particle and Fibre Toxicology* (2018) 15:31

Page 14 of 16

Metabolite Database and the LIPID MAPS Structure Database (www.metabolomicsworkbench.org and http://www.lipidmaps.org, both provided by the University of California, USA). MS/MS experiments in LIFT mode were performed for selected mass values to confirm structural assignments.

FT-IR imaging and hierarchical cluster analysis

An infrared hyperspectral image of the lung tissue sample after intratracheal instillation of SiO_2-FITC NPs was acquired using a Bruker Hyperion 3000 FT-IR microscope system equipped with a liquid nitrogen cooled single point mercury cadmium telluride (MCT) detector. Spectra were collected in transmission mode using 15× Cassegrain objectives. The sample was analyzed by automated raster scanning as a tile mosaic image with a spatial resolution of 100 μm, defined by the aperture and the step size. At every measurement position (area of 100×100 μm^2), an infrared spectrum consisting of 4 accumulations (scans) was collected. The total measured area was 7.1×6.6 mm^2. All spectra were recorded in the range of 400 to 4000 cm^{-1} with 4 cm^{-1} spectral resolution. A background spectrum was measured on the CaF_2 slide outside the tissue sample. Collected spectra were divided over background and automatically converted into absorbance by OPUS 7.0 software. Further spectral pre-processing (baseline correction, scaling, and standardization) and multivariate data analysis were performed with ImageLab software (v.1.94, Epina GmbH, Pressbaum, Austria). Baseline correction applied to spectra was based on the Lieber algorithm in 30 iterations through a 3rd order polynom. Spectral data was scaled between 0 and 1 and standardized (mean = 0.0, standard deviation = 1.0). Prior to hierarchical cluster analysis, spectra with poor signal-to-noise ratio (areas outside the sample) or those which were expected to exhibit properties significantly differing from the lung tissue under investigation (bronchus, bronchioles and blood vessels) were eliminated. These so-called "bad pixels" were excluded from further statistical evaluation. HCA was performed using Ward's method, Euclidean distance measure and 13 spectral descriptors consisting of important spectral features (proteins, lipids) for identifying tissue remodeling due to nanoparticle instillation.

Statistical evaluation

In vitro data were generated in triplicates and at least three independent repetitions were carried out. To test for significant differences in vitro, values from each concentration were compared to the non-treated controls using 2-way ANOVA with Dunnett's multiple comparisons test. In vivo experiments were carried out with 5 animals per group. BALF cell data were compared pair-wise to the corresponding control group for both AM and PMN by 2-way ANOVA with Dunnett's multiple comparisons test, BALF protein data were compared pair-wise to the corresponding control group by one-way ANOVA and post-hoc Dunnett's

multiple comparison test. A value of $p \leq 0.05$ was considered significant (*). All data are expressed as mean ± standard deviation (SD).

Additional file

Abbbreviations

AM: Alveolar macrophage; BALF: Broncho-alveolar lavage fluid; DAG: Diacylglyceride; DAPI: 4′,6-diamidin-2-phenylindol; EDTMP: Ethylenediamine tetra (methylene phosphonic acid); FT-IR: Fourier transform infrared (microspectroscopy); HCA: Hierarchical cluster analysis; m/z: Mass-to-charge ratio; MALDI-MS: Matrix-assisted laser desorption/ionization mass spectrometry; NP: Nanoparticle; PG: Phosphatidylglycerol; PI: Phosphatidylinositol; PLC: Phospholipid composition; PMN: Polymorphonuclear leukocytes; PS: Phoshatidylserine; SiO_2: Silica; SiO_2-FITC: Fluorescent SiO_2 (core labelled with fluorescein isothiocyanate); SiO_2-n: Pristine form of SiO_2; SiO_2-p: TPMP coated (phosphonated) SiO_2; TAG: Triacylglyceride; TPMP: 3-(tri-hydroxysilyl) propyl methyl phosphonat

Availability of data and materials

The mass spectrometric datasets generated and/or analyzed during the current study are not publicly available due to high complexity but are available from the corresponding author on reasonable request. Data from the animal study are shown as mean values and individual data are available from the corresponding author on reasonable request.

Authors' contributions

MG evaluated the data and wrote major parts of the manuscript. MH performed the MALDI-MS studies and evaluated the data, AV performed the in vitro and in vivo studies. AB performed FT-IR imaging measurements, KW evaluated the FT-IR imaging data. MS and BL supervised the measurements and contributed to the manuscript, MM-D planed the MALDI-MS experiments, interpreted the data and contributed to the manuscript, UK contributed to the design of the analytical parts of the study and evaluated the data. MW initiated and performed the study, conducted the in vivo experiments and wrote parts the manuscript. All authors discussed the results and approved the final manuscript.

Ethics approval

All animal experiments were ethically approved by local authorities (LANUV, Dortmund, Germany, Accession No. 84–02.04.2022.A157) and were carried out in the animal facility at the University Clinics of Essen, Germany.

Consent for publication

Not applicable.

Competing interests

Authors declare that there are no competing interests.

Großgarten *et al. Particle and Fibre Toxicology* (2018) 15:31

Page 15 of 16

Publisher's Note

Author details

[1]Institute of Inorganic and Analytical Chemistry, University of Münster, Corrensstraße 28/30, 48149 Münster, Germany. [2]Institute of Chemical Technologies and Analytics, TU Wien, Getreidemarkt 9, 1060 Vienna, Austria. [3]IBE R&D Institute for Lung Health gGmbH, Mendelstraße 11, 48149 Münster, Germany.

References

1. Napierska D, Thomassen LC, Lison D, Martens JA, Hoet PH. The nanosilica hazard: another variable entity. Part Fibre Toxicol. 2010;7:39.
2. Arts JHE, Muijser H, Duistermaat E, Junker K, Kuper CF. Five-day inhalation toxicity study of three types of synthetic amorphous silicas in Wistar rats and post-exposure evaluations for up to 3months. Food Chem Toxicol. 2007;45:1856–67.
3. Johnston CJ, Driscoll KE, Finkelstein JN, Baggs R, O'Reilly MA, Carter J, et al. Pulmonary chemokine and mutagenic responses in rats after subchronic inhalation of amorphous and crystalline silica. Toxicol Sci Off J Soc Toxicol. 2000;56:405–13.
4. Reuzel PGJ, Bruijntjes JP, Feron VJ, Woutersen RA. Subchronic inhalation toxicity of amorphous silicas and quartz dust in rats. Food Chem Toxicol. 1991;29:341–54.
5. Maser E, Schulz M, Sauer UG, Wiemann M, Ma-Hock L, Wohlleben W, et al. In vitro and in vivo genotoxicity investigations of differently sized amorphous SiO2 nanomaterials. Mutat Res Genet Toxicol Environ Mutagen. 2015;794:57–74.
6. Fenoglio I, Martra G, Coluccia S, Fubini B. Possible role of ascorbic acid in the oxidative damage induced by inhaled crystalline silica particles. Chem Res Toxicol. 2000;13:971–5.
7. Hemenway DR, Absher MP, Fubini B, Bolis V. What is the relationship between hemolytic potential and fibrogenicity of mineral dusts? Arch Environ Health. 1993;48:343–7.
8. Pandurangi RS, Seehra MS, Razzaboni BL, Bolsaitis P. Surface and bulk infrared modes of crystalline and amorphous silica particles: a study of the relation of surface structure to cytotoxicity of respirable silica. Environ Health Perspect. 1990;86:327–36.
9. Fubini B, Zanetti G, Altilia S, Tiozzo R, Lison D, Saffiotti U. Relationship between surface properties and cellular responses to crystalline silica: studies with heat-treated cristobalite. Chem Res Toxicol. 1999;12:737–45.
10. Panas A, Marquardt C, Nalcaci O, Bockhorn H, Baumann W, Paur H-R, et al. Screening of different metal oxide nanoparticles reveals selective toxicity and inflammatory potential of silica nanoparticles in lung epithelial cells and macrophages. Nanotoxicology. 2012;7:259–73.
11. Waters KM, Masiello LM, Zangar RC, Tarasevich BJ, Karin NJ, Quesenberry RD, et al. Macrophage responses to silica nanoparticles are highly conserved across particle sizes. Toxicol Sci. 2009;107:553–69.
12. Marzaioli V, Aguilar-Pimentel JA, Weichenmeier I, Luxenhofer G, Wiemann M, Landsiedel R, et al. Surface modifications of silica nanoparticles are crucial for their inert versus proinflammatory and immunomodulatory properties. Int J Nanomedicine. 2014;9:2815–32.
13. Landsiedel R, Sauer UG, Ma-Hock L, Schnekenburger J, Wiemann M. Pulmonary toxicity of nanomaterials: a critical comparison of published in vitro assays and in vivo inhalation or instillation studies. Nanomed. 2014;9:2557–85.
14. Wohlleben W, Driessen MD, Raesch S, Schaefer UF, Schulze C, von Vacano B, et al. Influence of agglomeration and specific lung lining lipid/protein interaction on short-term inhalation toxicity. Nanotoxicology. 2016;10:970–80.
15. Pattle RE. Properties, function, and origin of the alveolar lining layer. Proc R Soc Lond B Biol Sci. 1958;148:217–40.
16. Clements JA. Surface tension of lung extracts. Exp Biol Med. 1957;95:170–2.
17. Ruge CA, Kirch J, Cañadas O, Schneider M, Perez-Gil J, Schaefer UF, Casals C, Lehr CM. Uptake of nanoparticles by alveolar macrophages is triggered by surfactant protein A. Nanomedicine. 2011;7(6):690–3. https://doi.org/10.1016/j.nano.2011.07.009. Epub 10 Aug 2011
18. Kapralov AA, Feng WH, Amoscato AA, Yanamala N, Balasubramanian K, Winnica DE, et al. Adsorption of surfactant lipids by single-walled carbon nanotubes in mouse lung upon pharyngeal aspiration. ACS Nano. 2012;6:4147–56.
19. Stringer B, Kobzik L. Alveolar macrophage uptake of the environmental particulate titanium dioxide: role of surfactant components. Am J Respir Cell Mol Biol. 1996;14:155–60.
20. Seiler F, Rehn B, Rehn S, Bruch J. Evidence of a no-effect level in silica-induced rat lung mutagenicity but not in fibrogenicity. Arch Toxicol. 2001; 74:716–9.
21. Adachi H, Hayashi H, Sato H, Dempo K, Akino T. Characterization of phospholipids accumulated in pulmonary-surfactant compartments of rats intratracheally exposed to silica. Biochem J. 1989;262:781–6.
22. Rehn B, Seiler F, Rehn S, Bruch J, Maier M. Investigations on the inflammatory and genotoxic lung effects of two types of titanium dioxide: untreated and surface treated. Toxicol Appl Pharmacol. 2003;189:84–95.
23. Thrall RS, Swendsen CL, Shannon TH, Kennedy CA, Frederick DS, Grunze MF, et al. Correlation of changes in pulmonary surfactant phospholipids with compliance in bleomycin-induced pulmonary fibrosis in the rat. Am Rev Respir Dis. 1987;136:113–8.
24. Spyridakis S, Leondaritis G, Nakos G, Lekka ME, Galanopoulou D. A specific phospholipase C activity regulates phosphatidylinositol levels in lung surfactant of patients with acute respiratory distress syndrome. Am J Respir Cell Mol Biol. 2010;42:357–62.
25. Girod S, Galabert C, Lecuire A, Zahm JM, Puchelle E. Phospholipid composition and surface-active properties of tracheobronchial secretions from patients with cystic fibrosis and chronic obstructive pulmonary diseases. Pediatr Pulmonol. 1992;13:22–7.
26. Bivas-Benita M, Zwier R, Junginger HE, Borchard G. Non-invasive pulmonary aerosol delivery in mice by the endotracheal route. Eur J Pharm Biopharm. 2005;61:214–8.
27. Gidden J, Liyanage R, Durham B, Lay JO. Reducing fragmentation observed in the matrix-assisted laser desorption/ionization time-of-flight mass spectrometric analysis of triacylglycerols in vegetable oils. Rapid Commun Mass Spectrom. 2007;21:1951–7.
28. Horbett TA, Ratner BD, Schakenraad JM, Schoen FJ. Some background concepts. In: Ratner BD, Hoffmann AS, Schoen FJ, Lemons JE, editors. Biomater Sci. New York: Academic Press; 1996.
29. Albrecht C, Knaapen AM, Becker A, Höhr D, Haberzettl P, van Schooten FJ, et al. The crucial role of particle surface reactivity in respirable quartz-induced reactive oxygen/nitrogen species formation and APE/Ref-1 induction in rat lung. Respir Res. 2005;6:129.
30. Li R, Ji Z, Dong J, Chang CH, Wang X, Sun B, et al. Enhancing the imaging and biosafety of upconversion nanoparticles through phosphonate coating. ACS Nano. 2015;9:3293-306.
31. Cai X, Lee A, Ji Z, Huang C, Chang CH, Wang X, et al. Reduction of pulmonary toxicity of metal oxide nanoparticles by phosphonate-based surface passivation. Part Fibre Toxicol. 2017;14:13.
32. Helmke RJ, German VF, Mangos JA. A continuous alveolar macrophage cell line: comparisons with freshly derived alveolar macrophages. In Vitro Cell Dev Biol. 1989;25:44–8.
33. Dreisewerd K. Recent methodological advances in MALDI mass spectrometry. Anal Bioanal Chem. 2014;406:2261–78.
34. Spengler B. Mass spectrometry imaging of biomolecular information. Anal Chem. 2014;87:64–82.
35. Berry KAZ, Li B, Reynolds SD, Barkley RM, Gijón MA, Hankin JA, et al. MALDI imaging MS of phospholipids in the mouse lung. J Lipid Res. 2011;52:1551–60.
36. Schiller J, Hammerschmidt S, Wirtz H, Arnhold J, Arnold K. Lipid analysis of bronchoalveolar lavage fluid (BAL) by MALDI-TOF mass spectrometry and 31P NMR spectroscopy. Chem Phys Lipids. 2001;112:67–79.
37. Sommerer D, Süß R, Hammerschmidt S, Wirtz H, Arnold K, Schiller J. Analysis of the phospholipid composition of bronchoalveolar lavage (BAL) fluid from man and minipig by MALDI-TOF mass spectrometry in combination with TLC. J Pharm Biomed Anal. 2004;35:199–206.
38. Veldhuizen R, Nag K, Orgeig S, Possmayer F. The role of lipids in pulmonary surfactant. Biochim Biophys Acta. 1998;1408:90–108.
39. Schiller J, Süß R, Arnhold J, Fuchs B, Leßig J, Müller M, et al. Matrix-assisted laser desorption and ionization time-of-flight (MALDI-TOF) mass spectrometry in lipid and phospholipid research. Prog Lipid Res. 2004;43:449–88.
40. Postle AD, Heeley EL, Wilton DC. A comparison of the molecular species compositions of mammalian lung surfactant phospholipids. Comp Biochem Physiol - Mol Integr Physiol. 2001;129:65–73.
41. Zemski Berry KA, Hankin JA, Barkley RM, Spraggins JM, Caprioli RM, Murphy RC. MALDI imaging of lipid biochemistry in tissues by mass spectrometry. Chem Rev. 2011;111:6491–512.

Großgarten *et al. Particle and Fibre Toxicology* (2018) 15:31

Page 16 of 16

42. Kawada H, Horiuchi T, Shannon JM, Kuroki Y, Voelker DR, Mason RJ. Alveolar type II cells, surfactant protein a (SP-A), and the phospholipid components of surfactant in acute silicosis in the rat. Am Rev Respir Dis. 1989;140:460–70.

43. Griese M, Gobran LI, Rooney SA. ATP-stimulated inositol phospholipid metabolism and surfactant secretion in rat type II pneumocytes. Am J Physiol - Lung Cell Mol Physiol. 1991;260:L586–93.

44. Hallman M, Epstein BL, Gluck L. Analysis of labeling and clearance of lung surfactant phospholipids in rabbit: evidence of bidirectional surfactant flux between lamellar bodies and alveolar lavage. J Clin Invest. 1981;68:742–51.

45. Poelma DL, Ju MR, Bakker SC, Zimmermann LJ, Lachmann BF, van Iwaarden JF. A common pathway for the uptake of surfactant lipids by alveolar cells. Am J Respir Cell Mol Biol. 2004;30:751–8.

46. Kuronuma K, Mitsuzawa H, Takeda K, Nishitani C, Chan ED, Kuroki Y, et al. Anionic pulmonary surfactant phospholipids inhibit inflammatory responses from alveolar macrophages and U937 cells by binding the lipopolysaccharide-interacting proteins CD14 and MD-2. J Biol Chem. 2009; 284:25488–500.

47. Seiler F, Rehn B, Rehn S, Bruch J. Different toxic, fibrogenic and mutagenic effects of four commercial quartz flours in the rat lung. Int J Hyg Environ Health. 2004;207:115–24.

48. Eskelson CD, Stiffel V, Owen JA, Chvapil M. The importance of the liver in normal and silicotic lung-lipid homeostasis: 2. cholesterol. Environ Res. 1979; 19:432–41.

49. Naumann D. FT-infrared and FT-Raman spectroscopy in biomedical research. Appl Spectrosc Rev. 2001;36:239–98.

50. Dakhakhni TH, Raouf GA, Qusti SY. Evaluation of the toxic effect of the herbicide 2, 4-D on rat hepatocytes: an FT-IR spectroscopic study. Eur Biophys J. 2016;45:311–20.

51. Zelig U, Kapelushnik J, Moreh R, Mordechai S, Nathan I. Diagnosis of cell death by means of infrared spectroscopy. Biophys J. 2009;97:2107–14.

52. Lamberti A, Sanges C, Arcari P. FT-IR spectromicroscopy of mammalian cell cultures during necrosis and apoptosis induced by drugs. J Spectrosc. 2010; 24:535–46.

53. Eskelson CD, Stiffel V, Owen JA, Chvapil M. The importance of liver in normal and silicotic lung-lipid homeostasis. 1. Phospholipids. J Environ Pathol Toxicol Oncol. 1985;6:37–46.

54. Lin H, Luo Y, Sun Q, Zhang J, Tuo Y, Zhang Z, et al. Identification of pulmonary edema in forensic autopsy cases of sudden cardiac death using Fourier transform infrared microspectroscopy: a pilot study. Anal Chem. 2018;90:2708–15.

55. Izak-Nau E, Voetz M. As-produced: intrinsic physico-chemical properties and appropriate characterization tools. In: Wohlleben W, Kuhlbusch TAJ, Schnekenburger J, Lehr C-M, editors. Safety of Nanomaterials along their lifecycle. Release, exposure human hazards. Boca Raton: CRC Press; 2014. p. 3–24.

56. Wiemann M, Vennemann A, Sauer UG, Wiench K, Ma-Hock L, Landsiedel R. An in vitro alveolar macrophage assay for predicting the short-term inhalation toxicity of nanomaterials. J Nanobiotechnol. 2016;14:16. https://doi.org/10.1186/s12951-016-0164-2.

57. Lowry OH, Rosebrough NJ, Farr AL, Randall RJ. Protein measurement with the folin phenol reagent. J Biol Chem. 1951;193:265–75.

58. Silge A, Bräutigam K, Bocklitz T, Rösch P. ZrO_2 nanoparticles labeled via a native protein corona: detection by fluorescence microscopy and Raman microspectroscopy in rat lungs. Analyst. 2015;140:5120–8.

5.6   Publication VI

Image-Based Chemical Structure Determination

Johannes Ofner, Florian Brenner, Karin Wieland, Elisabeth Eitenberger, Johannes Kirschner, Christoph Eisenmenger-Sittner, Szilvia Török, Balazs Döme, Thomas Konegger, Anne Kasper-Giebl, Herbert Hutter, Gernot Friedbacher, Bernhard Lendl, Hans Lohninger; *Scientific Reports* 2017, 7, 6832, 10.1038/s41598-017-07041-x, CC-BY License (https://creativecommons.org/licenses/by/4.0/)

SCIENTIFIC REPORTS

OPEN

Image-Based Chemical Structure Determination

Johannes Ofner [1], Florian Brenner[1], Karin Wieland[1], Elisabeth Eitenberger[1], Johannes Kirschner[2], Christoph Eisenmenger-Sittner[2], Szilvia Török[3], Balazs Döme[3,4,5,6], Thomas Konegger[1], Anne Kasper-Giebl[1], Herbert Hutter[1], Gernot Friedbacher[1], Bernhard Lendl[1] & Hans Lohninger[1]

Chemical imaging is a powerful tool for understanding the chemical composition and nature of heterogeneous samples. Recent developments in elemental, vibrational, and mass-spectrometric chemical imaging with high spatial resolution (50–200 nm) and reasonable timescale (a few hours) are capable of providing complementary chemical information about various samples. However, a single technique is insufficient to provide a comprehensive understanding of chemically complex materials. For bulk samples, the combination of different analytical methods and the application of statistical methods for extracting correlated information across different techniques is a well-established and powerful concept. However, combined multivariate analytics of chemical images obtained via different imaging techniques is still in its infancy, hampered by a lack of analytical methodologies for data fusion and analysis. This study demonstrates the application of multivariate statistics to chemical images taken from the same sample via various methods to assist in chemical structure determination.

Chemical imaging has become a workhorse in analytical chemistry due to advanced method development, improved imaging speed, lower detection limits, and increased computational power. All major analytical methods have been extended for chemical imaging purposes, resulting in improved understanding of the heterogeneity and complexity of samples of interest. Successful chemical structure determination (CSD) combines different complementary analytical techniques applied to the same sample to generate a comprehensive analytical understanding of the sample under investigation. While the combination of complementary analytical methods to solve scientific questions regarding complex samples or chemical systems is a fundamental working principle in analytical chemistry, the application of this approach in chemical imaging has been rarely reported.

'Multimodal imaging,' 'correlative imaging,' and 'data fusion' are common catchphrases that refer to the topic of combined image-based analysis. In these approaches, the data from each technique is analysed separately and the resulting images are combined. Correlative microscopy using light and electron microscopy is discussed in detail by Hayat[1]. Modern sample preparation techniques have been developed to assist this correlative approach[2, 3]. The advantages of image fusion of imaging mass spectrometry and microscopy are described by Van de Plas et al.[4]. Approaches toward data correlation to address biological questions are reported by Cunha et al.[5], focusing on available software systems for multimodal imaging and giving the example of correlating secondary ion mass spectrometric (SIMS) images with those obtained by transmission electron microscopy. A similar approach is reported for energy dispersive X-ray (EDX) spectroscopy and electron microscopy[6]. Outside of the biological and life-science communities, data fusion became a topic of interest in surface science when time-of-flight-SIMS (ToF-SIMS) images were combined with scanning electron microscopic (SEM) images and analysed using multivariate statistics[7] and when images from X-ray photoelectron spectroscopy and atomic force microscopy (AFM) were fused[8]. AFM has also been successfully fused with data obtained from laser scanning microscopy[9]. All these studies provide additional scientific output by combining a chemical imaging technique with high-resolution imaging (HRI) and/or topographic imaging techniques such as SEM or AFM. A different approach to correlative imaging, however, is the fusion of different modalities of the same fundamental physico-chemical measurement

[1]Institute of Chemical Technologies and Analytics, TU Wien, Getreidemarkt 9, 1060, Vienna, Austria. [2]Institute of Solide State Physics, TU Wien, Wiedner Hauptstrasse 8, 1040, Vienna, Austria. [3]National Korányi Institute of Pulmonology, Budapest, Hungary. [4]Division of Thoracic Surgery, Department of Surgery, Comprehensive Cancer Center, Medical University of Vienna, Vienna, Austria. [5]Department of Thoracic Surgery, Semmelweis University and National Institute of Oncology, Budapest, Hungary. [6]Department of Biomedical Imaging and Image-guided Therapy, Division of Molecular and Gender Imaging, Medical University of Vienna, Vienna, Austria. Correspondence and requests for materials should be addressed to J.O. (email: johannes.ofner@tuwien.ac.at)
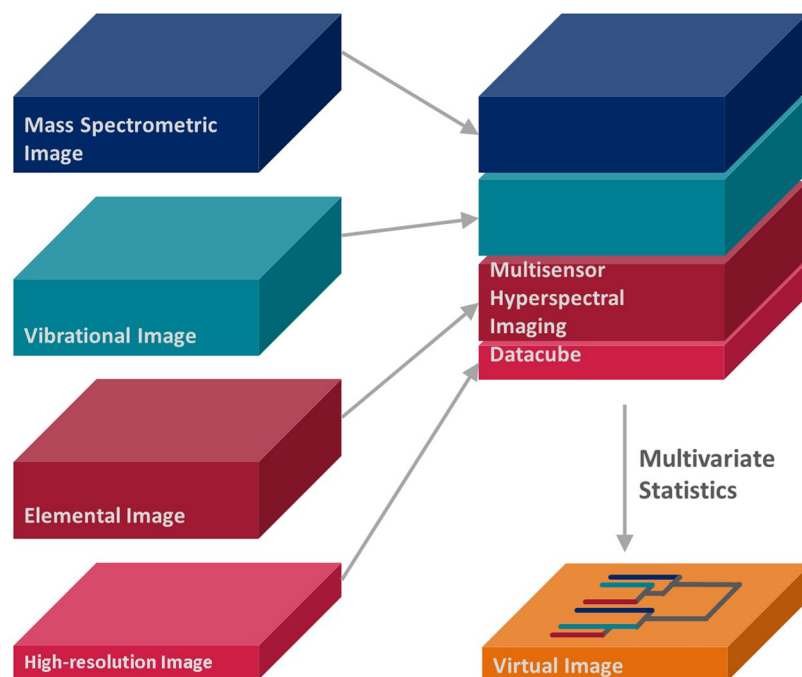
Figure 1. Basic concept of multisensor hyperspectral imaging with subsequent multivariate statistics to generate an analytical representation of a sample for image-based chemical structure determination.

principle of imaging techniques, that is, by fusing near-infrared, mid-infrared, and Raman micro-spectroscopic (RMS) images with subsequent multivariate data analysis[10]. A similar multimodal approach was applied to imaging tissues using SIMS and matrix-assisted laser desorption/ionization (MALDI)[11]. Another correlative technique is reported for imaging chromosomes by cryo-fluorescence and soft X-ray tomography (SXT)[12]. By the application of SXT, a three-dimensional reconstruction of the correlated dataset could be achieved. Recently, correlative 3-dimensional micro-spectroscopy of a single catalyst particle has been reported[13]. The detailed methodical approach is of this technique is summarized in a recent review[14].

Data fusion of single chemical images with HRI or topographic images or imaging of a sample by using different modalities of a single technique providing similar information, for instance, vibrational spectroscopy (infrared and RMS) or mass spectrometry (SIMS and MALDI), do not fulfil the requirements of CSD because hardly any complementary chemical information is generated. SIMS and RMS images have been correlated to visualize cell-scale molecular distributions[15]. Here, the complementary information of mass spectrometric and vibrational imaging are combined and compared at the image level. This is also reported for the combined use of laser-induced breakdown spectroscopy and laser ablation inductively coupled plasma mass spectrometry[16]. Contrary to these examples, fusion on the level of recorded datasets obtained from elemental (EDX) and vibrational (Raman) micro-spectroscopy (RMS) was reported in 2014[17]. The advantages of the combined multivariate analytical approach for this so-called multisensor hyperspectral imaging (MSHSI) dataset were recently compared to side-by-side interpretation of images[18].

To generate an approach to image-based CSD that is both comprehensive and complementary, imaging data obtained via different spectroscopic techniques must first be combined and then jointly analysed. Therefore, the imaging techniques must be non-destructive, must exhibit comparable spatial resolutions, and must return complementary chemical information. Additionally, the sample area of interest must be accessible by all these techniques. Elemental, vibrational, and mass spectrometric imaging can fulfil these requirements using EDX imaging applied by an electron microscope (where SEM also supplies the HRI), RMS imaging, and ToF-SIMS imaging (in the following paragraphs referred to as SIMS). RMS and EDX imaging are both non-destructive techniques; thus, multisensor fusion of these datasets with a SIMS dataset is possible when SIMS imaging is applied as the last technique. With spatial resolutions down to 50 nm for EDX, down to 100 nm for SIMS, and down to 200 nm for RMS, these techniques are comparable.

The present study demonstrates image-based CSD by merging EDX, RMS, and SIMS imaging datasets into a combined MSHSI datacube; subsequently, multivariate statistics are applied (Fig. 1) to generate a comprehensive analytical representation of the image. Spectral descriptor (SPDC)[17] based principal component analysis (PCA)[19], k-means cluster analysis[20] and hierarchical cluster analysis (HCA)[21], as well as vertex component analysis (VCA)[22], are applied to analyse the combined MSHSI datasets[18]. The application of multivariate MSHSI to image-based CSD will be introduced via the combined analysis of copper sulphide particles deposited on a purified aluminium substrate. Subsequently, with the aim of demonstrating the generic applicability of this new methodology to samples from the fields of life science, materials science, and geoscience, additional examples using, respectively, tumour cells, technical ceramics, and an environmental aerosol sample are given.
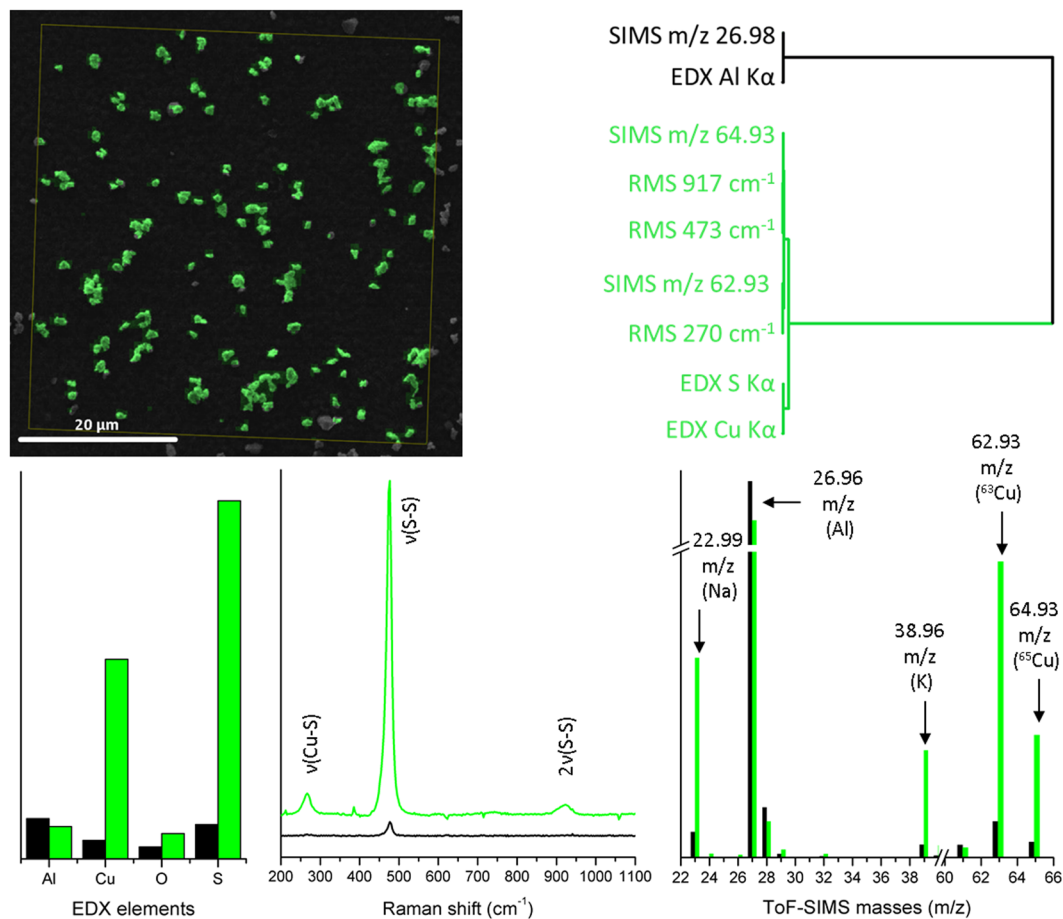
Figure 2. Superposition of the high-resolution SEM image with the CuS particle cluster of the HCA of the loadings of the PCA, dendrogram of the PCA-HCA indicating the background (black) and CuS particle cluster (green), and the extracted cluster spectra from the k-means clustering.

Results

Copper sulphide particles. To analyse the combined dataset obtained from RMS, EDX, and SIMS imaging in combination with the HRI of copper sulphide particles using MSHSI, spectral descriptors (SPDCs) were defined to extract the spectral information from the datacube. Copper sulphide is characterized by three Raman bands at 270 (ν(Cu–S)), 473 (ν(S–S)), and 917 (2ν(S–S)) cm^{-1} [23–25]. Additionally, Kα X-ray emissions are expected in the EDX spectrum for aluminium (background), copper, and sulphur. In the SIMS datacube, mass-to-charge (m/z) 26.98 for the aluminium substrate as well as 62.93 and 64.93 for the two copper isotopes are significant for the chosen system. Because the ToF-SIMS was operated in positive-ion mode, no SIMS signal of sulphur is expected.

The multisensor hyperspectral dataset was analysed using PCA on the basis of the defined SPDCs (more details are given in the Methods section). The first principal component describes 65.77% of the overall dataset variance. Based on the PCA of standardized SPDCs, an HCA of the loadings of the first principal component was carried out (Fig. 2, upper part). A detailed description of all applied multivariate statistical methods can be found at Ofner *et al.*[18]. The colours in Fig. 2 and the following figures represent the different unravelled species. The colour-coding links the detected species in the SEM or optical images with the related dendrograms of the clustering algorithms and the extracted mean spectra. Due to the fact, that all demonstrated spectra origin from multivariate analysis (especially k-means clustering, HCA or VCA) and are standardized mean spectra, no meaningful units can be given for the intensities of the ordinates of the spectra. Therefore, labels and units are not shown.

The dendrogram of the HCA of the loadings of the PCA (Fig. 2, upper part) significantly differentiates the background cluster (SIMS m/z 26.98 of aluminium and the EDX X-ray Kα emission of aluminium) and the particle cluster. This cluster contains all three Raman bands of copper sulphide (917 cm^{-1}, 473 cm^{-1}, and 270 cm^{-1}), the copper isotopes from the ToF-SIMS dataset (m/z 64.93 and m/z 62.93), and the related X-ray emissions from the EDX of the SEM (S Kα and Cu Kα).

The superposition of the SEM image and the sub-cluster image of the PCA-HCA of the MSHSI datacube indicates that not all particles are related to this sub-cluster of copper sulphide. Because the first principal component describes only 65.77% of the overall dataset, additional chemical information is assumed to be hidden in the MSHSI. A more detailed examination reveals the presence of oxygen (EDX), as well as impurities of Na (SIMS m/z 22.99), K (SIMS m/z 38.97), Ca (SIMS m/z 39.97), and other elements, originating from the sample
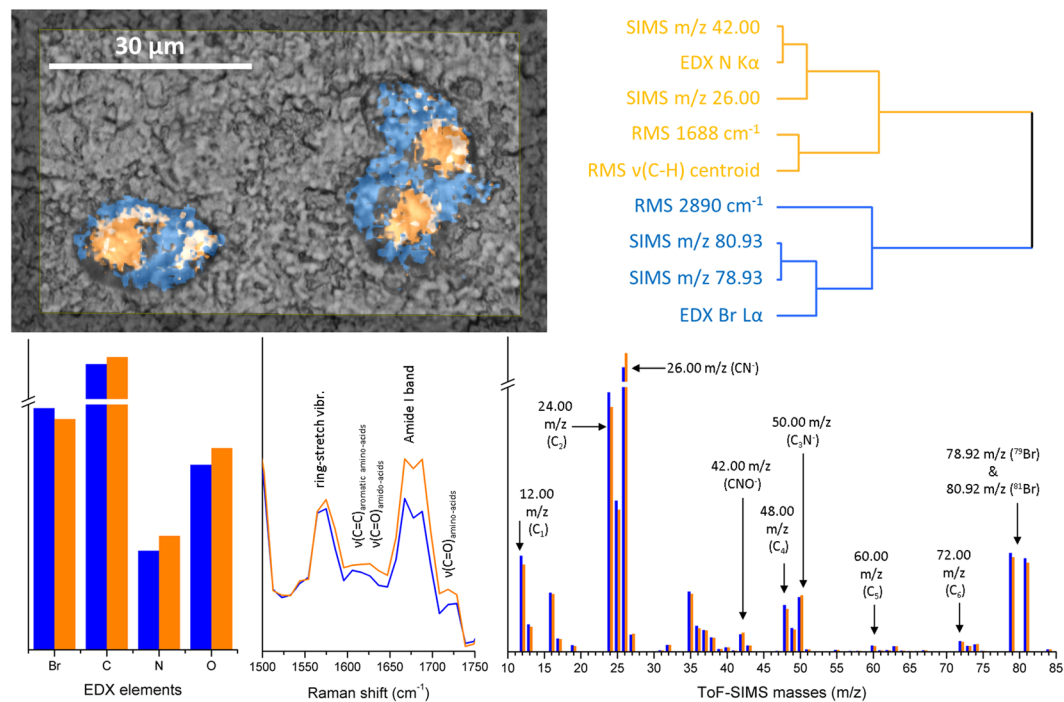
3

Figure 3. Superposition of a light-microscopic image of two tumour cells and results from the HCA of the PCA loadings and extracted cluster spectra from k-means clustering of the MSHSI dataset.

preparation process. However, the major component of interest, copper sulphide, could be clearly identified within the first principal component.

To extract the combined component spectra, k-means clustering standardized SPDCs of the MSHSI datacube, choosing two expected clusters, was performed (Fig. 2, lower part). The extracted cluster spectra exhibit the expected features. The EDX spectrum reveals the presence of Kα emissions of copper and sulphur for the green cluster, in addition to a slight increase of oxygen, which indicates the presence of copper oxide. The extracted Raman spectrum exactly replicates the Raman spectrum of covellite (CuS)[26]. The SIMS spectrum identifies the two copper isotopes ^{63}Cu and ^{65}Cu at their atomic weights of 62.93 and 64.93 and their expected isotope ratios of 69.17% and 30.83%, respectively. Additionally, the SIMS spectrum of the CuS sub-cluster (Fig. 2, green cluster) exhibits impurities of sodium (22.99 m/z) and potassium (38.96 m/z). The substrate (Fig. 2, black cluster) is characterized by an EDX Kα emission of aluminium, a nearly flat Raman baseline with traces of the CuS Raman spectrum, which is caused by the multisensor fusion of the single datasets with varying spatial resolution of the methods, and higher abundance of the mass 26.96 m/z (aluminium) in the SIMS spectrum.

The application of MSHSI to the simple example of CuS particles shows the advantages of this technique. While EDX allows rudimentary identification of the component elements, RMS reveals the chemical bonding and allows attribution to CuS, while SIMS confirms the presence of copper by identifying the masses and ratios of the isotopes as well as providing additional information on minor constituents, impurities, and contaminants. All this sample-specific information, which is necessary for definite chemical structure determination, is represented within a single sub-cluster of the multivariate k-means clustering, which proves the linkage of the individual analytical methods.

Tumour cells.　Tumour cells treated with a bromine-containing prodrug were also imaged using MSHSI (Fig. 3). To analyse the combined MSHSI datacube of this sample, HCA of the PCA loadings based on standardized SPDCs was performed, based on the concept of SPDCs (Fig. 3, upper part). The two sub-clusters of the HCA of the PCA show a distinction between the nucleus surrounded by the rough endoplasmic reticulum for protein biosynthesis (Fig. 3, orange sub-cluster) and the cytoplasm of the cell (Fig. 3, blue sub-cluster). The superposition of the cluster image with the optical image shows that both cells undergo cell division. The orange sub-cluster is defined by the SPDCs of the EDX nitrogen signal, the SIMS masses 26.00 and 42.00 m/z, which can be attributed to CN$^-$ and CNO$^-$ fragments, and the Raman amide I band at 1688 cm^{-1} as well as a centroid spectral descriptor, which is assigned to the ν(C–H) stretch region and exhibits a positive value at the location of the nucleus. The blue sub-cluster is characterized by a Raman band at 2890 cm^{-1}, the ν(C–H) of –CH$_2$– groups, which can be assigned to lipids, the EDX Lα emission of bromine, and the ToF-SIMS masses 78.93 m/z and 80.93 m/z, which represent the two bromine isotopes ^{79}Br and ^{81}Br, respectively.

The component spectra (Fig. 3, lower part) of the cell core and the cytoplasm were extracted using k-means clustering of standardized SPDCs. After q-normalization, the best results for the clustering process were obtained by choosing three expected clusters. The second k-means cluster was excluded from further processing because this cluster represents the margin of the cells, where a strong contribution from the background and background
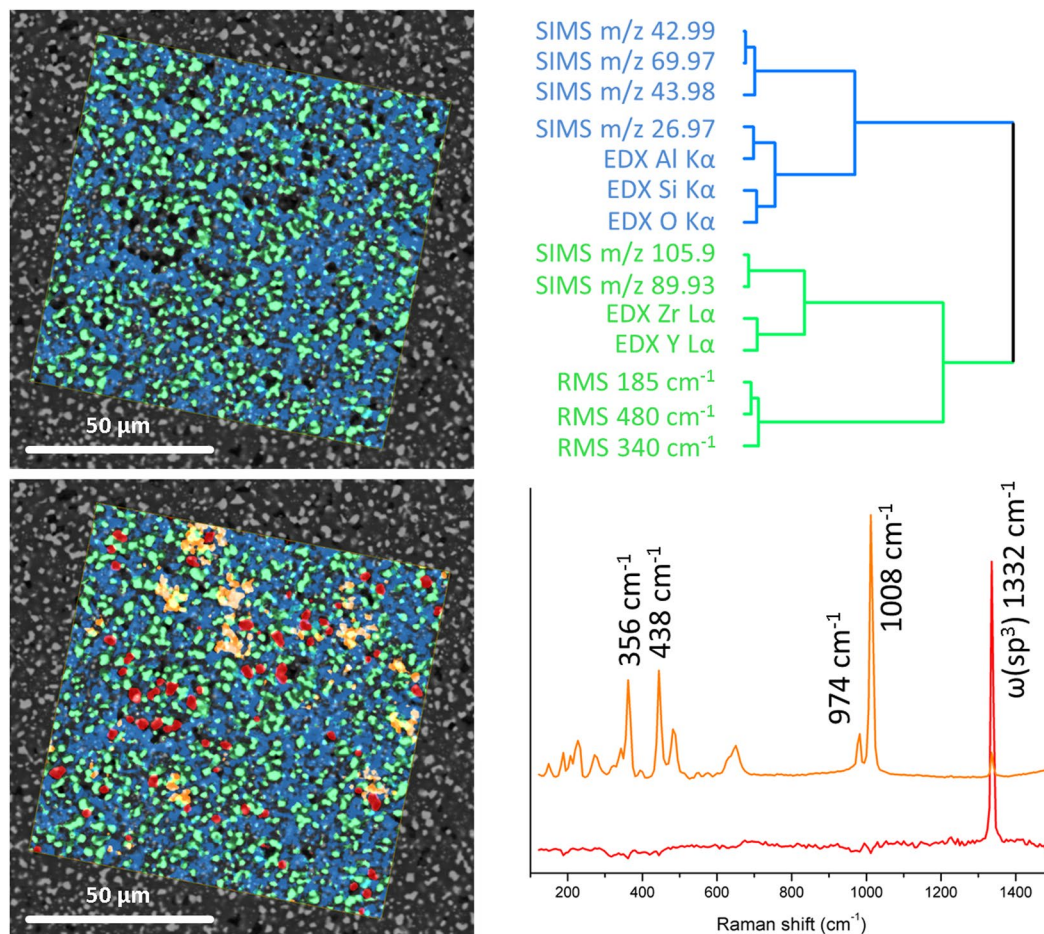
Figure 4. Superposition of the SEM image of the ceramic mullite/ZrO$_2$ composite with the image of the HCA of the PCA loadings (upper part) and with the extracted endmembers of the VCA (lower part), which represents the diamond Raman spectrum (red) and the ZrSiO$_4$ Raman spectrum (orange).

impurities is visible. The two remaining sub-clusters of the k-means clustering, which are comparable to the clusters of the HCA of the PCA loadings, improve the chemical interpretation of the nucleus and cytoplasm clusters. The nucleus sub-cluster (Fig. 3, orange spectra) exhibits an enhanced band at 1620 cm^{-1}, which can be assigned to the ν(C=O) of amino acids[27] or the ν(C=C) of aromatic amino acids[28] as well as the common ν(C=O) of esters[28] around 1730 cm^{-1}. Further, a strong increase of the amide I band at 1680 cm^{-1} is visible[29]. Additionally, both clusters exhibit the ring-stretch vibration of purine bases at about 1575 cm^{-1}[29]. The RMS spectra thus indicate an enhanced presence of proteins in the orange sub-cluster. This is also supported by the SIMS mass spectra, which show increased intensities in this sub-cluster of 26.00 (CN$^-$), 42.00 (CNO$^-$), and 50 (C$_3$N$^-$) m/z. In contrast, the blue sub-cluster of the HCA dendrogram of the PCA loadings depicting the cytoplasm supports the assignment of the Raman vibrations of lipids by the SIMS fragments 12 (C), 24 (C$_2$), 48 (C$_4$), 60 (C$_5$), and 72 (C$_6$) m/z, which represent lipid fragments. The increased presence of lipids in tumour cells, which is highlighted by the RMS centroid SPDC and the SIMS spectrum of the blue sub-cluster, is also reported in the literature[30]. The EDX spectrum indicates increased presence of carbon, oxygen, and nitrogen at the location of the cell cores, while the bromine-containing drug appears primarily in the cytoplasm. This distribution of bromine is also confirmed by the two SIMS masses 78.92 m/z (^{79}Br) and 80.92 m/z (^{81}Br). Thus, besides the localization of the cell cores, the distribution of the bromine-containing drug inside the cells could also be visualized using MSHSI.

Ceramic composite. As an example of the application of image-based chemical structure determination to the field of materials science, a ceramic composite prepared by the polymer-precursor method was analysed. The synthesis of this technical ceramic, which consists of ZrO$_2$-reinforced mullite (3Al$_2$O$_3$·2SiO$_2$), was based on the thermal conversion of methyl-polysilsesquioxane to highly reactive SiO$_2$, which subsequently reacted with Al$_2$O$_3$ to form a continuous mullite matrix. Additionally, ZrO$_2$ (yttrium-stabilized) was incorporated as particulate reinforcement. The full synthesis procedure and SEM image-based analytics have been described in previous studies[31, 32].

Based on the knowledge of the initial chemical composition, SPDCs were chosen to analyse the MSHSI dataset. HCA of the PCA loadings based on standardized SPDCs was performed, which indicated the main expected components (Fig. 4, upper part). The dendrogram is characterized by two main sub-clusters. The green
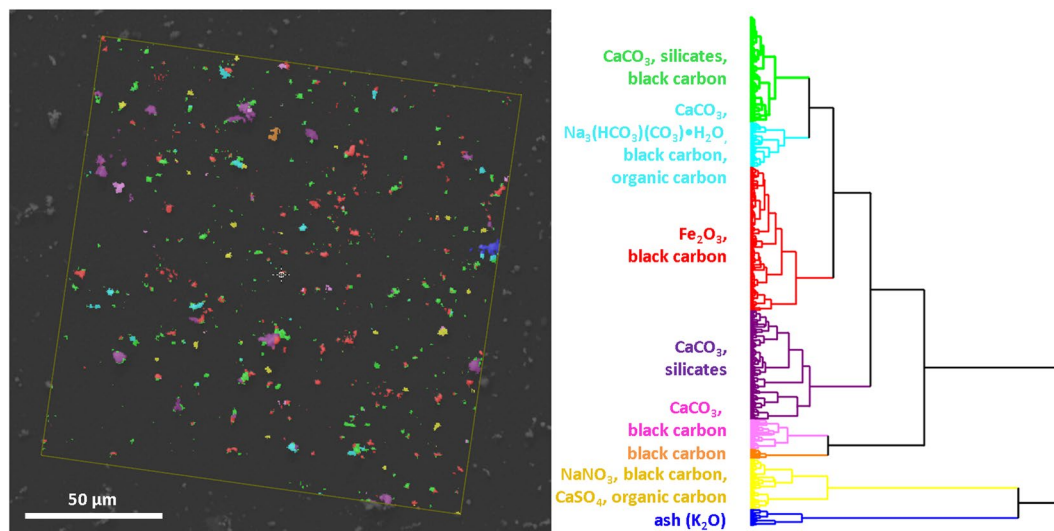
Figure 5. Superposition of the SEM image of the aerosol sample with the virtual image of the HCA of the MSHSI dataset and assignment of chemical species to the sub-clusters, based on extracted cluster spectra.

sub-cluster in Fig. 4 represents the yttrium-stabilized zirconia. This sub-cluster contains the EDX Lα X-ray emissions of zirconium and yttrium. Furthermore, the corresponding SIMS masses 89.93 m/z of Zr and 105.9 m/z of ZrO are included. The three RMS bands at 185 (two bands at 180 and 192 cm^{-1}), 340, and 480 cm^{-1} finally allow the assignment of this sub-cluster to monoclinic ZrO_2[33]. Hence, the green sub-cluster represents the yttrium-stabilized ZrO_2. The blue sub-cluster represents the matrix phase, in which the EDX X-ray Kα emissions of silicon, oxygen, and aluminium and the corresponding SIMS masses of 26.97 m/z (Al), 42.99 m/z (AlO), 43.98 m/z (SiO), and 69.97 m/z (Al$_2$O) can be found. These SPDCs indicate that this sub-cluster is representative of mullite ($3Al_2O_3 \cdot 2SiO_2$). However, the Raman bands of these species are not accessible due to the presence of the strong ZrO_2 bands.

The overall sample is characterized by pores, which are artefacts of the polishing process. Analysing these holes in detail revealed an enhanced amount of carbon (EDX Kα). Therefore, an additional species was expected. The EDX dataset only exhibited the information on the carbon content. Further, no significant masses could be found in the SIMS dataset for these parts of the sample. VCA was applied on the RMS portion of the MSHSI dataset and a spectral endmember, corresponding to the holes in the sample, was extracted (Fig. 4, lower part, red RMS spectrum). This endmember is characterized by a single Raman band at about 1332 cm^{-1} and correlated to high carbon content. Based on the literature, the red spots in Fig. 4 (lower part) can be assigned to diamond[34]. This vibration is evoked by the interpenetrating cubic sublattice and can be assigned to a lattice vibration of the sp^3 carbon bonds (ω(sp^3))[35]. Diamond paste was used to polish the sample, and the red spots indicate areas of diamond residue. The VCA algorithm also revealed an additional spectral endmember in the Raman datacube (Fig. 4, lower part, orange spectrum). According to the literature[36] and the RRUFF database[26], as well as expectations based on the synthesis method[31], this VCA endmember can be attributed to $ZrSiO_4$, which forms at the interface between the ZrO_2 particles and the mullite matrix.

By applying PCA-HCA and VCA to the MSHSI dataset of the ceramic sample, four main chemical species could be extracted from the SEM image. The yttrium-stabilized ZrO_2 is well represented by the RMS, EDX, and SIMS sub-datasets. By superimposition with the SEM image, the white particles could be identified as 3Y-ZrO_2. The mullite matrix is congruent with the gray areas in the SEM image and is characterized by the EDX and SIMS sub-datasets of the MSHSI datacube. Additionally, the RMS sub-dataset revealed the presence of $ZrSiO_4$ by PCA-HCA and diamond residues by VCA endmember extraction from the RMS sub-dataset, which was also confirmed by the enhanced carbon signal in the EDX dataset.

Environmental aerosol.　Atmospheric aerosols are complex mixtures of analytes from natural or anthropogenic sources that are formed and transformed in the environment. A combined analytical approach to this class of samples increases the value of the chemical analysis and enhances the understanding of the entire environmental system. During atmospheric sampling in the city of Vienna, a nearby building that had been affected by a fire was torn down.

The sample was imaged and the datasets were fused into the MSHSI datacube. Because this sample exhibited a high number of different chemical species, SPDCs had to be defined by an iterative process. Restrictive clustering algorithms such as k-means clustering would hamper the interpretation of the dataset because the expected number of clusters must be known in advance. An estimation of the expected number of species based on analysis of the eigenvalue plot of the PCA revealed eight to ten different chemical species. To allow a top-down analysis of these species, SPDC-based HCA (Ward's method with Euclidean distances) of the overall dataset was performed.

The analysis of the HCA of the MSHSI dataset revealed at least eight sub-clusters, which can be assigned to different chemical species (Fig. 5). All sub-clusters exhibit strong internal mixing of the single aerosol particles. The yellow sub-cluster shows typical urban aerosol composition and represents a minor part of the overall particle
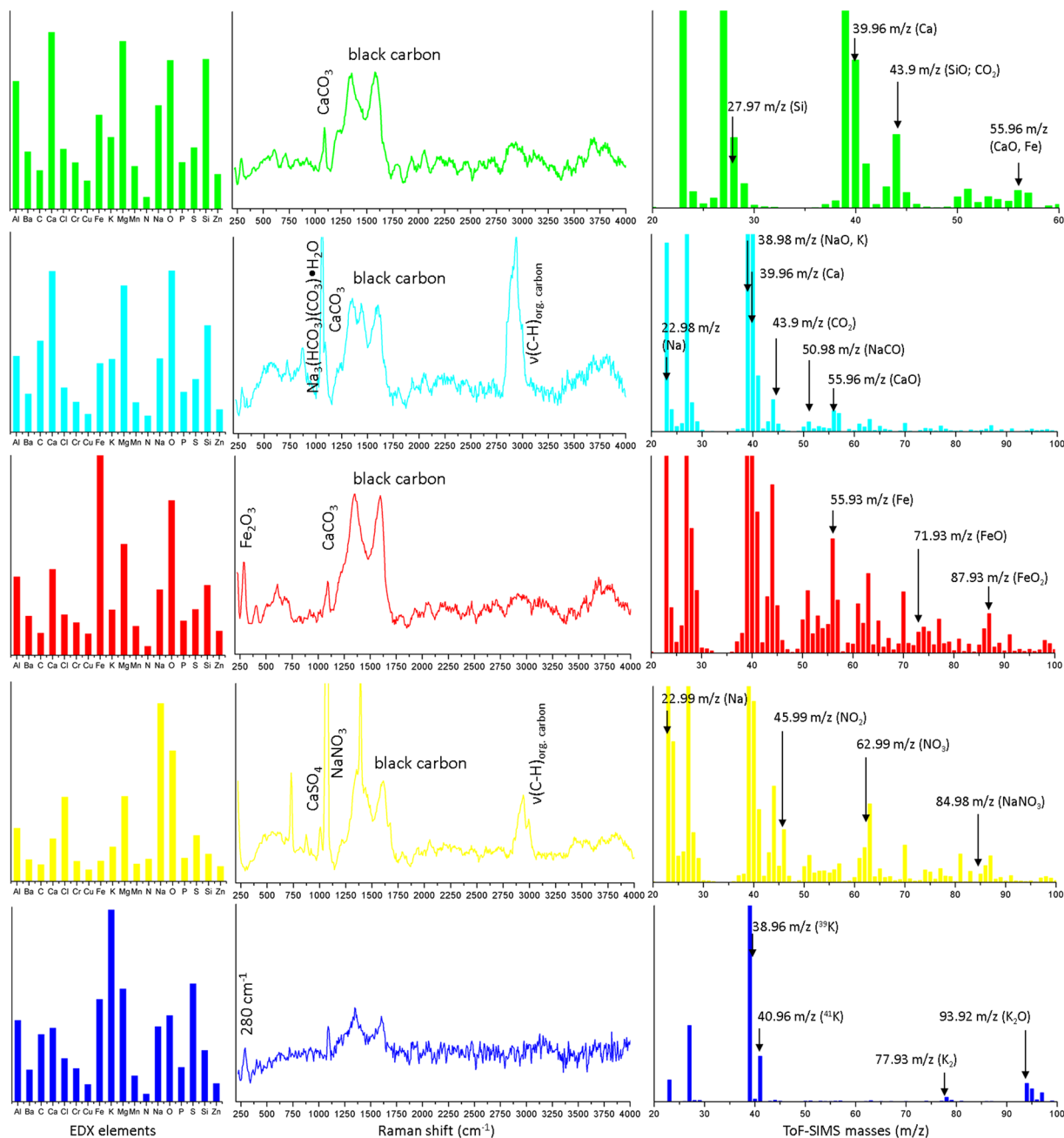
Figure 6. Examples of extracted sub-cluster spectra from the HCA of the environmental aerosol sample and assignment of spectral features.

composition. The blue sub-cluster, which is closely connected in terms of inter-cluster distance, can also be attributed to the urban background aerosol. The remaining sub-clusters can be attributed to the tearing down of the burned building.

The assignment of the individual sub-clusters (Fig. 5) to chemical species is achieved by analysing the sub-cluster spectra in parallel (Fig. 6).

The green sub-cluster is dominated by the EDX elements Ca, Mg, O, and Si with contributions from Fe and Na. The RMS dataset exhibits a band at about 1085 cm^{-1} that can be assigned to calcite or aragonite (CaCO$_3$) through comparison with reference spectra[26, 37]. Additionally, the Raman spectrum includes a contribution from black carbon (soot)[38], which can be attributed to the fire at the demolished building. The SIMS spectrum supports this interpretation by exhibiting contributions from the masses (*m/z*) 27.97 (Si), 39.96 (Ca), 43.9 (SiO or CO$_2$, as a fragment of the carbonate), and 55.96 (Fe or CaO). The green sub-cluster thus exhibits features typical of the building demolition process. The silicates and the CaCO$_3$ can be attributed to concrete.

The cyan blue sub-cluster exhibits features in the EDX spectrum similar to those of the green sub-cluster, with an enhanced contribution from carbon. However, the Raman spectrum is supplemented by a dominant band in

the spectral region of ν(C–H) stretching vibrations, which indicates the presence of organic carbon, and a sharp band at 1065 cm^{-1}. Additionally, the presence of black carbon is indicated. Analysing the SIMS spectrum showed the presence of 22.98 (Na), 38.98 (NaO, K), 39.96 (Ca), 43.9 (CO$_2$ from carbonates), 50.98 (NaCO), and 55.96 (CaO, Fe) m/z. Hence, the presence of some form of sodium carbonate is likely. Comparison of the Raman band at 1065 cm^{-1} with the RRUFF database[26] shows that it can likely be attributed to trona, a water-bearing sodium hydrogen carbonate with the molecular formula Na$_3$(HCO$_3$)(CO$_3$)·H$_2$O that is used as a fire-extinguishing agent. This sub-cluster can thus be attributed to demolition waste and the fire-extinguishing agent.

The EDX spectrum of the red sub-cluster is dominated by Fe and O. The Raman spectrum exhibits a band at 290 cm^{-1} along with bands of CaCO$_3$ and black carbon. In addition to the SIMS masses identified in the green sub-cluster, 55.93 (Fe), 71.93 (FeO), and 87.93 (FeO$_2$) m/z are also visible. Comparison with the RRUFF database[26] of the Raman spectrum and correlating the three MSHSI spectra of the red sub-cluster indicate that this sub-cluster exhibits contributions from hematite, a fingerprint of the structural steel and the technical building equipment.

The purple, pink, and orange sub-clusters are also related to building demolition debris. Therefore, their analysis is not described or shown in detail in Fig. 6. Still, the decreasing inter-cluster distance to the yellow and blue sub-clusters indicate that mineral dust also forms part of the urban background aerosol.

The remaining sub-clusters (yellow and blue) are significantly separated from the other clusters, indicating a different chemical background.

The EDX part of the yellow sub-cluster reveals the presence of Cl, Na, and O, with contributions of S. The Raman spectrum is dominated by the three distinct Raman bands of NaNO$_3$ at 725, 1070, and 1390 cm^{-1}, as well as the contributions from black carbon and organic carbon (ν(C–H)). The presence of NaNO$_3$ is also confirmed by the presence of 22.99 (Na), 45.99 (NO$_2$), 63.99 (NO$_3$), and 84.98 (NaNO$_3$) m/z in the SIMS spectrum. Additionally, the presence of NaCl, which is not visible in the RMS and SIMS datasets, can be extracted from the EDX dataset. The presence of CaSO$_4$ is indicated by the Raman band at 1017 cm^{-1} and the sulphur signal from the EDX dataset. This sub-cluster represents the expected typical aerosol composition from the city of Vienna based on the season.

The blue sub-cluster is characterized by high potassium content in the EDX spectrum and the SIMS spectrum, indicated by the masses 38.96 (^{39}K) and 40.96 (^{41}K) m/z. The SIMS spectrum also displays the masses 77.93 m/z (K$_2$) and 93.92 m/z (K$_2$O). The Raman spectrum exhibits a high noise level. However, the contribution from black carbon and the Raman band of CaCO$_3$ are still visible. Additionally a band at about 280 cm^{-1} is present, which can be assigned to K–O containing species[26]. Hence, the blue sub-cluster can be attributed to ash, pointing to the influence of wood combustion, which is known to be present in Vienna.

The application of HCA to the MSHSI dataset of the environmental aerosol sample assisted the identification of single precipitated particles and their attribution to different sources. The different contributions from the demolition of a building were clarified by analysing the combined EDX, Raman, and SIMS spectra. Several of the species were not visible in all three spectra, such as the silicates, K$_2$O, or the organic carbon. Therefore, the analysis of this dataset in parallel improves the analytical interpretation and enables a detailed understanding of the sample composition. However, some species, such as CaCO$_3$ and Fe$_2$O$_3$, could only be identified by analysing at least two or even all three of the spectra.

Discussion

The decisive advantages of image-based CDS by multivariate MSHSI are demonstrated via the combined analysis of copper sulphide particles. EDX, RMS, and SIMS SPDCs unravelled the chemical composition of these particles by merging the CuS signals from each of the three different methods within the same sub-cluster of the PCA-HCA dendrogram. The combinational analysis of the complementary imaging techniques was also verified via the subsequent k-means clustering.

Additional benefits of this method are shown by the three subsequent practical examples. For the cell sample, the spatial allocation of the bromine-containing drug (EDX and SIMS) as well as the correlation of the SIMS fragments of lipids with the –CH$_2$ band of the RMS could be extracted from the complex MSHSI dataset. In the case of the technical ceramic sample, the 3Y-ZrO$_2$ could be identified by all three analytical methods, while the chemical information about the mullite matrix (3Al$_2$O$_3$·2SiO$_2$) was accessible by only EDX and SIMS. The presence of diamond and ZrSiO$_4$ could only be extracted from the RMS dataset by VCA. Chemical analysis of the environmental aerosol sample required the combined interpretation of the cluster spectra from all three techniques: silicates (EDX), black and organic carbon (EDX and RMS), ash (EDX and SIMS), sodium nitrate (EDX, RMS, and SIMS), and sodium hydrogen carbonate (RMS and SIMS).

Multivariate analysis of a fused multisensor hyperspectral imaging dataset, obtained from complementary chemical imaging techniques, provides a unique method of image-based chemical structure determination, where the linkage of analytical information across various individual techniques is proven by the combined statistical approach. Hence, joint clustering of different elemental, vibrational, and mass spectrometric features allows direct interpretation of the investigated chemical compound or structure. Applying and combining complementary techniques of comparable spatial resolutions minimizes the risk of overlooking analytical information. Furthermore, cross-correlating different methods helps to prevent the over-interpretation of insufficient data. Hence, MSHSI provides a more focused method of image-based chemical structure determination. By applying three-dimensional or temporal-correlated imaging techniques, multivariate analysis of fused higher-dimensional or dynamical multisensor hyperspectral imaging datasets will deepen the understanding of complex materials and processes.

	CuS particles	Cell samples	Ceramics	Aerosol Sample
Laser & power	488 nm, 230 μW	632.8 nm, 6 mW	488 nm, 3 mW	488 nm, 1.1 mW
grating	1200 lines mm⁻¹	300 lines mm⁻¹	1200 lines mm⁻¹	600 lines mm⁻¹
CCD mode	EMCCD	conventional	EMCCD	EMCCD
EMCCD gain	230		230	230
objective & NA	100×, 0.9	100×, 0.9	50×, 0.8	100×, 0.9
integration time (s)	0.07	0.7	0.02	0.07
imaging area (μm)	100 × 100	80 × 50	200 × 200	200 × 200
sampled pixels	400 × 400	400 × 250	800 × 800	800 × 800
nominal spatial resolution	250 nm	200 nm	250 nm	250 nm
confocal spatial resolution	200 nm	260 nm	225 nm	200 nm

Table 1. Experimental parameters for Raman imaging of the different samples.

Methods

Materials, sampling, and substrates. For imaging of CuS and atmospheric particles, aluminium targets, obtained by sputtering highly purified aluminium onto microscope cover slips[39], were used as substrates.

CuS particles were purchased from Alfa-Aesar (99.8%, Alfa-Aesar, Ward Hill, MA, USA, CAS No. 1317-40-4). The liquid suspension consisting of the CuS particles and highly purified water (Milli-Q Millipore System) was nebulized using an aerosol generator (TOPAS aerosol generator ATM 220). A Sioutas cascade impactor with a Leland Legacy pump (both SKC, PA, USA) was deployed at a flow rate of 9 L min⁻¹ to precipitate the nebulized CuS particles onto the aluminium targets. The whole procedure was carried out so as to ensure a suitable spatial distribution of the CuS particles on the aluminium surface.

For the imaging of the cell samples, P31 tumour cells were grown in RPMI medium with 10% FBS and 1% penicillin/streptomycin on gold-coated silicon wafers (~24 h). Then the cells were treated with evofosfamide (50 μM). The cells were rinsed with deionised water and dried under vacuum conditions.

The ceramics sample was synthesized as described by Konegger et al.[31, 32]. A polished cross-section of the sample was analysed using the spectroscopic techniques without any further processing.

The aerosol sample was taken on 20 November 2016 at the Getreidemarkt in Vienna at the TU Wien. The sampling onto the described aluminium-coated glass cover slips was also done using a Sioutas cascade impactor in combination with a Leland Legacy pump at a flow rate of 9 L min⁻¹. Sampling time was 1.5 h, resulting in a total sampled air volume of 810 L. For the combined imaging, particles sampled on the second stage, with an aerodynamic particle diameter cut-off between 2.5 and 1 μm, were chosen.

Raman micro-spectroscopic imaging. Raman imaging was performed using a WITec alpha 300RSA + Raman microscope. This instrument is equipped with four Raman lasers (a 488 nm DPSS, a 532 nm frequency-doubled NdYAG, a 632.8 nm HeNe, and a 785 nm diode laser) and two lens-based spectrographs. The spectrograph used for the UV/VIS spectral region is equipped with a 300, 600, and 1200 lines per mm grating and an Andor Newton electron multiplying charge-coupled device (EMCCD). The spectrograph used for the NIR spectral region is equipped with a 300 and 600 lines per mm grating and an Andor iDus Deep Depletion CCD. Raman images were recorded using the software package WITec Control 4.1. The parameters for Raman imaging of the four samples are summarized in Table 1.

Electron microscopy and energy-dispersive X-ray imaging. Electron microscopy and EDX imaging was applied using a FEI Quanta 200 electron microscope with an EDAX EDX detector. Scanning electron microscope images were obtained in secondary and backscattered electron mode. EDX imaging was done at a resolution of 1024 × 768 pixels and an acceleration voltage of 20 kV. EDX images were accumulated for about one hour to achieve reasonable signal-to-noise ratios of the elemental distributions. The parameters for EDX imaging of the four samples are summarized in Table 2.

ToF-SIMS imaging. ToF-SIMS imaging was performed using a ToF-SIMS[5] (ION-TOF GmbH, Münster, Germany) equipped with a 25 keV bismuth liquid metal ion gun (LMIG). Burst alignment (BA) mode was applied on all samples with a pulse width of 57.4 ns for the analysis of areas from 100 μm × 100 μm to 300 μm × 300 μm utilizing Bi_3^+ primary ion clusters. The primary ion beam was scanned over the region of interest with a repetition rate of 14,300 Hz. Target currents of approximately 0.04 pA and spot size of approximately 200 nm are achieved, but the mass resolution is decreased to $m/\Delta m \sim 300$. For sputtering, a dual source column (DSC) was operated at 1 keV. In positive ion mode, sputtering was done with O_2^+ at a current of 190 nA, and in negative ion mode, sputtering was done with Cs^+ at a current of 75 nA. All samples were recorded in the non-interlaced sputter mode (the sputtering cycle and the analysis cycle are decoupled and separated by a specified pause time). During the pause time, a low energy electron flood gun (20 eV) was used to compensate surface charging.

Data preprocessing and handling. The software package WITec Project 4.1 was used for post-processing of the Raman images. Raman spectral images were exported as graphical ASCII files. EDX elemental images were post-processed using the EDAX software package TEAM and exported as CSV files. For data interpretation of the ToF-SIMS images, only masses above a certain threshold intensity were taken into consideration (e.g., 1% of

	CuS particles	Cell samples	Ceramics	Aerosol Sample
Magnification	2600×	4000×	1500×	1200×
SEM acceleration voltage (kV)	10	5	25	10
EDX imaged area (μm)	129 × 99	87 × 67	225 × 173	282 × 216
EDX spatial resolution (nm)	126	85	220	275
Exported elements from EDX	Al, Cu, O, S	Au, Br, C, Ca, Cl, K, Mg, N, Na, O, P, Pd, S	Al, C, Fe, Hf, O, Si, Y, Zr	Al, Ba, C, Ca, Cl, Cr, Cu, Fe, K, Mg, Mn, N, Na, O, P, S, Si, Zn

Table 2. Experimental parameters for SEM-EDX imaging of the different samples.

the base peak). Data evaluation was carried out by using ION-TOF SurfaceLab (Version 6.5, ION-TOF GmbH, Münster, Germany). The mass spectra were internally calibrated using well-known and easily assignable masses (e.g., Na^+, Al^+, K^+, C^-, C_2^-, P^-, PO^-, etc.). The error in calibration was kept below 100 ppm. The individual mass deviation of signals not used for calibration might be larger. An online mass shift correction and a spatial shift correction within the software package were used to achieve optimum mass assignment as well as highly resolved secondary ion images. For further data treatment, the secondary ion images were exported as BIF6 files.

Single imaging datasets were combined into multisensor hyperspectral datasets using the software package Imagelab (Epina GmbH, Austria). All datasets were imported and aligned to a common background image for each of the four samples. Finally, the individual hyperspectral datasets were combined to give a multisensor hyperspectral datacube as described by Lohninger and Ofner[17].

The final spatial resolution of the fused datasets is depending on the spatial resolutions of every single method and on the lateral offset as well as the rotation of the single datasets to each other. In general, a maximum decrease by the square-root of 2 of the worst spatial resolution can be expected (at maximum rotation). However, by ensuring a minimized rotational misalignment, spatial resolutions of the fused datasets can be expected to be hardly worse compared to the worst resolution of a single technique (CuS particles: 250 nm; Tumour cells: 260 nm; Ceramic Composite: 225 nm; Environmental aerosol: 275 nm).

SPDCs for the individual elements from the EDX and masses from the SIMS data cubes were defined by applying single intensity descriptors of the signals. For the RMS data cube, triangle template peaks, baseline-corrected and –uncorrected integral descriptors of selected bands as well as centroid descriptors (for the ν(C-H) spectral region) and ratio descriptors of two bands (ZrO_2-bands in the ceramics dataset) were defined. Further details on the definition of spectral descriptors, spectral preprocessing, and standardization and application of multivariate statistics to the multisensor hyperspectral datasets, as well as introductions to the different statistical methods, can be found in preceding studies[17, 18].

The authors provide the multisensor data sets and the spectral descriptors used in this study. Further information can be found in the ImageLab data repository (http://www.imagelab.at/en_data_repository.html datasets DS009 - DS012).

References
 1. Hayat, M. A. Correlative Microscopy in Biology. Instrumentation and Methods. (Academic Press, 1987).
 2. McDonald, K. L. A review of high-pressure freezing preparation techniques for correlative light and electron microscopy of the same cells and tissues. *J. Microsc.* **235**, 273–281 (2009).
 3. Zhang, P. Correlative cryo-electron tomography and optical microscopy of cells. *Curr. Opin. Struct. Biol.* **23**, 763–770 (2013).
 4. Van de Plas, R., Yang, J., Spraggins, J. & Caprioli, R. M. Image fusion of mass spectrometry and microscopy: a multimodality paradigm for molecular tissue mapping. *Nat Meth* **12**, 366–372 (2015).
 5. da Cunha, M. M. L. *et al.* Overview of chemical imaging methods to address biological questions. *Micron* **84**, 23–36 (2016).
 6. Wu, J. S. *et al.* Imaging and elemental mapping of biological specimens with a dual-EDS dedicated scanning transmission electron microscope. *Ultramicroscopy* **128**, 24–31 (2013).
 7. Sobol, O. *et al.* First use of data fusion and multivariate analysis of ToF-SIMS and SEM image data for studying deuterium-assisted degradation processes in duplex steels. *Surf. Interface Anal.* n/a-n/a, doi:10.1002/sia.6015 (2016).
 8. Artyushkova, K., Farrar, J. O. & Fulghum, J. E. Data fusion of XPS and AFM images for chemical phase identification in polymer blends. *Surf. Interface Anal.* **41**, 119–126 (2009).
 9. Chen, Y. Data fusion for accurate microscopic rough surface metrology. *Ultramicroscopy* **165**, 15–25 (2016).
10. Gowen, A. A. & Dorrepaal, R. M. Multivariate chemical image fusion of vibrational spectroscopic imaging modalities. *Molecules* **21** (2016).
11. Chughtai, S. *et al.* A multimodal mass spectrometry imaging approach for the study of musculoskeletal tissues. *Int. J. Mass Spectrom.* **325–327**, 150–160 (2012).
12. Smith, E. A. *et al.* Quantitatively imaging chromosomes by correlated cryo-fluorescence and soft x-ray tomographies. *Biophys. J.* **107**, 1988–1996 (2014).
13. Liu, Y., Meirer, F., Krest, C. M., Webb, S. & Weckhuysen, B. M. Relating structure and composition with accessibility of a single catalyst particle using correlative 3-dimensional micro-spectroscopy. *Nat Commun* **7**, 1–8 (2016).
14. Liu, Y., Kiss, A. M., Larsson, D. H., Yang, F. & Pianetta, P. To get the most out of high resolution X-ray tomography: A review of the post-reconstruction analysis. *Spectrochim. Acta - Part B At. Spectrosc.* **117**, 29–41 (2016).
15. Lanni, E. J. *et al.* Correlated Imaging with C 60 -SIMS and Confocal Raman Microscopy: Visualization of Cell-Scale Molecular Distributions in Bacterial Biofilms. *Anal. Chem.* **86**, 10885–10891 (2014).
16. Bonta, M. *et al.* Elemental mapping of biological samples by the combined use of LIBS and LA-ICP-MS. *J. Anal. At. Spectrom.* **31**, 252–258 (2016).
17. Lohninger, H. & Ofner, J. Multisensor hyperspectral imaging as a versatile tool for image-based chemical structure determination. *Spectrosc. Eur.* **26**, 6–10 (2014).
18. Ofner, J. *et al.* Chemometric Analysis of Multisensor Hyperspectral Images of Precipitated Atmospheric Particulate Matter. *Anal. Chem.* **87**, 9413–9420 (2015).

19. Jolliffe, I. T. Principal Component Analysis, Second Edition (2002).
20. MacQueen, J. B. Kmeans Some Methods for classification and Analysis of Multivariate Observations. *5th Berkeley Symp. Math. Stat. Probab. 1967* **1**, 281–297 (1967).
21. Kaufman, L. & Rousseeuw, P. J. *Finding Groups in Data*. (John Wiley & Sons, Inc., 1990), doi:10.1002/9780470316801.
22. Nascimento, J. M. P. & Dias, J. M. B. Vertex component analysis: a fast algorithm to unmix hyperspectral data. *IEEE Trans. Geosci. Remote Sens.* **43**, 898–910 (2005).
23. Phuruangrat, A., Thongtem, T. & Thongtem, S. Characterization of copper sulfide hexananoplates, and nanoparticles synthesized by a sonochemical method. *Chalcogenide Lett.* **8**, 291–295 (2011).
24. Frezzotti, M. L., Tecce, F. & Casagli, A. Raman spectroscopy for fluid inclusion analysis. *J. Geochemical Explor.* **112**, 1–20 (2012).
25. Milekhin, A. G. *et al.* Combination of surface- and interference-enhanced Raman scattering by CuS nanocrystals on nanopatterned Au structures. *Beilstein J. Nanotechnol.* **6**, 749–754 (2015).
26. Lafuente, B., Downs, R. T., Yang, H. & Stone, N. In *Highlights in Mineralogical Crystallography* 1–30 (DE GRUYTER, 2016), doi:10.1515/9783110417104-003.
27. Socrates, G. Infrared and Raman Characteristic Group Frequencies. (John Wiley & Sons, Ltd, 2011).
28. Huang, W. E., Li, M., Jarvis, R. M., Goodacre, R. & Banwart, S. A. *Shining light on the microbial world the application of Raman microspectroscopy. Advances in applied microbiology* **70** (Elsevier Inc., 2010).
29. Niaura, G. Raman Spectroscopy in Analysis of Biomolecules. *Encyclopedia of Analytical Chemistry*. doi:10.1002/9780470027318.a0212.pub3 (2014).
30. Baenke, F., Peck, B., Miess, H. & Schulze, A. Hooked on fat: the role of lipid synthesis in cancer metabolism and tumour development. *Dis. Model. Mech.* **6**, 1353–1363 (2013).
31. Konegger, T. Image-analytical evaluation of the spatial distribution of particulate fillers in ceramic composites prepared via the polymer-derived ceramics route. *Mater. Charact.* **86**, 9–20 (2013).
32. Konegger, T., Schneider, P., Bauer, V., Amsüss, A. & Liersch, A. Structure and performance of polymer-derived bulk ceramics determined by method of filler incorporation. *IOP Conf. Ser. Mater. Sci. Eng.* **47**, 12054 (2013).
33. Barberis, P., Merle-Méjean, T. & Quintard, P. On Raman spectroscopy of zirconium oxide films. *J. Nucl. Mater.* **246**, 232–243 (1997).
34. Solin, S. A. & Ramdas, A. K. Raman spectrum of diamond. *Phys. Rev. B* **1**, 1687–1698 (1970).
35. Prawer, S. & Nemanich, R. J. Raman spectroscopy of diamond and doped diamond. *Philos. Trans. A. Math. Phys. Eng. Sci.* **362**, 2537–2565 (2004).
36. Syme, R. W. G., Lockwood, D. J. & Kerr, H. J. Raman spectrum of synthetic zircon (ZrSiO 4) and thorite (ThSiO 4). *J. Phys. C Solid State Phys.* **10**, 1335–1348 (1977).
37. Buzgar, N. & Apopei, A. The Raman study of certain carbonates. *Geol. Tomul L* **3** (2009).
38. Ivleva, N. P., McKeon, U., Niessner, R. & Pöschl, U. Raman Microspectroscopic Analysis of Size-Resolved Atmospheric Aerosol Particle Samples Collected with an ELPI: Soot, Humic-Like Substances, and Inorganic Compounds. *Aerosol Sci. Technol.* **41**, 655–671 (2007).
39. Ofner, J. *et al.* A novel substrate for multisensor hyperspectral imaging. *J. Microsc.* **265**, 341–348 (2017).

Acknowledgements

Author Contributions

J.O., F.B. and H.L. conceived the study, processed the data, and wrote the manuscript. J.O. and B.L. did the Raman micro-spectroscopic imaging. J.O., E.E. and G.F. performed the electron microscopy and the EDX measurements. F.B. and H.H. performed the ToF-SIMS imaging and delivered the data. J.K. and C.E.-S. provided the sampling substrates. T.K. synthesized and provided the ceramics sample. S.T. and B.D. provided the tumour cells. A.K.-G. and K.W. assisted with the interpretation of the data and provided access to the sampling equipment. All coauthors discussed the results and commented on the manuscript.

Additional Information

Competing Interests: The authors declare that they have no competing interests.

Publisher's note: Springer Nature remains neutral with regard to jurisdictional claims in published maps and institutional affiliations.

5.7   Publication VII

Teaching an Old pET New Tricks: Tuning of Inclusion Body Formation and Properties by a Mixed Feed System in E. coli

David J. Wurm, Julian Quehenberger, Julia Mildner, Britta Eggenreich, Christoph Slouka, Andreas Schwaighofer, Karin Wieland, Bernhard Lendl, Vignesh Rajamanickam, Christoph Herwig, Oliver Spadiut*; Applied Microbiology and Biotechnology* 2017, 102, 667-676, 10.1007/s00253-017-8641-6,

BIOTECHNOLOGICAL PRODUCTS AND PROCESS ENGINEERING

CrossMark

Teaching an old pET new tricks: tuning of inclusion body formation and properties by a mixed feed system in *E. coli*

David J. Wurm[1] · Julian Quehenberger[1] · Julia Mildner[1] · Britta Eggenreich[1] ·
Christoph Slouka[1,2] · Andreas Schwaighofer[3] · Karin Wieland[3] · Bernhard Lendl[3] ·
Vignesh Rajamanickam[1,2] · Christoph Herwig[1,2] · Oliver Spadiut[1]

Abstract Against the outdated belief that inclusion bodies (IBs) in *Escherichia coli* are only inactive aggregates of misfolded protein, and thus should be avoided during recombinant protein production, numerous biopharmaceutically important proteins are currently produced as IBs. To obtain correctly folded, soluble product, IBs have to be processed, namely, harvested, solubilized, and refolded. Several years ago, it was discovered that, depending on cultivation conditions and protein properties, IBs contain partially correctly folded protein structures, which makes IB processing more efficient. Here, we present a method of tailored induction of recombinant protein production in *E. coli* by a mixed feed system using glucose and lactose and its impact on IB formation. Our method allows tuning of IB amount, IB size, size distribution, and purity, which does not only facilitate IB processing, but is also crucial for potential direct applications of IBs as nanomaterials and biomaterials in regenerative medicine.

Introduction

Escherichia coli is the most widely used host organism for recombinant protein production due to its well-studied genome, the existence of numerous cloning vectors and engineered strains, as well as the possibility of cheap and straight-forward cultivation to high cell densities yielding high

Julian Quehenberger and Julia Mildner contributed equally to this work.

Electronic supplementary material The online version of this article (https://doi.org/10.1007/s00253-017-8641-6) contains supplementary material, which is available to authorized users.

✉ Oliver Spadiut
oliver.spadiut@tuwien.ac.at

1   Research Division Biochemical Engineering, Institute of Chemical, Environmental and Biological Engineering, TU Wien, Vienna, Austria

2   Christian Doppler Laboratory for Mechanistic and Physiological Methods for Improved Bioprocesses, Institute of Chemical, Environmental and Biological Engineering, TU Wien, Vienna, Austria

3   Institute of Chemical Technologies and Analytics, TU Wien, Vienna, Austria

product titers (Choi et al. 2006; Huang et al. 2012; Joseph et al. 2015; Liu et al. 2015). As generally known, a careful balance between transcription and protein folding must be realized to increase the amount of soluble product (SP) in *E. coli*. If the folding machinery gets overwhelmed, correctly folded secondary structures cannot be formed and inclusion bodies (IBs) are produced (e.g., (Gatti-Lafranconi et al. 2011; Marschall et al. 2016)). In this respect, induction temperature, pH of the cultivation medium, and changes in the amino acid sequence of the product have a profound effect (Strandberg and Enfors 1991).

The by far most used *E. coli* strain is *E. coli* BL21(DE3) as it is known for a reduced amount of proteases and prevented plasmid loss (Jia and Jeon 2016; Liu et al. 2015; Rosano and Ceccarelli 2014). This strain is mostly used in combination with the T7-based pET expression system, which is usually induced by isopropyl-β-D-thiogalactopyranoside (IPTG), a nonmetabolizable molecular mimic of allolactose, known for strong induction (Bashir et al. 2016; Durani et al. 2012; Jia and Jeon 2016; Marbach and Bettenbrock 2012; Rosano and Ceccarelli 2014; Wurm et al. 2016). However, IPTG puts a high metabolic burden on *E. coli* (Dvorak et al. 2015; Haddadin and Harcum 2005), and thus causes the enhanced formation of IBs

Springer

(Sina et al. 2015; Zhang et al. 2015). For a long time, IBs were considered to be aggregates of misfolded and inactive product, which is why IB formation was highly undesired for decades (Baneyx 1999; Choi et al. 2006; Marston 1986). However, in the past few years, IBs were found to have many advantages, such as significantly higher primary yields, simple separation from cell matter, high purity, and resistance to proteolysis (Choi et al. 2006; Ramon et al. 2014; Yamaguchi and Miyazaki 2014). Consequently, marketed biopharmaceuticals from *E. coli*, such as hormones, growth factors, interleukins, and insulin, are nowadays mostly produced as IBs, followed by solubilization and refolding to get soluble target product (Eiberle and Jungbauer 2010; Schmidt 2004; Yamaguchi and Miyazaki 2014).

Furthermore, it was found that, depending on cultivation conditions, IBs contain correctly folded secondary structures (Gatti-Lafranconi et al. 2011). The presence of such structures actually allows a comparably mild treatment during IB processing to maintain the already correctly folded secondary structures and thus increase the refolding yield. Different products, such as granulocyte-colony stimulating factor, truncated forms of tumor necrosis factor, lymphotoxin α, and the marker protein green fluorescent protein, have already been successfully produced by that strategy (Jevsevar et al. 2005; Peternel et al. 2008a, b; Singh et al. 2015b; Villaverde et al. 2015).

However, most of the current recombinant protein production processes with *E. coli* still aim at the production of SP instead of IBs. In this respect, several approaches for tuning recombinant protein expression in BL21(DE3) and thus, the level of SP and IB have been proposed. While many studies suggest suboptimal growth conditions to slow down all cellular processes, including transcription and translation (Peternel and Komel 2011; Vera et al. 2007), others propose supplying limiting amounts of IPTG (below 1 μmol IPTG/g biomass) to tune down transcription (Striedner et al. 2003). In this respect, we used lactose as inducer instead of IPTG in previous studies (Wurm et al. 2017; Wurm et al. 2016), as it enhances correct protein folding and increases cell fitness (Bashir et al. 2016; Fruchtl et al. 2015; Ma et al. 2013; Wurm et al. 2016). We demonstrated that actually both SP titer and IB titer were influenced by the specific uptake rate of lactose ($q_{s,lac}$), which in turn depends on the specific uptake rate of glucose ($q_{s,glu}$; (Wurm et al. 2016, 2017)). We generated a mechanistic model (Wurm et al. 2016, 2017) for this delicate balance between ATP-related uptake of lactose at low $q_{s,glu}$ (Johnson and Brooker 2004; Kaback 2015) and carbon catabolite repression at high $q_{s,glu}$ ((Bruckner and Titgemeyer 2002; Kremling et al. 2015; Warner and Lolkema 2003); Supplementary Fig. S1).

In this follow-up study, we investigated the correlation between $q_{s,lac}$ and IB formation in more detail. For this purpose, we decoupled growth and induction by keeping $q_{s,glu}$ constant and applying different $q_{s,lac}$ to potentially vary IB titer and properties. Motivated by a study of Peternel et al., who

showed that IB properties strongly depend on cultivation conditions (Peternel et al. 2008b), we hypothesized that not only the amount of IBs, but also IB properties can be tuned by adjusting different $q_{s,lac}$ and thus different levels of induction. Furthermore, we analyzed the effects of these conditions on the expression of SP to retrieve information about the total expression capacity of *E. coli*. For this purpose, we used the model protein enhanced green fluorescence protein (eGFP), which is a representative of the beta-barrel protein class and prominent for protein quality studies.

Materials and methods

Strain

For all experiments, *E. coli* BL21(DE3) (Life technologies, Carlsbad, CA, USA), transformed with a pET21a(+) vector carrying the gene coding for enhanced green fluorescent protein (eGFP) was used as expression host.

Bioreactor cultivations

All fermentations comprised a batch cultivation followed by an uninduced fed-batch for biomass generation and a 12 h induction phase. Experiments were carried out in DASbox® Mini Bioreactors (Eppendorf, Hamburg, Germany) with a working volume of 250 mL. CO_2 and O_2 in the off-gas were analyzed by a DASGIP® GA gas analyzer (Eppendorf, Hamburg, Germany); pH by a pH-Sensor EasyFerm Plus (Hamilton, Reno, NV, USA); and dissolved oxygen (dO_2) by a Visiferm DO 120 electrode (Hamilton, Reno, NV, USA). dO_2 was kept above 40% oxygen saturation throughout the whole fermentation by supplying 2 vvm of a mixture of pressurized air and pure oxygen. Biomass concentration was estimated using a soft-sensor-tool (Wechselberger et al. 2013), feed-flowrates were adjusted with the DASbox® MP8 Multi Pump Module, pH was kept at 7.2 by supplying 12.5% NH_4OH, stirring speed was set to 2000 rpm, and temperature was set to 35 °C during batch and fed-batch and was lowered to 30 °C during induction. All process parameters were logged and controlled by the DASware® control.

Five hundred milliliters of sterile DeLisa pre-culture medium (DeLisa et al. 1999) supplemented with 0.1 g/L ampicillin and 8 g/L glucose were aseptically inoculated from frozen stocks (1.5 mL, − 80 °C). Pre-cultures were grown overnight (20 h) in 2500-mL high-yield shake flasks in an Infors HR Multitronshaker (Infors, Bottmingen, Switzerland) at 37 °C and 250 rpm. One hundred-fifty milliliters of DeLisa batch medium (DeLisa et al. 1999) supplemented with 0.1 g/L ampicillin and 10 g/L glucose were inoculated with 15 mL of pre-culture. After sugar depletion, a fed-batch phase to reach about 25 g_{cells}/L using a glucose feed with 250 g/L glucose was

carried out. Induction was performed by addition of 0.5 mM IPTG or supplementing the feed with different amounts of lactose to reach the $q_{s,glu}$ and $q_{s,lac}$ values displayed in Fig. 1c.

Sampling

Samples were taken at the beginning and end of the batch and fed-batch phase, furthermore during the induction phase after 0, 1, 2, 4, 7, 10 and 12 h. Quantification of biomass dry cell weight (DCW) was performed gravimetrically as in (Wurm et al. 2016); substrates and metabolites were measured by high-pressure liquid chromatography (HPLC) as in (Wurm et al. 2016).

Product analysis

Product titer quantification by reversed-phase HPLC Cell pellets of 5 mL fermentation broth were resuspended (100 mM Tris, 10 mM EDTA pH 7.4) to 4.0 g/L DCW and homogenized at

1500 bar for six passages (EmulsiflexC3; Avestin, Ottawa, Canada). After centrifugation (15 min, 13,000 rcf, 4 °C), the supernatant was used for analysis of SP. For IB quantification, the pellet was washed twice [(i) 50 mM Tris, 5 mM EDTA, pH 8.0; (ii) 50 mM Tris, 0.5 M NaCl, 0.02% (*w/v*) Tween 80, pH 8], aliquoted and stored at − 20 °C. Pellets were resuspended in a solution containing 1 part Tris-buffer (50 mM Tris, 5 mM EDTA, pH 8.0) and four parts solubilization buffer (6 M guanidine hydrochloride (GuHCl), 50 mM Tris, pH 8.0 with 5.0% (*v/v*) 2-mercaptoethanol added right before use), incubated for 2 h on a shaker at room temperature and vortexed every 30 min. Product quantification was carried out by HPLC analysis (UltiMate 3000; Thermo Fisher, Waltham, MA, USA) using a reversed phase column (EC 150/4.6 Nucleosil 300-5 C8; Macherey-Nagel, Düren, Germany). The product was quantified with an UV detector (Thermo Fisher, Waltham, MA, USA) at 280 nm using bovine serum albumin as standard. Mobile phase was composed of water (buffer A) and acetonitrile (buffer B) both supplemented with 0.1% (*v/v*) tetrafluoride acetic acid. A linear gradient from

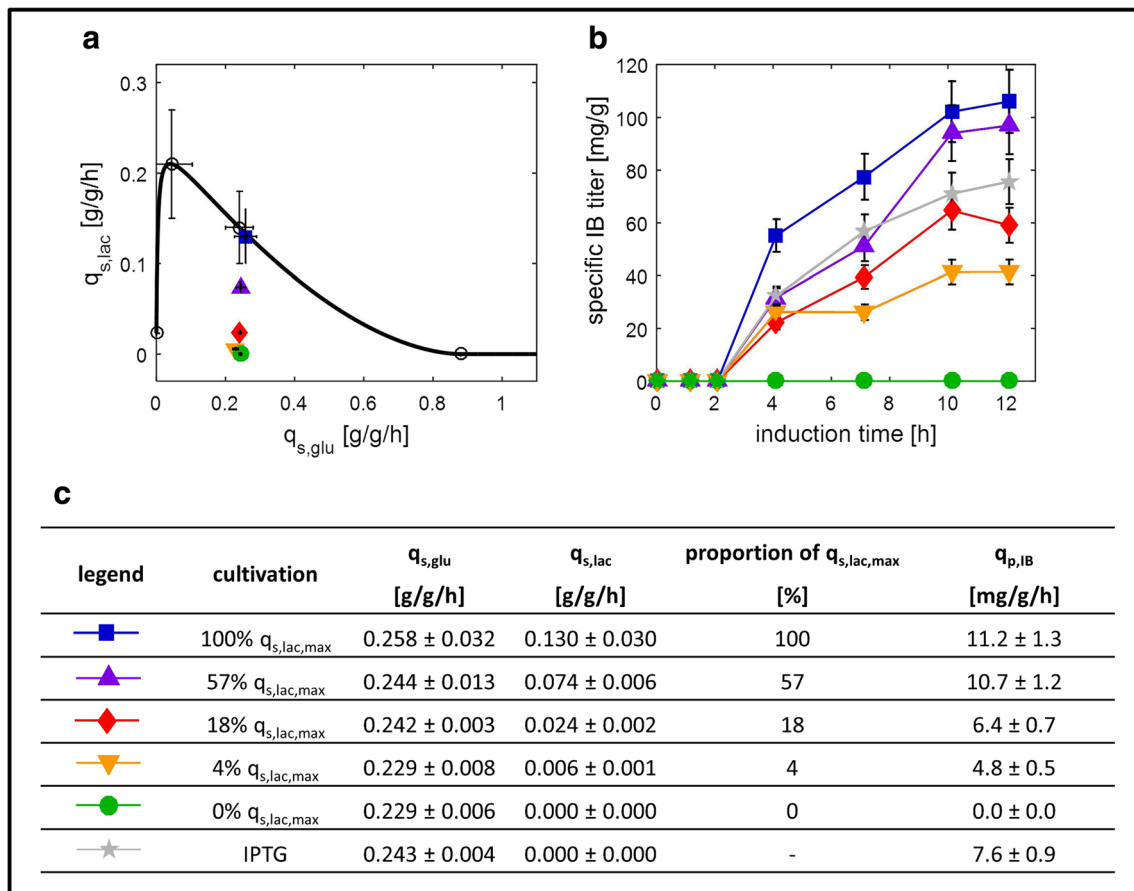| legend	cultivation	$q_{s,glu}$ [g/g/h]	$q_{s,lac}$ [g/g/h]	proportion of $q_{s,lac,max}$ [%]	$q_{p,IB}$ [mg/g/h]
■	100% $q_{s,lac,max}$	0.258 ± 0.032	0.130 ± 0.030	100	11.2 ± 1.3
▲	57% $q_{s,lac,max}$	0.244 ± 0.013	0.074 ± 0.006	57	10.7 ± 1.2
◆	18% $q_{s,lac,max}$	0.242 ± 0.003	0.024 ± 0.002	18	6.4 ± 0.7
▼	4% $q_{s,lac,max}$	0.229 ± 0.008	0.006 ± 0.001	4	4.8 ± 0.5
●	0% $q_{s,lac,max}$	0.229 ± 0.006	0.000 ± 0.000	0	0.0 ± 0.0
★	IPTG	0.243 ± 0.004	0.000 ± 0.000	-	7.6 ± 0.9

Fig. 1 Tuning IB formation rate. **a** Black line indicates the maximum specific uptake rate of lactose ($q_{s,lac}$) as a function of the specific uptake rate of glucose ($q_{s,glu}$) for an *Escherichia coli* BL21(DE3) strain producing enhanced green fluorescent protein (eGFP). Data points (open circles) were obtained from several batch and fed-batch cultivations and fitted by the mechanistic model according to our previous study (Wurm et al. 2016, 2017). Colored symbols indicate performed

experiments as shown in (**b**) and (**c**). Error bars indicate deviation of the respective q_s over induction time. **b** Specific IB titer in mg_{eGFP}/g_{cells} as a function of time for lactose and IPTG (0.5 mM) induction. **c** Summary of specific sugar uptake rates (q_s) and specific IB formation rates ($q_{p,IB}$). The error bars of the specific IB titers indicate the standard deviation (namely 11.25%), which was identified by performing biological replicates of the center point (i.e., 18% $q_{s,lac,max}$)

30% (v/v) acetonitrile to 100% acetonitrile was applied. The error bars in all figures displaying product titers were identified by performing biological replicates of the center point (18% $q_{s,lac,max}$) and was quantified to be 11.25% for IBs and 11.50% for SP.

Size determination by scanning electron microscopy (SEM)

Washed and aliquoted IB samples were resuspended in ultrapure water. One hundred microliters of appropriate dilution of the suspension were pipetted on a gold-sputtered (10–50 nm) polycarbonate filter (Millipore-Merck, Darmstadt, Germany) using reusable syringe filter holders with a diameter of 13 mm (Sartorius, Goettingen, Germany). One hundred microliters of ultrapure water were added and pressurized air was used for subsequent filtration. Additional 200 μL of ultrapure water were used for washing. The wet filters were fixed on a SEM sample holder using graphite adhesive tape and subsequently sputtered with gold to increase the contrast of the sample. SEM was performed using a QUANTA FEI SEM (Thermo Fisher, Waltham, MA, USA) using a secondary electron detector (SED). The acceleration voltage of the electron beam was set between 3 to 5 kV. The diameters of the IBs were evaluated by measuring 50 IBs on SEM pictures using the ImageJ plugin Fiji (Laboratory for Optical and Computational Instrumentation (LOCI), University of Wisconsin-Madison, USA).

Morphology analysis by atomic force microscopy (AFM) For determination of morphological aspects of IBs, samples were prepared the same way as for SEM except for gold sputtering, which was not necessary for these measurements. Measurements were performed on a WITec alpha 300RSA+ (WITec GmbH, Ulm, Germany) in tapping mode (AC).

Secondary structure analysis by infrared spectroscopy (IR) IR measurements were performed by an external-cavity quantum cascade laser-based IR transmission setup using the path length of 38 μm, described in detail by Alcaraz et al. (Alcaraz et al. 2015). Calculation of degree of spectral overlap by $s_{1,2}$ has been described by Schwaighofer et al. (Schwaighofer et al. 2016).

Solubilization and refolding of IB

Homogenized cell pellets were resuspended in ultrapure water and 30 μL of the suspension were pipetted into 96 microtiter plates. Subsequently, 70 μL of urea stock solution supplemented with 50 mM Tris at pH 8 were simultaneously added to each well (Qi et al. 2015).

Refolding was carried out at 30 °C for 4.5 h by diluting 10 μL of solubilizate with 190 μL of refolding buffer (50 mM Tris, 100 mM NaCl, 1 mM DTT, pH 7.5) (Enoki et al. 2004) resulting in a final protein concentration of 0.2 mg/mL.

Impurity monitoring

Impurity monitoring to asses purity after solubilization and refolding was carried out chromatographically (UltiMate 3000; Thermo Fisher, Waltham, MA, USA) using a high-performance size-exclusion chromatography column (MAbPac™ SEC-1, Thermo Scientific, Waltham, MA, USA). For solubilized samples a GuHCl buffer (4 M GuHCl, 50 mM Bis-Tris, 300 mM NaCl, pH 6.8) and for refolded samples a phosphate buffer (100 mM Na_2HPO_4, 300 mM NaCl, pH 6.8) were used as mobile phase. The flowrate was kept constant at 0.2 mL/min, the column oven temperature was 25 °C, and the method lasted 17 min. An exemplary chromatogram is displayed in Supplementary Fig. S2.

Results

Product titer

To potentially tune the titer of eGFP, we adjusted four different $q_{s,lac}$ at a $q_{s,glu}$ of around 0.25 g/g/h (Fig. 1a, c), which allows both cell growth and increased recombinant product formation (Wurm et al. 2016). Additionally, we performed a control experiment without induction to rule out effects of basal expression, as the pET system is described to be leaky (Huang et al. 2012; Jia and Jeon 2016), as well as an experiment where we induced with the standard inducer IPTG at a concentration of 0.5 mM (Bashir et al. 2016; Durani et al. 2012; Jia and Jeon 2016; Marbach and Bettenbrock 2012; Rosano and Ceccarelli 2014; Wurm et al. 2016). To assure reproducibility, we performed a biological replicate of the center point (i.e., 18% $q_{s,lac,max}$). The biomass concentration during induction of all cultivations can be found in the Supplementary Fig. S3.

IB titer

Figure 1b presents the specific IB titer, measured by reversed phase chromatography, as a function of time for 12 h of induction. Throughout the entire induction, there was a clear correlation between the specific IB formation rate ($q_{p,IB}$) and $q_{s,lac}$, namely, the higher $q_{s,lac}$ and the higher $q_{p,IB}$, leading to final titers which varied by a factor of nearly three after 12 h of induction (40 vs. 110 mg_{eGFPIB}/g_{cells}; Fig. 1b). Interestingly, we obtained a higher specific IB titer when we adjusted $q_{s,lac}$ at 100% $q_{s,lac,max}$ and 57% $q_{s,lac,max}$, respectively, compared to induction with 0.5 mM IPTG (Fig. 1b, c), emphasizing the power of lactose as a nontoxic and cheap inducer. Surprisingly, we found IBs only after more than 2 h of induction (Fig. 1b). Since we detected soluble eGFP right after induction (Supplementary Table S1), we speculate that the
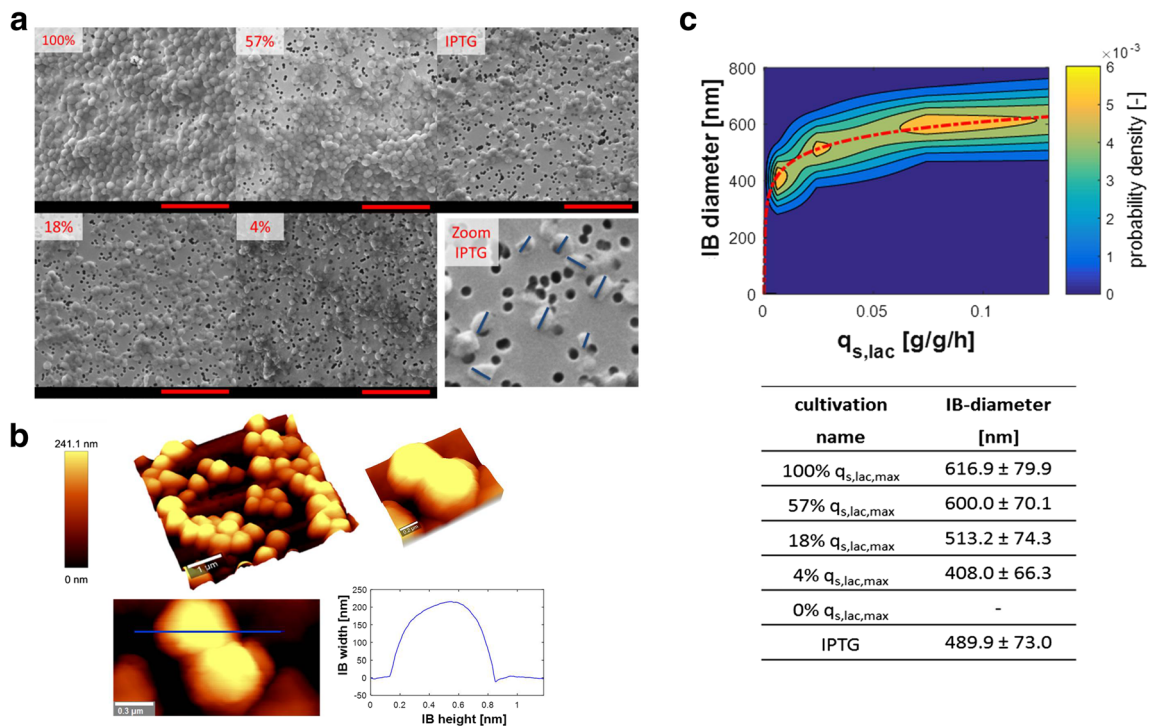
Fig. 2 Tuning the size of IBs. **a** Scanning electron microscopy pictures of IBs from different cultivations used to asses IB size, as exemplarily shown in lower right figure. Percentage indicates proportion of maximum specific lactose uptake rate ($q_{s,lac}$) used for induction. Red scale bars: 5 μm. 3.5-fold zoom for IPTG induction (lower right). **b** (i) exemplary atomic force microscopy picture of typical IBs showing spherical shape, (ii) and (iii) zoom in on IB particle, and (iv) topography cross-section of an isolated IB (indicated as a blue line in iii). **c** Probability density plot of IB size distribution after 12 h of induction as a function of $q_{s,lac}$ showing that IB size can be tuned by $q_{s,lac}$. Red-dashed line indicates logarithmic fit between IB size and $q_{s,lac}$ (degree of freedom = 2, R^2 = 0.99). IB diameter with standard deviation from different cultivations after 12 h of induction are shown in the table. Standard deviation was evaluated from measuring 50 IBs per sample

amount and the size of IBs in the first 2 h of induction were below the detection limit of the applied analytics.

Soluble and total product titer

Even though the main focus of this study was the investigation of IBs, we also analyzed SP and total product titers. With respect to SP, we observed the same correlation between $q_{s,lac}$ and q_p as seen for IBs during the first 4 h of induction, namely, the higher $q_{s,lac}$ and the higher $q_{p,SP}$. However, after 12 h of induction, the highest specific SP titer was obtained at the lowest $q_{s,lac}$. Apparently, cells which were strongly induced right from the beginning of induction somehow reduced $q_{p,SP}$ after a certain time, whereas cells induced at a low $q_{s,lac}$ of only 4% $q_{s,lac,max}$ steadily produced SP over time (Supplementary Table S1).

The total productivity also showed a clear trend in the first 4 h of induction, as increasing $q_{s,lac}$ gave more total product (Supplementary Table S1). However, after 12 h of induction, all induction conditions resulted in comparable amounts of total product.

Summarizing, with respect to product titer, we concluded that, (1) $q_{p,IB}$ can be tuned by $q_{s,lac}$ over the whole induction time; (2) in the first 4 h of induction, higher $q_{s,lac}$ gave higher $q_{p,SP}$, while after 12 h of induction, this situation was reversed; and (3) after 12 h of induction, the amount of total product was comparable for all induction conditions tested.

Tuning IB properties

In order to potentially link IB properties to induction conditions, we analyzed size, morphology, size distribution, and the presence of secondary structures of the formed IBs.

IB size

We assessed IB size by scanning electron microscopy (SEM; Fig. 2a), supported the results by atomic force microscopy (AFM; Fig. 2b) and correlated the IB size to the respective $q_{s,lac}$ (Fig. 2c). In fact, we were able to tune IB size by induction, as shown in Fig. 2c. A clear

Fig. 3 Size distribution of IBs over induction time. **a** Probability density plot of IB size distribution as a function of induction time indicating that IB size increases, while also, the distribution gets broader over time for different induction conditions. **b** IB diameter with standard deviation from different cultivations conditions at different time points of induction

cultivation name	4h induction	7h induction	10h induction	12h induction
100% $q_{s,lac,max}$	431.0 ± 53.4 nm	457.8 ± 56.5 nm	571.4 ± 64.1 nm	616.9 ± 80.7 nm
57% $q_{s,lac,max}$	368.5 ± 56.1 nm	482.1 ± 66.9 nm	514.0 ± 64.9 nm	600.0 ± 70.8 nm
18% $q_{s,lac,max}$	344.4 ± 60.1 nm	398.3 ± 60.1 nm	465.6 ± 69.0 nm	513.2 ± 75.0 nm
4% $q_{s,lac,max}$	370.5 ± 63.2 nm	398.0 ± 62.8 nm	401.7 ± 63.5 nm	408.0 ± 67.0 nm
0% $q_{s,lac,max}$	0 nm	0 nm	0 nm	0 nm
IPTG	401.2 ± 55.5 nm	432.9 ± 45.1 nm	591.4 ± 60.6 nm	489.9 ± 73.8 nm
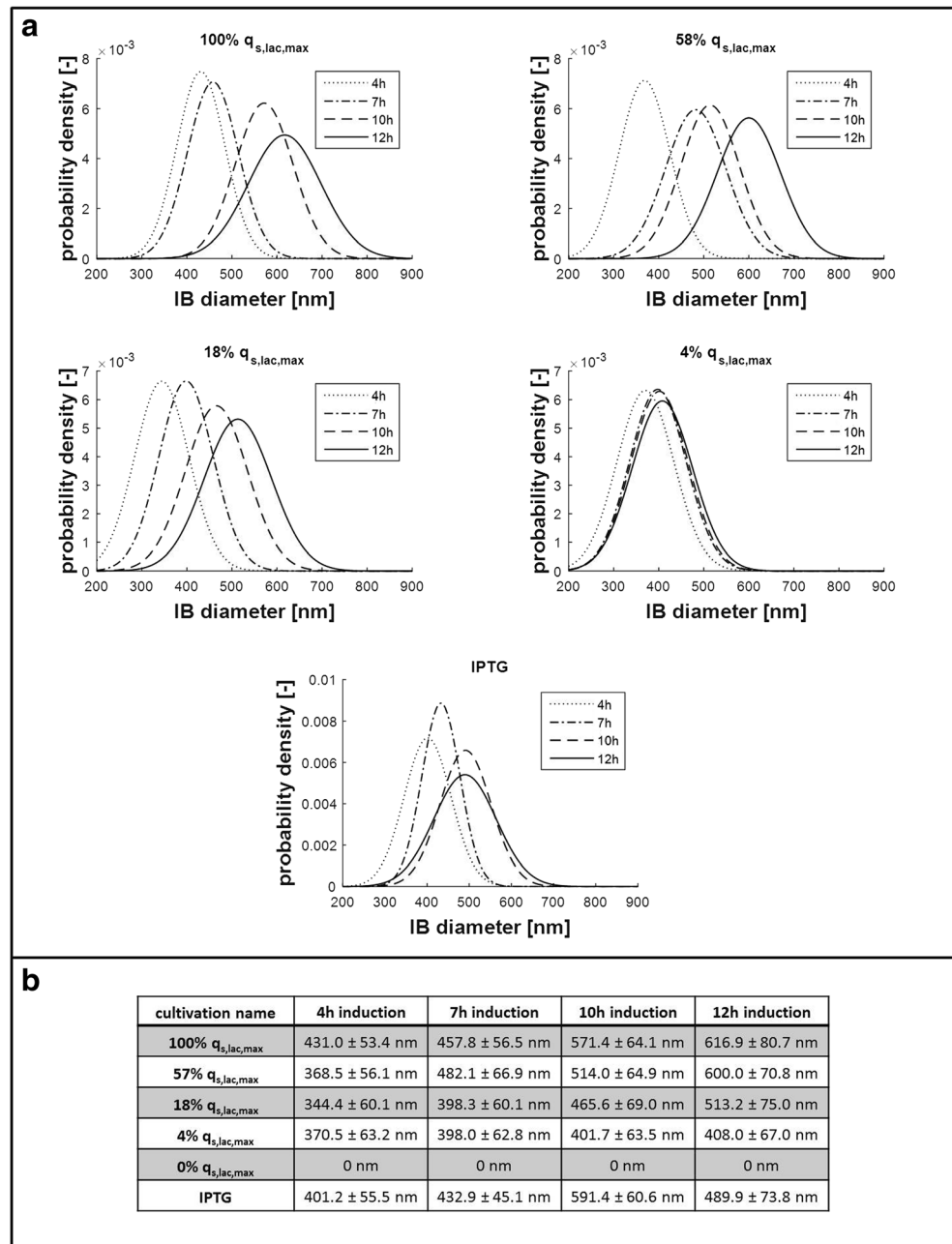
correlation between $q_{s,lac}$ and IB size was observed: smaller IBs were produced when less lactose was specifically taken up (logarithmic fit, degree of freedom = 2, $R^2 = 0.991$).

IB morphology

Using AFM analysis, we found that eGFP IBs were of spherical shape (exemplarily shown in Fig. 2b), whose surface area can be calculated by $A = d^2 \cdot \pi$. This underlines the high importance of the IB diameter (d) as it impacts the surface area (A), by the power of 2. Thus, it

is advantageous to produce large IBs in order to minimize the surface area, where impurities can potentially adhere to.

IB size distribution as a function of time

We found that not only IB size, but also IB size distribution increased as a function of induction time (Fig. 3). Although this trend was not as apparent for induction by IPTG, we observed an increasingly broad size distribution of formed IBs for all experiments with lactose induction (100% $q_{s,lac}$, 57% $q_{s,lac}$, 18% $q_{s,lac}$, and 4% $q_{s,lac}$). We explain this
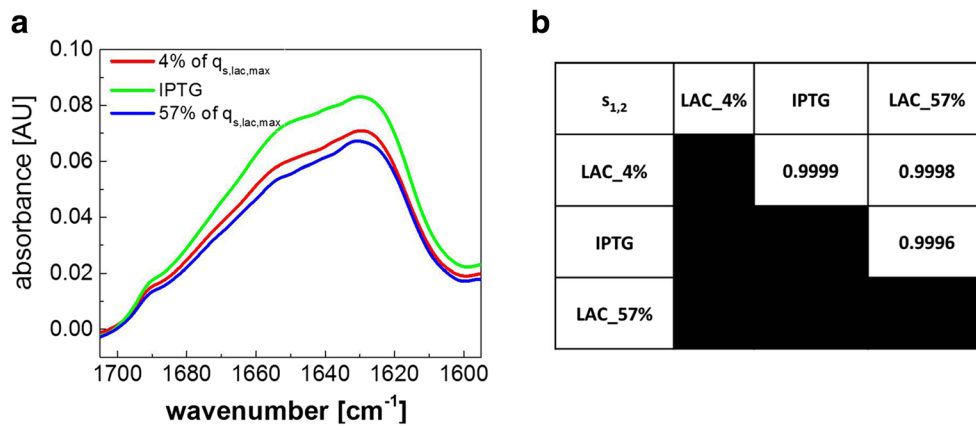
Fig. 4 Secondary structure of IBs measured by infrared (IR) spectroscopy. **a** IR spectra of IBs from different induction regimes. Maxima for β-sheet secondary structure appear at approx. 1630 and 1690 cm^{-1} in the IR spectrum, whereas the shoulder at approx. 1655 cm^{-1} is attributed to α-helical secondary structure. **b** Table shows degree of spectral overlap ($s_{1,2}$) for IBs from different induction regimes (4% $q_{s,lac,max}$ (small IBs, Ø = 408 nm); IPTG (medium IBs, Ø = 490 nm); and 57% $q_{s,lac,max}$ (large IBs, Ø = 600 nm)) calculated according to Schwaighofer et al. (Schwaighofer et al. 2016) demonstrating a very high degree of spectral overlap for all samples. The value of $s_{1,2}$ ranges from 0 to 1, corresponding to no overlapping and complete overlapping, respectively

phenomenon by the generally accepted hypothesis that the IB is passed on to only one daughter cell after cell division, leaving one daughter cell without IB and one daughter cell with an IB that continues to grow (Peternel and Komel 2011). Thus, in order to get an IB population of distinct size, which is not only important for IB processing, but also for potential direct application as nanomaterials and biomaterials (Diez-Gil et al. 2010; Garcia-Fruitos et al. 2009; Garcia-Fruitos et al. 2012; Peternel and Komel 2011; Upadhyay et al. 2012; Villaverde et al. 2015), we recommend short induction times.

IB secondary structures

The secondary structures found in the agglomerated product can affect its properties and also the processing of IBs. Therefore, we assessed the secondary structure of the IBs by infrared (IR) spectroscopy. IR spectroscopy showed high similarity and overlaps in the IR spectra of all IBs indicating that the amount of correctly folded secondary structures were not significantly different (evaluated by degree of spectral overlap > 99.9%, (Schwaighofer et al. 2016)) independent of the
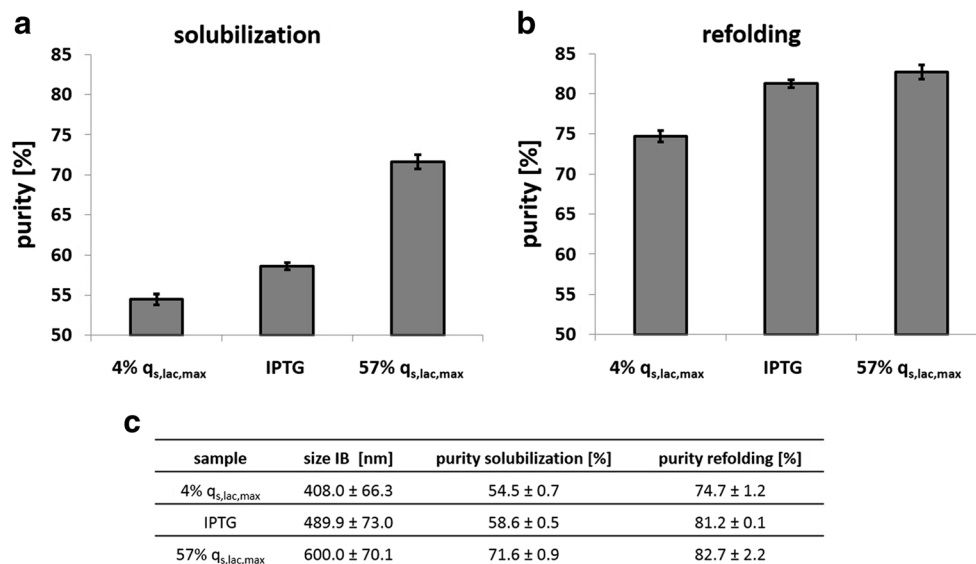

sample	size IB [nm]	purity solubilization [%]	purity refolding [%]
4% $q_{s,lac,max}$	408.0 ± 66.3	54.5 ± 0.7	74.7 ± 1.2
IPTG	489.9 ± 73.0	58.6 ± 0.5	81.2 ± 0.1
57% $q_{s,lac,max}$	600.0 ± 70.1	71.6 ± 0.9	82.7 ± 2.2

Fig. 5 Impact of IB size on IB purity. **a** Purity determined by HPLC impurity monitoring using size exclusion chromatography (SEC) after solubilization with 2 M urea of IBs with a small (Ø = 408 nm), medium (Ø = 490 nm) and large (Ø = 600 nm) diameter. Standard deviation was evaluated from technical duplicates. **b** Purity of eGFP determined by HPLC impurity monitoring using SEC after refolding. Standard deviation was evaluated from technical duplicates. **c** Overview of results from solubilization and refolding with standard deviations

induction strategy (exemplarily shown in Fig. 4 for 4% $q_{s,lac,max}$ (small IBs, $\varnothing = 408$ nm); IPTG (medium IBs, $\varnothing = 490$ nm); and 57% $q_{s,lac,max}$ (large IBs, $\varnothing = 600$ nm).

IB processing

We hypothesized that the IB diameter and thus the surface area are crucial for subsequent IB processing, as (1) more impurities can adhere on particles with a larger surface area and (2) solubilization efficiency depends on accessibility to protein aggregates. To test the impact of the specific surface area (nm^2/g_{IB}) on IB processing and potentially omit necessary IB washing steps during production processes, we solubilized the different IBs with 2, 4, and 6 M urea, respectively, without any prior washing step. We found solubilization yields of > 99% for all IB preparations and all three urea concentrations. Since solubilizing at lower urea concentrations has the advantage of conserving correctly folded secondary structures resulting in an increased refolding yield (Margreiter et al. 2008; Singh et al. 2015b; Upadhyay et al. 2012), we used 2 M urea for solubilization of IBs to analyze IB purity. We used IBs from induction with IPTG and 4% $q_{s,lac,max}$ and 57% $q_{s,lac,max}$, respectively, to cover IBs of different sizes (Fig. 5). As shown in Fig. 5a, the purity of the IBs differed vastly. The high specific surface area of the small IBs formed at 4% $q_{s,lac,max}$ caused the adherence of more impurities compared to the low specific surface area of large IBs formed at 57% $q_{s,lac,max}$ (Fig. 5a, c). While small IBs showed a purity of only 55%, large IBs had a purity of more than 70%. Fig. 5b shows the purity after refolding, which was done by a standard dilution approach tailored for eGFP (Enoki et al. 2004). The purity of all IB preparations increased after refolding, as host cell derived impurities precipitated during this process step. After refolding, the purity was increased to 75% for small IBs, 81% for medium IBs, and 83% for large IBs. This observation confirms our hypothesis that a higher specific surface area attracts more impurities. The purity of IBs is of great importance as the presence of impurities can potentially reduce the refolding yield (Singh et al. 2015a). Furthermore, IB purity is a key aspect once IBs are directly used as nanomaterials and biomaterials (Diez-Gil et al. 2010; Garcia-Fruitos et al. 2009, 2012; Peternel and Komel 2011; Upadhyay et al. 2012; Villaverde et al. 2015).

Summarizing, we were able to show that tailored induction by lactose not only allows tuning of IBs size, but also IB purity. For the three different IB preparations we obtained a comparable refolding yield of > 95%. We expected these comparable values since we had found the same amount of

correctly folded secondary structures in the different IBs by IR spectroscopy before (Fig. 4).

Discussion

In this study, we showed that a mixed feed strategy with glucose and lactose not only impacts total product, soluble product, and IB titer in *E. coli*, but also IB properties, which in turn affects IB processing. Our method of tailored lactose induction allows precise tuning of the specific IB formation rate and is, thus, a valuable alternative to expression tuning by reducing the overall cell metabolism. Moreover, our approach allows prolonged production times and thus higher overall titers. Furthermore, it is of great interest that the size and the size distribution of IBs can be tuned by our method.

Size is an important property of IBs, since it significantly impacts IB harvesting and processing (Upadhyay et al. 2012). Furthermore, IB size is a crucial factor for potential direct applications of IBs as nanomaterials and biomaterials in regenerative medicine (Diez-Gil et al. 2010; Garcia-Fruitos et al. 2009, 2012; Peternel and Komel 2011; Upadhyay et al. 2012; Villaverde et al. 2015). We also showed that IB size correlates with purity and thus affects IB processing. We suggest to induce the cells at $q_{s,lac,max}$ to obtain highest productivity and generate large IBs, which leads to a lower specific surface area and thus less adherent impurities. For eGFP IBs, we did not find any impact of induction on the amount of correctly folded secondary structures in the IBs. However, for more complex proteins, which often easily overwhelm the folding machinery, as well as for periplasmic proteins, where translocation is the rate limiting step, our strategy of tuning transcription by $q_{s,lac}$ might be required to obtain higher product titers. Also, when expressing a protein which is toxic to *E. coli* and negatively affects its metabolism, it is beneficial to regulate recombinant protein expression to reduce metabolic burden and potential cell death. Summarizing, we present a method, which allows (1) tuning the specific formation rate of IBs, as well as (2) adjusting size, size distribution, and purity of IBs, which is not only fundamental for IB processing, but also for applications where IBs are directly used.

Author contribution DJW, JQ and JM performed and evaluated the experiments. BE assisted in planning and carrying out downstream processing. DJW and CS performed and evaluated SE measurements. AS performed and evaluated IR measurements, KW performed and evaluated AFM measurements, and BL supervised these analyses. VR assisted in performing and evaluating chromatography for product analysis. OS planned, initiated and supervised the study. DJW, JQ, BE and OS

Compliance with ethical standards

Ethical approval This article does not contain any studies with human participants or animals performed by any of the authors.

Conflict of interest The authors declare that they have no conflict of interest.

References

Alcaraz MR, Schwaighofer A, Kristament C, Ramer G, Brandstetter M, Goicoechea H, Lendl B (2015) External-cavity quantum cascade laser spectroscopy for mid-IR transmission measurements of proteins in aqueous solution. Anal Chem 87(13):6980–6987. https://doi.org/10.1021/acs.analchem.5b01738

Baneyx F (1999) Recombinant protein expression in *Escherichia coli*. Curr Opin Biotechnol 10:411–421. https://doi.org/10.1016/S0958-1669(99)00003-8

Bashir H, Ahmed N, Khan MA, Zafar AU, Tahir S, Khan MI, Khan F, Husnain T (2016) Simple procedure applying lactose induction and one-step purification for high-yield production of rhCIFN. Biotechnol Appl Biochem 63(5):708–714. https://doi.org/10.1002/bab.1426

Bruckner R, Titgemeyer F (2002) Carbon catabolite repression in bacteria: choice of the carbon source and autoregulatory limitation of sugar utilization. FEMS Microbiol Lett 209(2):141–148. https://doi.org/10.1111/j.1574-6968.2002.tb11123.x

Choi JH, Keum KC, Lee SY (2006) Production of recombinant proteins by high cell density culture of *Escherichia coli*. Chem Eng Sci 61(3):876–885. https://doi.org/10.1016/j.ces.2005.03.031

DeLisa MP, Li JC, Rao G, Weigand WA, Bentley WE (1999) Monitoring GFP-operon fusion protein expression during high cell density cultivation of *Escherichia coli* using an on-line optical sensor. Biotechnol Bioeng 65(1):54–64. https://doi.org/10.1002/(Sici)1097-0290(19991005)65:1<54::Aid-Bit7>3.0.Co;2-R

Diez-Gil C, Krabbenborg S, Garcia-Fruitos E, Vazquez E, Rodriguez-Carmona E, Ratera I, Ventosa N, Seras-Franzoso J, Cano-Garrido O, Ferrer-Miralles N, Villaverde A, Veciana J (2010) The nanoscale properties of bacterial inclusion bodies and their effect on mammalian cell proliferation. Biomaterials 31(22):5805–5812. https://doi.org/10.1016/j.biomaterials.2010.04.008

Durani V, Sullivan BJ, Magliery TJ (2012) Simplifying protein expression with ligation-free, traceless and tag-switching plasmids. Protein Expr Purif 85:9–17. https://doi.org/10.1016/j.pep.2012.06.007

Dvorak P, Chrast L, Nikel PI, Fedr R, Soucek K, Sedlackova M, Chaloupkova R, de Lorenzo V, Prokop Z, Damborsky J (2015) Exacerbation of substrate toxicity by IPTG in *Escherichia coli* BL21(DE3) carrying a synthetic metabolic pathway. Microb Cell Fact 14:201. https://doi.org/10.1186/s12934-015-0393-3

Eiberle MK, Jungbauer A (2010) Technical refolding of proteins: do we have freedom to operate? Biotechnol J 5(6):547–559. https://doi.org/10.1002/biot.201000001

Enoki S, Saeki K, Maki K, Kuwajima K (2004) Acid denaturation and refolding of green fluorescent protein. Biochemistry 43(44):14238–14248. https://doi.org/10.1021/bi048733+

Fruchtl M, Sakon J, Beitle R (2015) Expression of a collagen-binding domain fusion protein: effect of amino acid supplementation, inducer type, and culture conditions. Biotechnol Prog 31:503–509. https://doi.org/10.1002/btpr.2048

Garcia-Fruitos E, Rodriguez-Carmona E, Diez-Gil C, Ferraz RM, Vazquez E, Corchero JL, Cano-Sarabia M, Ratera I, Ventosa N, Veciana J, Villaverde A (2009) Surface cell growth engineering assisted by a novel bacterial. Nanomaterial Adv Mater 21(42):4249–4253. https://doi.org/10.1002/adma.200900283

Garcia-Fruitos E, Vazquez E, Diez-Gil C, Corchero JL, Seras-Franzoso J, Ratera I, Veciana J, Villaverde A (2012) Bacterial inclusion bodies: making gold from waste. Trends Biotechnol 30(2):65–70. https://doi.org/10.1016/j.tibtech.2011.09.003

Gatti-Lafranconi P, Natalello A, Ami D, Doglia SM, Lotti M (2011) Concepts and tools to exploit the potential of bacterial inclusion bodies in protein science and biotechnology. FEBS J 278(14):2408–2418. https://doi.org/10.1111/j.1742-4658.2011.08163.x

Haddadin FT, Harcum SW (2005) Transcriptome profiles for high-cell-density recombinant and wild-type *Escherichia coli*. Biotechnol Bioeng 90(2):127–153. https://doi.org/10.1002/bit.20340

Huang CJ, Lin H, Yang X (2012) Industrial production of recombinant therapeutics in *Escherichia coli* and its recent advancements. J Ind Microbiol Biotechnol 39(3):383–399. https://doi.org/10.1007/s10295-011-1082-9

Jevsevar S, Gaberc-Porekar V, Fonda I, Podobnik B, Grdadolnik J, Menart V (2005) Production of nonclassical inclusion bodies from which correctly folded protein can be extracted. Biotechnol Prog 21(2):632–639. https://doi.org/10.1021/bp[0497839

Jia B, Jeon CO (2016) High-throughput recombinant protein expression in *Escherichia coli*: current status and future perspectives. Open Biol 6(8):160196. https://doi.org/10.1098/rsob.160196

Johnson JL, Brooker RJ (2004) Control of H+/lactose coupling by ionic interactions in the lactose permease of *Escherichia coli*. J Membr Biol 198:135–146. https://doi.org/10.1007/s00232-004-0667-x

Joseph BC, Pichaimuthu S, Srimeenakshi S, Murthy M, Selvakumar K, Ganesan M, Manjunath SR (2015) An overview of the parameters for recombinant protein expression in *Escherichia coli*. J Cell Sci 6(05):1. https://doi.org/10.4172/2157-7013.1000221

Kaback HR (2015) A chemiosmotic mechanism of symport. Proc Natl Acad Sci USA 112:1259–1264. https://doi.org/10.1073/pnas.1419325112

Kremling A, Geiselmann J, Ropers D, de Jong H (2015) Understanding carbon catabolite repression in *Escherichia coli* using quantitative models. Trends Microbiol 23:99–109. https://doi.org/10.1016/j.tim.2014.11.002

Liu M, Feng X, Ding Y, Zhao G, Liu H, Xian M (2015) Metabolic engineering of *Escherichia coli* to improve recombinant protein production. Appl Microbiol Biotechnol 99(24):10367–10377. https://doi.org/10.1007/s00253-015-6955-9

Ma X, Su E, Zhu Y, Deng S, Wei D (2013) High-level expression of glutaryl-7-aminocephalosporanic acid acylase from *Pseudomonas diminuta* NK703 in *Escherichia coli* by combined optimization strategies. J Biotechnol 168:607–615. https://doi.org/10.1016/j.jbiotec.2013.08.024

Marbach A, Bettenbrock K (2012) Lac operon induction in *Escherichia coli*: systematic comparison of IPTG and TMG induction and influence of the transacetylase LacA. J Biotechnol 157:82–88. https://doi.org/10.1016/j.jbiotec.2011.10.009

Margreiter G, Schwanninger M, Bayer K, Obinger C (2008) Impact of different cultivation and induction regimes on the structure of cytosolic inclusion bodies of TEM1-β-lactamase. Biotechnol J 3(9-10):1245–1255. https://doi.org/10.1002/biot.200800072

Marschall L, Sagmeister P, Herwig C (2016) Tunable recombinant protein expression in *E. coli*: enabler for continuous processing? Appl Microbiol Biotechnol 100(13):5719–5728. https://doi.org/10.1007/s00253-016-7550-4

Marston FA (1986) The purification of eukaryotic polypeptides synthesized in *Escherichia coli*. Biochem J 240(1):1–12. https://doi.org/10.1042/bj2400001

Peternel S, Komel R (2011) Active protein aggregates produced in *Escherichia coli*. Int J Mol Sci 12(12):8275–8287. https://doi.org/10.3390/ijms12118275

Peternel S, Grdadolnik J, Gaberc-Porekar V, Komel R (2008a) Engineering inclusion bodies for non denaturing extraction of functional proteins. Microb Cell Factories 7(1):34. https://doi.org/10.1186/1475-2859-7-34

Peternel S, Jevsevar S, Bele M, Gaberc-Porekar V, Menart V (2008b) New properties of inclusion bodies with implications for biotechnology. Biotechnol Appl Biochem 49(4):239–246. https://doi.org/10.1042/BA20070140

Qi XM, Sun YF, Xiong SD (2015) A single freeze-thawing cycle for highly efficient solubilization of inclusion body proteins and its refolding into bioactive form. Microb Cell Factories 14(1):24. https://doi.org/10.1186/s12934-015-0208-6

Ramon A, Senorale-Pose M, Marin M (2014) Inclusion bodies: not that bad. Front Microbiol 5:56. https://doi.org/10.3389/fmicb.2014.00056

Rosano GL, Ceccarelli EA (2014) Recombinant protein expression in *Escherichia coli*: advances and challenges. Front Microbiol 5:172. https://doi.org/10.3389/fmicb.2014.00172

Schmidt FR (2004) Recombinant expression systems in the pharmaceutical industry. Appl Microbiol Biotechnol 65(4):363–372. https://doi.org/10.1007/s00253-004-1656-9

Schwaighofer A, Alcaraz MR, Araman C, Goicoechea H, Lendl B (2016) External cavity-quantum cascade laser infrared spectroscopy for secondary structure analysis of proteins at low concentrations. Sci Rep 6(1):33556. https://doi.org/10.1038/srep33556

Sina M, Farajzadeh D, Dastmalchi S (2015) Effects of environmental factors on soluble expression of a humanized anti-TNF-alpha scFv antibody in *Escherichia coli*. Adv Pharm Bull 5(4):455–461. 10.15171/apb.2015.062

Singh A, Upadhyay V, Panda AK (2015a) Solubilization and refolding of inclusion body proteins. Methods Mol Biol 1258:283–291. https://doi.org/10.1007/978-1-4939-2205-5_15

Singh A, Upadhyay V, Upadhyay AK, Singh SM, Panda AK (2015b) Protein recovery from inclusion bodies of *Escherichia coli* using mild solubilization process. Microb Cell Factories 14(1):41. https://doi.org/10.1186/s12934-015-0222-8

Strandberg L, Enfors SO (1991) Factors influencing inclusion body formation in the production of a fused protein in *Escherichia coli*. Appl Environ Microbiol 57(6):1669–1674

Striedner G, Cserjan-Puschmann M, Potschacher F, Bayer K (2003) Tuning the transcription rate of recombinant protein in strong *Escherichia coli* expression systems through repressor titration. Biotechnol Prog 19(5):1427–1432. https://doi.org/10.1021/bp034050u

Upadhyay AK, Murmu A, Singh A, Panda AK (2012) Kinetics of inclusion body formation and its correlation with the characteristics of protein aggregates in *Escherichia coli*. PLoS One 7(3):e33951. https://doi.org/10.1371/journal.pone.0033951

Vera A, Gonzalez-Montalban N, Aris A, Villaverde A (2007) The conformational quality of insoluble recombinant proteins is enhanced at low growth temperatures. Biotechnol Bioeng 96(6):1101–1106. https://doi.org/10.1002/bit.21218

Villaverde A, Corchero JL, Seras-Franzoso J, Garcia-Fruitos E (2015) Functional protein aggregates: just the tip of the iceberg. Nanomedicine (Lond) 10(18):2881–2891. https://doi.org/10.2217/nnm.15.125

Warner JB, Lolkema JS (2003) CcpA-dependent carbon catabolite repression in bacteria. Microbiol Mol Biol Rev 67(4):475–490. https://doi.org/10.1128/MMBR.67.4.475-490.2003

Wechselberger P, Sagmeister P, Herwig C (2013) Real-time estimation of biomass and specific growth rate in physiologically variable recombinant fed-batch processes. Bioprocess Biosyst Eng 36(9):1205–1218. https://doi.org/10.1007/s00449-012-0848-4

Wurm DJ, Veiter L, Ulonska S, Eggenreich B, Herwig C, Spadiut O (2016) The *E. coli* pET expression system revisited-mechanistic correlation between glucose and lactose uptake. Appl Microbiol Biotechnol 100(20):8721–8729. https://doi.org/10.1007/s00253-016-7620-7

Wurm DJ, Hausjell J, Ulonska S, Herwig C, Spadiut O (2017) Mechanistic platform knowledge of concomitant sugar uptake in *Escherichia coli* BL21(DE3) strains. Sci Rep 7:45072. https://doi.org/10.1038/srep45072

Yamaguchi H, Miyazaki M (2014) Refolding techniques for recovering biologically active recombinant proteins from inclusion bodies. Biomol Ther 4(1):235–251. https://doi.org/10.3390/biom4010235

Zhang Z, Kuipers G, Niemiec Ł, Baumgarten T, Slotboom DJ, de Gier JW, Hjelm A (2015) High-level production of membrane proteins in *E. coli* BL21(DE3) by omitting the inducer IPTG. Microb Cell Factories 14(1):142. https://doi.org/10.1186/s12934-015-0328-z

Further author contributions

1) Tallian, C.; Herrero-Rollett, A.; Stadler, K.; Vielnascher, R.; Wieland, K.; Weihs, A. M.; Pellis, A.; Teuschl, A. H.; Lendl, B.; Amenitsch, H.; *Gübitz, G. M.* European Journal of Pharmaceutics and Biopharmaceutics Structural insights into pH-responsive drug release of self-assembling human serum albumin-silk fibroin nanocapsules. *Eur. J. Pharm. Biopharm.* **2018**, *133*, 176–187.

2) Quartinello, F.; Tallian, C.; Auer J.; Schön, H.; Vielnascher R.; Weinberger S.; Wieland K.; Herrero-Rollet, A.; Lendl, B.; Pellis, A.; Gübitz, G. M. Smart Tesctiles in Wound Care: Functionalization of Cotton/PET Blends with Antimicrobial Nanoparticles. *Submitted to ACS Applied Materials and Interfaces*

3) Comnea-Stancu, I. R.; Wieland, K.; Ramer, G.; Schwaighofer, A.; Lendl, B. On the Identification of Rayon/Viscose as a Major Fraction of Microplastics in the Marine Environment: Discrimination between Natural and Man-made Cellulosic Fibers by Fourier Transform Infrared Spectroscopy. *Appl. Spectrosc.* **2017**, *71*, 939–950.

4) Mozdyniewicz, D.; Schwaighofer, A.; Wieland, K.; Häubl, M.; Lendl, B. FTIR Micro-Spectroscopy for Characterisation of Radial Substituent Diffusion in Cellulose II-Beads. *Lenzinger Berichte* **2018**, *94*, 27–31.

6   Curriculum vitae

PERSONAL INFORMATION

Name	Karin Wieland
Address	Enzersdorferstraße 2/1
	A- 2345 Brunn am Gebirge, Austria
Mail	karin.wieland@tuwien.ac.at
Mobile	+43680 2423034
Date of birth	23 February 1989
Nationality	Austrian

EDUCATION

02/2015 to date	**PhD programme Technical Chemistry**
	Vienna University of Technology (TU Wien)
10/2012-12/2014	**Master programme Technical Chemistry - Biotechnology and Bioanalytics**
	Vienna University of Technology (TU Wien)
	Graduation with distinction
10/2008-10/2012	**Bachelor programme Technical Chemistry**
	Vienna University of Technology (TU Wien)
	Graduation with distinction

WORK EXPERIENCE AND INTERNSHIPS

02/2015	**Research for PhD thesis (TU Wien)**
	Vibrational spectroscopy of biological samples at the nanoscale
11/2017-01/2018	**Guest Researcher (NIST/CNST; Gaithersburg, MD)**
	Nanoscale imaging of liposomes as drug-carrier systems
07/2017-09/2017	**Guest Researcher (NIST/CNST; Gaithersburg, MD)**
	Nanoscale imaging of liposomes as drug-carrier systems
11/2013-07/2014	**Research for Master thesis (TU Wien)**
	Hyperspectral imaging of hyphae and spores of *Penicillium chrysogenum* using confocal Raman microspectroscopy (in collaboration with Sandoz GmbH)
03/2013-04/2013	**Research Internship (TU Wien)**
	Characterization of two quantum cascade lasers for quasi-simultaneous determination of NO and NO_2 concentrations
01/2011-02/2011	**Research Internship (TU Wien)**
	Time-resolved FTIR spectroscopy investigating RNA duplex formation

07/2010-12/2010	**Research for Bachelor thesis (TU Wien)**
	Time-resolved FTIR spectroscopy investigating H/D-exchange reaction of carbohydrates focusing on trehalose, glucose, maltose and sucrose
07/2006-07/2006	**Summer School Programme (University of Graz)**
	Analysis and identification of proteins

SKILLS & COURSES

Languages	German mother tongue
	English fluent
	French fluent
IT skills	ImageLab, CorelDRAW, Eigenvector Solo+MIA, Origin
	Python
ASCOS 2015	9th Advanced Study Course on Optical Chemical Sensors and Biosensors

ACHIEVEMENTS

12/2019	FemChem TU Wien Travel Grant
04/2018	ERC bursary awarded by FACSS (Federation of Analytical Chemistry and Spectroscopy Societies)
	Prozessanalytik-Award (Process Analytics Award for Master thesis)
09/2015	
10/2013-07/2014	*TUtheTOP* - The High Potential Programme at Vienna University of Technology
09/2012-07/2013	*"Leistungsstipendium"* of the Vienna University of Technology for special performances in studies and examinations

CONFERENCE CONTRIBUTIONS (presenting author underlined)

1. <u>K. Wieland</u>, V.U. Weiss, G. Ramer, A. Centrone, G. Allmaier, B. Lendl:
"Vibrational spectroscopy at the nanoscale – Analytical approaches for spectroscopy- based investigation of nanocarriers";
Invited talk: Agilent Forum Analytik, Vienna, Austria; February 12-13, 2019

2. <u>K. Wieland</u>, V.U. Weiss, G. Ramer, A. Centrone, G. Allmaier, B. Lendl:
"Improving chemotherapeutics' efficiency by monitoring drug encapsulation on a

single nanocarrier level.";
Poster: IRDG Christmas meeting, University College London; December 20, 2018.

3. <u>K. Wieland</u>, V.U. Weiss, G. Ramer, A. Centrone, G. Allmaier, B. Lendl:
"Accessing drug encapsulation in liposomal nanocarriers through hyphenation of nES-GEMMA and PTIR spectroscopy";
Talk: SciX 2018, Atlanta, GA, USA; October 22-26, 2018

4. <u>K. Wieland</u>, V.U. Weiss, G. Ramer, A. Centrone, G. Allmaier, B. Lendl: *"Nanoscale IR imaging for drug detection in nES-GEMMA size-selected nanocarriers"*;
Talk: acib Workshop Neosetac "Biomedical Applications of Nanotechnology", Tulln, Austria; October 2, 2018

5. <u>K. Wieland,</u> B. Lendl: *"Good vibrations in the micro- and nanoscale – Analytical approaches for the spectroscopic investigation of nES-GEMMA size-selected liposomes"*,
Invited talk: Seminar of Modern Analytical Chemistry, Vienna, Austria; June 22, 2018

6. <u>K. Wieland</u>, V.U. Weiss, G. Ramer, A. Centrone, G. Allmaier, B. Lendl: *"Nanoscale IR imaging of nES GEMMA size-selected liposomal drug delivery systems"*;
Talk: Spring SciX, Glasgow, Scotland; April 17-20, 2018

7. <u>K. Wieland</u>, V.U. Weiss, G. Ramer, A. Centrone, G. Allmaier, B. Lendl: *"Resonance enhanced PTIR imaging for the investigation of nES GEMMA size-selected liposomal drug delivery systems at the nanoscale"*;
Talk: Optics and Photonics Conference at John Hopkins University, Baltimore MD 21218-2608, USA; December 11, 2017

8. <u>K. Wieland</u>, C. Herwig, B. Lendl:
"Good Vibrations – Infrared and Raman spectroscopy in bio(techno)logical applications";
Invited talk: Seminar of Biosystems and Biomaterials Division, NIST (Gaithersburg, MD); September 5, 2017

9. <u>K. Wieland</u>, S. Tauber, H. Rasoulimehrabani, S. Radel, B. Lendl:
"Ultrasound-enhanced Raman Spectroscopy for Process Analytics";
Talk: PAC School (imPACts), Linz, Austria; June 7, 2017

10. I. Raluca Comnea-Stancu, <u>K. Wieland</u>, G. Ramer, A. Schwaighofer, B. Lendl:
"Classification and Investigation of Cellulosic Fibers by Vibrational Spectroscopy";
Poster: IRDG Christmas Meeting, University College London; December 19, 2016.

11. <u>K. Wieland</u>, H. Rasoulimehrabani, S. Tauber, C. Gasser, S. Radel, B. Lendl:
"Ultrasound-Enhanced In-line Raman Sensing of Solid Samples in Liquid

Matrices";
Poster: SciX 2016, Minneapolis, Minnesota, USA, September 18-23, 2016.

12. <u>K. Wieland</u>, J. Kuligowski, C. Koch, J. Ofner, D. Ehgartner, C. Herwig, B. Lendl:
"Using PLS-DA to evaluate the quality of spore inoculum to optimize biotechnological process control"
Poster: XVI Chemometrics in Analytical Chemistry, Barcelona, Spain, June 6-10, 2016.

13. <u>K. Wieland</u>, C. Koch, M. El-Zahry, J. Ofner, H. Grothe, H. Lohninger, C. Herwig, B. Lendl:
"Hyperspectral imaging of hyphae and spores of P. chrysogenum using confocal Raman spectroscopy and SERS";
Poster: ICORS XXIV, Jena, Germany, August 10-15, 2014.

14. K. Wieland, <u>A. Hobro</u>, C. Wagner, W. Buchegger, M. Vellekoopp, B. Lendl:
"Time-resolved Studies of RNA Duplex Formation using a Microfluidic Mixing Device";
Poster: ICAVS VI, Sonoma County, California; June 09-12, 2011.

15. <u>G. Ramer</u>, K. Wieland, C. Wagner, W.H. Buchegger, M. Kraft, M. Vellekoop, B. Lendl:
"2D-CoS Time-Resolved Infrared Spectroscopy of Sugar HD-Exchange";
Poster: 2DCoS-6, Sonoma County. California; June 9-12, 2011.

16. <u>K. Wieland</u>, C. Wagner, W.H. Buchegger, M. Vellekoop, M. Kraft, B. Lendl:
"TR-FTIR studies of H/D exchange in carbohydrates using a microfluidic system";
Poster: IRDG Christmas Meeting 2010, University College London; December 16, 2010.